Large Eddy Simulations of Flow and Heat Transfer in the Developing and 180° Bend Regions of Ribbed Gas Turbine Blade Internal Cooling Ducts with Rotation – Effect of Coriolis and Centrifugal Buoyancy Forces

Evan A. Sewall

Dissertation submitted to the faculty of the Virginia Polytechnic Institute and State University in partial fulfillment of the requirements for the degree of

Doctor of Philosophy
In
Mechanical Engineering

Danesh K. Tafti; Chair
Karen A. Thole; Co-Chair
Clinton L. Dancey
Wing F. Ng
Saad A. Ragab

November 28, 2005
Blacksburg, VA

Keywords: Large Eddy Simulation (LES), Ribbed Ducts, Coriolis Effects, Centrifugal Buoyancy, Developing Flow, 180° Bend

Large Eddy Simulations of Flow and Heat Transfer in the Developing and 180° Bend Regions of Ribbed Gas Turbine Blade Internal Cooling Ducts with Rotation – Effect of Coriolis and Centrifugal Buoyancy Forces

Evan A. Sewall

ABSTRACT

Increasing the turbine inlet temperature of gas turbine engines significantly increases their power output and efficiency, but it also increases the likelihood of thermal failure. Internal passages with tiny ribs are typically cast into turbine blades to cool them, and the ability to accurately predict the flow and heat transfer within these channels leads to higher design reliability and prevention of blade failure resulting from local thermal loading. Prediction of the flow through these channels is challenging, however, because the flow is highly turbulent and anisotropic, and the presence of rotational body forces further complicates the flow. Large Eddy Simulations are used to study these flows because of their ability to predict the unsteady flow effects and anisotropic turbulence more reliably than traditional RANS closure models.

Calculations in a stationary duct are validated with experiments in the developing flow, fully developed, and 180º bend regions to establish the accuracy and prediction capability of the LES calculations and to aid in understanding the major flow structures encountered in a ribbed duct. It is found that most flow and heat transfer calculations come to within 10-15% of the measurements, typically showing excellent agreement in all comparisons.

In the developing flow region, Coriolis effects are found to destabilize turbulence and increase heat transfer along the trailing wall (pressure side), while decreasing leading wall heat transfer by stabilizing turbulence. Coriolis forces improve flow turning in the 180º bend by shifting the shape of the separated recirculation zone at the tip of the dividing wall and increasing the mainstream flow area. In addition, turbulence is attenuated near the leading wall throughout the bend, while Coriolis forces have little effect on trailing wall turbulence in the bend.

Introducing and increasing centrifugal buoyancy in the developing flow region increases trailing wall heat transfer monotonically. Along the leading wall, buoyancy increases the size of the recirculation zones, shifting the peak heat transfer to a region upstream of the rib, which decreases heat transfer at low buoyancy parameters but increases it as the buoyancy parameter is increased beyond a value of 0.3. Centrifugal buoyancy in the 180º bend initially decreases the size of the recirculation zone at the tip of the dividing wall, increasing flow area and decreasing flow impingement. At high buoyancy, however, the recirculation zone shifts to the middle of the bend, increasing flow resistance and causing strong flow impingement on the back wall.

The Boussinesq approximation is used in the buoyancy calculations, but the accuracy of the approximation comes into question in the presence of large temperature differences. A variable property algorithm is developed to calculate unsteady low speed flows with large density variations resulting from large temperature differences. The algorithm is validated against two test cases: Rayleigh-Bénard convection and Poiseuille-Bénard flow.

Finally, design issues in rotating ribbed ducts are considered. The fully developed assumption is discussed with regard to the developing flow region, and controlling the recirculation zone in the 180º bend is suggested as a way to determine the blade tip heat transfer and pressure drop across the bend.

Granting Institution

The research was supported by the US DOE, Office of Fossil Energy, National Energy Technology Laboratory. Any opinions, findings, conclusions, or recommendations expressed herein are those of the author and do not necessarily reflect the views of the DOE. This work was also supported by National Computational Science Alliance under MCA98N042N and utilized the IA-64 Itanium Linux cluster at the National Center for Supercomputing Applications.

To Emily, whose hard work, love, and encouragement
were a vital part in the completion of this project

Acknowledgements

I am extremely grateful for the guidance and patience of my advisor, Dr. Danesh Tafti, who set up this project and worked alongside me with every part of it. It's been a consistent struggle to keep me on task and to help me along when I reached roadblocks that I had no idea how to get around. Without your help I wouldn't know 10% of what I know now about CFD or LES.

I am also thankful to my co-advisor, Dr. Karen Thole, who not only kept me as an "adopted member" of the VTEXCCL lab, but oversaw the experimental part of this project and offered a tremendous amount of technical help, advice, and encouragement.

Thanks to all five of my committee members: Dr. Tafti, Dr. Thole, Dr. Ragab, Dr. Dancey, and Dr. Ng. You've have taught me in classes, given me guidance on this project, and put up with all the scheduling conflicts!

The test facility was built by a Senior Design group from the Class of 2003: Todd Beirne, Rob Bellonio, Susan Brewton, Avery Dunigan, Jeff Hodges, Scott Walsh, and Al Wilder. You were an excellent group to work with, and you produced a well-built test rig that eventually produced an excellent set of data and went on to become a teaching tool for future ME lab projects. Thanks, guys!

The laser Doppler velocimetry (LDV) measurements were carried out by Andrew Graham, who spent countless hours in the lab taking data. Your ability to overcome countless problems and persevere at obtaining accurate data sets was extremely important for me in having measurements with which to validate my calculations.

The heat transfer measurements were set up by Kaitlin Keim and Sara Borka. This turned out to be an extremely tedious process in converting the test section to a heated test section and benchmarking the setup. The measurements were taken by Sara and became another important part in validating my work.

I have been very privileged to work alongside the other members of the HPCFD Lab: Samer Abdel-Wahab, Sundar Narayan, Wilfred Patrick, Aroon Viswanathan, Shi-Ming Li, Ali Rozati, Anant Shah, Mohammed Elyan, Pradeep Gopalakrishnan, and Keegan Delaney. It's been a joy to work with all of you. Thanks for keeping me sane, helping me out with countless questions about everything, and for sitting through hours of practice presentations. And no, I can't get you all jobs once I start work!

I would like to extend a special thanks to Andrew Duggleby, who's encouraged me as a friend who actually understands my research. Thanks for keeping me going during all the frustrating times.

Finally, this project could never have been accomplished without the support and encouragement of my wife, Emily, who has spent too many nights going to bed alone while her husband worked late at the lab. Thank you for being patient with me, loving me, and encouraging me every single day of this project, and thanks for all the gourmet meals and snacks you've brought to the lab on nights that I've worked late!

Table of Contents

List of Figures

List of Tables

Nomenclature

a^i	contravariant basis vector
Bo	buoyancy parameter ($=\left(\frac{\Delta\rho}{\rho}\right)\cdot\left(\frac{r}{D_h}\right)\cdot \mathrm{Ro}^2$)
C_p	specific heat
C_s	square root of the Smagorinsky constant
D_h	hydraulic diameter, characteristic length
e	rib height
f	Fanning friction factor
g	square of the Jacobian of the coordinate transformation
$\overline{G}$	implicit top-hat filter
k	thermal conductivity
ΔL	change in streamwise position between two pressure measurements
Nu	local Nusselt number
$\overline{\mathrm{Nu}}$	spatially averaged Nusselt number
P	rib pitch
p	non-dimensional pressure
Pr	Prandtl number $(=\mu C_p/k)$
q''	non-dimensional heat flux on duct walls and ribs, the characteristic temperature for uniform heat flux cases is $\frac{q''D_h}{k}$
r	non-dimensional rotation radius
r_0	non-dimensional rotation radius at duct entrance
Re	Reynolds number ($= \bar{u}_{in} D_h / \nu$)
Ri	Richardson number ($= \beta\cdot(r_0 + x)\cdot \mathrm{Ro}^2$)
Ro	Rotation number ($= \Omega D_h / \bar{u}_{in}$)
S	strain rate tensor
t	non-dimensional time
T	temperature, characteristic temperature for constant temperature cases is (T_s - T_{in})
TKE	turbulent kinetic energy described by: $TKE = \frac{\left(\overline{u'}^2 + \overline{v'}^2 + \overline{w'}^2\right)}{2\overline{u_{in}}^2}$
$\vec{u}$	Cartesian velocity vector (u,v,w) or (u_1,u_2,u_3)
$\bar{u}_{in}$	inlet flow velocity / mean bulk flow velocity, characteristic velocity
u	Streamwise velocity, nondimensionalized by the characteristic velocity
v	Nondimensional cross-stream velocity
w	Nondimensional spanwise velocity
$\vec{x}$	physical coordinates (x,y,z) or (x_1,x_2,x_3)
β	thermal expansion coefficient
Ω	heat transfer surface area
ρ	density

θ non-dimensional temperature, $\left(\frac{T-T_{in}}{\frac{q''D_h}{k}}\right)$ (uniform heat flux) or $\left(\frac{T-T_{in}}{T_s-T_{in}}\right)$ (constant temperature)

$\vec{\xi}$ computational coordinates (ξ,η,ζ)

μ dynamic viscosity

v kinematic viscosity

subscripts:

in inlet to calculation domain; average bulk velocity

ref reference

rms root mean square; fluctuating quantities nondimensionalized by the characteristic velocity

s surface; Smagorinsky constant

t turbulent

0 normalizing parameter (smooth duct)

1 streamwise component of velocity vector

Chapter 1. Introduction

The goal of the project "Enhanced Prediction Techniques Based on Time-Accurate Simulations for Turbine Blade Internal Cooling" was to apply, develop, and demonstrate the use of Large Eddy Simulations (LES) and Detached Eddy Simulations (DES) as high-accuracy prediction tools for large domains in the analysis of gas turbine blade ribbed internal cooling ducts with rotation. Experiments in a stationary ribbed duct were also proposed for use as a benchmarking tool in quantifying the accuracy of the calculations. In the project, three domains were considered: the developing flow region, fully developed flow in a periodic duct, and flow in a 180º bend. For each of these domains, three flow conditions were considered: flow in a stationary duct, flow in a rotating duct with only Coriolis effects present, and flow in a rotating duct with both Coriolis effects and centrifugal buoyancy forces. In all cases studied, square-edged ribs placed orthogonal to the flow (α = 90º) were included on both walls, the channel aspect ratio was 1:1, and the flow Reynolds number was 20,000.

Rotating ribbed duct flows are excellent candidates for numerical calculations because of the difficulties involved in obtaining accurate measurements in rotating domains. Because these conditions differ so much from canonical flowfields, extension of Reynolds Averaged Navier-Stokes (RANS) closure models to these cases is difficult because of the lack of knowledge about the flowfields and empirical data needed to derive phenomenologically correct turbulence models. Plus, most RANS models do not accurately capture the flow and heat transfer in highly anisotropic flowfields with consistency. LES calculations are more physically consistent but have been limited until recently by the extremely large computational requirements. Finer grid requirements and time-dependency make LES calculations orders of magnitude more

"expensive" than RANS calculations, even on present-day computers. Access to larger parallel systems, however, has made LES calculations feasible for larger domains and higher Reynolds numbers. They have proven themselves to be extremely capable of correctly reproducing the magnitudes of friction factor, mean and turbulent flowfields, and heat transfer with a high degree of accuracy, most always within 10-15% and in many cases within experimental uncertainty.

Ribbed duct flows have been studied experimentally for decades, and with the advent of industrial computational fluid dynamics (CFD) tools they have been studied computationally, as well, within the past decade. RANS models typically do not capture all of the physical effects correctly, but occasional studies report on accurate comparisons with experiments and they are the only efficient tools available for computational predictions of turbulence. Therefore, RANS models are currently the industry standard for predicting flow and heat transfer in ribbed internal cooling ducts in gas turbine blades. Recent work in academia, however, has pursued the use of LES in predicting turbulent flows in gas turbine blades because of increased accuracy and consistency (where RANS models often produce varying results, depending on the models used). With only a few exceptions, these calculations have focused on small fully developed domains with streamwise periodic boundary conditions because of the grid size limitation. In addition, Reynolds numbers for these domains have rarely reached over values of 10,000, with the majority of LES studies performed at Reynolds numbers of approximately 5,000.

The uniqueness of this study lies in the use of LES predictions in calculating the flow and heat transfer in the developing flow and 180º bend domains, which are roughly ten times the size of a periodic domain. Additionally, very few studies have been conducted in the developing flow region or the 180º bend region of ribbed ducts in gas turbine blades, and this study presents a unique look at the flowfields and turbulence and their relationship to heat transfer by producing

a complete set of highly accurate flow and heat transfer predictions over the entire domains. Of those studies, only a handful have taken flow measurements, so very little is understood about the underlying physics behind the heat transfer measurements, which are more available. The Reynolds number of 20,000 in this study is also progressive, being more representative of actual operating conditions and requiring a much larger computational grid than the lower Reynolds numbers.

The work presented in this dissertation is part of a combined effort to complete both LES and DES calculations of the three domains and three flow conditions considered. The first part of the project included fully developed calculations in stationary and rotating ducts, which were conducted by D.K. Tafti and S. Abdel-Wahab, a Masters student who graduated in 2004. The most recent work has included full channel DES calculations in stationary and rotating ducts, which are currently underway and are being conducted by a Ph.D. student, A.K. Viswanathan, who is scheduled to graduate in 2006. The LES calculations in the developing flow and 180º bend domains, as well as the experimental validation, are all included in this part of the project, which was carried out with the assistance of D.K. Tafti in the calculations and K.A. Thole in the experiments. The specific tasks of the project, along with the responsible persons, are outlined in the following work plan:

1. LES
   a. Fully-developed regime with ribs **(S. Abdel-Wahab / D.K. Tafti)**
      i. Stationary ribbed duct
      ii. Rotating ribbed duct with Coriolis Forces
      iii. Rotating ribbed duct with Coriolis forces and centrifugal buoyancy
   b. Developing Flow regime with ribs **(E.A. Sewall)**
      The calculations will start a sufficient distance upstream of the first rib in the passage and continue into the passageway till the flow is fully developed.
      i. Auxiliary calculations in smooth fully developed duct to generate time-dependent velocity inlet boundary conditions.
      ii. Stationary ribbed duct
      iii. Rotating ribbed duct with Coriolis forces
      iv. Rotating ribbed duct with Coriolis and centrifugal Buoyancy
   c. U-bend with ribs **(E.A. Sewall)**
      These calculations will start upstream of the U-bend such that the inlet plane is outside the domain of influence of the U-bend and will extend downstream of the U-bend into the second-pass including the first few ribs.
      i. Stationary U-bend
      ii. Rotating U-bend with Coriolis forces
      iii. Rotating U-bend with Coriolis and centrifugal Buoyancy

2. DES
   a. Implement suitable RANS model into computer code GenIDLEST under DES framework. Current candidates are SA model (Spalart and Almaras, 1994), k-ω or Menter's SST model (1993). **(A.K. Viswanathan)**
   b. Smooth duct fully-developed. Test model for different mesh resolutions and evaluate accuracy against LES and experiments. **(A.K. Viswanathan)**
      i. Stationary duct
      ii. Rotating duct with Coriolis forces
      iii. Rotating duct with Coriolis and centrifugal buoyancy.
   c. Ribbed duct, fully developed. Test model for different mesh resolutions and evaluate accuracy against LES and experiments. **(A.K. Viswanathan)**
      i. Stationary duct
      ii. Rotating duct with Coriolis forces
      iii. Rotating duct with Coriolis and centrifugal buoyancy

3. LES/DES in full two-pass channel with ribs.
   a. Effects of Coriolis forces. **(A.K. Viswanathan; DES only)**
   b. Effect of buoyancy. **(A.K. Viswanathan; DES only)**

4. Experimental Measurements
   a. Spatial maps of all the mean and turbulent quantities of all three components in the ribbed duct **(E.A. Sewall / K.A. Thole)**
      i. Developing region
      ii. Fully-developed region
      iii. In the 180° bend region

A table listing the publications produced as a result of this project is provided as Appendix A. Currently, 14 conference papers and 6 journal papers have been published from the work. From the LES calculations of the developing flow and 180º bend (Part 1b & 1c) and the

experimental measurements (Part 4), 5 conference papers and 2 journal papers have currently been published.

The objective of the LES part of the project is to study the flow and heat transfer in stationary and rotating ribbed gas turbine blade internal cooling ducts, specifically in the developing flow region and the 180° bend regions. The challenge to overcome in this study is to extend the LES calculations to domains larger than that of a fully developed periodic duct. The physical phenomena investigated in this study are those of rotational Coriolis effects and centrifugal buoyancy forces and their interaction with the flow, turbulence, and heat transfer of the already turbulent and anisotropic ribbed duct flows.

This dissertation begins with a comprehensive literature review of previous work in ribbed ducts as Chapter 2. Because the LES work involves extensive validation with experiments, both experimental and computational works were reviewed. Chapter 3 outlines the computational methodology and calculation details, including the basis for the LES model and a description of GenIDLEST, the program used to carry out the calculations. Chapter 4 details the results in stationary ducts, both in the developing and 180º bend domains. Because most experiments have been conducted in this regime, as well, the chapter focuses on validation of the results and establishing the computational accuracy and reliability of the calculations. This is also important because of the difficulty in obtaining good validation experiments in rotating ducts, and even though every available validation study in rotating ducts is used, it is sometimes important to rely on the computational accuracy of stationary predictions when the data needed to validate rotating calculations is simply not available. Chapter 5 presents results for rotating ducts with Coriolis effects only, both in the developing flow and 180º bend domains, and Chapter 6 presents results for rotating ducts that include both Coriolis and centrifugal buoyancy forces. Centrifugal

buoyancy forces take into account the variation of fluid densities using the Boussinesq approximation. This approximation, which accounts for density variations in incompressible calculations, does not capture the correct relationship between temperature and fluid momentum with very large temperature differences, so an algorithm was developed for calculating unsteady flows with density variations in the presence of large temperature gradients. Chapter 7 outlines the details of this algorithm and validates the algorithm with Rayleigh-Bénard convection and Poiseuille-Bénard channel flow comparisons. Finally, Chapter 8 draws conclusions from the work.

Several appendices have also been included after the main text. Appendix A is a table containing the references of all of the papers that have been published from this project. Appendix B is a derivation of the Coriolis and centrifugal buoyancy terms starting from the dynamics equations of a particle in motion rotating about an arbitrary axis. Appendix C describes the procedure used for extracting, conditioning, and implementing time-dependent boundary conditions in an LES calculation. This procedure was used to generate the inlet conditions for the 180º bend calculations. Finally, Appendix D is a continuation of Chapter 4, the LES calculations in stationary ducts. It is a paper published in the ASME Journal of Turbomachinery outlining two calculations comparing a 180º bend with and without a rib in the bend.

Chapter 2. Literature Review

This is a review of the literature in gas turbine blade ribbed internal cooling ducts covering the previous 3 ½ decades. The gas turbine industry is considered by many to be a very mature field, with an extremely large volume of literature existing on topics related to turbine blade cooling. This review is intended to summarize the current knowledge in the area in an effort to establish the motivation for development of the next generation of computational fluid dynamics (CFD) codes using large massively parallel computers for highly accurate simulations, such as Direct Numerical Simulations (DNS) and Large Eddy Simulations (LES). The current practice of numerical simulation in industry is to solve the Reynolds Averaged Navier-Stokes (RANS) equations to obtain mean flowfields in complicated geometries. In RANS calculations of turbulent flows, semi-empirical models based on flow physics and tuned to experiments are used to predict the turbulence and its effect on the mean flowfields, but the accuracy and dependability of these models is questionable. A more dependable calculation method with a higher reliability and confidence level could make significant advances.

This review of past studies covers experimental and numerical studies in gas turbine blade ribbed internal cooling ducts. Most research began experimentally, but the increase in CFD capabilities and turbulence modeling in the 1980's brought about a new topic of computational studies in internal cooling flows related to gas turbine blade internal cooling. This chapter is divided into five sections. The first section describes the parameters governing the flow through the duct and the rotation speed of the duct, and the next three discuss studies carried out on each of the three domains studied in this project: the developing flow, fully developed, and 180º bend regions. The fourth section discusses recent works on LES calculations in ribbed ducts.

2.01 Problem Description

The cross-section of a typical turbine blade is pictured in Figure 2.1(a). The blade shows four ribbed channels, pin fin cooling, and film cooling out the leading edge. The range of duct aspect ratios can be seen in the figure, as can the complexity of the cooling schemes. This project focuses entirely on the ribbed ducts. The development of flow at the entrance and the 180º bend connecting two ducts are both considered in this study, along with fully developed flow in the middle regions. Both experimental and computational studies are considered. A typical experimental test rig used to study rotating ducts is shown in Figure 2.1(b). Computational studies commonly focus on a single rib with periodic flow and heat transfer boundary conditions upstream and downstream, and some show results over an array of ribs. Flow and heat transfer results are usually reported, and an example of a calculation of a duct with V-shaped ribs is shown in Figure 2.1(c).

The flow and heat transfer depend on many different geometric parameters that characterize the shape of the duct and ribs. These parameters are shown graphically in Figure 2.2. The parameters include the channel aspect ratio, the rib height (i.e. a ratio of rib height to duct hydraulic diameter, e/D_h; in rectangular ducts, a ratio of rib height to channel height, e/H, is sometimes given, as well), the spacing between ribs (i.e. a ratio of rib pitch to rib height, P/e), the alignment of the ribs (e.g. ribs on only one wall, ribs on two walls in a staggered arrangement, or ribs on two walls in an in-line arrangement), and the angle of the ribs (given as an angle with respect to the flow direction; $\alpha = 90º$ denotes a typical placement of ribs orthogonal to the flow direction). In rotating cases, the mean rotation radius (r/D_h) is also an important parameter. The duct heating is also an important parameter.

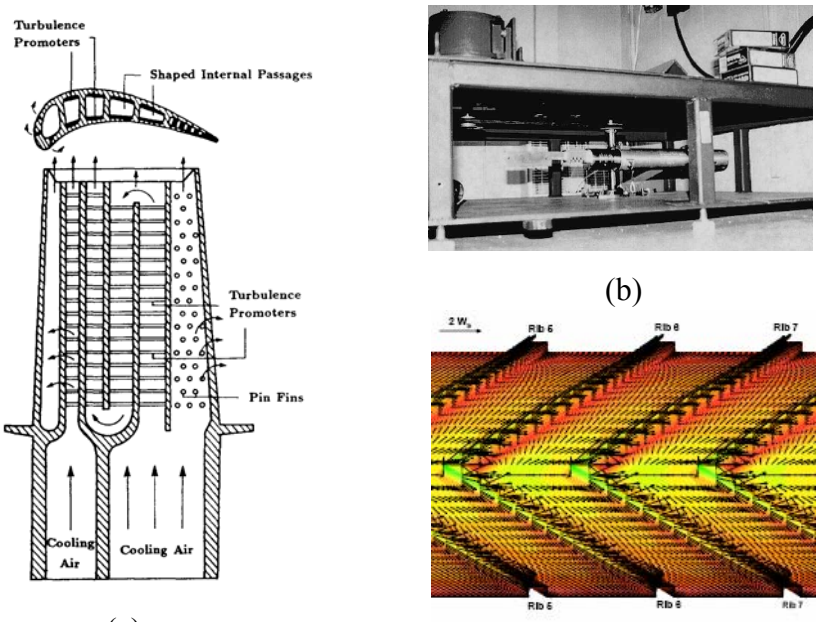

Figure 2.1. (a) A diagram of a gas turbine blade cooling scheme (Han, 1988) shows a number of cooling schemes used in internal cooling. (b) The rotating experimental test rig of Park et al. (1988) shows a typical setup for studying rotating ducts. (c) Computational results by Su et al. (2003) show flow vectors and heat transfer contours in a high aspect ratio duct with V-shaped ribs.

Heating is typically implemented as a constant temperature or uniform heat flux boundary condition, though mass transfer experiments are sometimes also used, where a naphthalene sublimation technique is used to simulate a constant temperature boundary condition. The nondimensional parameters governing the flow are the Reynolds number (ratio of momentum to viscous forces), the rotation number (ratio of rotation to momentum), and a centrifugal buoyancy parameter (ratio of rotational buoyancy force to inertia). The Reynolds number typically ranges from 5,000 – 100,000, with 20,000 – 30,000 being a typical value for aerospace propulsion applications. The rotation number is usually less than 0.5, and the buoyancy parameter is also typically less than 0.5, although it can reach as high as unity in high temperature situations.

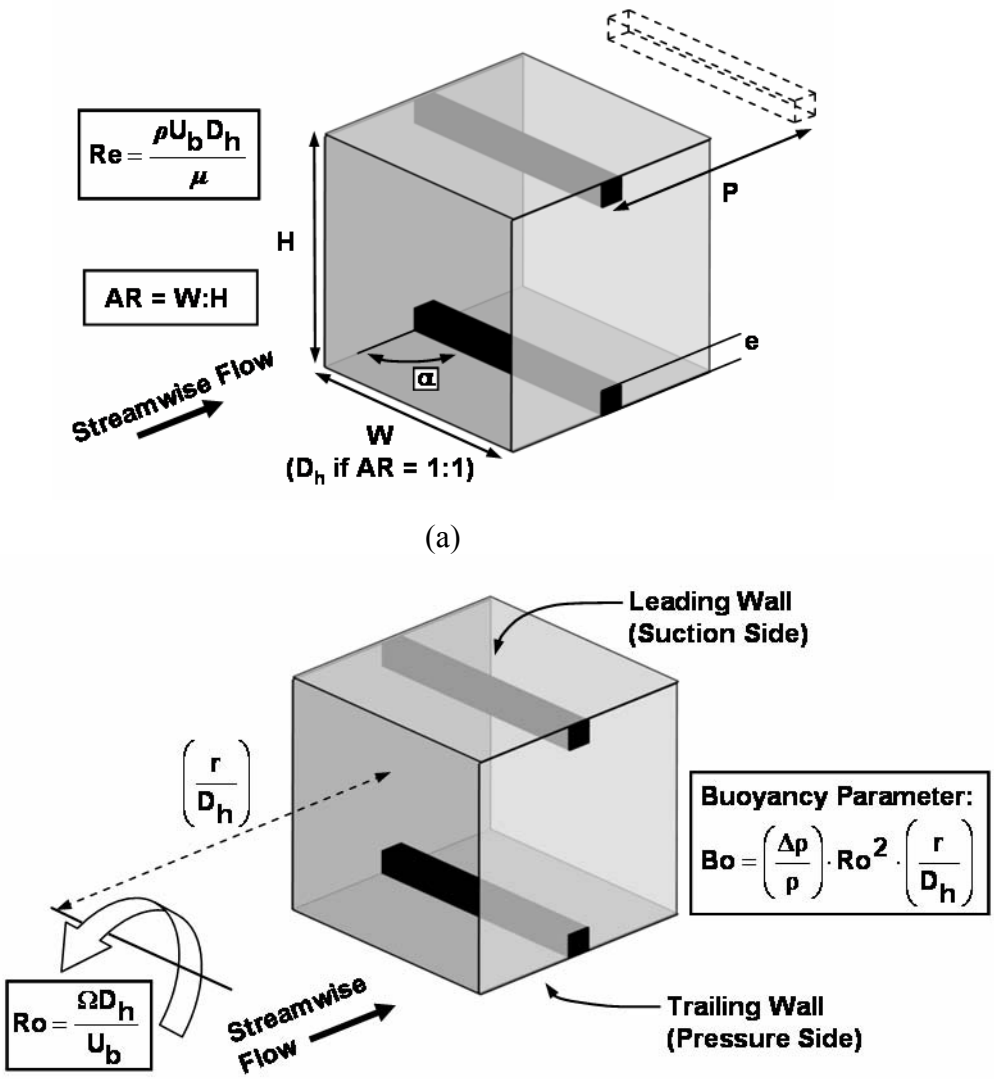

Figure 2.2. The geometric parameters and nondimensional flow parameters govern the characteristics of ribbed duct flow in (a) stationary and (b) rotating ducts.

In a rotating duct, Coriolis forces act to stabilize and attenuate turbulence along the leading side of a duct and to destabilize and augment turbulence on the trailing side. A second effect of Coriolis forces is the development of secondary flow cells in the cross section of the duct, which develop strong upwash/downwash regions. The direct effect on turbulent structure causes the heat transfer on the trailing wall to increase significantly, while heat transfer on the leading wall

is decreased because of the attenuation of turbulence. Secondary flows resulting from the strong movement of fluid from the trailing wall to the leading wall work to increase heat transfer along the smooth side wall.

Centrifugal buoyancy is an additional effect found in heated rotating ducts. As a result of high heat transfer coefficients on the trailing wall due to Coriolis effects, the fluid near the wall is at a lower temperature and has a higher density than the fluid on the leading wall (in radially outward flow). Centrifugal forces act to accelerate the fluid near the trailing wall more strongly because of the higher density, assisting the Coriolis forces that work to destabilize the turbulence along the trailing wall. In radially inward flow, the fluid near the leading wall is cooler due to the effect of Coriolis forces. In this case, the centrifugal buoyancy force acts in a direction opposite to the mainstream flow direction, but the opposing action is stronger along the leading wall than on the trailing wall because of the higher fluid density.

2.02 Stationary Developing Flow

The entrance region of stationary smooth ducts with a high aspect ratio was studied by Sparrow and Cur (1982), who determined that inlet flow separation plays an important part in developing flow heat transfer. The thermal entrance length was determined to be between five and seven hydraulic diameters for symmetric heating and twice that length when the duct was heated asymmetrically. An in-depth study of buoyancy in water-filled vertical channels was carried out by Dutta et al. (1999), and the formation of large-scale buoyancy-driven structures was found to cause a greater increase in the heat transfer when buoyancy opposed the flow than in cases where buoyancy aided the flow.

Developing flow in stationary ribbed ducts was studied by Sparrow and Tao (1983, 1984), and they observed almost immediate fully developed flow when the flow was disturbed by round

disturbance rods against the walls. When rods were included along both walls, the heat transfer was increased approximately 40%, and a test at constant pumping power determined that the performance of the cooling duct was most effective with both walls disturbed. An experimental study by Han and Park (1988) covered the heat transfer results over a range of parameters in a ribbed duct and showed a periodically repeating heat transfer pattern forming after the third or fourth ribs. The smooth wall heat transfer, however, was still not fully developed at the eighth rib. Likewise, laser holographic interferometry experiments by Liou and Hwang (1992a) in a 4:1 aspect ratio duct resulted in similar conclusions with friction and heat transfer measurements. Chen et al. (2000) presented mass transfer experiments in a two-pass ribbed duct and showed very little flow development near the inlet. Local values of fully developed heat transfer were also shown in the study. A fifth study, by Wang et al. (2001), showed that streamwise periodic heat transfer and friction coefficient patterns were attained after two or three ribs, which is consistent with the first two studies, but no flow information was provided in relation to these effects in any of these studies.

2.03 Developing Flow with Rotation

The entrance region of smooth rotating circular ducts was studied by Lokai and Gunchenko (1979), Johnson and Morris (1984), and Elfert (1994). The developing length was determined by Lokai and Gunchenko to be between 15 and 20 diameters, with several correlations derived describing the heat transfer augmentation due to rotation. Johnson and Morris studied the friction factor characteristics of smooth circular ducts rotating parallel to the flow axis. Elfert studied radially inward flow in a smooth rotating circular duct using a nonintrusive Laser-2-

Focus velocimeter (L2F) and measured turbulence levels of 5-15% across stationary and rotating ducts up to Re = 60,000.

A comparison of developing flow in rotating smooth-walled circular and square-walled ribbed ducts was made by Chang and Morris (1998). An important conclusion from this study was that, though the effects of rotation and buoyancy were qualitatively similar between the two studies, the leading wall heat transfer impediment due to rotation was more severe in the ribbed duct, while the effect on the trailing surface was reduced in the ribbed duct. Also, a smaller degree of peripheral variation was observed in the ribbed duct.

A study of ribbed duct flow in a rotating duct by Fann et al. (1994) provided local heat transfer augmentation ratios measured by thermocouples placed along the ribbed wall of three cooling passages. Seven different rib configurations were studied over a series of low rotation numbers, and the results were discussed in terms of the configurations that produced the highest heat transfer augmentation, which was a 45º rib configuration in most regions. Fully developed results were also reported in the study. A rotating ribbed duct developing flow study by Park et al. (1998) reported that leading wall heat transfer spanwise symmetry is highly sensitive to the rotation number in radially outward flow. Another conclusion was that heat transfer in a rotating ribbed duct is not affected as significantly by rotation as rotating smooth duct flow is. A third important conclusion drawn from the study was that varying the Reynolds number did not significantly change the shapes of the local heat transfer distributions on the walls. A third study of developing flow in rotating ribbed ducts, by Chang and Morris (2003), formed a number of correlations relating the heat transfer to Reynolds number, rotation number, and the buoyancy parameter for operating conditions reaching into the low range of actual engine conditions. The

facility only studied five ribs, however, which could bias averaged results and introduce inaccuracies because of the proximity of the outlet to the ribbed test section.

2.04 Developing Flow Computational Studies

A number of computational studies of developing flow in smooth ducts have been reported in the literature. One of the earliest was by Prakash and Zerkle (1992), who used a k-ε model to simulate flow in one and two-pass ducts. Comparisons with experiments were shown, and comparisons of leading wall heat transfer, though not extremely good, were much better than trailing wall comparisons. A revision to the k-ε model by Dutta et al. (1994) to better account for Coriolis and buoyancy effects improved centerline heat transfer predictions in a rotating smooth duct so that they compared better with averaged heat transfer augmentation experiments than the unmodified model did.

Nilsen et al. (1994) used an algebraic second-moment closure model in a two-dimensional calculation of a rotating duct with reasonable success. Bo et al. (1995) calculated the flow in a smooth rotating duct with a number of models, including an eddy viscosity model and an algebraic stress model, and concluded that the second moment closure would be required to capture the effects of near-wall turbulence transport. Effects of rotation on the entrance region of rotating smooth ducts with laminar flow were investigated by Yan and Soong (1995), and another study by the same authors, Soong and Yan (1999), observed the effects of laminar flow through a smooth duct rotating about an axis parallel to the flow direction (i.e. not orthogonal to the axis, like most rotating turbine blade studies are). Okita and Iacovides (2003) used a high-Reynolds-Number eddy viscosity model and differential stress model to calculate the flow and heat transfer in the smooth developing flow region in a rotating duct. The differential stress

model was found to produce better results, but both models diverged from the measurements as flow progressed downstream in the duct. In a stationary fully developed ribbed duct, comparisons with experiments were inconsistent because of the lack of the models' abilities to capture all of the turbulent effects.

Few computational studies have been reported on the developing flow region of ribbed ducts. Bonhoff et al. (1997) discussed a calculation using a differential Reynolds Stress Model (and commented on an RNG k-ε model from a previous case) of an entire channel with 12 ribs, angled at 45º, in each of two flow passages. A number of computational studies used Reynolds Stress Models to calculate the flow in rotating ducts with 45º ribs (Jang et al., 2001; Al-Qahtani et al., 2002a,b). Comparisons with experiments in these experiments showed fair agreement.

2.05 Stationary Fully Developed Flow

The majority of experimental ribbed duct studies have measured the flow and heat transfer in the fully developed region because it is characteristic of most of the duct and the analysis can be simplified because upstream and downstream effects are ignored. Many of these studies have compared heat transfer augmentation and friction factor results between cases with different geometric configurations. Table 2.1 outlines each stationary experimental study mentioned in this section and the minimum and maximum geometrical parameters used to define the ribs and flow conditions.

A number of studies have focused solely on the flow characteristics of stationary ribbed duct flows. A study by Satoh et al. (1987) used a laser Doppler velocimeter (LDV) to study the flow in a circular tube with discrete ribs in the flow, and turbulence intensities of over 20% were recorded.

Table 2.1. Geometric Parameters Governing Experiments in Stationary Fully Developed Ribbed Ducts (top value = minimum; bottom = maximum)

Author (Year)	Aspect Ratio (W:H)	Rib Alignment	Rib Angle (α)	Rib Height (e/D_h)	Rib Height (e/H)	Rib Pitch (P/e)	Reynolds Number
Sato et al. (1987)	3:2	discrete / staggered	---	0.06	0.08	---	10,000 30,000
Sato et al. (1989)	5:1	top + bottom	90º	0.12	0.20	7	20,000
Hirota et al. (1992)	square	variable	90º	0.02	---	10	65,000
Liou et al. (1993)	2:1	top + bottom	90º	0.10	0.13	10	33,000
Islam et al. (2002)	5:1	one wall	90º	0.10	0.17	10 20	7,000 20,000
Rau et al. (1998)	square	Variable	90º	0.10	---	9	30,000
Casarsa et al. (2002)	square	One wall	90º	0.30	---	10	40,000
Chanteloup et al. (2002)	square	top + bottom staggered	45º	0.10	---	10	50,000
Mahmood (2002)	4:1	top + bottom staggered	45º	0.08	0.13	10	10,000 90,000
Han et al. (1978)	12:1	top + bottom	45º 90º	0.03 0.10	---	5 20	3,000 20,000
Han (1984)	square	top + bottom	90º	0.02 0.06	---	10	7,000 90,000
Han (1988)	1:4 4:1	top + bottom	90º	0.05 0.08	---	10 20	10,000 60,000
Lau et al. (1991)	square	top + bottom discrete	30º 90º	0.06	---	10	10,000 80,000
Lau et al. (1991)	square	top + bottom discrete	30º 90º	0.06	---	10	10,000 80,000
Liou and Hwang (1992)	4:1	top + bottom	90º	0.06 0.10	0.10 0.17	10 20	5,000 54,000
Baughn and Yan (1992)	square	top + bottom	90º	0.06	---	10	15,000 80,000
Mochizuki et al. (1997)	square	top + bottom	30º 90º	0.09	---	11	4,000 30,000
Taslim and Wadsworth (1997)	square	top + bottom staggered	90º	0.13 0.25	---	5 10	10,000 55,000
Korotky and Taslim (1998)	square	top + bottom staggered	90º	0.13 0.25	---	5 10	10,000 55,000
Astarita and Cardone (2003)	square	top + bottom	30º 45º	0.10	---	10	16,000 30,000

An LDV probe was used by Sato et al. (1989) to measure the flow characteristics in a rectangular duct with large ribs ($e/H = 0.2$) to compare three different rib alignments. The friction factor was found to be the same among all three cases, while the velocity fluctuations were found to be higher throughout the duct in the staggered and unsymmetrical staggered arrangement. The author recommended the use of the unsymmetrical staggered arrangement because of the increased turbulence with the no increase in friction factor. Another flowfield study, by Hirota et

al. (1992), used hot-wire anemometers to study the flow in a square duct with very small ribs (e/D_h = 0.02) and commented on the turbulent energy production among ducts with no ribs, one ribbed wall, and two ribbed walls. Another LDV investigation of fully developed ribbed duct flow by Liou et al. (1993) found the maximum turbulent kinetic energy to be near the ribbed wall in the recirculation region just upstream of reattachment, while the minimum was found in the recirculation zone near the rib. The shift in maximum streamwise velocity near the ribbed walls towards the outside walls was also observed in this study. A connection between the anisotropy in turbulence and regions of secondary flows suggested that the anisotropy may be responsible for driving some of these flows. Islam et al. (2002) studied turbulent water flow in a ribbed duct using particle image velocimetry (PIV). This study reported that the reattachment length of the flow downstream of the ribs is dependent on Reynolds number up to Re = 15,000, at which point it remains steady at a value of approximately four rib heights.

A combined LDV and liquid crystal heat transfer study by Rau et al. (1998) identified several of the flow features found in the fully developed section of a ribbed channel and discussed some of the issues with secondary flow effects and turbulence in fully developed ribbed duct flow. The size of the recirculation zone downstream of the rib was discussed, and three other recirculation zones were described, which are found upstream, on top, and downstream of the rib. A study by Casarsa et al. (2002) studied ribs with a very high blockage ratio (e/D_h = 0.3) using PIV and Liquid Crystal Thermometry. Results emphasized the three-dimensionality and anisotropy of the flow near the ribs in the highly turbulent regions. Chanteloup et al. (2002) used a stereoscopic PIV system and liquid crystals to study flow in a duct with 45º ribs and presented a clear characterization of the flowfield and its interaction with the wall heat transfer when the ribs were angled. As a result of this study, it is important to note that the driving force and the

resulting flowfield are remarkably different when the ribs are angled. Therfore, studies focusing on angled ribs will be mentioned but not discussed in detail from now on in this review. One such study, by Mahmood et al. (2002), used flow visualization and infrared imaging to study the flow and heat transfer with 45º angled ribs across a broad range of Reynolds numbers.

Several studies have focused solely on friction and heat transfer in stationary ribbed ducts for the purpose of creating correlations based on a number of different criteria. An early study by Han et al. (1978) compared heat transfer results when a number of parameters were varied, including rib height, rib pitch, rib shapes, and rib aspect ratio. Another study, by Han (1984), varied the rib height, rib pitch, and compared the results with smooth channel results. A third study by Han (1988) varied the channel aspect ratio, the rib height, and rib pitch. Two studies by Lau et al. (1991a,b) focused on discrete rib turbulators and compared the performance to transverse ribs. A study by Liou and Hwang (1992) varied the rib height and rib pitch in a 4:1 aspect ratio duct. Each of these studies was used to derive correlations of friction and heat transfer based on the rib geometry and Reynolds number.

A study by Baughn and Yan (1992) in a stationary fully developed ribbed duct measured heat transfer with liquid crystals. Local heat transfer contours were shown on the ribbed wall and on top of the ribs. Mochizuki et al. (1997) studied the heat transfer for a number of different rib configurations and angles in a ribbed duct using over 300 thermocouples distributed throughout a two-pass duct. Averaged heat transfer was studied in ducts with large ribs ($e/D_h = 0.133 – 0.250$) in a staggered arrangement by Taslim and Wadsworth (1997) and Korotky and Taslim (1998). Taslim and Wadsworth studied the heat transfer averaged over the surface of ribs with sharp corners, and Korotky and Taslim compared the heat transfer results for ribs with rounded corners to those results. The comparisons depended heavily on rib size and rib pitch, but for the smallest

rib height (e/D_h = 0.133) and the largest rib pitch (P/e = 10), which are the closest parameters to the calculations in the current project, the difference in heat transfer augmentation was negligible over the range of Reynolds numbers studied (Re = 10,000 – 50,000), while the friction factor was smaller for rounded ribs by about 30%. Finally, a heat transfer study using infrared thermography by Astarita and Cardone (2003) compared two different rib angles and a number of different rib configurations.

2.06 Fully Developed Flow with Rotation

Experiments in rotating ducts are outlined in Table 2.2. Nearly all of the facilities used in these tests used square ducts, so the aspect ratio and the rib height based on channel height are not listed in the table. The range of rotation numbers is added to the table, however, along with the rotation radius. The rotation radius is the average length from the axis of rotation to the test section, and it is an important factor in determining the buoyancy parameter. Rotating ducts present a challenge to the engineer, as obtaining measurements in a rapidly rotating channel and exporting them to a measurement device can be an extremely challenging task. Despite the difficulties, however, a number of researchers have obtained valuable local and averaged flow and heat transfer information in rotating ducts.

Bons and Kerrebrock (1998) used a PIV system to measure the flow and an infrared camera to measure the heat transfer in a rotating duct with smooth walls. One study, by Tse and Steuber (1997), presented LDV measurements in a rotating duct with 45º ribs. Hsieh et al. (1997) reported LDV measurements in a rotating ribbed duct at a number of different flow conditions and also reported averaged heat transfer measurements from thermocouple measurements of 15 copper sections.

Table 2.2. Geometric Parameters Governing Experiments in Rotating Fully Developed Ribbed Ducts

Author (Year)	Rib Alignment	Rib Angle (α)	Rib Height (e/D_h)	Rib Pitch (P/e)	Rotation Radius (r/D_h)	Reynolds Number	Rotation Number
Bons and Kerrebrock (1998)	---	---	---	---	40	8,100 10,000	0.00 0.29
Tse and Steuber (1997)	top + bottom	45º	0.10	5	49	25,000	0.24
Hsieh et al. (1997)	top + bottom	90º	0.20	5	19	5,000 10,000	0.00 0.16
Lokai and Limanski (1975)*	---	---	---	---	26	9,000 40,000	0.00 0.02
Wagner et al. (1991)	---	---	---	---	49	25,000	0.00 0.50
Wagner et al. (1991)	---	---	---	---	49	25,000	0.00 0.50
Taslim et al. (1991)	top + bottom	90º	0.13 0.33	10	21	15,000 50,000	0.01 0.10
Wagner et al. (1992)	top + bottom	90º	0.10	10	49	25,000	0.00 0.35
El-Husayni et al. (1994)	top + bottom staggered	60º	0.24	10	13	5,000 23,000	0.00 1.00
Parsons et al. (1994)	top + bottom	90º	0.13	10	30	2,500 25,000	0.00 0.35
Parsons et al. (1995)	top + bottom	60º 90º	0.13	10	30	2,500 25,000	0.00 0.35
Hibbs et al. (1996)	top + bottom	90º	0.10	10	---	5,000 30,000	0.00 0.30
Park et al. (1997)	top + bottom	90º	0.06 0.10	10 16	30	5,500 10,000	0.09 0.24
Park et al. (1997)	top + bottom	90º	0.03 0.10	10 16	30	5,500	0.24
Nikitopoulos et al. (2000)	top + bottom	var.	---	7 10.5	---	30,000	0.00 0.30

*Round tube; all other studies have square ducts

The leading and trailing walls were heated with different heat flux boundary conditions. Both Coriolis and buoyancy forces were shown to be significant at the higher rotation numbers.

An early study by Lokai and Limanskii (1975) showed the increase in average heat transfer as a result of rotation in smooth round ducts and derived a correlation for the heat transfer augmentation over a stationary duct as a function of rotation number and Reynolds number. Wagner et al. obtained averaged heat transfer augmentation measurements in rotating smooth ducts to study the Coriolis (1991a) and Coriolis plus centrifugal buoyancy (1991b) forces in smooth ducts.

Taslim et al. (1991) used liquid crystals to study the heat transfer in ribbed rotating ducts over a range of flow conditions. Wagner et al. (1992) reported averaged heat transfer augmentation ratios in three passes of a rotating duct with rounded ribs across a range of rotation and buoyancy conditions. An interesting trend from this study was an initial decrease in leading wall heat transfer with buoyancy parameter followed by an increase with a further increase in the buoyancy parameter. This trend was not explained because only heat transfer data was available. A study by El-Husayni et al. (1994) investigated a number of different thermal boundary conditions (one, two, or four heated walls) and their effects on wall heat transfer in both smooth ducts and ducts with ribs angled at 60º to the flow. This study also noted the interesting trend of an initial decrease in heat transfer on the leading wall at low rotation numbers to a minimum, followed by a subsequent increase with rotation number after some critical rotation number was reached. The trailing wall heat transfer was shown to be more affected by the boundary conditions than the leading wall. A comparison of constant temperature, uniform heat flux, and uneven temperatures in a rotating ribbed duct was done by Parsons et al. (1994), who used thermocouples to measure average heat transfer across copper sections. The study found a constant temperature boundary condition to have a lower rate of heat transfer than a uniform heat flux condition. Another study by Parsons et al. (1995) used the same test configuration to study the difference between 60º and 90º rib angles and the degree of twist in the rotating duct. A mass transfer experiment by Hibbs et al. (1996) in a rotating duct compared a smooth duct with a ribbed duct. The effect of rotation on mass transfer was found to be larger at low rotation numbers in the smooth ducts, but in the ribbed ducts, only the trailing wall (upstream leg) and leading wall (downstream leg) were significantly affected. A mass transfer study on rotating ribbed ducts at Reynolds numbers of 5,500 and 10,000 and rotation numbers of 0.09 and 0.24, by

Park et al. (1997a,b), reported results from a number of different rib placement configurations. This study found that an increase in rotation number caused significant spanwise variation of the local heat transfer between the ribs on the leading wall. Experiments performed by Nikitopoulos et al. (2000) in a rotating duct compared 12 different profiled ribs with rectangular ribs and found that profiled ribs allow for increasing three-dimensionality of the flow, which increases wall heat transfer when combined with the effects of rotation.

2.07 Fully Developed Computational Studies

Many early computational studies in the fully developed region of ribbed ducts have used k-ε turbulence models for closure. It is widely known that these models are based on the assumption of isotropic turbulence, and as a result many turbulence-driven secondary flows are often not seen at all. Iacovides and Launder (1991) used a high Reynolds number k-ε model to simulate flow in fully developed rotating smooth ducts. The influence of initial conditions on the final results was studied, and results showed up to a 90% increase of heat transfer augmentation over a stationary case when the duct was rotating up to a rotation number of 0.2. A study in a rotating duct with ribs has been presented by Prakash and Zerkle (1995), who used a k-ε model to find excellent agreement with correlations from experimental studies. Liou et al. (1993) used a k-ε algebraic stress model (k-ε-A) and found good overall agreement with experiments but underpredicted the reattachment length and miscalculated the region of maximum shear above the rib. Another study (Acharya, 1993), using a k-ε model on a two-dimensional geometry, showed how this model could not predict the shape of the recirculation region or the turbulent shear stress distribution downstream of the rib. Two and three dimensional calculations by Arts (1997) using a k-l model showed that the two-dimensional flow calculations performed much

better than the three-dimensional calculations because the three dimensional effects, which are difficult to calculate, could be ignored. A conclusion reached by this study was that more complicated models would be required to improve the flow predictions.

Second moment closure models provide an additional level of complexity over the simpler one and two-equation models. Algebraic stress models and differential stress models have both shown to provide an increased level of accuracy in complex turbulent flowfields. Iacovides (1998) used a one-equation effective viscosity model and differential stress model in a three-dimensional calculation and found that in some cases at the centerline the effective viscosity model greatly underpredicted shear stress values. The differential stress model performed much better in reproducing the flow in the symmetry plane. A differential stress model used by Iacovides and Raisee (2000) in two-dimensional calculations showed the difficulty of these models in predicting heat transfer in rib-induced separated regions. Jia et al. (2002) used an explicit algebraic stress model to calculate flow and heat transfer in a duct with V-shaped ribs and found upstream-pointing ribs to perform much better than parallel ribs or downstream pointing ribs. One study comparing an eddy viscosity model with an algebraic stress model (Saidi, 2001) showed how inconsistent comparisons of mean flow and turbulence with experimental data can still result in a correct prediction of centerline heat transfer on the ribbed wall. Additionally, average side wall heat transfer is predicted to within 5% for all models used, but the contours on the side wall are completely reversed from those found in the experiments. Computational results such as this one make it clear that bad flow and heat transfer predictions can still result in accurate averaged results by chance, but it is dangerous to rely on such a code for predictions because any changes to the geometry and flow conditions will most likely not produce to same correct average values. It is imperative that both the flow and turbulence (when

available) be predicted accurately in order to produce reliable heat transfer augmentation predictions.

More recent studies have used more complicated turbulence models to try to capture the anisotropy of the flow. A computational study by Iaccarino et al. (1999) demonstrated the success of a modified v^2-f model over the predictions by a second moment closure model in a rotating two-dimensional channel flow calculation, a rotating backward-facing step, and in a rotating cavity. Two-dimensional calculations by Ooi et al. (2000) demonstrated the effectiveness of a modified v^2-f model in predicting ribbed ducts flows much more effectively than the Spalart-Allmaras and standard k-ε models. Another study by Ooi et al. (2002) further demonstrated the accuracy of a v^2-f model over the simpler models. The calculations with the v^2-f model showed good agreement with experiments in the duct symmetry plane but failed to correctly predict the secondary flows that heavily influence the side wall heat transfer. Sleiti and Kapat (2004) compared a number of eddy viscosity models with a Reynolds Stress Model and found the Reynolds Stress Model to produce results far superior to the other models. V-shaped ribs with a high aspect ratio (AR = 4:1) were studied by Su et al. (2003) with a Reynolds Stress Turbulence Model.

2.08 Stationary 180º Bend

Early on, very few studies were reported in the 180º bend region, but recent studies have shown more interest in the domain. It is characterized by a few very basic flow structures combined with some very complicated flow, turbulence, and heat transfer effects. One early study of the bend by Metzger and Sahm (1986) reported average heat transfer augmentation values in a smooth 180º bend and showed significant changes in the heat transfer over several

averaged areas. A number of aspect ratios and tip clearances were studied, and the bend studied had sharp corners, a very thin divider, and constant temperature walls. The study found that the side walls (inner and outer walls) transferred much more heat than the top and bottom walls. Top and bottom wall heat transfer did increase downstream of the bend, however.

A PIV study by Schabacker et al. (1998) in a 180° bend region with smooth walls and a dividing wall with a thickness of $0.1D_h$ showed the presence of a large recirculation region (diameter of 0.3 D_h) in the upstream corner of the bend in the symmetry plane and a smaller one in the downstream corner. A noticeable characteristic of the measurements in the symmetry plane is the separation bubble hugging the inside wall downstream of the dividing wall and remaining separated until reattachment about 1.5 to 1.6 D_h downstream of the divider. A set of counter-rotating vortices (Dean-type secondary motion) is observed parallel to the dividing wall in the bend. Downstream of the bend the vortices vanish rapidly, but the velocity field does not return to a fully developed state until at least 10 ribs downstream. The flowfield from these measurements was found to be highly three-dimensional, with a maximum turbulent kinetic energy value of 28%, found in the shear layer between the separation bubble and the downstream shear flow. A comparison of dividing wall thicknesses in smooth walled bend region by Liou et al. (1999) showed that the width of the divider has a significant effect on the size and location of the separation bubble found in the downstream leg. A tighter turn causes a separation bubble that extends far into the downstream leg, while a larger divider allows for reattachment before flow reaches the downstream leg. The pair of Dean vortices is also influenced by the divider thickness. Increasing the divider size causes the separation to move further upstream, introducing a low-speed cross-stream mean velocity zone which lowers the dominant cross-stream velocities. A second pair of counter-rotating vortices driven by the Dean vortices is

found in the case with the medium sized dividing wall. The two peak values of turbulent kinetic energy are found at the separation point of the divider wall and the reattachment point, but peak values in this case are slightly lower than what was reported by Shabacker et al., falling closer to 20%. Finally, with regards to heat transfer, variations in wall thickness are shown to influence heat transfer values inside the bend and in the downstream leg, while only having a very weak influence on the upstream side.

A follow-up study using liquid crystals to study the heat transfer in ducts with different dividing wall thicknesses was also done by Liou et al. (2000). The study found that the local heat transfer maximum on the inside wall moves upstream with an increase in divider width. Local heat transfer also decreased on the blade tip with increasing dividing wall thickness, while the magnitude of maximum heat transfer on the outside walls remained the same. The smaller dividing wall thicknesses produce higher average heat transfer augmentation values in the bend. An infrared camera study, by Astarita and Cardone (2000), in smooth 180º bends with different aspect ratios (AR = 1:1 – 5:1; $W/D_h = 0.2$) reported heat transfer contours on the top and bottom walls of the test sections. Three high heat transfer areas were identified: the first was near the end wall, a second was found downstream of the bend near the outer wall, and a third started two diameters downstream of the bend near the inner wall. Three low heat transfer regions were identified as well: the first was in the upstream corner of the bend, the second was found on the downstream side of the blade tip wall, and the third was located near the dividing wall immediately downstream of the bend.

An infrared thermography study by Cardone et al. (1998) of the bend region in stationary and rotating smooth ducts reported on the average heat transfer values in a square duct and a wall dividing thickness of 0.2 D_h. Averaged results indicated that bend effects to not reach more than

1 D_h upstream from the turn. The highest heat transfer occurred on the downstream part of the bend, immediately before flow entered the downstream leg. A second peak in heat transfer was observed about 1.5 channel widths downstream of the bend, corresponding with reattachment of the separation bubble on the inside wall. In addition to the averaged values, a contour of heat transfer augmentation was shown, showing the highest values of heat transfer to be near the back wall. High values were also observed near the outside wall, where flow separating from the dividing wall is forced towards the outside. A mass transfer experiment by Park and Lau (1998) reported heat (mass) transfer contours comparing a stationary duct (Re = 5,500), a duct rotating orthogonally about its axis (Ro = 0.24), and a duct rotating about an axis skewed diagonally by 45º. The study found that the diagonal rotation does not significantly alter the shape of the mass transfer distribution in the turn except for the creation of an isolated region on the trailing wall downstream of the dividing wall.

A number of experiments studying flow and heat transfer in stationary ribbed 180º bends characterize the effects that the bend has on those flows, as well. In this case, the bend geometry is taken into account because a difference between a bend with sharp or rounded corners produces different results. Also, as Liou et al. (2000) reported, the dividing wall thickness can also affect the flow characteristics. Whether or not ribs should be placed in the bend is another question to be answered by such studies, and of course the rib geometry is an important factor. These factors for the ensuing stationary ribbed duct studies with 180º bends are listed in Table 2.3.

Son et al. (2002) compared the flow effects in a smooth and rib-roughened 180º bend using PIV.

Table 2.3. Rib and Bend Geometry for Stationary Experimental Studies in 180º Bends

Author (Year)	Bend Geometry	Dividing Wall Thickness	Rib in Bend?	Rib Angle (α)	Rib Height (e/D_h)	Rib Pitch (P/e)	Re
Son et al. (2002)	Sharp Corners	¼ D_h	Yes	90º	0.125	10	30,000
Han et al. (1988)	Sharp Corners	¼ D_h	No	90º	0.063 0.094	10 20	15,000 60,000
Chandra et al. (1988)	Sharp Corners	¼ D_h	No	45º 90º	0.063	10	15,000 60,000
Mochizuki et al. (1999)	Sharp Corners (AR = 1:2)	1¼ D_h	No	60º 90º	0.100	10	15,000
Ekkad and Han (1997)	Sharp Corners (Ribs on 1 Wall)	¼ D_h	Yes	60º 90º	0.125	10	6,000 60,000
Ekkad et al., (2000)	Sharp Corners	1/8 D_h	Yes	90º	0.100	10	10,000 50,000
Astarita et al., (2002)	Sharp Corners (AR = 2:1)	1/3 D_h	No	60º	0.150	10	16,000 60,000

By comparing with previous heat transfer studies in the bend, this study concluded that the primary driving force in heat transfer was the secondary flow vortex structures and impingement on the walls, rather than on the flow turbulence itself. The study found the globally averaged turbulent kinetic energy in the ribbed duct to be 30% higher than the smooth duct, while the globally averaged heat transfer was found to be 33% higher.

A mass transfer study comparing smooth and ribbed ducts was conducted by Han et al. (1988) for Reynolds numbers ranging from Re = 15,000 – 60,000. The study found an overall increase in heat transfer due to the presence of ribs, and higher heat transfer augmentation was found in the section downstream of the bend for both the smooth and ribbed duct cases. The results showed a weak dependence of heat transfer augmentation ratio on Reynolds number. Increasing the size of the ribs increased the heat transfer, while increasing the spacing of the ribs decreased heat transfer. A similar study by Chandra et al. (1988) with the same geometry (with the exception of rib angle) and flow conditions was used to study the effect of rib angle on heat transfer by varying the angle from 45º - 90º. A study by Mochizuki et al. (1999) used thermocouples to quantify the heat transfer augmentation in smooth and ribbed ducts. Heat

transfer in the bend was found to be similar between the smooth and ribbed duct cases, with the 90º ribs having the highest magnitude by a slight margin. The 60º ribs produced the highest heat transfer in the straight passages. Overall, the 90º ribbed case resulted in more than a 50% increase in heat transfer in the upstream leg, a slight increase in the bend, and approximately a 30% increase in the downstream leg.

A liquid crystal study by Ekkad and Han (1997) reported heat transfer contours on the ribbed wall of the 180º bend of a two-pass duct. Average heat transfer augmentation ratios showed consistently higher heat transfer downstream of the bend, and comparisons were made among four different configurations of ribs. Ekkad et al. (2000) studied the effect of taper in ribbed ducts. The smooth tapered ducts showed an extremely large increase in heat transfer augmentation ratios over smooth straight ducts in and downstream of the bend, while tapering ribbed ducts only showed a small increase. Astarita et al. (2002) used infrared thermography to study the local heat transfer augmentation in the 180º bend of ducts with 60º ribs, and comparisons were made between symmetric and asymmetric heating and in-line vs. staggered rib alignments.

A study by Mochizuki et al. (1994) used 70 thermocouples to measure the heat transfer throughout three passages of a rotating smooth duct. A flow visualization study at low speed in a stationary duct was used to interpret the heat transfer results and make hypotheses as to the flow structures in the rotating duct. The flow was found to be strongly three-dimensional, and the heat transfer augmentation in the bend was found to be much higher than in the straight passages. For high rates of rotation, the heat transfer augmentation was considered to be affected strongly by the buoyancy parameter.

2.09 180º Bend with Rotation

Experiments have also been conducted in rotating ribbed ducts with 180º bends, as well. In addition to the parameters considered in Table 2.3, the rotation number is another important factor in these studies, as well. The experiments in the rotating ribbed ducts are tabulated in Table 2.4.

Table 2.4. Rib and Bend Geometry for Rotating Experimental Studies in 180º Bends

Author (Year)	Bend Geometry	Dividing Wall Thickness	Rib in Bend?	Rib Angle (α)	Rib Height (e/D_h)	Rib Pitch (P/e)	Re	Ro
Liou et al. (2002)	Sharp Corners	½ D_h	Yes	90º	0.136	10	10,000	0.00 0.20
Iacovides et al. (2001)	Sharp Corners	---	No	45º	0.100	10	36,000 100,000	0.00 0.20
Servouse and Sturgis (2003)	Sharp Corners	½ D_h	No	60º	0.100	10	5,000 25,000	0.03 0.33
Azad et al. (2002)	Sharp Corners (Rounded Inside Wall)	½ D_h	No	45º	0.094	10	5,000 25,000	0.04 0.21

Studying the fluid flow in a rotating ribbed duct is extremely difficult because of the rotating domain and the high turbulence involved. Nevertheless, three studies have accomplished this task. Liou et al. (2002) studied a rotating ribbed duct, measuring the flow with an LDV and the heat transfer with liquid crystals. The Reynolds number was 10,000, and the rotation number was varied between 0.0 and 0.2. Rotation was shown to have a significant impact on the flowfield, as the separation bubble downstream of the dividing wall was eliminated in the rotating ribbed duct (but had been seen in the rotating smooth duct). The average heat transfer was also shown to increase steadily with rotation number, with the downstream leg on the leading side having twice the heat transfer downstream for the high rotation number. On the trailing wall at the highest rotation number, the heat transfer augmentation decreased by a factor of two. Iacovides et al. (2001) used LDA and liquid crystals in a rotating water flow channel to study ribs angled at 45º. The Reynolds number was 36,000, and the rotation number was 0.1 and

0.2. A third study, by Servouse and Sturgis (2003), used PIV and an infrared pyrometer to measure the flow and heat transfer in a ribbed 180º bend with ribs angled at 60º and found differences of up to 150% in local heat transfer augmentation ratios between the side walls in the bend.

A heat transfer study in a ribbed 180º bend with 45º ribs was carried out by Azad et al. (2002). Two different rib configurations were compared to a smooth duct, and both orthogonal and angled rotation were studied, as well. The flow conditions included Reynolds numbers of 5,000 – 25,000, and the rotation numbers studied included Ro = 0.04 – 0.21. A rib configuration of parallel ribs was found to produce the optimum heat transfer, and rotation at an oblique angle was shown to have a smaller effect on leading and trailing wall heat transfer augmentation.

2.10 Calculations of a 180º Bend

Few calculations have been reported in the 180º bend region. An attempt to calculate the flow characteristics around a 180° bend using a k-ε model was reported by Besserman and Tanrikut (1992). The corners of the bend were rounded and the rounded dividing wall was about twice as wide as the channel width, most likely preventing separation at the bend near the dividing wall. A comparison of two wall treatments was made, and the two-layer wall integration technique was shown as a necessity in accurately predicting the top and bottom wall heat transfer in the bend. Though both models could accurately predict the secondary roll cells in the bend region (2 cells at the mid-turn and 4 cells entering the downstream leg), the model using wall functions failed to accurately predict the heat transfer in several locations. Both models failed to predict the heat transfer augmentation along the inside walls. Though the flowfield was simpler than many patterns typically found in bend regions, the mean flow

predictions turned out very well, as well as the heat transfer predictions in many cases. One case with 90º ribs in the upstream and downstream legs and angled ribs in the bend was simulated by Zhao and Tao (1997) using a k-ε model with wall functions, but heat transfer results were not well predicted. A low-Reynolds-number SST model was used by Lin et al. (2001) in the calculation of flow in a two-pass duct with 45º ribs and a smooth U-bend. A previously mentioned study, by Okita and Iacovides (2003), reported on a calculation of a ribbed bend with a high-Reynolds-number effective-viscosity-model and high-Reynolds-number differential stress model. Many of the heat transfer features on the inside and outside walls were correctly predicted by the differential stress model. A calculation by Gu et al. (2002) compared a two-equation k-ε model with a Reynolds-Stress Model in predicting flow and heat transfer in a smooth 180º bend. Turbulence anisotropy was found to be less of a factor in prediction accuracy when shear is the dominant term in the mean strain-rate tensor.

In summary, several distinct characteristics of flow and heat transfer are found in the vicinity of a smooth 180° bend region in a square cross-section turbine blade. These observations are not characteristic of all turning regions, however, as the flow characteristics are highly dependent on the geometry. Flow approaching the bend near the divider wall suddenly separates from the wall if the corner of the wall is sharp, while flow along the outside wall is entrained into a recirculation zone in the upstream corner. The separated flow on the inside reattaches to the wall in the downstream leg if the divider is thin or directly to the divider if it is thick enough. The rest of the flow in the bend is forced to the outside wall as a result of the separation bubble. Another recirculation region is found in the downstream corner of the bend. In a plane perpendicular to the flow direction and parallel to the divider wall, a pair of Dean vortices is found, which are counter-rotating vortices forcing flow towards the outside wall in the symmetry plane and

pulling flow towards the downstream leg of the duct near the top and bottom walls. High heat transfer regions are seen in the middle of the back wall as a result of the Dean vortices. In addition, high heat transfer has been observed on the top and bottom walls up against the back wall, on the outside wall at the entrance of the downstream leg, and at the location of reattachment in the downstream leg (if the divider region is thin enough to force flow separation).

2.11 LES Calculations

LES calculations have been applied to engineering applications in the past decade, but they have not become common in internal flow applications until more recently. LES calculations of stationary smooth ducts have been presented by Kajishima and Miyake (1993), who studied the mechanism of secondary flows and the ability of eddy viscosity turbulence models to predict such flows. The extension to LES from an Euler/RANS code was studied by Choi et al. (2000) in simulations of fully developed flow in a smooth duct. Xu and Pollard (2001) used LES to study flow in a square annular duct, and Hébrard and Métais (2004) applied LES to a heated S-curved duct. In rotating duct flows, Murata and Mochizuki (1999) varied the cross-sectional aspect ratio in a fully developed duct at low Reynolds numbers (Re = 4,000) and discussed the effect of indirect influences by the Coriolis induced secondary flow and the direct effect of Coriolis forces on the fluctuating components based on changes in the aspect ratio. Pallares and Davidson (2000) studied the flow in a rotating duct and concluded that, based on detailed observation of the terms of the transport equations and spatial distribution of the Reynolds stresses, rotation significantly reduces the overall turbulence level of the flow. A second study by the same authors (2002) compared the differences between a constant temperature boundary

condition and a uniform heat flux condition on the walls and found that centrifugal buoyancy dramatically affects the turbulence level in the flow. Swirling flow in a rotating circular pipe was studied by Feiz et al. (2003), who made several comparisons with DNS data and reported much better comparisons with the DNS results when the dynamic Smagorinsky model was used instead of the traditional model. Murata and Mochizuki (2004) compared the flow and heat transfer in a stationary two-pass smooth duct with that of a rotating duct and found a four-fold increase in friction factor over the stationary duct and a significant increase in heat transfer with rotation. Buoyancy effects were studied by the same author (2004) in a rotating two-pass smooth duct, and the trailing wall heat transfer was affected more than the leading wall because the longitudinal vortex structure near the trailing surface was maintained, while it was weakened by the opposing buoyancy contribution. The Reynolds numbers simulated in the previous two studies were less than 10,000.

Two authors used LES to study basic isolated features that are found in ribbed duct flows. Yang and Ferziger (1993) studied a periodic domain with a single large rib at Re = 3,000 using LES and found that the dynamic Smagorinsky model compared better with DNS data than the traditional model did. Sugawara et al. (2004) used LES at a higher Reynolds number (Re = 15,000) to study two-dimensional flow and heat transfer moving through a sudden expansion pipe with an expansion ratio of 2.0. The traditional Smagorinsky model was used in this study, and the time-averaged heat transfer was severely underestimated along the entire length of the duct. Time-averaged velocity, flow rate, and turbulence fluctuations compared very well with experiments, however. A detailed investigation of the unsteady characteristics of temperature, enstrophy (vorticity strength), skin friction, and the velocity gradient tensor was presented, as well.

A number of LES studies have been carried out in the fully developed section of ribbed ducts. Each study has contributed something to the overall understanding of the flow and heat transfer characteristics of ribbed duct flows. Variations in Reynolds number, aspect ratio, rib angle, and rib sizes have all been reported in different studies, and a comparison of the domains studied is given in Table 2.5.

Table 2.5. LES Studies in Periodic Ribbed Ducts

Author (Year)	Re	Aspect Ratio (W:H)	Rib Angle (α)	Rib Height (e/D_h)	Rib Pitch (P/e)	LES Model
Braun et al. (1999)	6,000	1:1	90º	0.05	10	Dynamic
Murata and Mochizuki (2000)	4,100 9,200	1:4 1:1	90º	0.10	10	Dynamic
Murata and Mochizuki (2001)	480 4,100	1:1	60º 90º	0.10	10	Dynamic
Murata and Mochizuki (2001)	2,500 9,500	1:1	60º 90º	0.10	10	Lagrangian Dynamic
Murata and Mochizuki (2003)	2,700 9,200	1:4 4:1	60º 90º	0.10	10	Dynamic / Lagrangian Dynamic
Jordan (2003)	8,000	Round	90º	0.12	5	Dynamic
Cui et al. (2003)	10,000	1:2 1:1	90º	0.08	1 9	Dynamic
Saha and Acharya (2003)	12,500	1:1	90º	0.10	10	Dynamic
Tyagi and Acharya (2004)	12,500	1:1	90º	0.10	10	Dynamic Mixed Model
Ahn et al., (2004)	30,000	∞:1	90º	0.10	10	Dynamic
Watanabe and Takahashi (2002)	117,000	2:1	90º	0.08	10	Smagorinsky / Dynamic
Takahashi and Watanabe (2004)	50,000 120,000	1:2 2:1	60º	0.08	11.5	Dynamic
Tafti (2005)	20,000	1:1	90º	0.10	10	Dynamic
Abdel-Wahab and Tafti (2004)	20,000	1:1	45º 90º	0.10	10	Dynamic

Braun et al. (1999) used LES to study periodically fully developed flow in a duct with very small (e/D_h = 0.006) roughness elements on one wall at a Reynolds number of 10,000. A comparison of the ribbed wall LES Nusselt number with the experimental Nusselt number yielded highly unsatisfactorily results, but because the experimental duct length was only about 10 rib pitches, it was indicated that fully developed flow would take a much longer duct because

the ribs were so small. Therefore, the fully developed heat transfer results would not compare well with the experiments because the experimental flow was still developing.

Murata and Mochizuki (2000) studied fully developed flow in a rotating smooth duct with ribs at three different aspect ratios, all of which had a Reynolds number less than 10,000. Wall shear stress was found to correlate extremely closely with high heat transfer in the instantaneous field, and rotation was shown to have a significant effect on exaggerating the difference in heat transfer between the leading and trailing walls. In the high aspect ratio ducts, the Coriolis forces affected the flow and heat transfer more strongly than in the square ducts. This study made a clear presentation of the characteristics of time-averaged flow in a rotating duct.

Rib angles of 60º and 90º were studied in a stationary fully developed duct by Murata and Mochizuki (2001), and the differences between laminar ($Re < 1000$) and turbulent ($Re > 3000$) flow were studied for both rib angles. Since laminar flow is not unsteady, the heat transfer gradients were much shallower than in the turbulent flow cases, which showed a sharp increase in heat transfer at the flow reattachment region between the ribs. Upstream of the ribs in the 60º case, the shear stress is negative in the turbulence case, while it is positive and strong in the laminar case, though both cases show similarly high values of heat transfer. In the 90º rib case, the laminar flow fails to reattach, and as a result the high heat transfer upstream of the ribs is not observed. Another study by the same authors (2001) used LES to study buoyancy in ducts with the same rib angles. The friction factor was found to increase with buoyancy in the 90º case, while the opposite was true in the 60º case. The main flow and heat transfer characteristics of the flow were unchanged with increases in buoyancy, but higher values were found along the trailing side with the increase.

A low Reynolds number (Re < 7,500) study in fully developed periodic ducts by Murata and Mochizuki (2003) used an LES calculation to study the effect of different aspect ratios on a duct with ribs angled at 60º to the flow. Aspect ratios from 1:4 to 4:1 were studied, and the effect of rotation was considered, as well. Coriolis effects were found to strengthen the secondary flows induced by the angled ribs, which introduced a difference in heat transfer augmentation between the two side walls. The magnitude of the difference in heat transfer augmentation between the two side walls appeared to be heavily dependent on the aspect ratio, or more specifically the distance between the two side walls. With the exception of the case with an aspect ratio of 4:1, rotation was shown to decrease the heat transfer averaged over the entire duct.

With a focus on marine applications, Jordan (2003) used LES to calculate the flow and pressure losses within a ribbed circular duct at a Reynolds number of 8,000. In this case, the ribs were more closely spaced than in typical turbine applications, but the results are similar. The strongest vorticity was found to be limited almost entirely to the core flow region. The effect of ribs, which are present in the flow to control the pressure recovered by turbulent ingestion, was shown to have the strongest irrecoverable pressure loss produced largely at the rib crest. Even though the experimental Reynolds number (4×10^6) measured on a submarine was three orders of magnitude higher than the LES Reynolds number, the predictions and experiments agreed well with each other, indicating that the salient turbulent physics produced at both Reynolds numbers are essentially scale-similar.

Cui et al., (2003) observed flow and turbulence effects in a duct with ribs on one wall and studied the result of varying the rib pitch between a case of full reattachment between the ribs and one in which the ribs were so close together that the flow failed to reattach. The LES study, at a Reynolds number of 10,000, found the length and time scales of the turbulence to be

dependent on the size and pitch of the ribs. Time averaging of the flow led to the classical semi-logarithmic velocity distribution, displaced from the law of the wall by the so-called roughness function. Though the classification of d-type (scales with duct diameter) and k-type (scales with rib height) roughness was shown to agree with the definitions derived from laboratory experiments, the effect of roughness elements on the opposite sides of the duct indicates that there is a large scale interaction between the flow near the ribs and the outer flow. The conclusion from this is that d-type and k-type classification is an oversimplification and must be studied more systematically.

A comparison between unsteady RANS calculations (URANS) across a wide range of Reynolds numbers and an LES calculation at Re = 12,500 in periodic ribbed duct flows was carried out by Saha and Acharya (2003) to investigate the accuracy gained over the computational cost involved. The URANS calculations showed much less unsteadiness than the LES calculations, and the averaged wall heat transfer augmentation values for both cases only compared to within about 30% of experiments. A similar trend seen earlier is also shown in the URANS calculations. Though increasing the density ratio at a constant rotation number did not affect the leading wall heat transfer, increasing the rotation number at a constant density ratio past a buoyancy parameter of 0.3 resulted in a minimum value of leading wall heat transfer augmentation, followed by an increase with rotation number. The effect is attributed to increases in buoyancy effects and the growth of the vortices near the ribs.

Instantaneous flow and heat transfer fields were reported in a fully developed periodic duct by Tyagi and Acharya (2004). The LES simulation at a Reynolds number of 12,500 focused on large scale coherent structures, which were thought to play a significant role in fluid mixing and heat transfer. The study stressed the importance of using more than a single ribbed module

because of low frequency fluctuations in the temperature field. Proper Orthogonal Decomposition of the flowfield found the low dimensionality of the system to be significant.

Ahn et al. (2004) presented a comparison of sharp-edged and circular ribs using LES calculations in channel flow at a Reynolds number of 30,000. The study found that the heat transfer augmentation was similar in both cases, but the friction factor augmentation was slightly less in the rounded rib case. The distribution of heat transfer along the centerlines was similar in shape and magnitude, but the gradients were smaller in the rounded rib case because of the smaller and weaker recirculation zones generated by the rounded ribs. Overall, the thermal performance of the rib, which takes into account the heat transfer and friction, was increased by about 5% for the rounded rib case.

Watanabe and Takahashi (2002) used an LES calculation to study flow in a duct with ribs on both walls (one heated wall) at a very high Reynolds number (Re = 117,000). Both a traditional Smagorinsky model and a local dynamic model were used in the flow, along with an attenuation function in the vicinity of the walls. The peak heat transfer regions upstream of the rib and downstream in the large reattachment region were attributed to the advection of coherent vortices near the reattachment point and in a region immediately upstream of the rib. The periodic calculations showed excellent agreement with the measurements.

High Reynolds number LES calculations of a periodic duct with crossed 60º angled ribs and different aspect ratio ducts were carried out by Takahashi and Watanabe (2004). The Reynolds number was varied between 50,000 and 120,000 in the stationary duct experiments. Flow and heat transfer results showed that the channel aspect ratio is related to the formation of the rib-induced separation vortex behind the rib, and the vortex shedding is strongly related to channel heat transfer. As a result of the trends in friction factor and heat transfer augmentation,

correlations were derived for a momentum transfer roughness function and a heat transfer roughness function, and they agreed fairly well with previous correlations derived from experiments.

An LES study by Tafti (2005) reported mean flow, turbulence, and heat transfer augmentation ratios for two different grid resolutions and compared the differences between using a Dynamic Smagorinsky model and using no model. The Reynolds number in this study was consistent across the entire study and had a value of 20,000. The study found that both mesh resolutions (96^3 and 128^3) predicted heat transfer and friction quantities to within 5-10% of the experimental values when the Dynamic Smagorinsky model was used.

Another study, by Abdel-Wahab and Tafti (2004), reported fully developed flow and heat transfer LES calculations in a rotating ribbed duct with both Coriolis and buoyancy forces included. The influence of buoyancy was shown to influence trailing wall heat transfer augmentation by 10-20% over those of rotating ducts with only Coriolis effects, while leading wall heat transfer augmentation was unaffected by the addition of buoyancy. Friction factor, on the other hand, was found to be augmented by 15-20% as a result of buoyancy forces.

All of the LES studies described to this point have used domains of periodic ducts or smaller. To the author's knowledge, only one other study has presented LES results on ribbed ducts larger than a periodic domain. Murata and Mochuzuki reported on the effects of Coriolis effects (2004a) and centrifugal buoyancy effects (2004b) in an entire two-pass duct at $Re < 5{,}000$. This low Reynolds number flow allows for a coarse grid as compared to what would be required at higher Reynolds numbers, and in this case the total number of grid points used in the study was 2.7 million. Rib configurations of 90º ribs, 60º ribs facing inward, and 60º ribs facing outward were compared in the calculations. The heat transfer characteristics in the stationary 180º bend

were all found to be similar across the three rib configurations shown. The flow in the straight passes was found to develop quickly, and the angled ribs were shown to quickly develop secondary flow patterns both in the upstream and downstream regions of the stationary duct. When the duct was rotating, interesting flow effects were observed in the bend, including the heat transfer being separated into two different sections in the bend and two sections in the downstream leg of the duct. With the addition of buoyancy forces, the aiding effect of buoyancy was seen in increased heat transfer augmentation on the trailing side of the upstream duct and the leading side of the downstream duct, while the opposing effect of buoyancy was found to suppress heat transfer on the leading wall of the upstream duct and to slightly increase heat transfer on the trailing side of the downstream duct.

Chapter 3. Computational Methodology

This chapter describes the calculation details. The first section outlines the governing equations and the subgrid scale model used, the second section describes the computational details of the developing flow calculation, the third section outlines the details of the 180º bend calculation, and the fourth section describes the post-processing for both a constant temperature boundary condition and a uniform heat flux boundary condition.

3.01 Governing Equations

The equations governing the flow are the time-dependent Navier-Stokes and energy equations in transformed coordinates $\vec{\xi} = \vec{\xi}(\vec{x})$. The flow is assumed to be incompressible, and all fluid properties are assumed to be constant. The equations, as well as all results presented in this dissertation, are given in terms of non-dimensional variables:

Continuity:

$$\frac{\partial}{\partial \xi_j}\left(\sqrt{g}\overline{U}^j\right) = 0, \tag{1}$$

Momentum:

$$\frac{\partial}{\partial t}\left(\sqrt{g}\overline{u}_i\right) + \frac{\partial}{\partial \xi_j}\left(\sqrt{g}\overline{U}^j\overline{u}_i\right) = -\frac{\partial}{\partial \xi_j}\left(\sqrt{g}\left(\vec{a}^j\right)_i\overline{p}\right) + \frac{\partial}{\partial \xi_j}\left(\left(\frac{1}{\mathrm{Re}} + \frac{1}{\mathrm{Re}_t}\right)\sqrt{g}g^{jk}\frac{\partial \overline{u}_i}{\partial \xi_k}\right), \tag{2}$$

and Energy:

$$\frac{\partial}{\partial t}\left(\sqrt{g}\overline{\theta}\right) + \frac{\partial}{\partial \xi_j}\left(\sqrt{g}\overline{U}^j\overline{\theta}\right) = \frac{\partial}{\partial \xi_j}\left(\left(\frac{1}{\mathrm{PrRe}} + \frac{1}{\mathrm{Pr}_t\mathrm{Re}_t}\right)\sqrt{g}g^{jk}\frac{\partial \overline{\theta}}{\partial \xi_k}\right), \tag{3}$$

where $\vec{a}^i$ are the contravariant basis vectors (the notation $\left(\vec{a}^{\,j}\right)_k$ is used to denote the *k*-th component of vector $\vec{a}^{\,j}$. $\left(\vec{a}^{\,j}\right)_k = \partial\xi_j/\partial x_k$), $\sqrt{g}$ is the Jacobian of the transformation, g^{ij} are the elements of the contravariant metric tensor, $\sqrt{g}U^j = \sqrt{g}\left(\vec{a}^{\,j}\right)_k u_k$ is the contravariant flux vector, u_i is the Cartesian velocity vector, and θ is the non-dimensional temperature defined as $\theta = \dfrac{T^* - T_{in}^*}{T_s^* - T_{in}^*}$ with a constant temperature boundary condition and $\theta = \dfrac{T^* - T_{in}^*}{\dfrac{q''^* D_h^*}{k^*}}$ with a uniform heat flux boundary condition (where an asterisk denotes dimensional quantities). The overbar denotes grid filtered quantities with an implicit top-hat filter, $\overline{G}$.

In rotating ducts, the Coriolis terms are modeled by the following source term included on the right hand side of the momentum equation (a complete derivation is given in Appendix B):

$$-2\sqrt{g}\,\mathrm{Ro}\,\overline{u}_m \in_{i3m}, \tag{4}$$

where Ro is the rotation number. In radially outward flow, this term enhances turbulence production on the trailing wall and attenuates turbulence on the leading wall, while the opposite is true for radially inward flow. Centrifugal buoyancy forces are modeled using the Boussinesq approximation and implemented in the momentum equations with the following term:

$$-\sqrt{g}\cdot\mathrm{Ri}\cdot\left(\overline{\theta} - \overline{\theta}_{ref}\right)\delta_{i1}, \tag{5}$$

where Ri is the Richardson number defined as $\beta\cdot\mathrm{Ro}^2\cdot r$. The term β is the volumetric thermal expansion coefficient, and r is the nondimensional rotational radius that is implemented as a function of x in these calculations. In this case, fluid that is warmer than the bulk fluid, such as that near the leading wall in radially outward flow, acts as a sink in the streamwise momentum equation, while the cooler fluid near the trailing wall acts as a source.

Re_t, the inverse of the non-dimensional eddy-viscosity, is modeled as:

$$\frac{1}{\mathrm{Re}_t} = C_s{}^2(\sqrt{g})^{2/3}\left|\bar{S}\right|, \tag{6}$$

where $\left|\bar{S}\right|$ is the magnitude of the strain rate tensor given by $\left|\bar{S}\right| = \sqrt{2\overline{S_{ik}}\,\overline{S_{ik}}}$.

The strain rate tensor is given by:

$$\bar{S}_{ik} = \frac{1}{2}\left((\vec{a}^m)_k \frac{\partial \overline{u_i}}{\partial \xi_m} + (\vec{a}^m)_i \frac{\partial \overline{u_k}}{\partial \xi_m} \right), \tag{7}$$

and the Smagorinsky constant, $C_s{}^2$, is obtained via the Dynamic subgrid stress model (Germano et al., 1991). The dynamic quality of this model makes it particularly suitable for the developing flow calculations because of its validity in all flow regimes, laminar, transitional, and turbulent. To this end, a second test filter, denoted by $\hat{G}$, is applied to the filtered governing equations with the characteristic length scale of $\hat{G}$ being larger than that of the grid filter, $\overline{G}$. The test filtered quantity is obtained from the grid filtered quantity by a second-order trapezoidal filter which is given by $\hat{\varphi} = \frac{1}{4}\left(\overline{\varphi}_{i-1} + 2\overline{\varphi}_i + \overline{\varphi}_{i+1}\right)$ in one dimension. The resolved turbulent stresses, representing the energy scales between the test and the grid filters, $L_{ij} = \widehat{\overline{u}_i\overline{u}_j} - \hat{\overline{u}}_i\hat{\overline{u}}_j$, are then related to the subtest, $T_{ij} = \widehat{\overline{u_i u_j}} - \hat{\overline{u}}_i\hat{\overline{u}}_j$, and subgrid-scale stresses $\tau_{ij} = \overline{u_i u_j} - \overline{u}_i\overline{u}_j$ through the identity $L_{ij} = T_{ij} - \hat{\tau}_{ij}$.

The anisotropic subgrid and subtest-scale stresses are then formulated in terms of the Smagorinsky eddy viscosity model as:

$$\tau_{ij}^a = -2C_s^2(\sqrt{g})^{2/3}\widehat{\left|\bar{S}\right|\bar{S}}_{ij} \text{ and} \tag{8}$$

$$T_{ij}^{a} = -2C_s^2\alpha\left(\sqrt{g}\right)^{2/3}\left|\hat{\bar{S}}\right|\hat{\bar{S}}_{ij}, \tag{9}$$

using the identity

$$L_{ij}^{a} = L_{ij} - \frac{1}{3}\delta_{ij}L_{kk} = -2C_s^2(\sqrt{g})^{2/3}\left(\alpha\left|\hat{\bar{S}}\right|\hat{\bar{S}}_{ij} - \widehat{\left|\bar{S}\right|\bar{S}_{ij}}\right) = -2C_s^2(\sqrt{g})^{2/3}M_{ij}. \tag{10}$$

Here α is the square of the ratio of the characteristic length scale associated with the test filter to that of the grid filter and is taken to be $\left[\hat{\Delta}_i / \bar{\Delta}_i = \sqrt{6}\right]$ for a three-dimensional test filtering operation (Najjar and Tafti, 1996). Using a least-squares minimization procedure of Lilly (1992) a final expression for C_s^2 is obtained as:

$$C_s^2 = -\frac{1}{2}\frac{1}{(\sqrt{g})^{2/3}}\frac{L_{ij}^{a}\cdot M_{ij}}{M_{ij}\cdot M_{ij}}, \tag{11}$$

where the local value of C_s^2 is constrained to positive values. The turbulent Prandtl number, Pr_t, is assumed to have a constant value of 0.5 in the energy equation (Moin et al., 1991).

The governing equations for momentum and energy are discretized with a conservative finite-volume formulation using a second-order central difference scheme on a non-staggered grid topology. The Cartesian velocities, pressure, and temperature are calculated and stored at the cell center, whereas contravariant fluxes are calculated and stored at the cell faces. For the time integration of the discretized continuity and momentum equations, a projection method is used. The temporal advancement is performed in two steps, a predictor step, which calculates an intermediate velocity field, and a corrector step, which calculates the updated velocity at the new time step by satisfying discrete continuity. The energy equation is advanced in time by the predictor step. Details about the algorithm, functionality, and capabilities can be found in Tafti (2001).

The computer program GenIDLEST (**Gen**eralized **I**ncompressible **D**irect and **L**arge-**E**ddy **S**imulations of **T**urbulence) used for these simulations has been applied to many different cases, ranging from louvered fins to fully developed ribbed ducts, and in all of these cases it has been consistently established through comparison with experiments that predictions of mean flow, turbulent quantities, and heat transfer are accurate to within $\pm 10\%$ of experiments and in some cases to within experimental uncertainty.

3.02 Developing Flow Calculation Description

The objective of the developing flow calculations is to explore the effects of rotation on the hydrodynamic and thermal development length at the duct entrance and to understand the development of secondary flows and their impact on the wall heat transfer distribution. In rotating ducts, the flow has a long development length that covers a significant portion of the duct, so it is important that the features found in the developing flow region be well understood. A straight domain with nine ribs is used to model the developing region, and the details are discussed in this section.

Calculation Domain

The computational domain used for studying the developing flow region consists of two sections, an entry region where the developing effects are studied and a long outflow region to eliminate any disturbances from the exit region. The model, shown in Figure 3.1, consists of a ½ D_h smooth entrance region, eight ribs in succession, and an exit consisting of one rib and a long exit channel. A stationary calculation requires approximately five ribs to achieve fully developed flow, and based on preliminary studies of rotating duct flow, eight ribs were deemed sufficient for obtaining nearly fully developed flow in the rotating cases. The goal of obtaining a

sufficiently long developing flow length was to observe the flow development to a point where wall heat transfer began to reach a steady value but not necessarily in the classical sense, where two boundary layers meet in the center of the duct and flow characteristics stop changing in the streamwise direction.

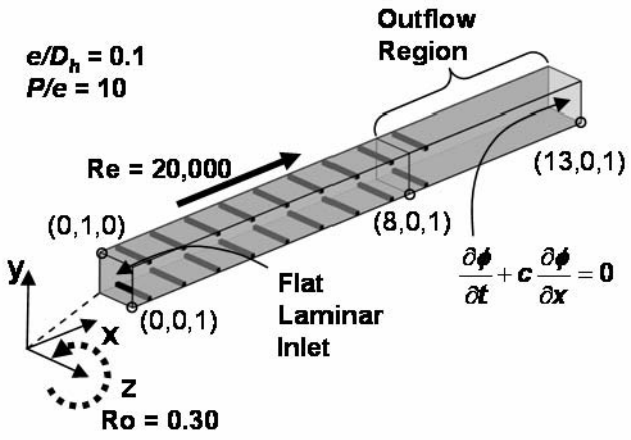

Figure 3.1. The developing flow domain includes eight ribs plus an extension region, which includes a ninth rib and a smooth region to allow turbulence to dissipate.

The developing flow channel has an aspect ratio of 1:1. Based on the definitions described in the diagram of a single ribbed module in Figure 3.2, the geometric ratios governing the rib placement are e/D_h = 0.1 and P/e = 10, which are typical in many computational and experimental studies. At the entrance, the centerline of the first rib is ½ D_h downstream of the inlet plane.

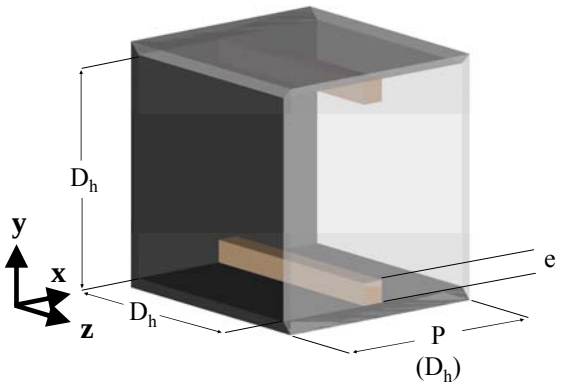

Figure 3.2. The geometric parameters governing ribbed duct flow show that e represents the rib height, D_h represents the duct height, which is also the hydraulic diameter, and P represents the rib pitch. The ratio of rib height to hydraulic diameter in this study is $e/D_h = 0.1$, and the ratio of rib pitch to rib height is $P/e = 10$.

Nondimensionalization

The governing flow and energy equations are non-dimensionalized by a characteristic length scale, given by the channel hydraulic diameter (D_h), and a characteristic velocity scale, given by the channel bulk velocity ($\overline{u_{in}}$). The characteristic temperature scale was given by ($T_s^* - T_{in}^*$) for the constant temperature cases and $\left(\frac{q''^* D_h^*}{k^*}\right)$ for the uniform heat flux cases. The non-dimensional time step in the calculation is non-dimensionalized by the channel hydraulic diameter and bulk flow velocity and is set to a value of 5×10^{-5}.

Boundary Conditions

The two boundary conditions imposed on the walls, reflecting the no-slip boundary condition and a zero pressure gradient at the walls, are the following:

$\vec{u} = 0$, and (12)

$$\nabla p \cdot \vec{n} = 0 . \tag{13}$$

The duct surfaces and ribs are heated with the same boundary condition in each calculation. The stationary case is heated with a constant temperature boundary condition, and both a constant temperature and uniform heat flux case are presented for a rotating duct with Coriolis effects. For the rotating ducts with buoyancy effects, the walls and ribs were heated with a uniform heat flux boundary condition. In the constant temperature cases, the boundary condition implemented at the walls is described by the following:

$$\theta_s = 1 , \tag{14}$$

while the boundary condition implemented at the walls in the uniform heat flux cases is described as:

$$\nabla \theta \cdot \vec{n} = 1 . \tag{15}$$

In each of the developing flow cases, a uniform laminar plug flow velocity profile is applied as the inlet boundary condition. The inlet test conditions in the experimental rigs used by J.C. Han and T.-M. Liou (Han and Park, 1988; Liou and Hwang, 1992), as well as many others in the open literature, are simulated by flow exiting a plenum through a sharp contraction into the test section. This produces separated flow with a low level of turbulence at the inlet. The only difference between these two studies and the current study is the absence of separated flow. This difference, however, is inconsequential by the time the flow reaches the second rib. Another set of calculations with fully developed turbulent flow profiles was also performed and it was found that the calculated heat transfer coefficients were nearly identical after the second rib. The non-dimensional inlet temperature field is zero by definition.

At the outflow boundary, a convective condition of the type:

$$\frac{\partial \phi}{\partial t} + c \frac{\partial \phi}{\partial x} = 0 \tag{16}$$

is applied, where c is the mean convective velocity and ϕ is the variable being convected out (u,v,w, or θ).

Calculation Details

In the stationary fully developed calculations by Tafti (2005) and the rotating fully developed calculations by Abdel-Wahab and Tafti (2004a,b; 2005), two different grid resolutions were used for the domain discretization. Grid independence studies by both authors compared results found when the periodic module was discretized with 96 grid points on a side (total size = 96^3) and when the module was discretized with 128^3 grid points. When the Dynamic Smagorinsky subgrid scale model was used, Tafti (2005) showed differences of less than 3% between the two grid resolutions, and both meshes predicted the local and mean heat transfer augmentations to within experimental uncertainty on the ribbed and smooth walls. In fully developed rotating ducts, Abdel-Wahab compared the two grid resolutions and their effect on Coriolis and buoyancy results, and his study showed that the 96^3 grid showed differences of less than 5% in nearly all comparisons. Because the differences between the two grid resolutions are small and the calculation domains used in this study are nearly 10 times the periodic grid size, the 96^3 mesh was used for each ribbed section.

The developing flow domain was parallelized across 320 domains, and each calculation utilized 160 processors of an IA-64 Itanium 2 Linux cluster at NCSA at Champaign, Illinois. The original calculations were run on the first generation cluster, and each time step consumed approximately 0.5 μs/grid node of wall clock time. The second generation cluster, built with Itanium 2 processors, consumed approximately 0.12 μs/grid node of wall clock time for each time step. The original calculations required approximately 22 hours of wall clock time to

calculate a single non-dimensional time unit, while the second generation computers require only 8.5 hours to calculate a time unit.

The Reynolds number based on the inlet velocity, which is also the bulk fluid velocity, is 20,000, Prandtl number is 0.7, and the rotation number (rotating cases only) is 0.3.

At each time step, the diffusion terms are treated implicitly, and the average L_1 residual norm of global mass balance is converged to 1×10^{-8}, while the momentum and energy equations are converged to 1×10^{-7}.

The calculation was initiated by assuming initial conditions similar to a fully developed channel and integrating in time until the flow reached a statistically stationary state. The time evolution of bulk quantities such as Nusselt number, wall heat flux, friction drag losses, and form drag losses were observed until all values reached a uniform state. Once stationary conditions were established, sampling to obtain mean and turbulent quantities was carried out for approximately 10 to 20 time units, depending on the calculation. Initial mean quantities were obtained by sampling over one time unit before obtaining turbulent statistical quantities.

3.03 180º Bend Calculation Description

The 180º bend produces extremely high heat transfer rates, along with a large pressure drop. Because these contribute to the overall heat transfer and friction factor characteristics of a blade, it is important to understand the flow and heat transfer characteristics of this region. The layout of the 180º bend, as well as boundary conditions and computational details, are described in this section.

Calculation Domain

The computational domain used for studying the 180º bend region, shown in Figure 3.3, extends from three ribs in the upstream leg to three ribs downstream and is followed by a smooth extension region. No rib is included in the bend in all studies reported in this text, but Appendix D is a publication in the *ASME Journal of Turbomachinery* detailing a comparison in a stationary duct between placing a rib in the bend and having no rib in the bend. As shown in the figure, the inside and outside walls have square corners, and the upstream and downstream ribs are placed immediately upstream and downstream of the inlet and outlet, respectively. The dividing wall has a thickness of ½ D_h. The ribs are place directly at the entrance and exit to the bend: the downstream face of the last rib in the upstream duct is aligned with the tip of the dividing wall (i.e. the last rib upstream is immediately upstream of the bend entrance), and the upstream face of the first downstream rib also lines up with the dividing wall. A fully turbulent inlet boundary condition was applied, as will be discussed later, and a convective outflow boundary condition was applied at the downstream side of the smooth extension region. The Cartesian coordinate system used for the calculation and for reporting results is shown in Figure 3.3. The streamwise direction, x, ranges from the inlet (x=0) to the back wall (x=4), and the cross-stream direction, y, ranges from the trailing wall (y=0) to the leading wall (y=1). The z-direction ranges from the outer wall of the downstream side (z=0) to the outer wall of the upstream side (z=2.5). The duct aspect ratio is 1:1, and the geometric ratios governing rib placement are the same as those in the developing flow region described earlier (e/D_h = 0.1 and P/e = 10).

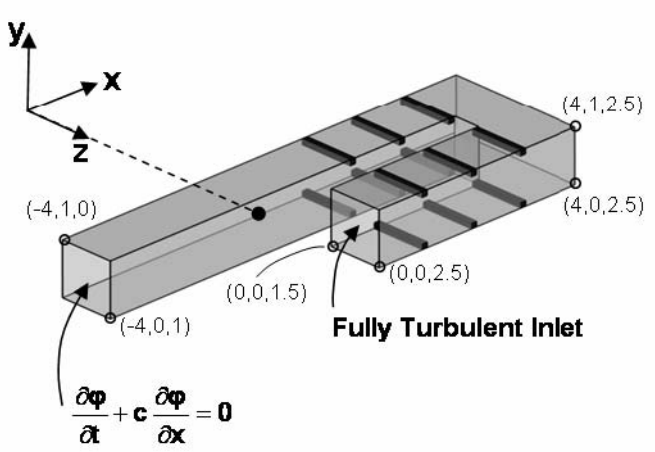

Figure 3.3. The 180º bend domain consists of three ribs upstream and downstream of the bend. An extension region is included downstream to negate effects from the outflow boundary condition. The dividing wall is ½ D_h in width, and the duct cross-sectional area is 1 D_h^2 throughout the bend.

Nondimensionalization

The governing flow and energy equations are non-dimensionalized by a characteristic length scale, given by the channel hydraulic diameter (D_h), a characteristic velocity scale, given by the channel bulk velocity ($\overline{u_{in}}$), and a characteristic temperature scale, given by ($T_s - T_{in}$) for the constant heat flux case and $\left(\frac{q''D_h}{k}\right)$ for the uniform heat flux case. The non-dimensional time step in the calculation is non-dimensionalized by the channel hydraulic diameter and bulk flow velocity and is set to a value of 5×10^{-5}.

Boundary Conditions

The boundary conditions imposed on the walls, reflecting the no-slip boundary condition and a zero pressure gradient at the walls, are described by Eqs. (12) & (13) in the Developing flow section. The duct surfaces and ribs are heated with the same boundary condition in each

calculation. The stationary case and the rotating calculation with Coriolis effects are each heated with a constant temperature boundary condition. For the rotating ducts with buoyancy effects, the walls and ribs were heated with a uniform heat flux boundary condition. In the constant temperature cases, the boundary condition implemented at the walls is described by Eq. (14), and in the uniform heat flux cases, the boundary condition is described by Eq. (15).

A fully developed turbulent profile was implemented at the inlet boundary condition to reproduce the same scenario as a 180º bend found at the end of a long duct. In this case, a series of time-dependent planes were extracted from a location downstream of the eighth rib in the developing flow calculation with the same Reynolds number, rotation number, and buoyancy parameter. The planes were implemented in succession at the inlet to the 180º bend until the end of the set was reached, at which point they would be repeated to represent an infinitely long fully developed flow condition. Details about the extraction and processing procedure, as well as the tests to ensure that a sufficiently long set of frames was extracted, are outlined in Appendix C.

At the outflow boundary, the same convective condition described in the developing flow section by Eq (16) is applied.

Calculation Details

The calculation domains presented in this dissertation are an extended channel consisting of nine ribs and a 180º bend consisting of six ribs and a bend region. For the same reasons mentioned earlier in the developing flow section, the 96^3 mesh is used for each ribbed section.

The Reynolds number based on the inlet velocity, which is also the bulk fluid velocity, is 20,000, Prandtl number is 0.7, and the rotation number (rotating cases only) is 0.3.

The 180º bend calculation was divided into 304 domains and utilized 154 processors of an IA-64 Itanium 2 Linux cluster at NCSA at Champaign, Illinois. The original calculations were run on the first generation cluster, and each time step consumed approximately 0.5 μs/grid node of wall clock time. The next generation cluster, built with Itanium 2 processors, consumed approximately 0.12 μs/grid node of wall clock time for each time step. The original calculations required approximately 22 hours of wall clock time to calculate a single non-dimensional time unit, while the next generation computers require only 8.5 hours to calculate a time unit.

The diffusion terms are treated implicitly, and the average L_1 residual norm of global mass balance is converged to 1×10^{-8}, while the momentum and energy equations are converged to 1×10^{-7}. The calculations utilized 112 processors of an IA-64 Itanium Linux cluster. Each time step took about 0.5 μsecs/grid node of wall clock time.

The calculation was initiated by assuming initial conditions similar to a fully developed channel and integrating in time until the flow reached a statistically stationary state. The time evolution of bulk quantities such as Nusselt number, wall heat flux, friction drag losses, and form drag losses were observed until all values reached a uniform state. Once stationary conditions were established, sampling to obtain mean and turbulent quantities was carried out for approximately 10 to 20 time units, depending on the calculation. Initial mean quantities were obtained by sampling over one time unit before obtaining turbulent statistical quantities.

3.04 Post Processing

Once the calculation is completed, the final step is to compile the data into a form that can be studied and compared with others. This section outlines the post processing, including the data

reduction for the constant temperature and uniform heat flux cases as well as additional averaging based on symmetry.

Data Reduction – Constant Temperature Calculations

The local Nusselt number as related to the *non-dimensional* heat flux and non-dimensional temperature is calculated as:

$$\mathrm{Nu} = \frac{q''}{\theta_s - \theta_{ref}}, \tag{17}$$

where q'' is the non-dimensional heat flux at the walls, $\theta_s = 1$ is the surface boundary condition, and θ_{ref} is the reference temperature defined as:

$$\theta_{ref} = \frac{\iint |u_1| \theta dA_x}{\iint |u_1| dA_x}, \tag{18}$$

where θ is the non-dimensional temperature defined as:

$$\theta = \frac{T^* - T_{in}^*}{T_s^* - T_{in}^*}. \tag{19}$$

The surface-averaged Nusselt number is area weighted as:

$$\overline{\mathrm{Nu}} = \frac{\iint_S \mathrm{Nu} \cdot dS}{\iint_S dS}, \tag{20}$$

where S denotes the surface under consideration. Finally, the Fanning friction factor is calculated in terms of the non-dimensional pressure gradient as:

$$f = -\frac{1}{2}\frac{\Delta p}{\Delta L}, \tag{21}$$

where ΔP is the area averaged pressure difference at two flow cross-sections separated by L.

The reference values for the Nusselt number and friction factor are obtained from the Dittus-Boelter and Blasius correlations, respectively(Incropera and DeWitt, 2002):

$$\mathrm{Nu}_0 = 0.023 \cdot \mathrm{Re}^{0.8} \cdot \mathrm{Pr}^{0.4} \tag{22}$$

and

$$f_0 = 0.046 \cdot \mathrm{Re}^{-0.2}. \tag{23}$$

Data Reduction – Uniform Heat Flux Calculations

The local Nusselt number as related to the non-dimensional temperature is calculated as:

$$\mathrm{Nu} = \frac{1}{\theta_s - \theta_{ref}}, \tag{24}$$

where θ_s is the calculated surface temperature, and θ_{ref} is the reference temperature defined as:

$$\theta_{ref} = \frac{\iint |u_1| \theta dA_x}{\iint |u_1| dA_x}, \tag{25}$$

where θ is the non-dimensional temperature defined as:

$$\theta = \frac{T^* - T_{in}^*}{\frac{q''^* D_h^*}{k^*}}. \tag{26}$$

The surface-averaged Nusselt number is area weighted as:

$$\overline{\mathrm{Nu}} = \frac{\iint_\Omega \mathrm{Nu} \cdot dS}{\iint_\Omega dS}, \tag{27}$$

where S denotes the surface under consideration. The friction factor calculation and reference values are the same as those listed in Eqs. (27) & (28).

Symmetry-Based Averaging

The calculation results were completed over the entire domain in each case, but in the post-processing step, some cases could be averaged further into smaller zones to take advantage of symmetry in the data.

The stationary developing flow calculations have a symmetry plane in both the *y*-direction and *z*-direction, so the results could be four-way averaged to quadruple the sampling time. The rotating developing flow calculations have a symmetry plane in the *z*-direction, which could be used to double the sampling time.

For the stationary calculations, a *y*-symmetry plane allowed for doubling the sampling time, but no symmetry averaging could be obtained in the rotating 180º bends.

Chapter 4. Stationary Developing Flow and 180° Bend[1]

Stationary calculations provide the baseline cases for studying rotational effects. Understanding the effects of ribs on the flow and turbulence without rotation also introduces a framework for presenting results in a rotating ribbed duct. Stationary calculations are also the easiest to validate, as experimental measurements are more readily available and attainable in a stationary duct than in a rotating duct. Through comparisons with experiments, the reliability of the LES calculations in ribbed duct flows can be established, and the understanding of the prediction capability can be extended to rotating calculations, where validation measurements are much more difficult to attain.

In this project, a stationary test rig was designed and built by a group of Seniors as a design project during the 2002-2003 academic year to provide a set of measurements for validating the calculations. Afterwards, several flow field and heat transfer experiments were carried out by undergraduate researchers. In addition to the measurements obtained from this project, other friction factor, flowfield, and heat transfer measurements from the open literature were used in validation of the current work.

The objective of this chapter is to validate the LES calculations against experiments at a Reynolds number of 20,000. Comparisons with flow, turbulence, and heat transfer experiments are presented in each of the developing flow, fully developed, and 180° bend regions. Additionally, the important flow physics found in stationary ducts are discussed alongside the comparisons via mean and turbulent quantities in the three regions.

[1] Reproduced in part with permission from ASME and Elsevier

4.01 Experimental Apparatus

The data included in this chapter, including flow field and pressure drop measurements, was acquired in a ribbed channel facility. Figure 4.1 shows an overall schematic of the facility, which was a closed-loop design. Air was supplied to the channel by means of a 2 hp fan. Downstream of the fan, the air passed through a large diffuser, a heat exchanger, and a nozzle having an area ratio of 10:1. The nozzle was designed through CFD simulations to give a uniform inlet profile at the entrance to the channel. The ribbed channel of square cross-section (AR = 1:1) consisted of a straight section, followed by a 180° sharp turn, followed by another straight portion. Upon exiting the return leg of the test section, the air passed through a venturi flowmeter before returning to the fan. The venturi flowmeter was calibrated against a laminar flow element whereby the laminar flow element was calibrated by the manufacturer. The venturi was used rather than the laminar flow element because it incurred a lower pressure drop to the system. Coarse adjustments to the flowrate were made using a large gate valve immediately upstream of the fan, while fine adjustments were made using a motor controller connected to the fan. All of the flow field and heat transfer measurements were performed at a Reynolds number of 20,000, which was set based on the bulk velocity as calculated from the venturi flowmeter. Air temperatures and absolute pressures were also taken into account in this calculation with both being measured just before the inlet to the test section.

The test section, which was designed to insure good measurement resolution while matching the computational results, included a square channel made of Lexan. Lexan provided a surface that was optically acceptable for the laser Doppler velocimeter (LDV) measurements. The inner channel width and height were 14.9 cm with a wall thickness of 0.95 cm. The channel was approximately 3.53 m in length upstream of the 180° sharp bend that maintained the same channel dimensions. The downstream leg of the ribbed channel extended another 1.47 m.

Attached to the bottom and top walls of the channel were ribs machined from Delrin, which is a low friction, inflexible polymer. The ribs were square in cross-section with a rib height of 1.49 cm (e/D_h = 0.1). The location of the first rib was placed at 6.7 cm (0.45 rib pitches) downstream of the contraction exit, which is 4.5 rib heights for the baseline case and 2.7 rib heights for the larger ribs.

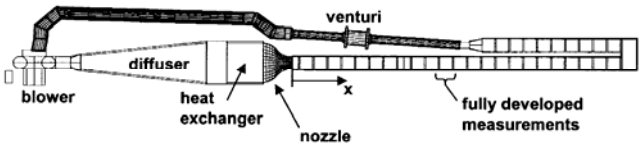

Figure 4.1. The closed loop test facility includes a 2 hp blower, a plenum with a heat exchanger, 1½ ribbed channels, and a venturi flow meter downstream of the return leg.

Prior to making the LDV measurements, pressure drop measurements were completed for a range of conditions to allow friction factors to be compared with the literature and calculations. To determine the increased frictional losses resulting from the ribs, pressure taps were installed along the entire channel length of the smooth side wall and were spaced 14.9 cm apart and located directly between the ribs. Both average (over many ribs) friction factors as well as local (across one rib) friction factors were calculated. The average friction factors included all of the ribs extending from the fourth rib to the 23rd rib. The normalizing relation for the friction factors was (Incropera and DeWitt, 2002):

$$f_0 = 0.046\,Re^{-0.2} \tag{1}$$

Flowfield measurements for this study included the mean and the corresponding root-mean-square (rms) velocities. A two-component back-scatter fiber optic LDV system was used in this study that consisted of a 5 Watt laser and a TSI model 9201 Colorburst beam separator. Velocity

data was processed using TSI model IFA 755 Digital Burst Correlator controlled using TSI's FIND software. The LDV was positioned on the side of the test channel to capture the streamwise (u) and vertical (v) components of the velocity. To capture the smallest control volume, a 450 mm focusing lens was used in conjunction with a beam expander. The probe volume length and diameter were 0.32 mm and 44 microns, respectively. The LDV probe was tilted at 10° to allow for measurements very near the surface. For the LDV measurements, each mean and rms velocity was averaged between 10,000 and 20,000 points, which took nominally 20 seconds to acquire. All measurements were corrected for bias errors using the well accepted time weighted average correction scheme. The flow was seeded using olive oil having a nominal particle diameter of 1 micron.

An infrared camera was used to measure the heat transfer augmentation on one ribbed wall section and one smooth side wall section in the fully developed region of the duct. Each picture covered an area that was approximately 14.9 cm by 14.9 cm with the area being divided into 360 by 240 pixel locations. At each viewing location five images were averaged, with each image being averaged over 16 frames, providing a total of 80 data points averaged at each pixel location. Calibration of the infrared camera was made using three thermocouples embedded in each wall examined. Thermocouples were also used to monitor the bulk fluid temperature. A uniform heat flux boundary condition was imposed on the walls by a series of foil resistance heaters mounted to the walls and ribs. Foil heaters were applied to all surfaces of the ribs on a separate electrical circuit to apply the same heat flux boundary condition as that on the walls. The voltage across a precision resistor in series with the heaters and the voltage across the heaters were used to obtain the heat flux on the walls. The heat transfer was obtained by calculating the Nusselt number with the following equation:

$$\mathrm{Nu} = \frac{q''}{(T_s - T_b)} \cdot \frac{D_h}{k}, \tag{2}$$

where T_s is the surface temperature measured by the infrared camera and T_b is the bulk fluid temperature interpolated from a measured inlet temperature to the measurement location by an energy balance. The heat transfer measurements were normalized by the Dittus-Boelter correlation (Incropera and DeWitt, 2002):

$$\mathrm{Nu}_0 = 0.023 \cdot \mathrm{Re}^{0.8} \cdot \mathrm{Pr}^{0.4} \tag{3}$$

Overall uncertainties were calculated for the friction factors and flow field measurements according to the partial derivative method described by Moffat (1988). The total uncertainty of all measurements was calculated as the root of the sum of the squares of the precision uncertainty and the bias uncertainty. The precision uncertainty was based on a 95% confidence interval. The estimate of bias uncertainties for the mean velocities was 1%. The precision uncertainty for the streamwise rms velocities was 2.6%. For the friction factors, the uncertainty was calculated to be 6%. For the heat transfer measurements, the uncertainty at a Nusselt number of 85 was 6.9% and at a Nusselt number of 165, the uncertainty was 12.9%.

4.02 Distributions of Mean Flow and Turbulent Quantities in Developing and Fully Developed Regions

The focus of this section is to quantify the prediction accuracy of the calculations with a series of comparisons with experiments and other calculations. The prediction accuracy of the LES calculations compared to that of standard RANS calculations is of interest to help qualify the tradeoff between the industry standard RANS calculations and the more expensive but less empirical LES calculations. Along with validation, however, several explanations of the characteristics of stationary flow in the developing and 180º bend regions are discussed.

Two instantaneous plots of the streamwise distribution of temperature are shown in Figure 4.2. Figure 4.2(a) is a vertical plane between the two side walls ($z = 0.5$), and Figure 4.2(b) is a horizontal cutting plane between the ribbed walls ($y = 0.5$). The vertical plane includes the ribbed walls at either side, whereas the horizontal planes are bounded by the smooth channel walls. In the vertical plane, the development of the thermal boundary layer is aided by the presence of the ribs and the large scale coherent vorticity generated by the separated shear layers. The rapid mixing provided by the large scale structures results in substantial growth of the thermal boundary layer. In the horizontal plane, however, the thermal boundary layer development is quite slow in comparison and shows little penetration into the center of the channel. It can be concluded from these plots that the thermal flow is not fully developed in the classical sense. By that it is meant that the non-dimensional temperature profiles are still evolving in the streamwise direction. However, as will be shown in subsequent results, this does not have as large of an effect on the heat transfer augmentation as it would in a plain duct flow.

In the developing flow region, measurements were taken to compare with the predictions and to verify the capability of the calculations to accurately predict hydrodynamic development in the ribbed duct. In the calculations, a fully laminar flat velocity profile was implemented at the inlet. For comparison purposes, the test section entrance was designed to have a flat velocity profile, as well, and the measured profile came very close to accomplishing this, as can be observed in Figure 4.3. The figure shows the horizontal and vertical streamwise velocity profiles at the duct inlet, and the nondimensional velocity has a value very close to unity across the duct. Streamwise rms quantities, which are not shown in the figure, are also very small, around 2-3%, but they are slightly larger than the value of 0% specified at the developing flow inlet in the calculations.

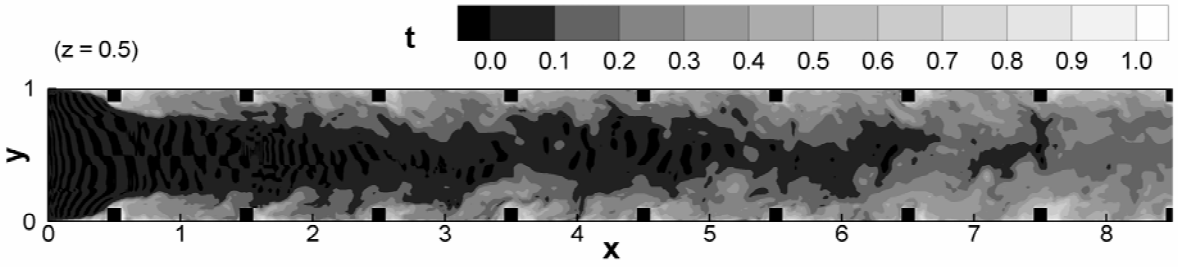

(a)

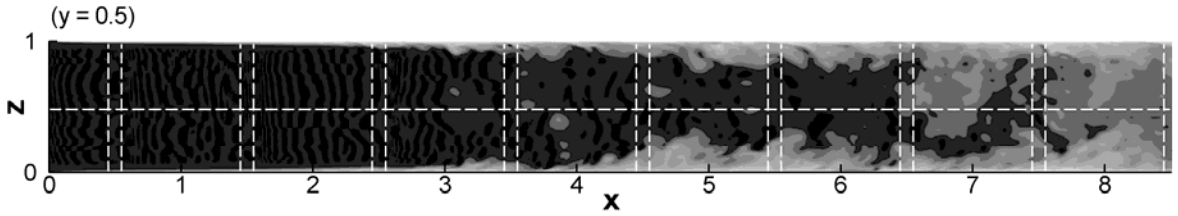

(b)

Figure 4.2. (a) Vertical and (b) horizontal planes of the instantaneous temperature show that the temperature effects reach the center of the duct near the seventh and eighth ribs.

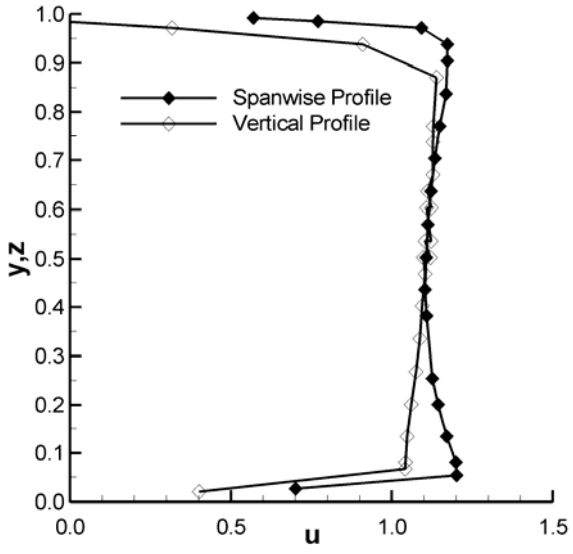

Figure 4.3. The velocity profile at the duct inlet is flat and very similar to a plug flow, which meets the design criteria for the experiments.

Figure 4.4 shows the measured and predicted centerline streamwise velocity and streamwise, vertical, and spanwise (predicted only) turbulent quantities. At the entrance, a spike in the streamwise velocity shows the sudden acceleration of the flow due to the contraction forced by the first ribs past the entrance to the duct. The acceleration is followed by a region of deceleration resulting in a pressure recovery. The less dramatic effect in the experiments is attributed to the presence of turbulence at the inlet (2–3%). The measured centerline velocity increases until flow reaches the seventh rib, after which it settles down into a periodic pattern. The computations, on the other hand, settle into a periodic pattern after the fourth rib. The predicted flow transitions to turbulence immediately after the first rib as the separated shear layers on the ribs develop three-dimensional instabilities. The turbulence generated near the ribbed walls diffuses to the center of the channel as flow moves into the duct with a steady near-linear increase in turbulence intensities up to about the eighth rib. The figure shows that increasing the calculation resolution to 128^3 from 96^3 improves the centerline velocity prediction. The overprediction of streamwise turbulence intensity at the center of the channel is also suspected to be a caused by the coarse-mesh resolution. The results are consistent with a grid dependence study of fully developed calculations reported in Tafti (2005). They showed that at low resolution (96^3) higher turbulence levels are predicted at the center of the channel than at higher resolution (128^3). The initial underprediction of the turbulence intensities near the inlet is a result of the preexisting turbulence in the experiments, whereas no turbulence was specified at the inlet of the calculation. In the fully developed region, the turbulence quantities are approximately 16%, 11%, and 12% for u_{rms}, v_{rms}, and w_{rms}, respectively. These are similar to the measured values of 14% and 11% for u_{rms} and v_{rms} as reported by Rau et al. (1998). Overall, the comparison between the measured and predicted quantities is excellent between the high

resolution fully developed calculations and measurements, and somewhat good agreement is seen between the low resolution developing flow and fully developed calculations. It is noted that the overprediction of turbulence is only present at the center of the channel because of the coarse mesh and does not influence the prediction of the ribbed wall heat transfer coefficient, which is much more dependent on near wall turbulence intensities. This same effect was observed in an earlier grid dependence study (Tafti, 2005).

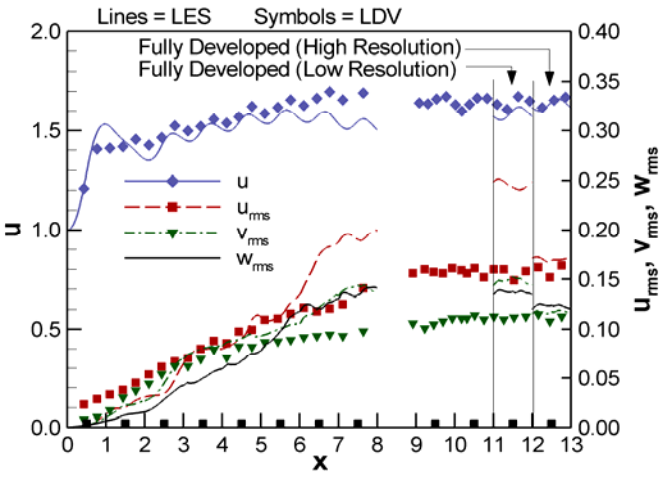

Figure 4.4. The streamwise velocity and turbulence quantities in all three directions shows longer development length in the channel center as compared to near the ribbed walls, which is typically reported as three to four ribs. (symbols = measurements; solid lines = predictions)

Mean and turbulent profiles in the symmetry plane midway between pairs of ribs in the developing flow region are shown in Figure 4.5. The negative value in the streamwise velocity profile (Figure 4.5(a)) near the entrance shows the presence of the large recirculation region stretching past the midpoint between the first two ribs, while the other profiles show no evidence of recirculation, indicating that reattachment has occurred before the midpoint. In Figure 4.5(b), the streamwise turbulence profiles are shown. Downstream of the first rib, the rms value peaks

at 40% in the shear layer above the rib with values as high as 22% near the ribbed wall. At the channel center, the calculations predict a value of 1.2%, while the experiments show 5.8%. As the flow evolves in the duct, the maximum is found in the shear layer at rib height (y = 0.1) and has a value of 32%, 20% less than the peak in the profile downstream of Rib 1. In the channel center, the computations show values of 2-6%, while the experiments show 9-10%. The difference throughout the first four ribs is approximately 4%. Figure 4.5(c) shows the vertical, or cross-stream, fluctuations. Similar to the streamwise turbulence, the peak after the first rib (32%) also flattens out as the turbulence diffuses towards the center of the duct. The centerline experimental cross-stream rms values reach about 8%. Finally, Figure 4.5(d) shows the calculated spanwise fluctuations (LDV measurements were not taken of w_{rms}). The high magnitudes downstream of Rib 1 (peak of 40%) show that the flow immediately becomes three-dimensional. The spanwise turbulence continues to remain high in the shear layers as the flow develops but also has a well-defined peak near 25% in the boundary layer on the ribbed wall. Turbulence develops rapidly near the ribbed wall and reaches near-fully-developed values by the third or fourth rib.

Near the ribbed walls, the recirculation zones formed from the ribs take on a distinct structure, identified by the large recirculation zone downstream of the ribs where separated flow reattaches and subsequently reverses direction and is swept backwards towards the rib. This phenomena is shown in Figure 4.6(a-b) through mean streamline patterns in the center of the channel at z = 0.5 and the variation of the streamwise velocity near the ribbed wall at the mid-height of the ribs (y = 0.05). Also shown in Figure 4.6(b) are the fully developed LES computations of Tafti (2005) and the experimental measurements of Rau et al. (1998).

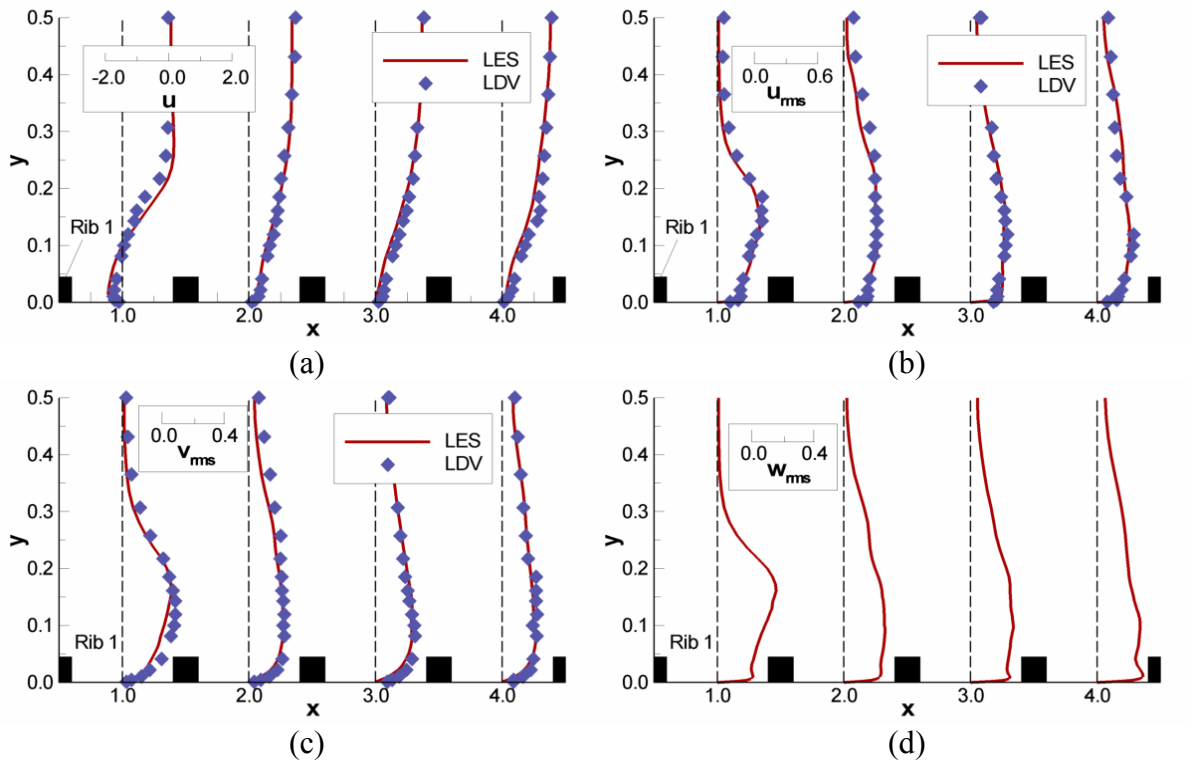

Figure 4.5. Vertical profiles of (a) streamwise velocity, (b) streamwise rms, (c) vertical rms, and (d) spanwise rms between ribs downstream of the entrance show the effect of flow development on the velocity and turbulence profiles.

The streamline pattern in Figure 4.6(a) shows the presence of a massive separation region behind the first rib, which extends all the way to the second rib. However, this quickly leads to recirculation regions which are more in agreement with fully developed flow conditions. This is reflected in the distribution of the streamwise velocity at $y = 0.05$ midway up the rib in Figure 4.6(b). Upstream of the first rib, the negative velocity is a consequence of the rib leading edge eddy. Immediately downstream of the first rib, the positive spike in the velocity is a result of the counter-rotating eddy which is driven by the main recirculating region. In the recirculation region, the streamwise velocity reaches a maximum negative value of 0.4 in the separation zone, which is much larger than that encountered after the second rib. Downstream of the second rib,

the flow quickly approaches a quasi-fully-developed periodic variation, which agrees well with the experimental as well as computational fully developed velocity profiles.

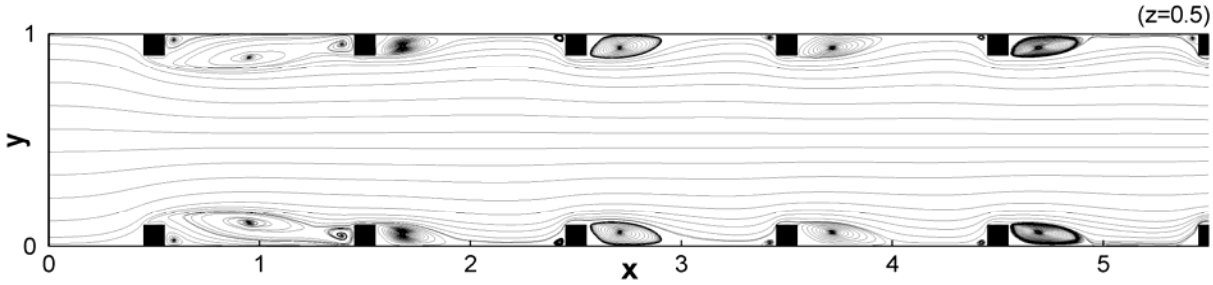

(a)

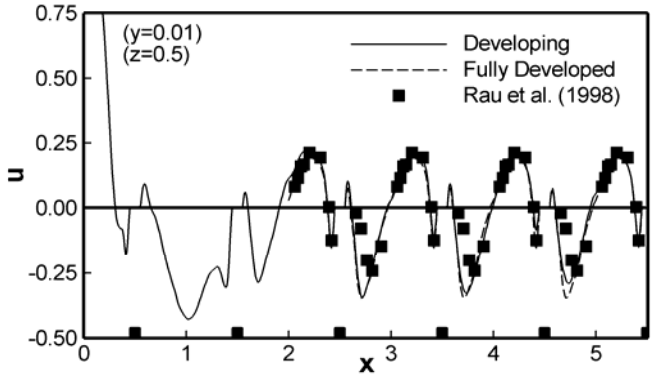

(b)

Figure 4.6. (a) The streamlines in the symmetry plane show the large recirculation region after the first rib followed by a quickly developing quasi-periodic pattern of recirculation zones. (b) The large recirculation region is seen as a negative streamwise velocity near the wall (y = 0.05) in the symmetry plane. Results compare well with the fully developed calculation and experiments very soon after the third rib.

The rapid development of turbulence quantities near the ribbed wall is highlighted in Figure 4.7, which shows spanwise fluctuations (w_{rms}) in a plane through the mid-height of the ribs (y = 0.05). Spanwise turbulent fluctuations first develop upstream of the first rib in the region where the inlet flow impinges on the rib. The rib-wall junction is home to highly unsteady secondary vortices, and the development of w_{rms} in this region is directly attributed to these structures. This

region subsequently exhibits high intensities at downstream ribs. Downstream of the first rib, the spanwise fluctuations exhibit values as high as 35% in the separated shear layer. Downstream of the second rib, the maximum value in the shear layer decreases to about 25%. The distribution of w_{rms} in this plane is fairly well established as early as the second rib and quickly settles down into a periodic pattern with small variations.

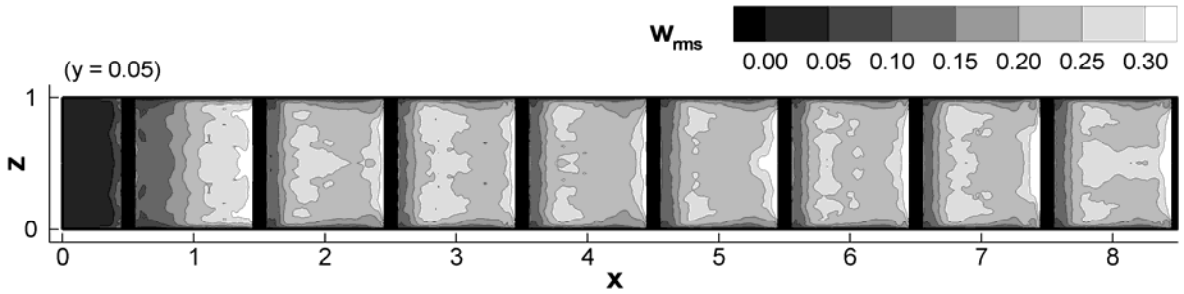

Figure 4.7. Spanwise fluctuations in a plane passing through the mid-height of the ribs show a rapid increase and attainment of near-fully-developed conditions in near wall turbulence.

Figure 4.8(a) shows the variation of streamwise velocity in the symmetry plane of the duct in the fully developed region. The predictions show the reattachment point of the main recirculation zone to be located about four rib heights downstream of the rib (x = 0.95) and the experiments of Rau et al. reach a similar conclusion (x = 0.950 - 0.975) (Rau et al., 1998). The LDV measurements show reattachment to be somewhere between x = 0.83 and x = 1.00, which is in line with Rau et al. and the predictions. These results are consistent with a Particle Image Velocimetry (PIV) study of turbulent water flow through a ribbed duct, which found that flow reattachment remains constant at about four rib heights ($x \approx 0.95$) after the Reynolds number increases past a critical value of 15,000 (Islam et al., 2002).

In Figure 4.8(b-d), the evolution of turbulence along one rib pitch in the symmetry plane is shown. The streamwise peak value of nearly 50% is observed in the shear layer on top of the rib, which decays to a maximum of near 30% downstream of the rib. Near the ribbed wall in the boundary layer, maximum values close to 20% are sustained over most of the pitch. In contrast to u_{rms}, the maximum value of v_{rms} maintains a maximum value of approximately 25% over the full pitch. Finally, the calculated values of w_{rms} in the symmetry plane are shown in Figure 4.8(d) (LDV measurements were not taken of w_{rms}). The spanwise fluctuations look similar to the streamwise fluctuations near the wall, with values of approximately 20% in the boundary layer. All three turbulent fluctuations that are generated in the separated shear layer are transported to the vicinity of the wall as the shear layer reattaches and in the process augment near wall turbulence and heat transfer.

4.03 Mean Flow and Turbulent Quantities in 180^o Bend

The flow entering the bend in a ribbed duct is characterized by high turbulent intensities (between 35%-50% in shear layers) and a mean velocity profile which is considerably more non-uniform in the cross-section (maximum of 1.6-1.7 times the bulk velocity versus 1.1-1.2 for a smooth duct). Figure 4.9 shows the basic flow features of the bend in a symmetry plane that lies directly between the ribbed walls. The streamwise flow begins to be affected by the turning region about 1 D_h upstream of the last rib. The flow accelerates considerably on the inside of the turn, forming a strong shear layer at the upstream edge of the bend. Since the bulk of the flow is pushed towards the downstream side of the bend, a large recirculation region forms at the upstream outer corner. Similarly, a smaller recirculation zone forms in the downstream outer corner.

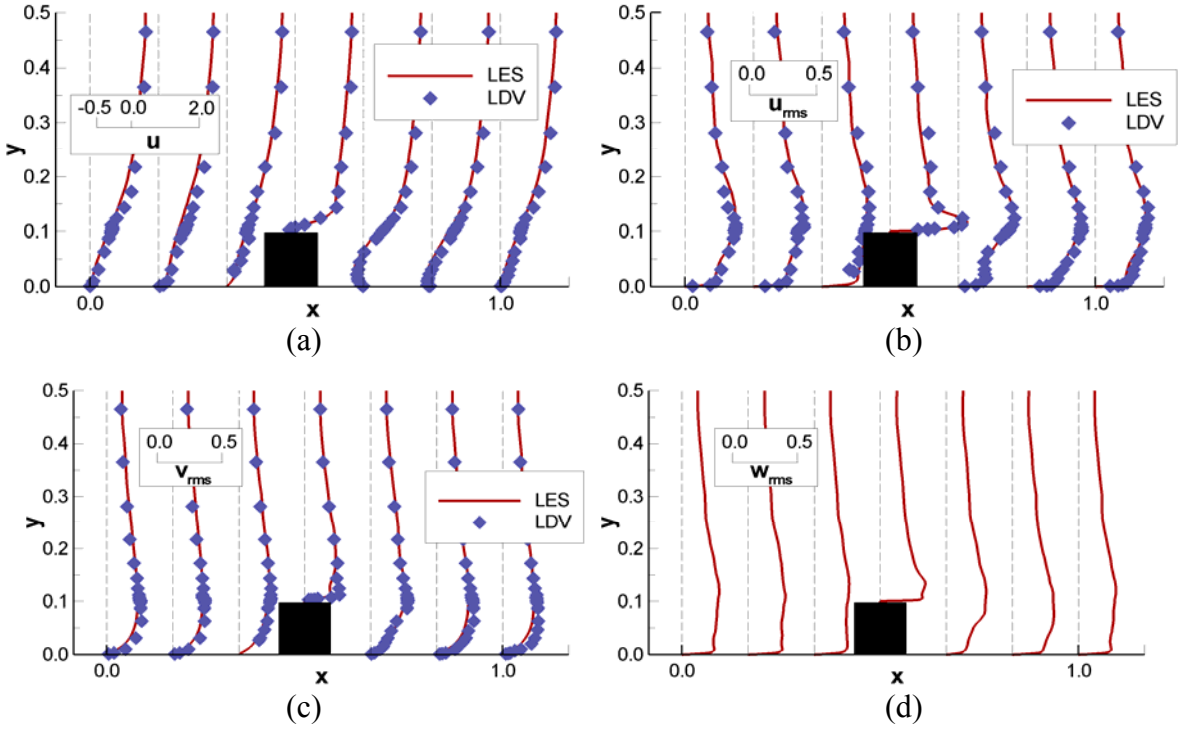

Figure 4.8. Measurements of the (a) streamwise velocity, (b) streamwise fluctuations, (c) vertical fluctuations, and (d) spanwise fluctuations in the center plane show the peak values of all quantities near the ribs and their effects on the rest of the duct.

The shear layer which forms at the upstream edge of the bend separates from the inside of the bend and forms a recirculation zone at the tip of the dividing wall. The rest of the flow going into the bend impinges on the back wall as it is redirected. Coming out of the bend, the flow once again impinges on the outer wall of the downstream leg. In doing so, the separated shear layer is not allowed to follow its natural trajectory but is pushed back and forced to attach at the downstream inner corner of the bend.

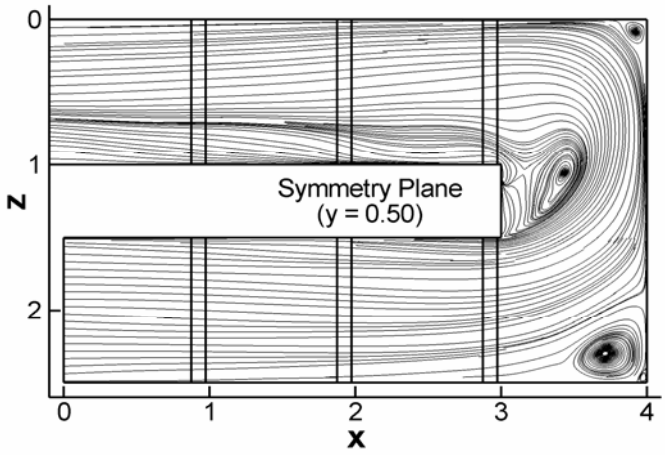

Figure 4.9. The main flow features in the 180º bend include recirculation in the upstream corner, separation and reattachment at the end of the divider, and recirculating region in the downstream corner. The bulk fluid impinges on the back wall and the outside wall downstream.

Figure 4.10 shows a series of LDV profiles at different *y*-locations and their comparisons with LES data in the midplane of the bend. A negative velocity represents flow in the streamwise direction, while a positive velocity represents flow reversal. At all *y*-locations, the velocity in the outer part of the bend (x =3.6 to 4) is quite uniform with a magnitude of approximately 1.5 times the bulk velocity. However, at the inside of the bend, the streamwise velocity steadily decreases (smaller w values) as y increases with a reversal in the flow direction occurring between y = 0.27 and y = 0.44. The profile at y = 0.27 shows a velocity of nearly zero, indicating that the recirculation zone occupies about 40% of the height of the duct. The size of the recirculating flow is predicted exactly, as shown by the location of zero velocity between the streamwise and recirculating flows. In Figure 4.10(b), the streamwise fluctuations (w_{rms}) are plotted at the same locations. Streamwise *rms* values reach a maximum of 50% at the inside of the bend, while the minimum turbulence is about 20%. The profiles show that the turbulence actually decreases at the center of the duct, in the middle of the recirculation bubble, while the peak value is found at

the edge of the recirculation zone, which coincides with the trajectory of the shear layer from the bend.

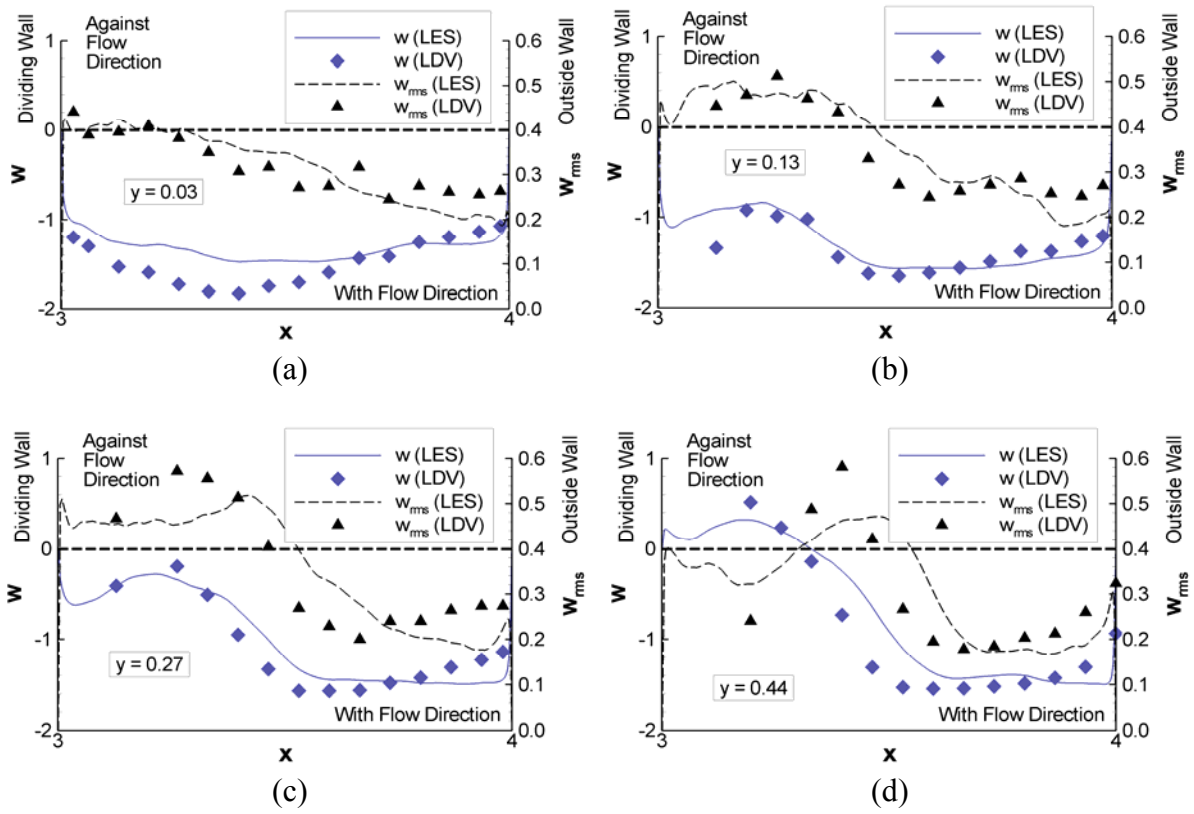

Figure 4.10. Profiles of the streamwise velocity and streamwise fluctuations in the bend region, parallel to the dividing wall, show the recirculation region near the dividing wall and the increased turbulence on the inside of the bend region. The maximum streamwise turbulence on this portion of the bend is more than 50%.

4.04 Secondary Flow in Developing and Fully Developed Regions

An important aspect of duct flows is the presence of secondary cross-sectional flows, which have a large impact on heat transfer augmentation on the side walls. In 90° ribbed ducts, these flows are driven by the periodic flow disturbance caused by the ribs and the junction flow where the rib meets the side wall (Tafti, 2005). The combined effect of the rib and the side walls induces weak secondary flows in the cross-section of the duct. In the vicinity of the rib-side wall

junction, strong localized unsteady vortical structures are generated. As these vortical structures convect over the rib they draw fluid in towards the side wall. This effect, together with the vertical velocity induced by rib blockage, produces impingement and upward flow along the side walls in the vicinity of the ribs. Figure 4.11(b) illustrates this effect in the cross-sectional quadrant, showing the strong inward flow towards the wall, impingement, and a vertical flow towards the center of the channel. Lateral impingement velocities as high as 30% of the mean streamwise velocity are found in this region. Near and before reattachment, the separated shear layer draws fluid in from the center of the duct towards the ribbed wall. Instantaneous data (not shown) indicates that this is once again induced by the rotational velocity of the vortices in the shear layer. This effect is shown in Figure 4.11(c). Once the shear layer reattaches, the downward motion towards the ribbed wall is still present but weakens considerably as shown in Figure 4.11(a). Except in the immediate vicinity of the rib, the secondary flow is weak. Because of the highly localized nature of the secondary flow, which is mostly driven by instantaneous vorticity at the rib junction with the smooth wall, it is quite challenging to predict with eddy-viscosity RANS models (Prakash and Zerkle, 1995; Ooi et al., 2002; Arts et al., 1997; Saidi and Sundén, 2001). This is unlike the secondary flows experienced in skewed ribs (Bonhoff et al., 1997; Shih et al., 1998; Bonhoff et al., 1999; Astarita et al., 2002; Astarita and Cardone, 2003; Lin et al., 2001; Jang et al., 2001; Al-Qahtani, 2002a; Al-Qahtani et al., 2002b; Iacovides et al., 2003; Abdel-Wahab and Tafti, 2004), which are much stronger and coherent and are driven by the rib geometry and hence easier to predict.

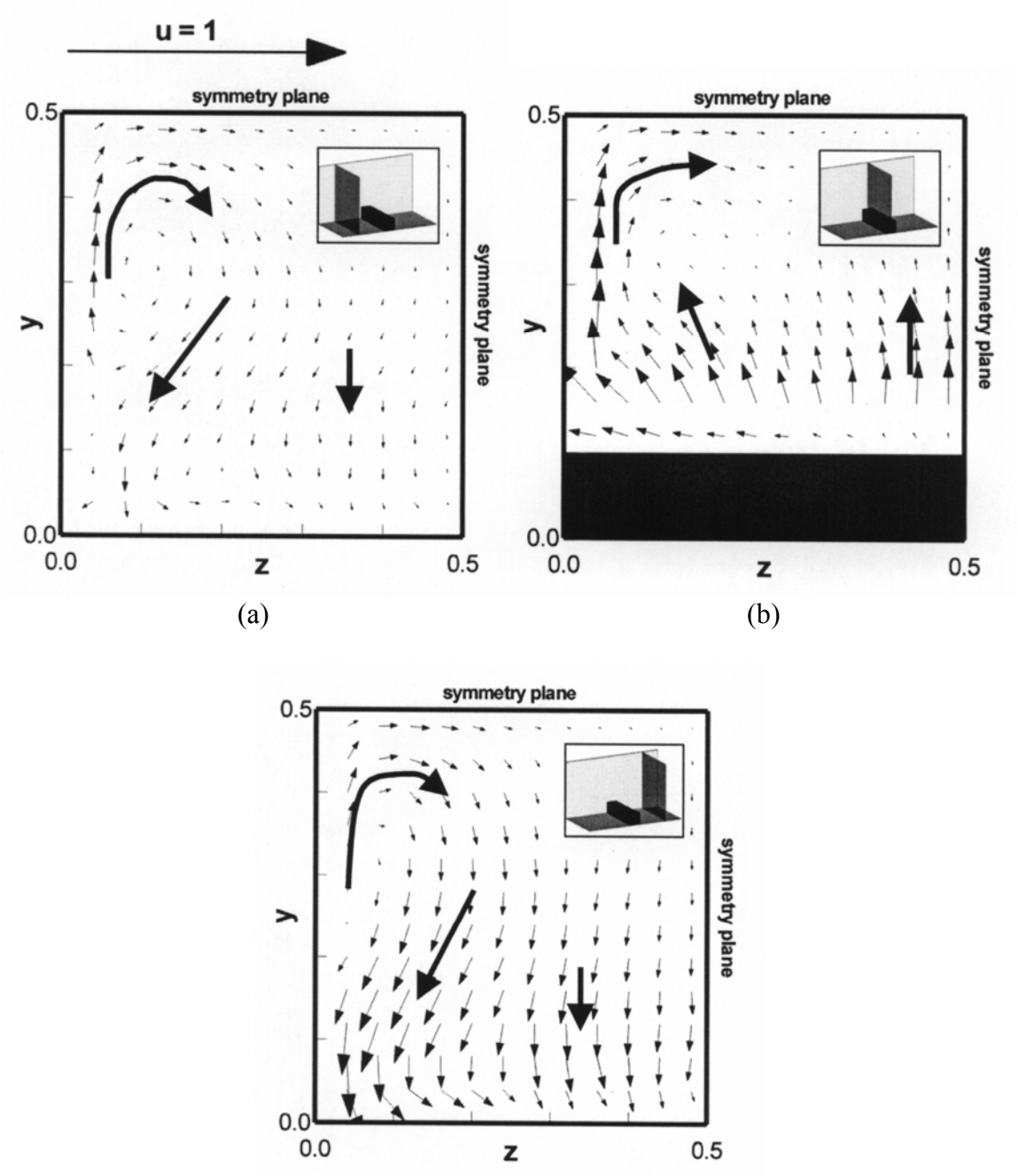

Figure 4.11. Cross-stream flow vectors at (a) x = 0.17 (1/3 D_h upstream of rib), (b) x = 0.50 (on top of rib), and (c) x = 0.83 (1/3 D_h downstream of rib) in ¼ of the channel cross section. The extent and strength of the secondary flow in the quadrant changes with axial location.

Figure 4.12 shows the development of the secondary flow by way of the spanwise mean velocity near the smooth side wall at a location 5% of the channel width away from the wall. The region of strong impingement is established by the third rib, whereas the flow pattern at the center of the duct continues to develop beyond the third rib and reaches a developed state by the sixth rib. A closer look at the secondary flow pattern in the cross-section of the duct (not shown) indicates that the secondary flow pattern evolves even further downstream of the sixth rib. However, the evolution is weak and does not have a major impact on the flow field. Hence, the fully developed secondary flow as shown in Figure 4.11 does not differ considerably from that in the developing region after the sixth rib.

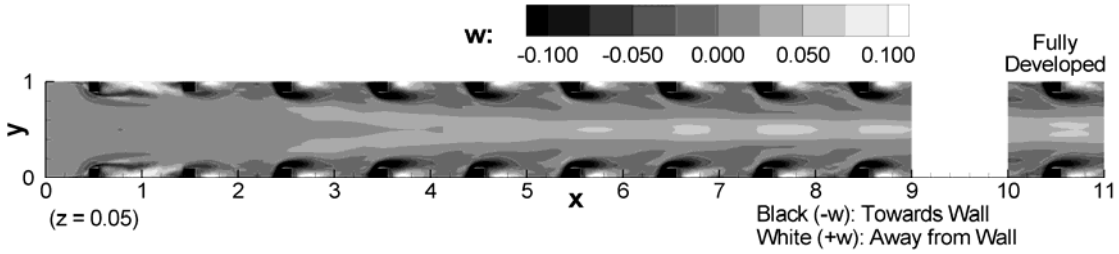

Figure 4.12. The spanwise velocity near the smooth side wall shows impingement on the walls above the ribs, along with inward facing flow downstream of the ribs and in the center of the duct. This flow is identical to the fully developed flow after the fifth rib.

4.05 Secondary Flow in 180^o Bend

Figure 4.13 shows a plane parallel to the dividing wall and perpendicular to the flow direction at the center of the 180^o bend. The flow vectors show a pair of counter-rotating Dean vortices. These are similar to those found in experimental studies of smooth ducts (Liou et al., 1999; Schabacker et al., 1998; Son et al., 2002) and ducts with 45º ribs (Bonhoff et al., 1997; Shih et al., 1998). Similar flow patterns have also been observed in calculations of smooth 180º bends (Lin et al., 2001; Besserman and Tanrikut, 1992; Gu et al., 2002) and bends connecting

ducts with 45º angled ribs (Lin et al., 2001; Al-Qahtani et al., 2002a). The impingement of the secondary Dean vortices on the back wall of the bend, at the top and bottom walls towards the outside of the bend, and at the inside of the bend leads to considerable heat transfer enhancement at these locations.

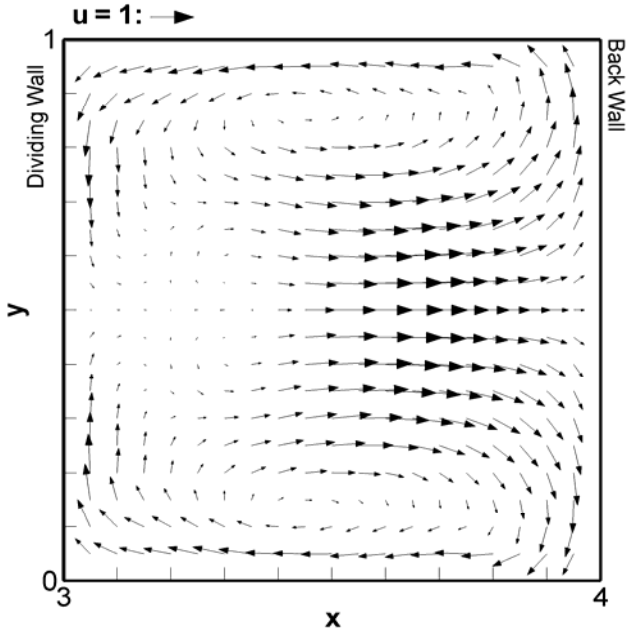

Figure 4.13. Vectors in the midplane of the 180º bend show the counter-rotating Dean vortices typically found in flow in a bend. This secondary flow mechanism is responsible for forcing fluid towards the outside wall in the center and up against the inside dividing wall from the top and bottom walls.

4.06 Friction Losses

Table 4.1 shows a comparison of the fully developed friction factor results from a number of different sources. It is important to note that the friction factor is typically measured by pressure taps along the ribbed or smooth walls, which can potentially produce results that differ from each other, while it is best to report calculated friction factors with area-averaged pressure drops. In Table 4.1 the area-averaged friction factor augmentation is given, along with local values corresponding to the locations of pressure taps on the ribbed and smooth walls. These values are

compared with the experiments from the present study and those of Rau et al. (1998). Because the local pressures are very sensitive to changes in the flow, comparisons between the two measurement types are expected to be close, but not necessarily exactly the same. It has been reported by Rau et al. (1998) and Tafti (2005) that the major contributor to the friction factor is the form loss, which was reported to contribute 85% of the friction factor in Rau et al. (1998) and 91% in Tafti (2005). This high contribution indicates that other flow patterns, such as secondary flows, contribute very little to the overall pressure drop.

Table 4.1. Fully Developed Friction Factor Augmentation

Case	f / f_0			Re
	Area Averaged	Smooth Wall	Ribbed Wall	
Developing Rib 7	9.63	8.82	9.01	20,000
Developing Rib 8	9.84	8.34	9.34	20,000
Fully Developed	8.60	---	---	20,000
Experiments	---	8.23	---	20,000
Rau et al. (1998)	---	---	9.50	30,000

Figure 4.14 shows the variation of friction factor augmentation calculated from the pressure drops in the 180º bend. The overall area-averaged pressure drops for the groups highlighted in the diagram were obtained from the calculation. The augmentation across Group 1 has a value of 9.8, which is consistent with other reported fully developed friction factors shown earlier in Table 4.1. The friction factor across Group 2 increases significantly, indicating a strong pressure drop across the rib into the bend. A similar pressure drop across the bend in Group 3 shows the losses occurring between the last rib downstream of the upstream leg of the duct and the first rib in the downstream leg. The most significant friction factor is found in Group 4, where a strong

pressure loss occurs across the first rib in the downstream leg. In Group 5, a small negative friction factor indicates the presence of a pressure recovery, where the downstream pressure is higher than the upstream pressure. The recovery is small, indicating that the pressures before and after the second rib in the downstream leg of the duct are equivalent. Two pressure taps were used in the experiments to measure the pressure drop across the bend; their locations are shown in the diagram in Figure 4.14. The taps were placed along the inside wall, midway between two ribs, at the mid-height of the duct. The friction factor augmentation over the entire 180º bend was found by these pressure measurements to be 22.8. The calculated friction factor, based on area averaged pressures at the same streamwise locations as the pressure taps, has a value of 23.1, which is 1.3% greater than the measured value. Additional pressure taps downstream of the bend show that the friction factor returns to the fully developed value of approximately 10 fairly quickly. Good agreement between the calculations and experiments indicates that the LES calculations are capable of accurately reproducing the measured values of pressure drop.

4.07 Heat Transfer Augmentation

An accurate determination of the flow physics is paramount for heat transfer predictions, which depend strongly on both the mean flow effects and turbulence. In this section, comparisons between calculations and experiments of the heat transfer augmentation in the developing flow, fully developed, and 180º bend regions are presented.

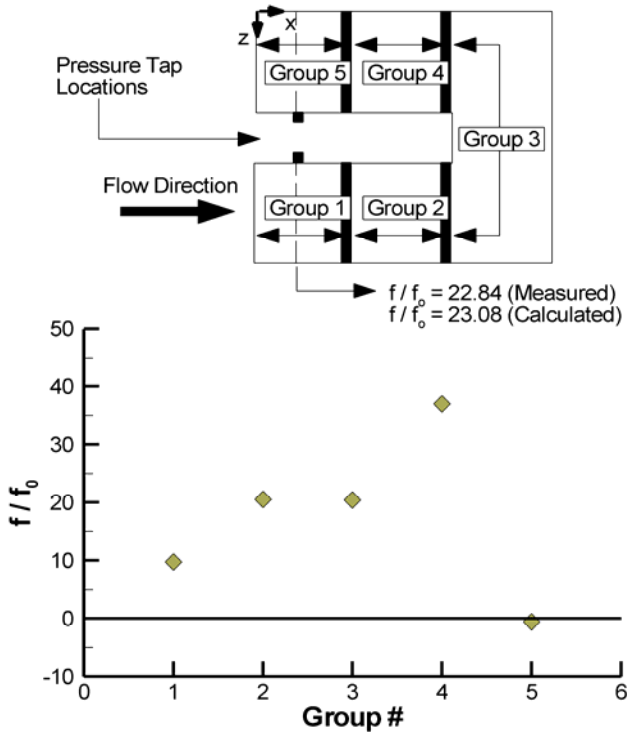

Figure 4.14. The friction factor in the 180º bend shows the sharp increase in the pressure drop across the final rib in the upstream leg and the first rib in the downstream leg. A pressure recovery (negative friction factor) is shown immediately downstream of the bend. The calculated and measured friction factors across the bend show excellent agreement between the two values.

Experimental studies in the developing flow region are far outnumbered by those in the fully developed region, and many experiments in the developing flow region are reported on test sections with ribs smaller than (Han and Park, 1988) or larger than (Liou and Hwang, 1992) those of the current study. One study, however (Fann et al., 1994), reported results with similar geometric characteristics and a Reynolds number of 20,000. The channel aspect ratio was 1:1, and the ribs were slightly smaller (e/D_h = 0.08) and spaced slightly farther apart (P/e = 11). These differences are minor, however, and a comparison of four equally-distributed points between the third and fourth ribs (Figure 4.15(a)) and the fifth and sixth ribs (Figure 4.15(b))

shows very good agreement. The magnitudes of the two comparisons are equal to each other, which further supports the assertion that the ribbed wall heat transfer augmentation develops very quickly in the developing flow region (Han and Park, 1988; Liou and Hwang, 1992; Sewall and Tafti, 2004).

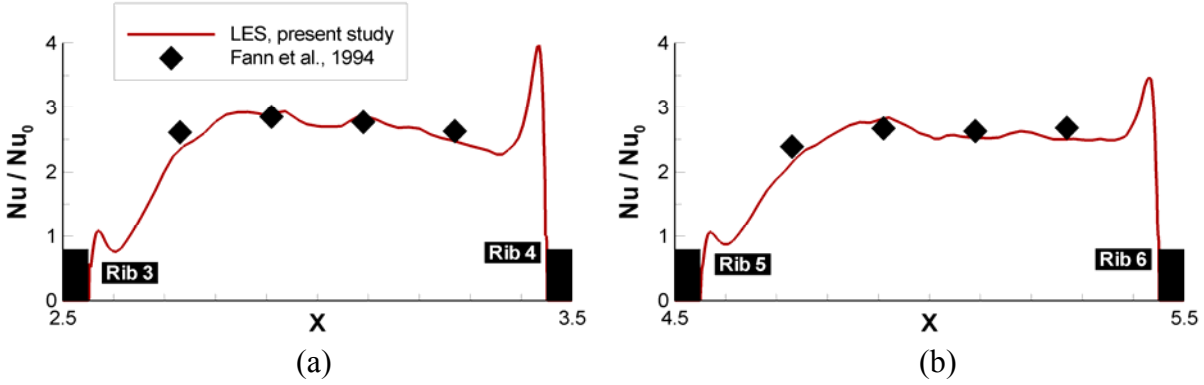

Figure 4.15. Comparisons between the local heat transfer measurements of Fann et al. (1994) between (a) Ribs 3 & 4 and (b) Ribs 5 & 6 show the good agreement between the calculations and experiments in the developing flow region.

Furthermore, because ribbed wall flow and heat transfer are known to develop very quickly, within three or four ribs of the inlet, developing flow ribbed wall heat transfer calculations can be compared with fully developed measurements. Figure 4.16(a) displays the streamwise distribution along the center of the duct at $z = 0.5$ together with the fully developed experimental data of Rau et al. (1998) and the fully developed computations of Tafti (2005) for comparison. The Nusselt number drops sharply from the entrance of the duct to the first rib due to the developing thermal boundary layer.

Downstream of the first rib, a sharp increase in the augmentation ratio culminates to a peak value of 4.5 just upstream of the second rib. This correlates with the corresponding increase in turbulent kinetic energy near the ribbed wall as turbulence is generated by the first rib. Similar

to the observations made for turbulent kinetic energy near the ribbed wall, the augmentation ratio settles down to a quasi-periodic state immediately after the second rib. Compared to the fully developed computations and experiments, the augmentation ratio is lower in the region of reattachment and downstream of it. The underprediction seems to be present at all ribs and does not show any particular trend. Figure 4.16(b) shows the distribution of the augmentation ratios along the smooth wall one rib height upstream of Rib 8, along with comparisons with the fully developed calculation and the measurements of Rau et al. (1998).

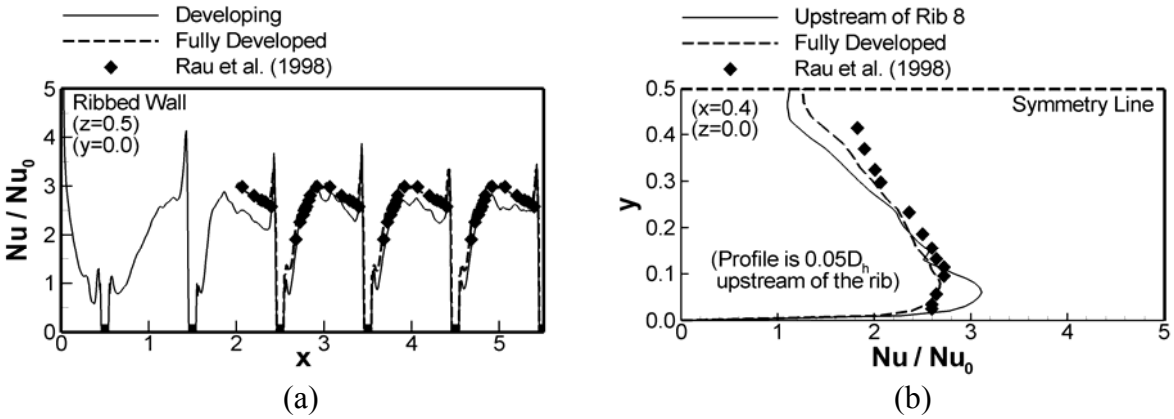

Figure 4.16. (a) The heat transfer enhancement on the ribbed wall quickly settles into a fully developed pattern. This is where many authors determine fully developed length. (b) The vertical profile of Nu/Nu_o on the smooth wall immediately before a rib (x = 0.4) shows good agreement with experiments near the wall but lower heat transfer in the center of the channel.

Heat transfer studies in the fully developed section are common and are typically used for validation of numerical calculations. Two common comparisons of heat transfer measurements were reported by Rau et al. (1998), which show experimental measurements for a case very similar to the present one (e/D_h = 0.1, P/e = 9) but with a Reynolds number of 30,000. One is a line along the centerline of the ribbed wall, and the other is a vertical line on the smooth wall that

is one rib height upstream of the centerline of the rib. The infrared camera measurements for Re = 20,000 and Re = 30,000 are shown along with the measurements of Rau et al. for those two locations in Figure 4.17. The values are shown to compare very well. On the ribbed wall, the calculation shows a region of high heat transfer augmentation upstream of the rib, and this region is either too small for observation or lost in the shadow of the rib in the measurements. In Figure 4.17(b), the agreement with the measurements is good, also. The high heat transfer shown near the ribbed walls is a consequence of the secondary flows pictured in Figure 4.11, which increases the heat transfer due to lateral flow impingement upstream of the rib. In the channel center, the heat transfer is slightly underpredicted, but the overall comparison is very good. The accurate prediction of these two curves is difficult to achieve because of the recirculation of flow near the ribs and the localized secondary flow effect. Many computational studies have attempted to correctly predict this smooth wall heat transfer effect using different turbulence models with little success (Ooi et al., 2002; Arts et al., 1997; Saidi and Sundén, 2001; Sleiti and Kapat, 2004).

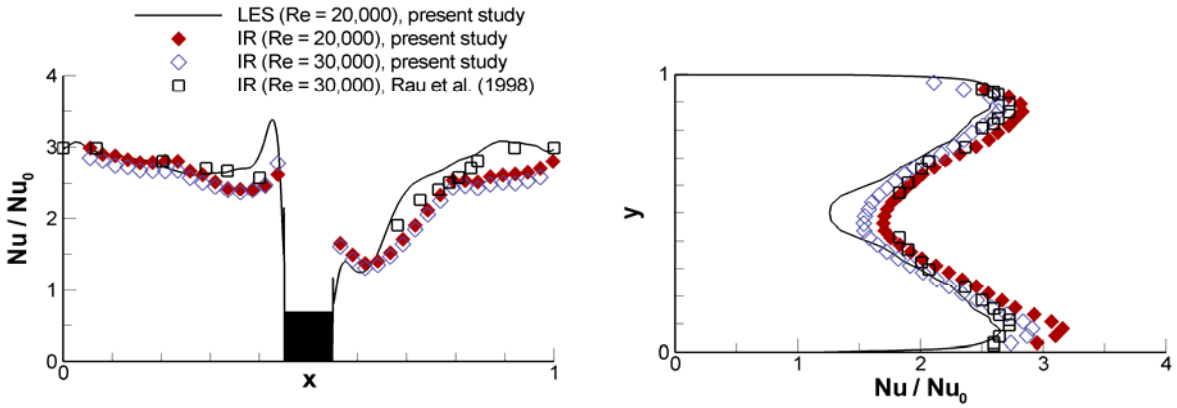

Figure 4.17. Comparisons between the heat transfer calculations and experiments of Rau et al. (1998) on (a) the centerline of the ribbed wall and (b) a vertical line on the smooth side wall upstream of the rib show excellent agreement between experiments and calculations.

In the 180º bend region, a mass transfer experiment by Han et al. (1988) showed results for a channel with geometry similar to that of the present study (e/D_h = 0.094, P/e = 10) with a Reynolds number of 30,000. No rib is included in the bend in either case. One difference between the two studies is the width of the dividing wall between the upstream and downstream ducts, which is ¼ D_h in the experiments and ½ D_h in the calculations. This parameter has an important effect on the flow and heat transfer characteristics, as was shown in a smooth wall 180º bend study by Liou et al. (1999). Comparisons between six lines on the ribbed walls are shown in Figure 4.18. The lines are local mass transfer measurements along three lines in each leg of the bend. One line is along the center, one is between the center and inside wall ("inner line"), and the other is between the center and outside wall ("outer line"). Comparisons upstream of the bend are shown in Figure 4.18(a), and comparisons downstream of the bend are shown in Figure 4.18(b). Agreement between the experiments and comparisons upstream of the bend is very good. The magnitudes of the inner, center, and outer lines do not vary much, indicating that the bend has very little effect on the flow upstream. Downstream, the measured heat transfer is higher coming out of the bend on the outer line than the predictions show, but this is expected because the thinner dividing wall in the experiments induces a stronger flow separation, increasing the heat transfer along the outside line. Careful study of the heat transfer magnitudes shows that the bend has a strong influence on increasing the heat transfer augmentation downstream, which is a positive result produced by the presence of the bend.

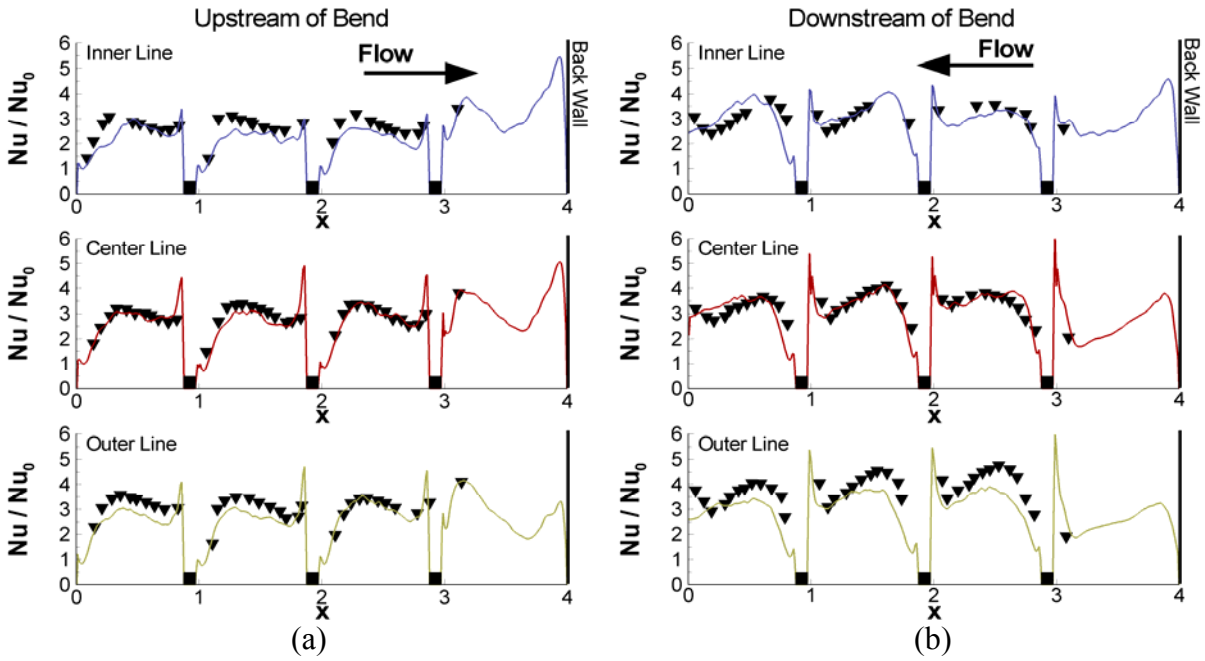

Figure 4.18. Comparisons of heat transfer augmentation between the LES calculation and the mass transfer experiments of Han et al. (1988) along the inner line, center line, and outer line of (a) the region upstream of the bend and (b) the region downstream of the bend show the good agreement between the calculations and experiments.

Figure 4.19 is a comparison of averaged heat transfer augmentation in the 180° bend with the averaged mass transfer measurements of Han et al. (1988). The upstream ribbed wall heat transfer augmentation is lower than the measurements, but the computational value compares well with fully developed heat transfer augmentation values of 2.40 reported elsewhere (Rau et al., 1998; Tafti, 2005). Also, the mass transfer measurements also reported that comparisons with previous heat transfer measurements showed that the mass transfer augmentation was higher than the heat transfer augmentation by as much as 10 percent. Within the bend, the ribbed wall heat transfer augmentation is slightly higher than the measurements. Though the values are similar, local heat transfer augmentation contours from the calculations show high heat transfer regions very close to the side walls in the bend. Because the mass transfer measurements only

account for lines near the center of the bend and do not resolve the entire area, it is suspected that they may not take into account these high heat transfer regions, resulting in a lower heat transfer augmentation value than was reported by the calculations. Downstream of the duct, the mass transfer measurements again show values larger than the computations. The larger value is expected because of the similarly high value upstream of the duct and because of a difference in dividing wall thicknesses, where the bend used in the measurements had a wall thickness that was ½ that of the computational wall thickness. As shown in the local heat transfer comparisons, the thinner dividing wall increases separation from the dividing wall, resulting in a higher heat transfer augmentation downstream.

Comparisons of the smooth side walls are shown in Figure 4.19(b). Upstream, the measurements are similar on the inside and outside walls, as expected. The heat transfer augmentation value is slightly larger on the sides, as well, corresponding to the higher value as seen in part (a). The side wall values increase sharply in the bend, and downstream of the duct, the measurements are higher than the predictions. The calculated side wall values show the downstream heat transfer augmentation to be higher along the outside walls, but the measurements show the opposite to be true. Based on a series of heat transfer measurements in smooth ducts with different dividing wall thicknesses, however, Liou et al. (2000) showed that downstream the inner wall heat transfer augmentation should be much less than the outer wall heat transfer. This is consistent with the computations but not with the measurements, though the values are close.

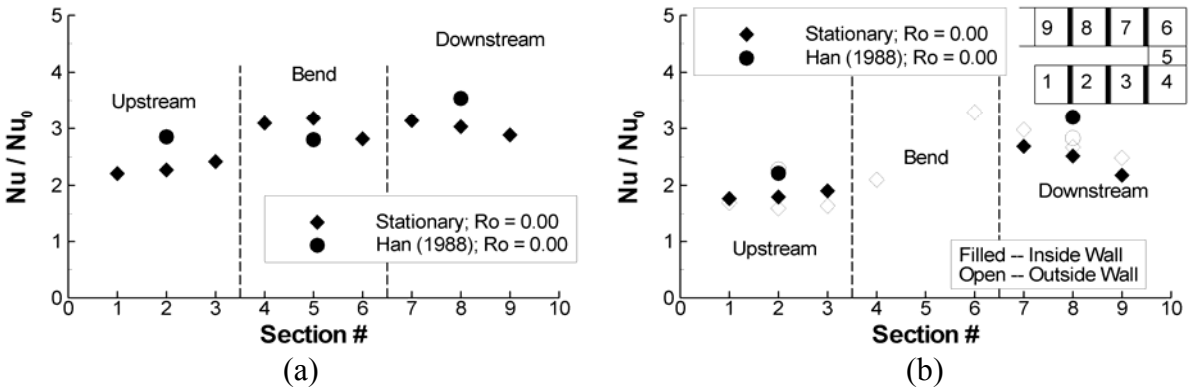

Figure 4.19. Group averaged heat transfer augmentation values on (a) the ribbed wall and (b) the smooth wall show the increase in heat transfer across the bend. The ribbed wall calculations are compared with the measurements of Han et al. (1998) and show good agreement in the upstream and downstream ducts.

4.08 Summary and Conclusions

Modeling ribbed duct flows is a significant challenge facing the gas turbine industry. The current industry standard is to use RANS simulations with a variety of turbulence models. These techniques are relied upon heavily mostly because of their ease of use and fast turnaround time in obtaining results. However, the models seldom accurately reproduce the range of physics encountered in internal cooling ducts. The present study validates the use of LES for predicting flow and heat transfer with experiments and elucidates on the detailed physics encountered in the developing flow region, the fully developed region, and the 180^{o} bend region.

The results show that the heat transfer is augmented over that of a smooth duct by a factor between 2 and 3. The friction is augmented by a factor of 10, primarily due to form losses from the ribs. The primary mechanism of heat transfer augmentation is the generation of unsteady vortical structures in separated shear layers on ribs and at rib junctions with the ribbed and smooth walls. The unsteady vorticity, which continuously replenishes and mixes fluid in wall boundary layers, manifests itself in the mean as increased turbulent intensities in boundary

layers. While secondary flows in the duct cross-section and the 180^o bend have a large impact on heat transfer, they do not have as large an impact on frictional losses, which are dominated by form losses.

Among the major flow features predicted with accuracy are shear layer transition at the entrance of the duct; the distribution of mean and turbulent quantities in the developing, fully developed, and 180^o bend; the development of secondary flows in the duct cross-section and the 180^o bend; and friction and heat transfer augmentation. In all different aspects, it is found that LES produces the correct physics both qualitatively and quantitatively to within 10-15%.

The following conclusions are made in the developing flow region:

a) The exact nature of the hydrodynamic inlet conditions do not have a big impact on the friction and heat transfer augmentation after the second rib. Calculations with fully developed turbulent flow inlet conditions exhibit very similar trends as the laminar inlet after the third rib, except slightly higher augmentations are found at the center of the smooth wall.

b) The mean flow velocities reach a near fully developed state by the fourth or fifth rib downstream of the entrance to the duct

c) Turbulent profiles indicate that turbulence is nearly fully developed in the vicinity of the ribbed wall by the third or fourth rib. However, it is not fully developed at the center of the duct.

d) The state of development of turbulence near the duct walls has a direct impact on the state of development of the heat transfer coefficient. Heat transfer coefficients at the ribbed wall reach a fully developed state after the third rib. The smooth wall, on the other hand, exhibits fully developed augmentation ratios in the vicinity of the ribbed wall but lower augmentation ratios at the center of the channel. Hence, the smooth wall shows a slight but steady increasing trend in the surface averaged heat transfer augmentation up to the sixth rib in the calculation. However, it is within 10% of its fully developed value.

e) The friction coefficient exhibits a large value across the first rib but quickly settles down to its fully developed value by the fourth rib.

f) In spite of the subtle differences in the development of mean flow and turbulent quantities, from a design engineer's perspective, the friction and heat transfer in the stationary ribbed duct are to within 10% of their fully developed values after the third rib.

The following conclusions are made in the 180º bend region:

g) Flow vectors showed a pair of counter-rotating Dean vortices in the mid-plane of the bend and a large recirculation zone at the tip of the dividing wall.

h) The friction factor increases by a factor of two across the last rib in the upstream leg of the bend. The friction factor is approximately four times as large as that of a straight ribbed duct across the first rib in the downstream leg.

i) Adding a rib to the bend increases the friction factor by 82%, while it only increases the heat transfer by 20%. Though the tradeoff is significant, it may still be advisable to place a rib in the bend if the 20% increase in heat transfer is worth the pressure loss incurred by doing so.

LES provides a robust, reliable, and accurate prediction tool for heat transfer characteristics in the developing region of internal cooling ducts. It predicts all the major flow features accurately, particularly secondary flows, which commonly used RANS two-equation eddy-viscosity models cannot reproduce. Presently, the computational expense of LES prevents it from being used in a design setting. However, the exponential increase in raw computing power is making LES more and more accessible for such purposes. Calculations such as those presented in this chapter can be used as an establish benchmark for the rotating calculations discussed in the following chapters.

Chapter 5. Rotating Developing Flow and 180° Bends with Coriolis Effects[1]

Coriolis effects are one of the two significant results of turbine blade rotation, and in this chapter only these effects are included in the simulations. While centrifugal buoyancy is highly important in turbine blade heat transfer studies, isolating Coriolis effects can aid significantly in gaining an understanding of the physics associated with turbine blade cooling. Centrifugal buoyancy effects will be included in the following chapter.

This chapter is divided into two sections. In the first, Coriolis effects are studied in the developing flow region. The rotational effects are observed immediately at the entrance and have a significant effect on flow and heat transfer development length. The influence of Coriolis effects on the recirculation zones and secondary flows will also be considered. In the 180° bend, Coriolis effects are interesting because they have an opposite effect in radially inward flow than in radially outward flow. The focus of this section will be on validating the rotating calculation with experiments and understanding the effects of rotation on the heat transfer in the bend.

5.01 Developing Flow

When the rotational axis is perpendicular to the plane of mean shear, Coriolis forces have a considerable effect on the mean flow as well as on turbulent fluctuations. These effects are manifested as stabilization/destabilization of turbulence at the leading/trailing walls, respectively, and the generation of spanwise roll cells or secondary flows. Coriolis forces have a direct impact on the production of turbulent fluctuations at the trailing and leading edges of the duct. At the trailing wall, Coriolis forces reinforce the production of turbulence, whereas at the

[1] Reproduced in part with permission from ASME

leading wall they act to damp production. Hence, heat transfer augmentation increases at the trailing wall and decreases at the leading wall compared to a stationary channel. The secondary flow set up in the cross-section of the duct increases heat transfer augmentation at the side walls of the duct. In fully developed calculations (Abdel-Wahab and Tafti, 2004) at Ro = 0.18, 0.35 and 0.67, the heat transfer coefficient on the trailing wall increased 50% to 60% over a non-rotating duct, whereas at the leading wall the heat transfer decreased 30% to 50%. The secondary flow resulted in smooth wall augmentations of 20% to 30% over a stationary duct.

Table 5.1 summarizes the mean flow and heat transfer results from this study. It shows the reattachment lengths behind each rib; the friction coefficients calculated using pressure values at the leading, trailing, smooth walls, and the integrated pressure at a cross-section; and heat transfer augmentation. The averaged values of each ribbed section encompass an area ranging from $0.5D_h$ upstream of the rib center to $0.5D_h$ downstream. For comparison, results from the fully developed calculation of Abdel-Wahab (2004) are also shown.

A noticeable feature of Table 5.1 is the reattachment lengths, especially along the leading wall. The value of rib 6 stands out as a significantly high value. These measurements are difficult to quantify exactly, however, given the highly unsteady nature of the flow in the reattachment region and the finite sampling used to obtain the mean values. As will be shown later (Figure 5.1(d)), all of these values are subject to interpretation and will differ depending on whether the reattachment point is based on the farthest downstream point of recirculation or the point where the bulk of the flow stops recirculating. A second point of interest found in the table is the negative friction factors encountered across rib 2. The large initial pressure drop across rib 1 results from the large recirculation zone that forms behind the rib. This causes a large pressure drop, some of which is recovered as the flow expands once again across rib 2.

Table 5.1. Summary of Results

	Computations e/D_h **= 0.1,** P/e **= 10**								
	Rib 1	**Rib 2**	**Rib 3**	**Rib 4**	**Rib 5**	**Rib 6**	**Rib 7**	**Rib 8**	**F.D. (Abdel-Wahab, 2005)**
Leading Reattachment Length (x_r / e)	9.0	3.6	5.6	5.3	5.6	7.4	6.0	5.3	5.4
Trailing Reattachment Length (x_r / e)	7.6	3.1	3.3	3.5	3.3	3.7	3.5	3.7	3.4
	f / f_0 ($f_0 = 0.046 \cdot Re^{-0.2}$)								
Leading Wall Pressure Taps	85.8	-39.5	18.3	4.6	10.1	8.6	9.2	7.6	---
Trailing Wall Pressure Taps	78.4	-34.0	14.2	5.9	12.2	6.2	7.4	10.0	---
Smooth Wall Pressure Taps	59.7	-20.4	13.7	8.2	8.7	9.1	8.4	8.5	---
Area Averaged Pressure Drop	69.2	-30.7	15.5	6.7	9.8	9.2	8.5	8.5	9.6
	Nu / Nu_0 ($Nu_0 = 0.023 \cdot Re^{0.8} \cdot Pr^{0.4}$)								
Rib	1.75	2.88	2.80	2.64	2.60	2.63	2.68	2.81	2.97
Leading Wall	1.68	2.09	1.73	1.58	1.42	1.30	1.23	1.26	1.36
Trailing Wall	1.99	2.87	2.58	2.69	2.71	2.88	3.02	3.19	3.63
Smooth Wall	2.05	1.73	1.80	1.80	1.80	1.88	1.92	2.00	2.32
Overall w/ Rib	1.90	2.20	2.08	2.05	2.02	2.07	2.11	2.20	2.48

5.02 Mean Flow in the Developing Region

Figure 5.1(a) shows the development of the mean streamwise flow velocity at the center of the duct (z = 0.5). On encountering the first rib, the uniform flow accelerates to account for the flow blockage. At this stage of development, the flow is symmetric about the center, but soon after that, by the second rib, asymmetries in the profile are clearly visible. The flow at the center

of the channel decelerates between the second and the third rib as it recovers and redistributes in the channel cross-section. This region is characterized by a large pressure recovery as shown in Table 5.1. After the third rib, the velocity distribution assumes a quasi-periodic variation from one rib to the other. However, as the flow proceeds into the channel, the maximum in the profile shifts towards the leading side of the duct and decreases gradually.

Figure 5.1(b) shows the evolution of the streamwise velocity at the center of the duct. Also shown is the fully developed flow velocity together with the developing velocity in a stationary duct up to rib 5 (Sewall and Tafti, 2004). Interestingly, the centerline velocity of the rotating duct coincides with that of the stationary duct until after the fourth rib, when it starts to decrease due to a shift in the maximum velocity away from the center. At the eighth rib, the variation is close to the fully developed distribution. Figure 5.1(c) shows the streamwise velocity distribution across the cross-section of the duct at z = 0.5 at streamwise locations midway between ribs 8 and 9. Also plotted are stationary and rotating duct fully developed profiles. The developing flow velocity profile at rib eight is close to the fully developed profile, yet not exactly the same. An important difference is that the gradient near the trailing wall still lags the fully developed flow gradient, whereas the gradient at the leading wall matches the fully developed gradient quite closely. It is noted that the rotating channel profile is steeper at the trailing wall in comparison to the stationary channel. At the rotating leading wall, vestiges of the separation zone created by rib eight are still present midway between the ribs, both in the developing and fully developed flow calculations.

A more detailed picture of the effect of Coriolis forces on the structure of the recirculating regions behind each rib is shown in Figure 5.1(d), together with the reattachment lengths in Table 5.1. As in a stationary channel (Sewall and Tafti, 2004), large recirculation zones form

behind the first rib because of the laminar flow upstream. The destabilizing/stabilizing effect of Coriolis forces on the trailing and leading sides, respectively, is evident almost immediately. Turbulent kinetic energy distributions (which will be shown later in Figure 5.5(a)) near the trailing and leading sides, show that Coriolis forces have an immediate impact on the turbulence as it begins to be generated in the wake of the first rib. This in turn directly impacts the reattachment length, which is larger on the leading side of the duct. At the second rib, the recirculation regions collapse dramatically, both on the trailing and leading sides, after which there is a settling out on both sides to their fully developed values of approximately 3.4 and 5.4, respectively. The collapse of the separation regions coincides with the region of large pressure recovery after the second rib.

Figure 5.2(a) shows the streamwise velocity distribution normal to the smooth walls in the plane $y = 0.5$. Initially the maximum in the profile occurs at the center of the channel, but as the effect of Coriolis forces starts acting on the mean flow, the peak in the profile shifts toward the smooth walls. Figure 5.2(b) shows the profiles at selected streamwise locations, midway between ribs 1 and 2, between 5 and 6 and between 8 and 9. Also shown for comparison are the equivalent fully developed stationary and rotating profiles. Between ribs 1 and 2, except for the thin boundary layer near the walls, the profile assumes a plug shape in the rest of the cross-section. In Figure 5.2(a), the shift in the maximum from the center towards the walls begins to occur after rib 4 and is well established between ribs 5 and 6 as seen in Figure 5.2(b). The profile evolves further and closely approximates the fully developed profile between ribs 8 and 9. In contrast, the stationary channel has the expected uniform flow profile. The distortion in the streamwise profile for the rotating channel is a consequence of the cross-sectional secondary flow which is established after rib 3 and gains in strength further downstream into the channel.

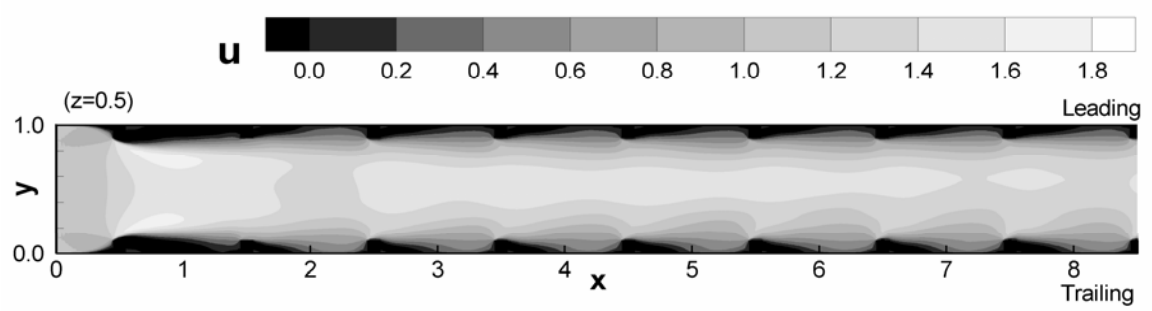

(a)

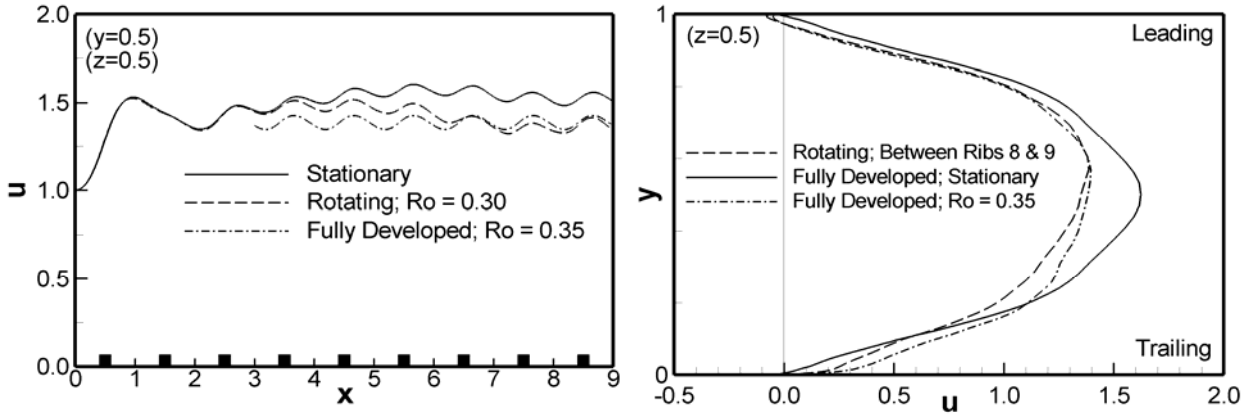

(b) (c)

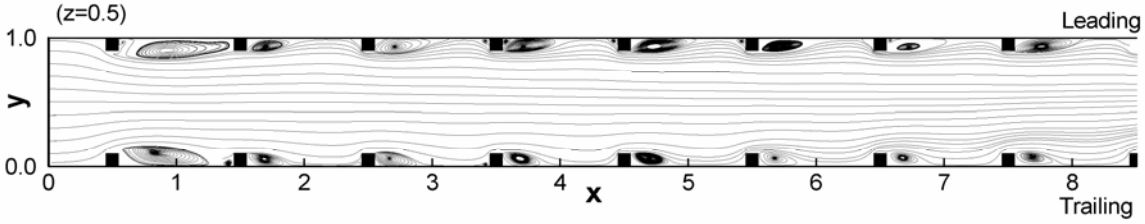

(d)

Figure 5.1. (a) The mean streamwise velocity contour shows the sudden flow acceleration initially followed by expansion and a peak velocity skewed towards the leading side. (b) The centerline streamwise velocity diverges from the stationary profile (Sewall and Tafti, 2004) as a result of Coriolis forces. (c) The vertical profile between two ribs is compared with the stationary (Tafti, 2005) and rotating (Abdel-Wahab and Tafti, 2004) cases. (d) Streamlines show the enlarged recirculation regions after the first rib, as well as longer reattachment lengths on the leading side.

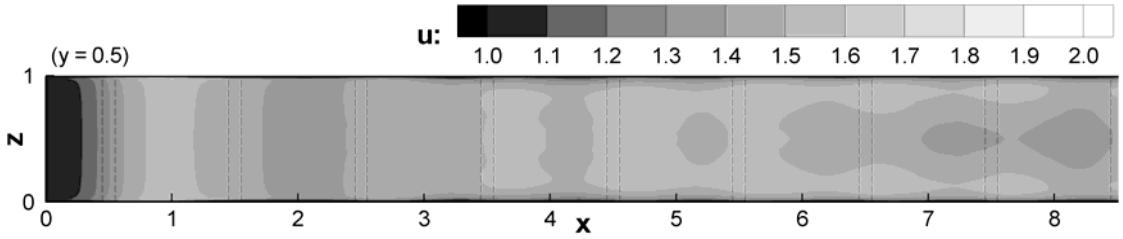

(a)

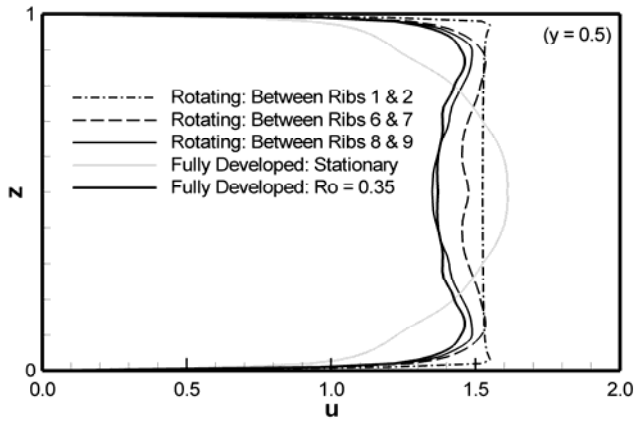

(b)

Figure 5.2. (a) The horizontal distribution of the mean streamwise velocity normal to the smooth walls shows the maximum velocity transitioning to near the smooth walls instead of in the center. (b) Horizontal profiles between the ribs at various streamwise positions shows the transition from a flat profile at the inlet to the fully developed profile (Abdel-Wahab and Tafti, 2004) between the eighth and nine ribs.

Figure 5.3(a-b) characterize the secondary flow showing the distribution of mean cross-stream velocity (v) and mean spanwise velocity (w) in two halves of the duct cross-section at rib 4 and rib 8, where it is assumed that the flow is symmetric about the center plane. At both locations, the induced secondary flow impinges on the smooth wall on top of the rib and then creates a strong upwash from the trailing to the leading side along the smooth wall. The flow is well established by the fourth rib and the maximum cross-stream and spanwise velocities grow from 0.34 to 0.48 and 0.20 to 0.32, respectively, between ribs 4 and 8. The corresponding

maximum velocities for fully developed flow are 0.55 and 0.31 (Abdel-Wahab and Tafti, 2004). Figure 5.3(c-d) show the distribution of cross-stream velocity at $z = 0.01$ and spanwise velocity at $z = 0.04$ to elaborate further on the development of the secondary flow. Both z-locations correspond to the maximum cross-stream and spanwise velocities observed in Figure 5.3(a-b). The essential features of the secondary flow are well established by the third rib and gain strength further downstream. The strongest flow occurs above the rib at the trailing side, while it is weakened considerably at the leading side.

The effect of rotation on mean temperature evolution is shown in Figure 5.4(a) along the length of the duct, together with temperature profiles at selected x-locations (Figure 5.4(b)), and the streamwise evolution of temperature at locations close to the trailing and leading walls (Figure 5.4(c)). Much like the mean velocity, the large scale effects of Coriolis forces are clearly visible after rib 4 as the temperature profile gets biased toward the trailing side. Figure 5.4(b) shows this trend with greater clarity. As the flow moves downstream into the duct, temperature gradients increase at the trailing wall and decrease at the leading wall. A finer detail of asymmetries between the leading and trailing walls can be discerned from Figure 5.4(c), which shows that in the close vicinity of the leading and trailing walls, the temperature develops asymmetries immediately following the first rib that increase downstream.

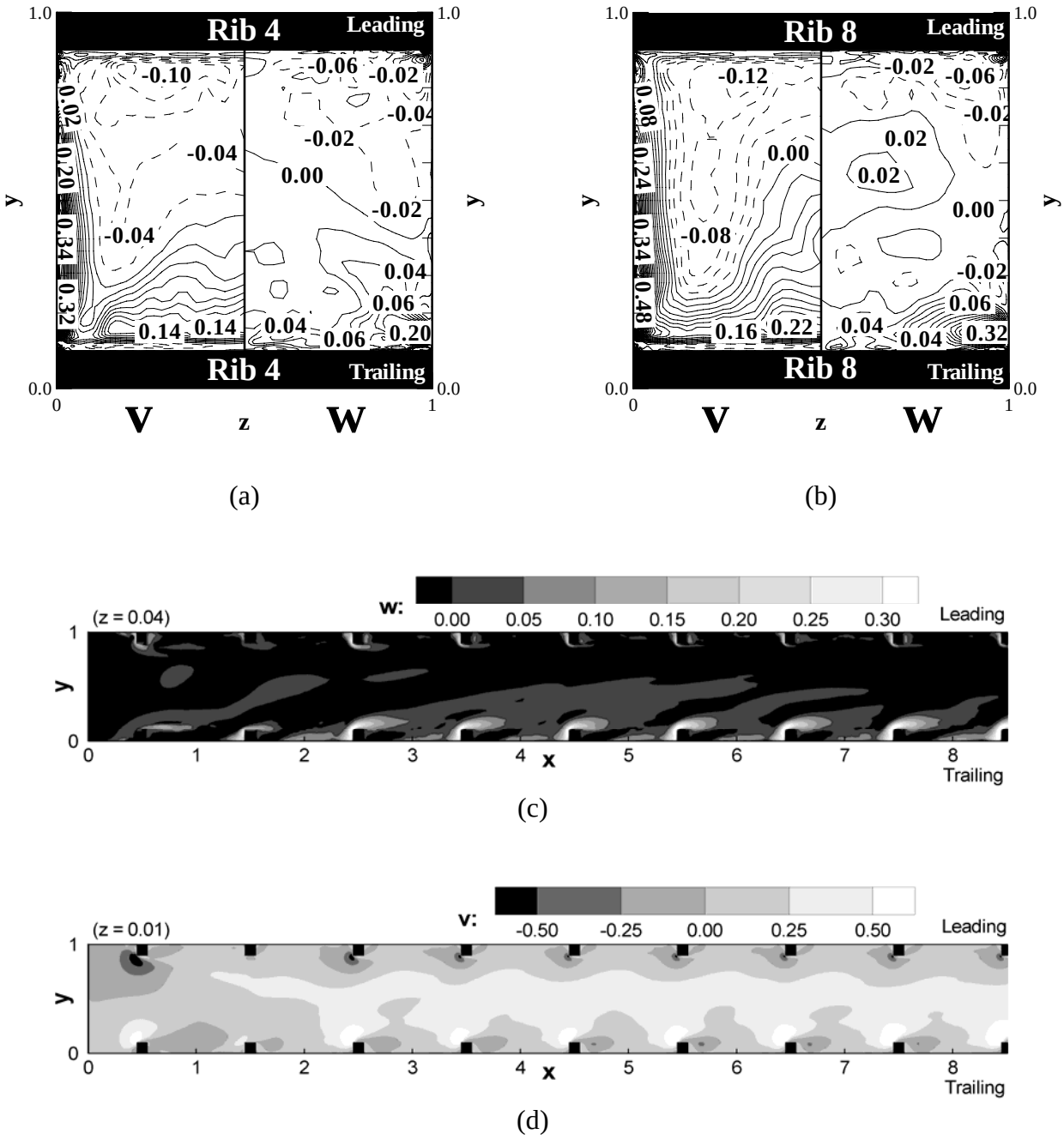

Figure 5.3. Two cross-sectional planes of the vertical and lateral velocities on top of (a) rib 4 and (b) rib 8 show the high lateral velocity impinging on the smooth wall and causing the upwash along the smooth wall and increasing heat transfer. The (c) streamwise distribution of the lateral velocity and (d) spanwise distribution of vertical velocity show the development of smooth wall impingement and vertical secondary flow near the smooth walls.

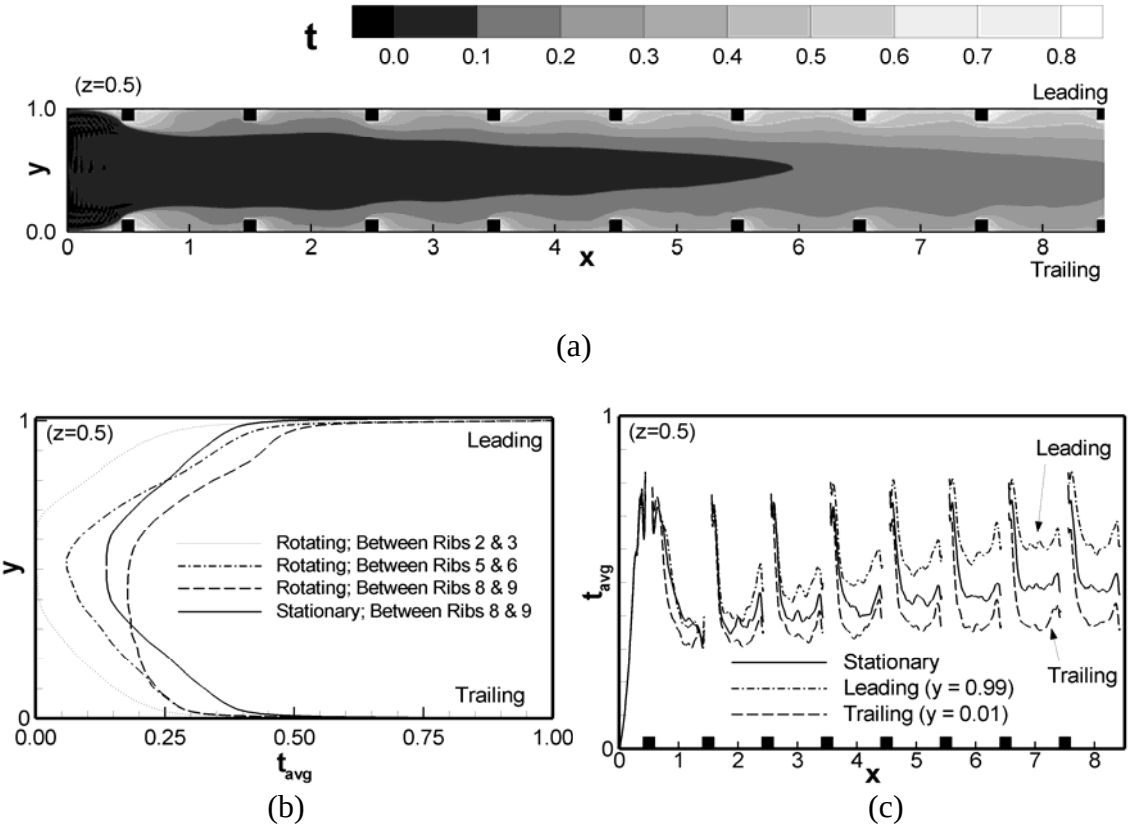

Figure 5.4. (a) The average temperature contour in the channel center (z = 0.5) shows the effects of the recirculation zones on the temperature distribution as well as the "bending" of the cooler temperature towards the trailing wall. (b) The vertical contours of temperature between several ribs show the higher temperatures near the leading walls, which damps heat transfer. (c) The streamwise distribution of temperature near the leading and trailing walls shows the divergence of temperature from the stationary temperature profile (Sewall and Tafti, 2004) immediately after the first rib.

5.03 Turbulence in the Developing Flow Region

The development of turbulence near walls dictates the heat transfer augmentation. Figure 5.5(a) shows the development of turbulent kinetic energy (*tke*) at the center of the duct (z = 0.5) at locations near the trailing and leading wall. For comparison, the development in a stationary duct together with the fully developed distribution in a rotating duct is also shown. The incoming laminar flow develops turbulence upstream of the first rib which peaks in the

stagnation region at 0.02 for the stationary as well as the rotating channel. The generation of turbulence is brought about by the destabilizing effect of the secondary flow eddies which form in the stagnation region. The vorticity production in the unstable separated shear layer on the first rib contributes to the large increase in *tke* in its wake. The impact of Coriolis forces on turbulence is established immediately after the first rib; the growth and magnitude of *tke* is larger on the trailing side than on the leading side. The difference in magnitude between the two sides increases as the flow moves further downstream into the duct; turbulence at the trailing edge increases whereas that at the leading edge decreases gradually. Between the eighth and ninth ribs, the magnitudes and distribution are comparable to the fully developed rotating channel. It is interesting to note that the difference in turbulent energy between the leading and trailing walls is apparent long before the secondary flows are even formed at about the third or fourth rib. This indicates that the direct effect of Coriolis forces on turbulent structure is much more dominating than the effect of the secondary flow.

It will be seen later (Figure 5.7) that heat transfer augmentation is closely related to the level of turbulence rather than the presence of absence of any secondary flow. This has important implications for RANS modeling of rotating ducts. In addition, the spikes seen in the plot in the downstream section can be attributed to establishment of secondary flows. The region in front of the ribs is home to highly unsteady vortices, and the establishment of the secondary flow in the cross-section adds to their unsteadiness. Plots of the isolated rms velocities (which are not shown here) indicate that these spikes are due solely to the augmented levels of spanwise turbulence levels w_{rms}. The finite sampling time of this highly unsteady region in front of the ribs also contributes to the uneven nature of *tke* levels.

Figure 5.5(b-c) show contours of *tke* at a location in the vicinity of the smooth wall (z = 0.01) surrounding the eighth rib and the fully developed distribution from Abdel-Wahab and Tafti (2004). The values in both plots are nearly identical, indicating that turbulence is close to fully developed conditions near the smooth wall at the eighth rib. Turbulence levels as high as 15% are seen at the trailing wall rib, while they do not reach values any higher than 6% at the leading wall.

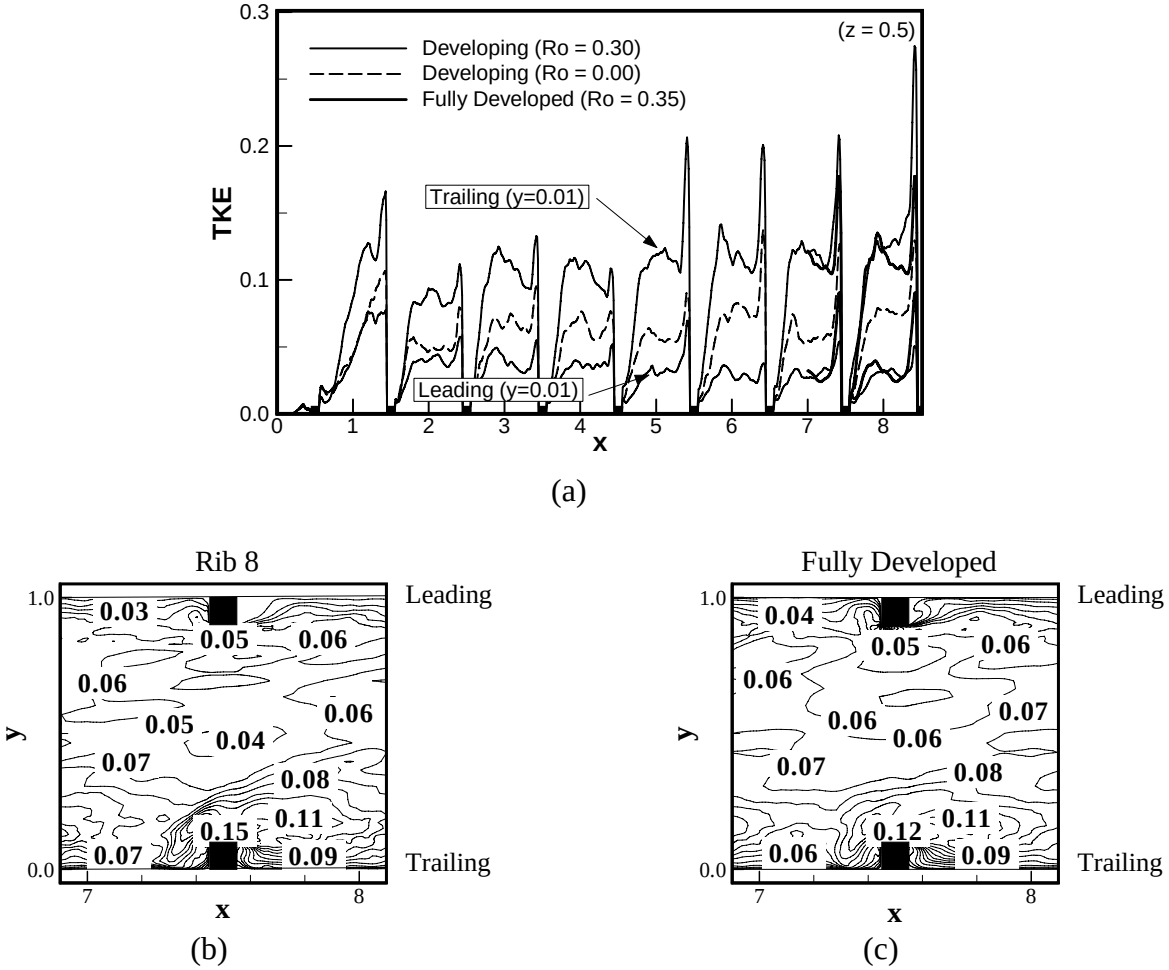

Figure 5.5. (a) Streamwise distribution of the turbulent kinetic energy shows that rotation immediately affects turbulence, as it diverges from the stationary flow after the first rib, but areas of high turbulence immediately before the ribs do not develop until the sixth rib. Turbulent kinetic energy contours near the smooth side wall (z = 0.01) for (b) the eighth rib and (c) the fully developed case of Abdel-Wahab and Tafti (2004) show that the turbulence near the smooth wall is nearly fully developed by the time the flow reaches the eighth rib.

5.04 Developing Flow Heat Transfer Augmentation

Contours of the heat transfer enhancement are shown in Figure 5.6 for the leading wall (Figure 5.6(a)), trailing wall (Figure 5.6(b)), and smooth wall (Figure 5.6(c)) surrounding the eighth rib, which show the regions of high and low heat transfer. The highest heat transfer enhancement occurs on the smooth wall impingement area immediately above the trailing wall rib, while the lowest is seen just downstream of the leading wall ribs. The smooth wall shows a steady decrease of heat transfer enhancement from the trailing wall to the leading wall. It is noted that the maximum enhancement of 4.4 in the reattachment region is found to occur not at the center of the duct but skewed toward the side. A similar pattern is seen in the fully developed calculations of Abdel-Wahab and Tafti (2004) at Ro = 0.35.

Figure 5.7 shows the centerline heat transfer augmentation along the ribbed walls. The mass transfer data taken by Hibbs et al. (1996) with similar geometry characteristics (e/D_h = 0.1 and P/e = 10.5), as well as similar flow characteristics (Re = 10,000 and Ro = 0.3), is included as a comparison, and good agreement is found between the two. Differences near the inlet are attributed to different inlet conditions, which do not have any effect after the second rib.

Figure 5.7(b) shows the enhancement of smooth side wall heat transfer in the rotating case over the fully developed stationary smooth side wall heat transfer from Tafti (2005) at a location midway between ribs. The augmentation near the trailing side due to rotation is very evident, as well as the degradation on the leading side. However, the heat transfer augmentation lags the fully developed values uniformly across the smooth wall.

The laterally averaged heat transfer enhancement at each x location along the ribbed and smooth walls is shown in Figure 5.7(c). Notably, rotation has an immediate impact on the augmentation ratios on the trailing and leading sides of the duct, right from the first rib.

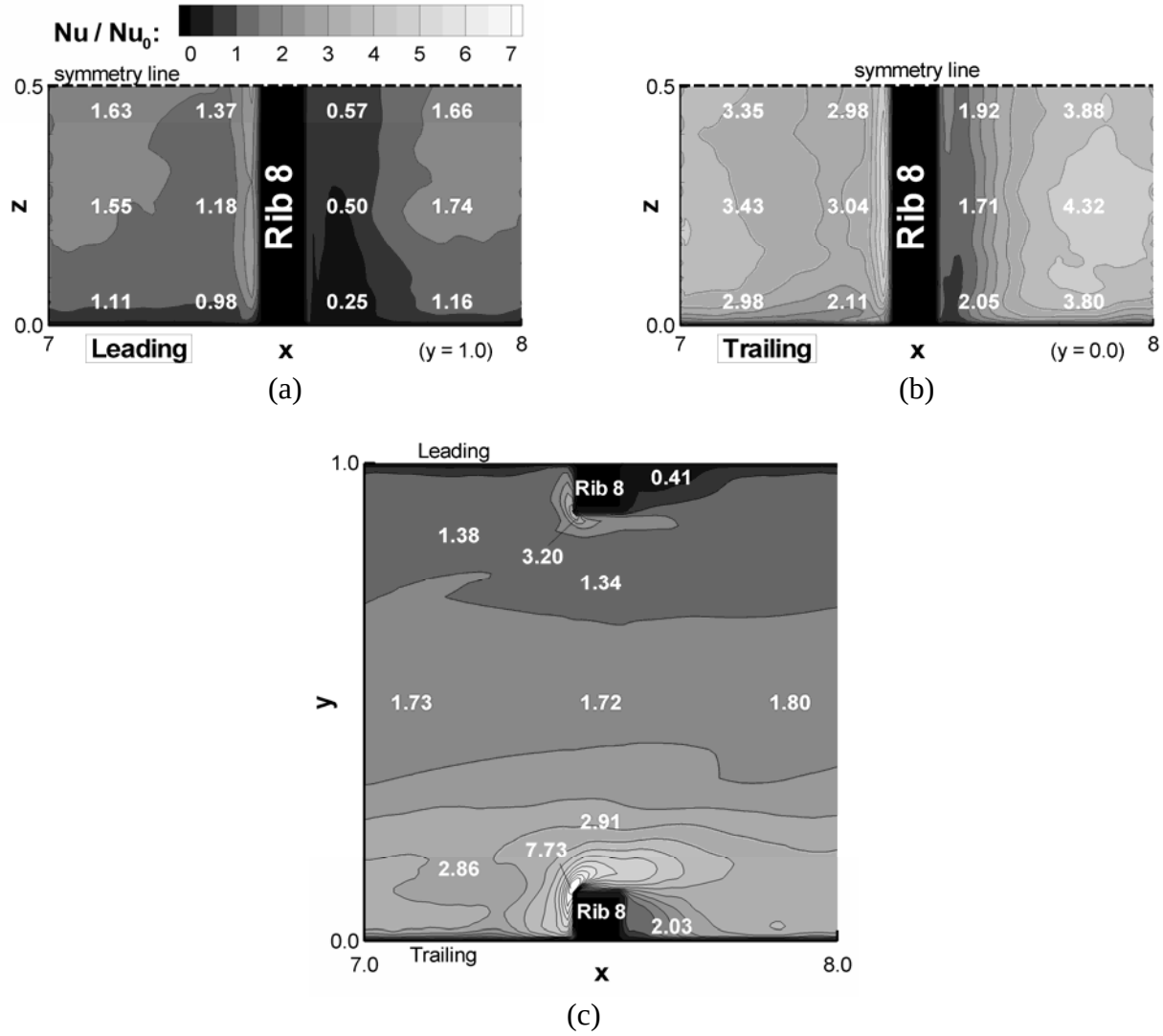

Figure 5.6. The heat transfer enhancement contours along the (a) leading, (b) trailing, and (c) smooth side walls shows the contrast between the leading and trailing walls. Flow impingement above the ribs is shown in part (c), and the high heat transfer areas immediately before the ribs and in the reattachment regions (a) and (b) are also clearly shown on the leading and trailing sides.

At this stage of development, cross-sectional secondary flows have not developed, and the only mechanism which influences this is the augmentation/attenuation of turbulence directly by the action of Coriolis forces. The trailing side heat transfer augmentation increases steadily while the leading side augmentation decreases. There is also a steady increase in the augmentation on

the smooth wall. While the leading side augmentation is very close to its fully developed value, both the smooth and the trailing wall are below their respective fully developed distributions at the ninth rib. In Figure 5.7(d), the rib averaged values are shown for the leading, trailing, and smooth walls. At the leading wall, the steady decrease in heat transfer can be observed, reaching the fully developed values at the fifth or sixth rib. Along the trailing wall the steady increase indicates that at least a few more rib lengths are needed before the heat transfer reaches its fully developed value. This is also the case with the smooth wall heat transfer.

5.05 Constant Temperature vs. Uniform Heat Flux Boundary Conditions

A comparison between a calculation with a uniform heat flux boundary condition and a constant temperature boundary condition, (both of which have been averaged for approximately 10 time units plus bi-directional averaging) is shown in Figure 5.8. Because the spanwise direction is symmetric, only one side of the duct is shown, so in the figure, the top half represents quantities for the uniform heat flux case and the bottom half represents the constant temperature case. Contour values for locations reflected on both sides show a comparison of the quantities at a number of different locations. The values are mirrored about the centerline, so to compare a value at the same location on the other side, one must consider its reflection about the centerline. Figure 5.8(a) displays the streamwise velocity comparison, where very few differences exist between the two cases, and this can be attributed to statistical variance. The same consistency is found in Figure 5.8(b), where a comparison of streamwise turbulence quantities show very similar values between the two cases. The conclusion to be drawn from this is that, as expected, the flow and turbulence between the two calculations, which were run independently with the same parameters, are essentially the same.

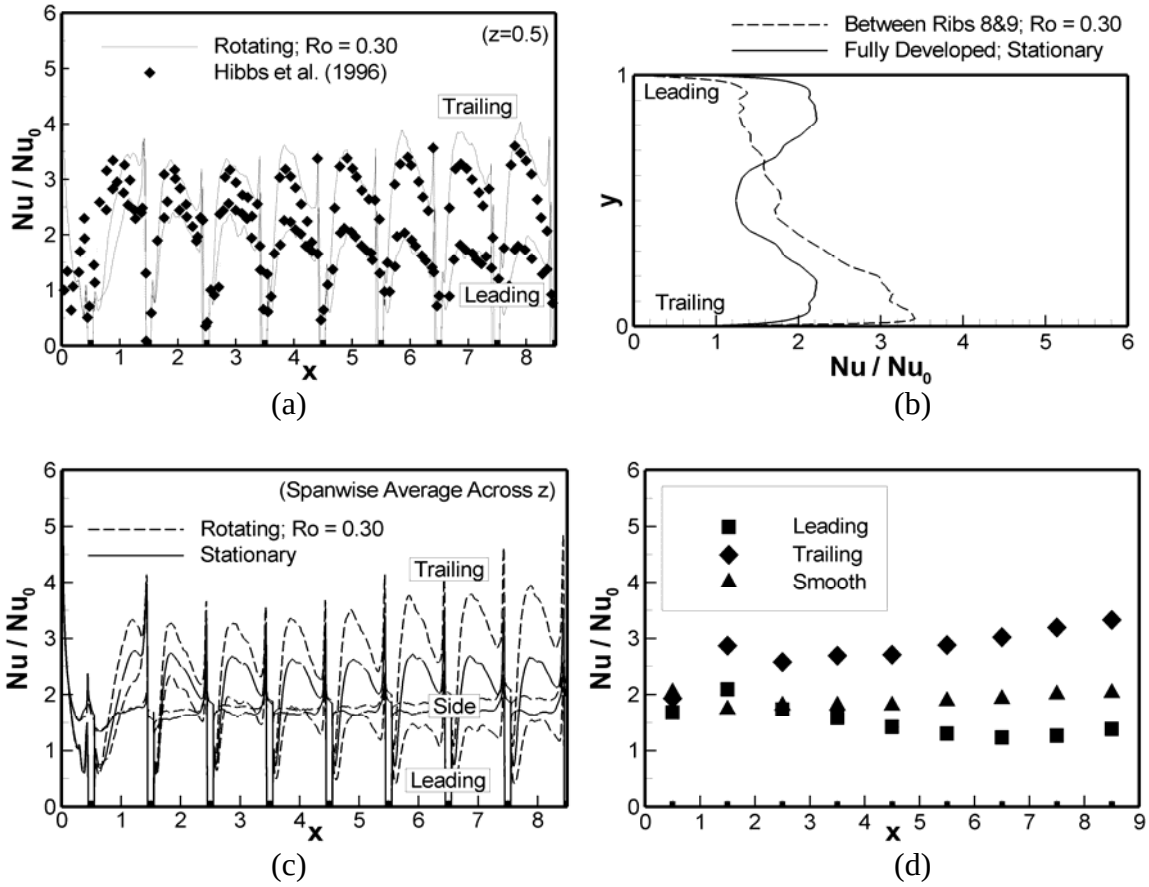

Figure 5.7. (a) The centerline augmentation ratios compare very well with the mass transfer experiments of Hibbs et al. (1996). (b) A vertical profile on the smooth side wall shows the heat transfer augmentation near the trailing side and damping near the leading side. (c) The laterally averaged heat transfer enhancement shows a similar difference between the leading and trailing sides. (d) Rib averaged values show a steady increase on the trailing and side walls and a fairly constant augmentation along the leading wall.

When the heat transfer augmentation between the two cases is compared, however, significant differences are apparent. Figure 5.8(c) shows that the peak heat transfer in the reattachment region downstream of the rib has a much higher value of heat transfer in the uniform heat flux case than in the constant temperature case. Other differences can also be observed upstream of the rib and in the contours on top of the rib. Though heat transfer values near the symmetry plane are similar between the two cases, significant differences are observed between the

centerline and side walls. As a result, centerline heat transfer augmentation would be expected to be similar between the two cases, but spanwise averaged and rib averaged heat transfer are expected to be higher with a uniform heat flux boundary condition.

A comparison of the centerline heat transfer augmentation and the rib averaged heat transfer augmentation is shown in Figure 5.9. Both the calculation with a uniform heat flux boundary condition and the calculation with a constant temperature boundary condition are shown in the figure. The two cases are identical along the centerline, but it is clearly shown that the uniform heat flux case has a much large rib averaged heat transfer value on the trailing wall. A comparison with the fully developed calculation, which also has a uniform heat flux boundary condition, shows a discrepancy on the centerline, where the trailing wall heat transfer is still increasing with the flow direction. However, the rib averaged values compare extremely well with the fully developed calculation. This comparison shows that a difference in boundary conditions is significant in rotating ribbed duct flows.

5.06 Developing Flow Friction Factor

The non-dimensional pressure distribution relative to the inlet is shown in Figure 5.10(a). The difference in the pressure at the leading and trailing sides is a direct consequence of rotation and the effect of Coriolis forces. Assuming a uniform bulk flow velocity and a balance between Coriolis forces and the pressure gradient in the cross-stream direction, the calculated non-dimensional pressure difference between the trailing and leading sides of the duct can be calculated to be approximately 0.6, which agrees well with the calculated difference in the computations. In Figure 5.10(b), the friction factor is calculated by using the area weighted average pressure difference across a rib pitch as in Eq. (18). The trends at the first three ribs are very similar to that observed in a stationary channel.

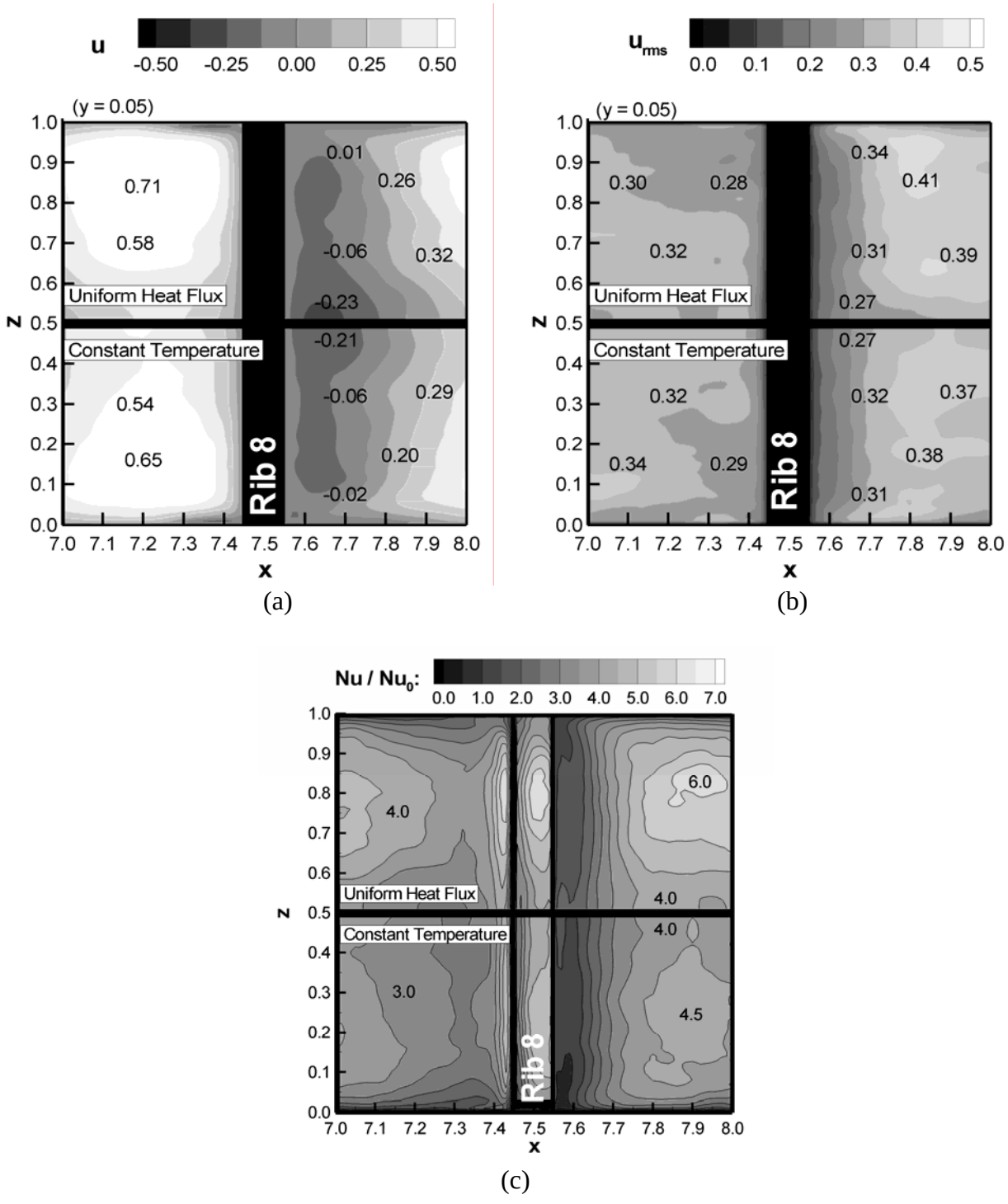

Figure 5.8. A comparison between a uniform heat flux boundary condition (top) and a constant temperature boundary condition (bottom) for (a) streamwise velocity near the trailing wall, (b) streamwise fluctuations near the trailing wall, and (c) heat transfer augmentation on the trailing wall shows that significant heat transfer differences exist, despite the similarity in flow and turbulence.

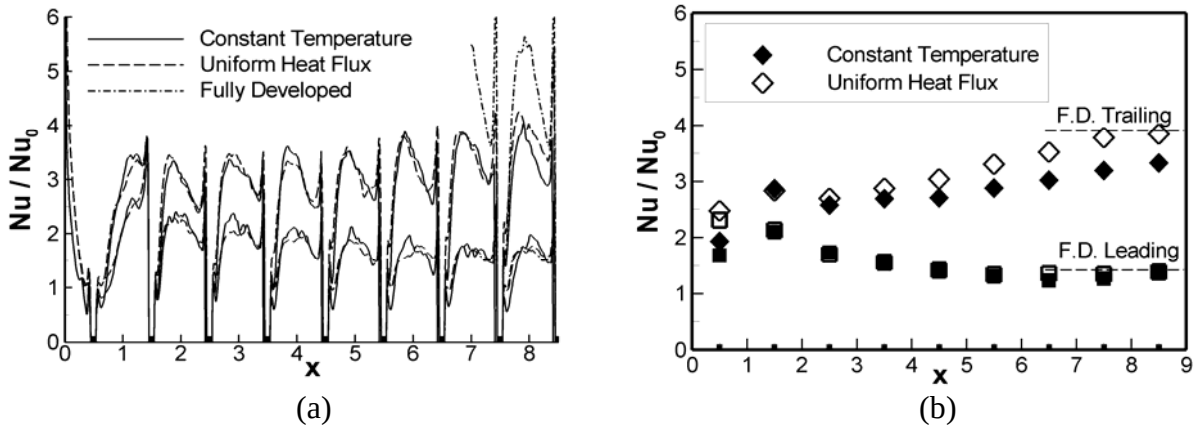

Figure 5.9. Heat transfer comparisons between the constant temperature boundary condition and uniform heat flux boundary condition along (a) the duct centerline and (b) the rib averages show that a comparison between the two is close on the centerline but is much different on the trailing wall rib average. The fully developed values (uniform heat flux boundary condition) compare well with the averaged developing flow values near the eighth and ninth ribs.

It shows the large pressure drop at the first rib, a pressure recovery at the second rib, and the slow settlement towards a steady value of 8.5 at the last two ribs. This value is less than that for the fully developed case, but from all other indications the flow and heat transfer are not fully developed at the ninth rib.

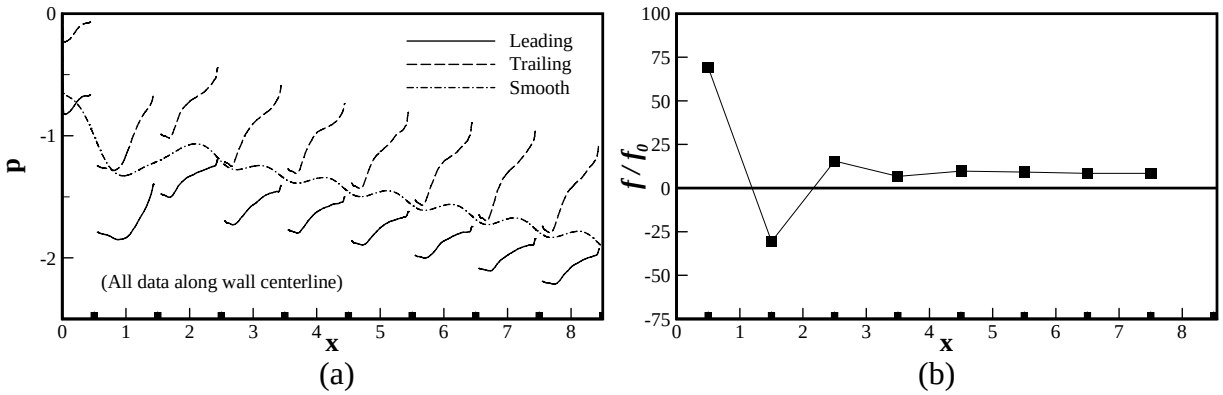

Figure 5.10. (a) The pressure relative to the entrance shows a dramatic difference between the leading and trailing wall pressure. (b) The friction factor reflects the large pressure drop at the entrance, followed by a pressure recovery. The final friction factor settles down to a friction factor enhancement of approximately 8.5.

5.07 Mean Flow in the 180º Bend

In a rotating duct, Coriolis effects manifest themselves in both the mean flow field and the turbulent fluctuations. Primarily, strong cross-stream momentum forces the mainstream flow towards either the leading or trailing wall, increasing turbulent shear along that wall while attenuating turbulence on the opposite wall. Streamwise momentum is also affected through a coupling with the cross-stream velocities through rotation. The coupling of streamwise and cross-stream momentum through rotation causes a unique asymmetry in the flow that is reversed as the mainstream flow changes directions in the 180° bend.

In a plane directly between the leading and trailing walls, a comparison of streamlines between the stationary and rotating ducts is shown in Figure 5.11. Generally, the two figures are similar, both showing a large recirculation zone at the tip of the dividing wall as a result of flow separation from the inside wall. Though the size and shape of the two are similar, closer observation reveals that the recirculation in the rotating case is angled towards the downstream duct more sharply and does not stretch as far into the bend as that in the stationary case. Additionally, both calculations show the presence of recirculation zones in the upstream and downstream corners of the bend, though the upstream recirculation is much smaller because of rotation.

Figure 5.12 shows the contours of flow velocity in the streamwise direction at cross-sectional planes going into the bend, in the middle of the bend, and coming out of the bend. The left side of the figure shows contours for the stationary case, while the right side shows the same planes in the rotating case. Going into the bend, the streamwise velocity accelerates on the inside of the bend, whereas the flow accelerates on the outside as it emerges from the bend.

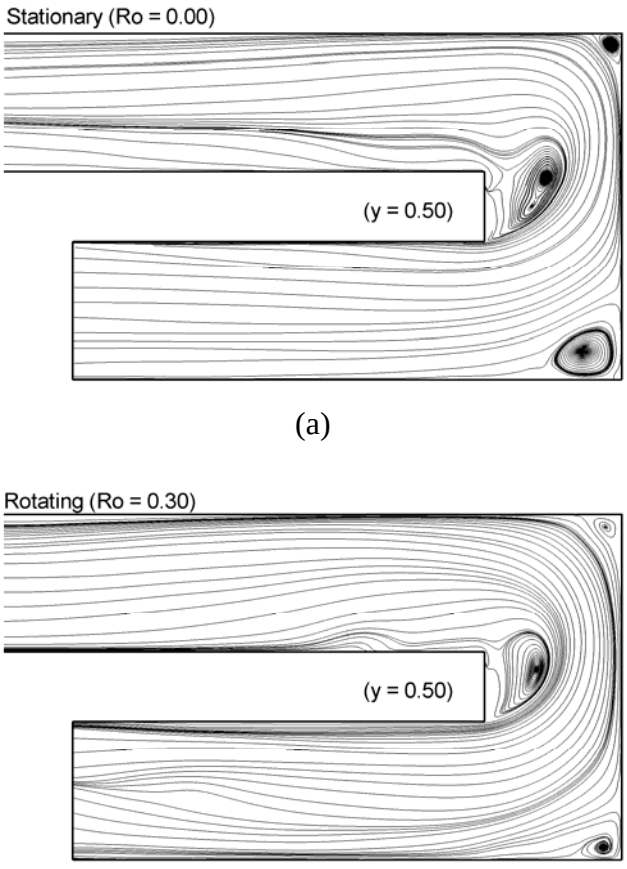

Figure 5.11. Streamlines at the mid-height between the ribbed walls of the (a) stationary and (b) rotating ducts show the reduction in size of the corner recirculation zones and the change in shape of the recirculation bubble at the tip of the dividing wall as a result of rotation.

It is found that rotation skews the streamwise velocity profile toward the leading side of the duct as the flow enters the bend, which agrees with the fully-developed calculations of Abdel-Wahab & Tafti (2004). This is contrary to what is observed by Liou et al. (2000) at Re=10,000, in which the streamwise velocity profile is skewed towards the trailing side of the duct[2].

The reversed flow in the middle of the bend occupies a much larger area in the cross section in the rotating case, and the center of the reversal is shifted towards the trailing wall, making it

[2] Fully-developed calculations at Re=10,000 confirms the experimental result of Liou et al. (2000). Hence, the location of the maximum streamwise velocity is dependent on the Reynolds number.

less visible in the mid-height streamlines shown in Figure 5.11. The peak velocity magnitude of the reversed flow is 50% higher in the rotating case than in the stationary case, indicating much stronger recirculation due to Coriolis forces. The streamwise velocity near the back wall is lower with rotation, but the recirculation zone is also smaller, allowing a larger area for the mainstream flow.

Downstream of the bend, rotation decreases the shift of the velocity profile towards the outside wall by increasing the velocity in the center (between the inside and outside walls) and decreasing the velocity at the outside wall. This results in a flatter horizontal velocity profile.

Comparison of the streamwise velocity profile at a distance 0.125 from the trailing and leading walls at the center of the bend in Figure 5.13 shows that rotation does not have a large effect on the streamwise flow in the bend. Figure 5.13 also shows LDV measurements in a stationary duct at the same y-location.

In the midplane of the bend, parallel to the dividing wall between the upstream and downstream ducts, a set of counter-rotating Dean vortices are clearly visible. In Figure 5.14(a), for the stationary duct, the strongest motion is at the mid-height of the duct directed towards the back wall, resulting in strong impingement on the back wall. The recirculation zone referred to earlier in Figure 5.11 is easily seen as the circular area near the dividing wall with no secondary flow present. As a comparison, the same plane in the rotating case is shown in Figure 5.14(b). Coriolis effects are observed in the attenuation of the mainstream flow towards the back wall. However, unlike Liou et al. (2002), who observed that rotation produced a strong asymmetry in the Dean vortices, dramatically increasing the size of the vortex near the leading side of the duct, no such phenomenon was observed in the current simulations.

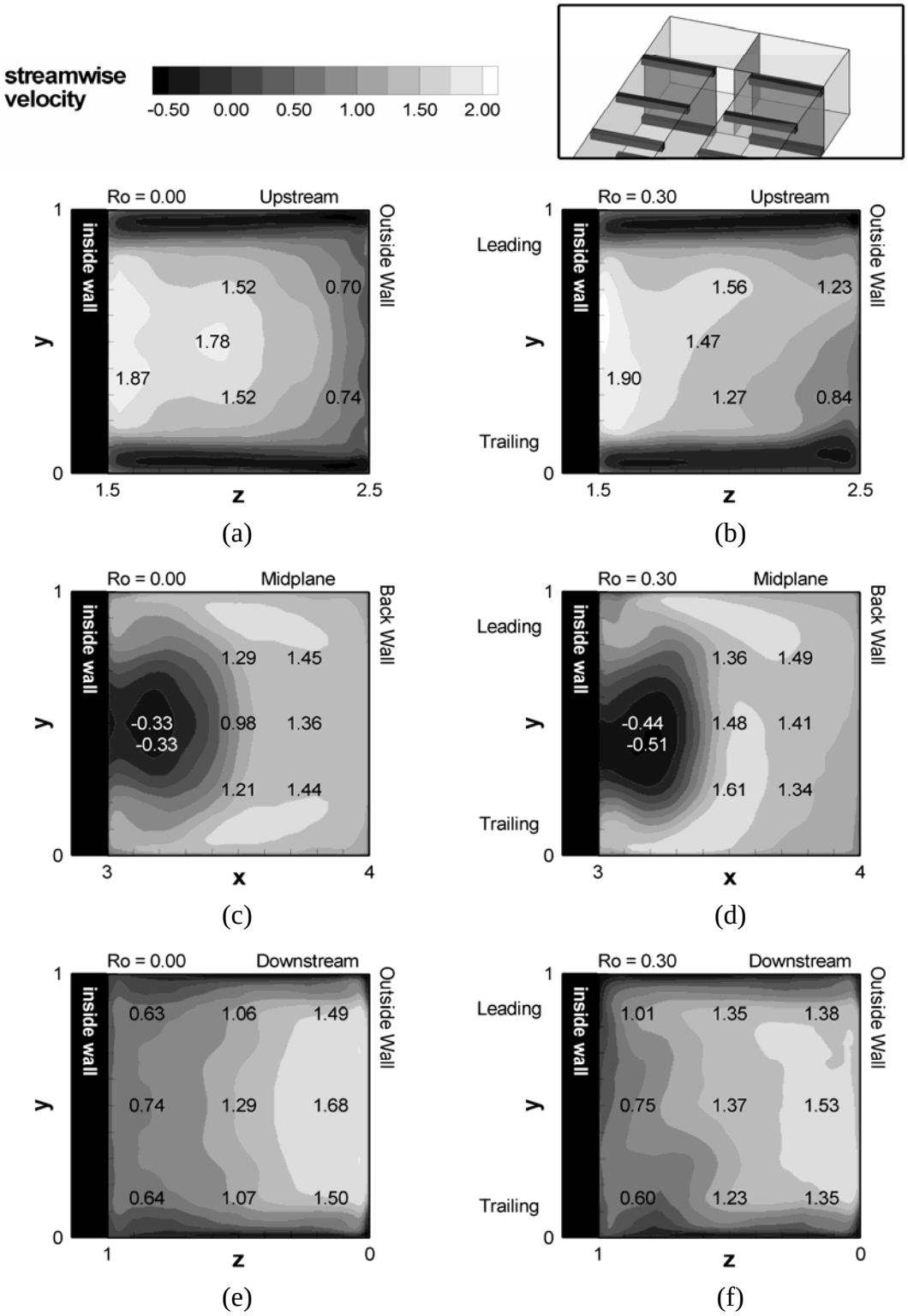

Figure 5.12. Contours of streamwise velocity in the (a,b) upstream, (c,d) midplane, and (e,f) downstream cross-sections shows the progression of mainstream flow through the duct. The stationary contours on the left are compared to rotating contours on the right.

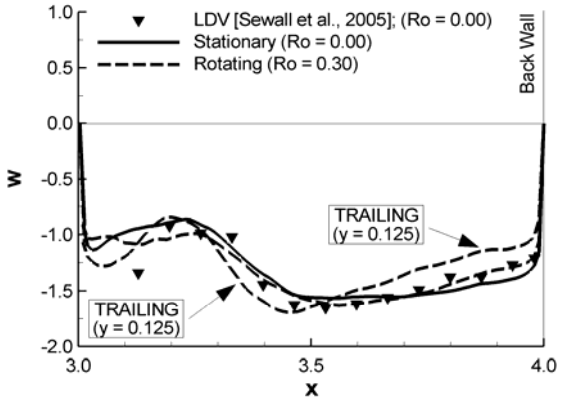

Figure 5.13. Profiles of the streamwise velocity in the midplane of the bend show minor differences between the stationary and rotating ducts.

This difference is attributed to the lower Reynolds number of 10,000, which allows Coriolis forces to have a stronger effect on the secondary flows.

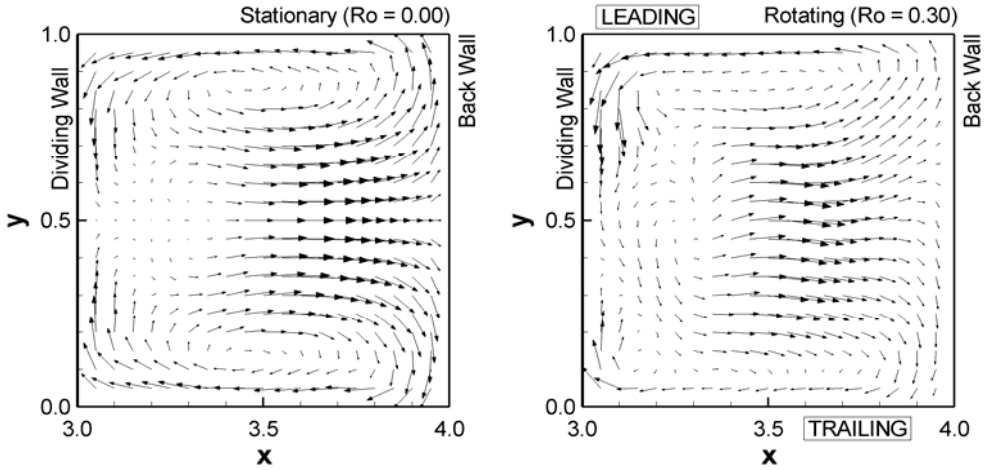

Figure 5.14. Vectors in the midplane of (a) the stationary duct and (b) the duct with Coriolis effects present show the rotation effects of elongation of the vortices and the strengthened downwash near the leading wall along the dividing wall.

In Figure 5.15, two sets of streamwise velocity contours (flow oriented as streamwise in the upstream duct) 0.1 D_h upstream of the bend show the strength of the impingement flow on the back wall. In the stationary case (top), the symmetric velocity shows a large elongated region of strong flow impingement on the back wall. In the rotating case, two effects are evident, the overall impingement velocity is much weaker than the stationary case and the center of impingement is shifted towards the leading wall. This is a consequence of the asymmetric velocity profile approaching the bend. As mentioned earlier, rotation tends to shift streamwise momentum towards the leading wall, as a result of which the fluid near the trailing side of the duct turns much quicker than at the leading side.

5.08 Turbulence in the 180° Bend

Turbulent kinetic energy in the bend is shown in Figure 5.16 with the same orientation as the streamwise velocity contours shown previously in Figure 5.12. In the upstream planes, Figure 5.16(a) and (b), the shear layer downstream of the trailing wall ribs is enhanced by rotation, and the turbulence along the outside wall is stronger with rotation. Near the leading wall, very little difference is shown between the stationary and rotating cases.

In the middle of the bend, Figure 5.16(c) and (d), the two large horizontal high turbulence regions in the stationary case are due to the shear layers from the upstream ribs. The displacement of the shear layers at the inside of the bend is a result of the secondary flow transport induced by the Dean vortices. The vertical high turbulence region in the middle of the plane is a result of the separated shear layer at the inside of the bend. The turbulence reflects the values at the entrance to the bend, as the peak value of 47% is found near the dividing wall in the shear layer downstream of the trailing wall rib.

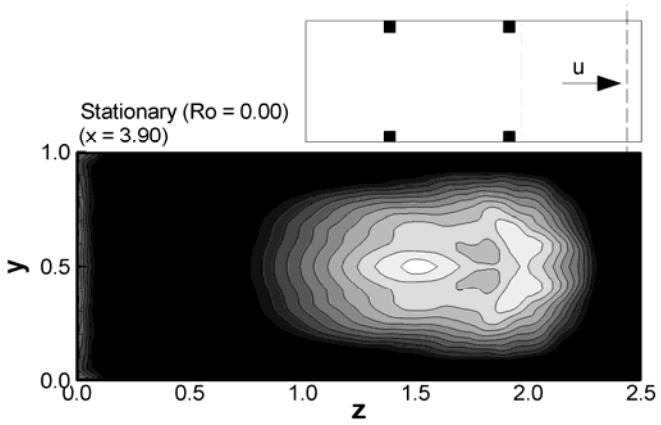

(a)

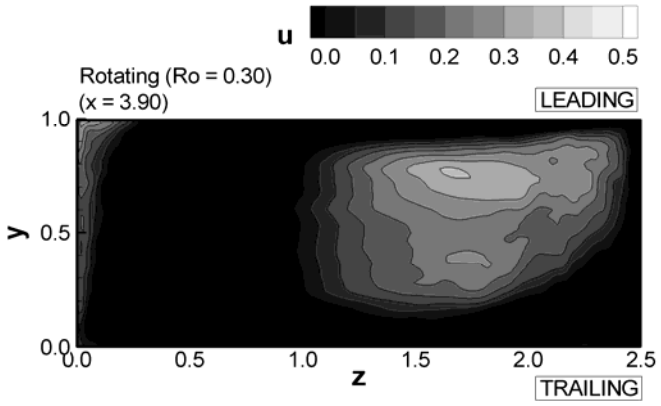

(b)

Figure 5.15. Streamwise velocity impinging on the back wall in (a) the stationary duct and (b) the rotating duct shows a decrease in wall impingement strength and shift towards the leading wall as Coriolis forces act on the impinging flow.

This maximum value represents a 42% increase over the turbulent kinetic energy at this location in the stationary case. In the rotating case, the trailing wall turbulence is strengthened, while the leading wall turbulence is attenuated, which is a consequence of the action of Coriolis forces on turbulence in the upstream leg of the duct. Near the back wall on the leading side, low turbulence (less than 10%) occupies nearly 45% of the cross-section along the leading wall. This effect is reversed when the flow enters the downstream leg after the bend.

Exiting the bend, the stationary duct experiences a peak in turbulence (49%) along the inside wall at the mid-height of the duct. With rotation, the distribution of turbulent kinetic energy is asymmetric, with the trailing side having a larger value (48%) than the leading side (45%). Overall, the distribution of turbulence across the exit plane is similar between the stationary and rotating cases.

The peak turbulent kinetic energy in the bend midplane is often reported as a characteristic value of the turbulence in the bend. Direct comparison of turbulent kinetic energy values is difficult because of differing geometry and flow conditions, so a comparison of important parameters across four ribbed cases is made in Table 5.2. Several smooth wall flowfield studies [Schabacker et al., 1998; Liou et al., 2000; Liou et al., 2002; Son et al., 2002] also reported peak turbulent kinetic energy values in the bend, and results varied inconsistently from 6% to 25% with little correlation with Reynolds number across the four studies. For the stationary case with ribs, Son et al. measured the two-dimensional turbulent kinetic energy in the midplane of the bend to be 15% based on the streamwise velocity (w) and the spanwise velocity (u), while the maximum turbulent kinetic energy in the bend from the LES calculation using those two components was 27% (3D TKE = 36%), which is still larger than the PIV measurements. This larger value is attributed to having ribs on both walls, as opposed to only one wall, as studied by Son et al. In a rotating duct with a Reynolds number of 10,000, a rotation number of 0.15, and larger ribs, Liou et al. measured a maximum two-dimensional turbulent kinetic energy value of 28% in the bend using the spanwise (u) and cross-stream fluctuations (v). In the rotating LES case, the three-dimensional turbulent kinetic energy was found to be 47%, while the two-dimensional turbulent kinetic energy using the same components as Liou et al. (u and v) came out to be 30%, which is only 7% higher than that measured by Liou et al.

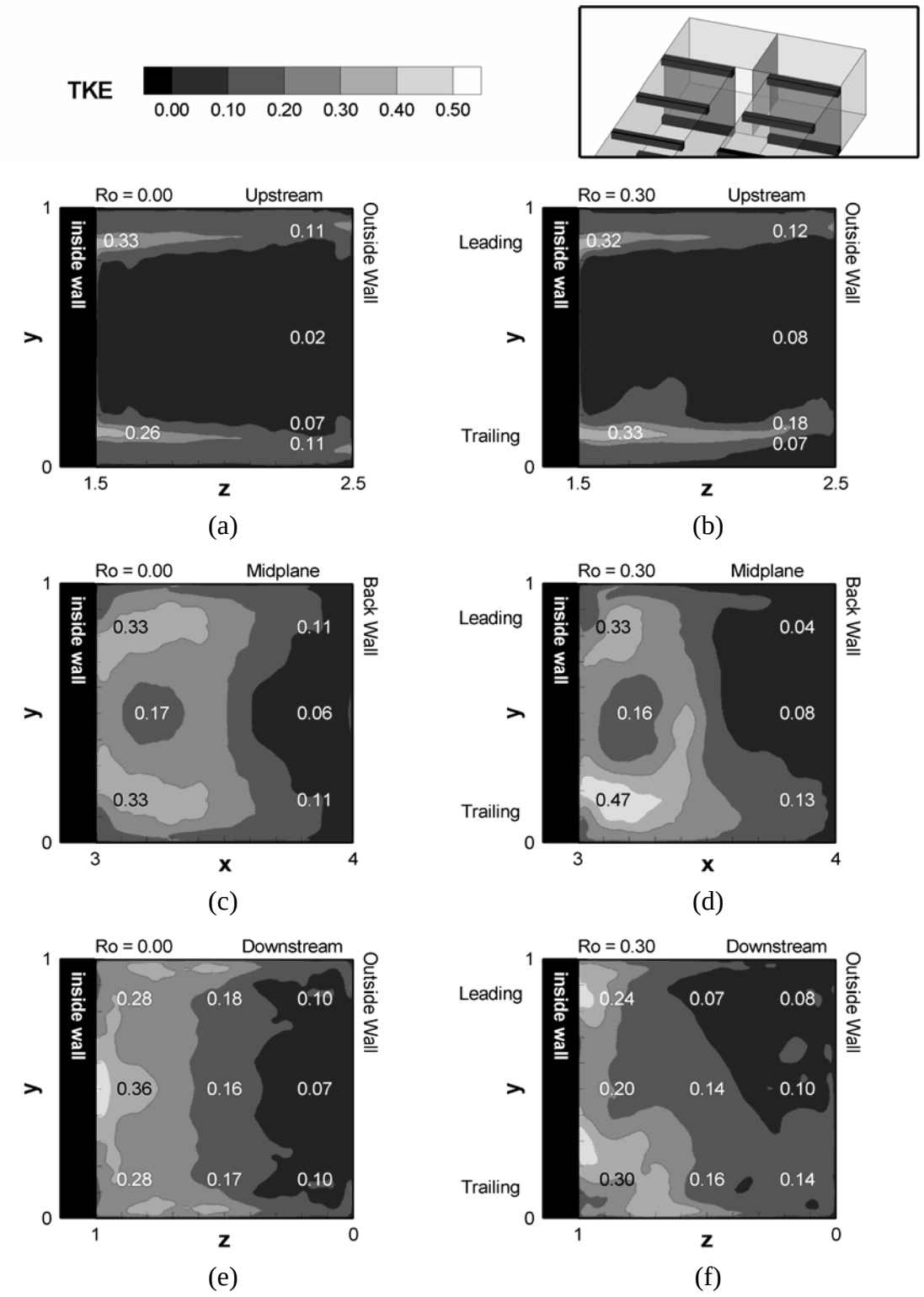

Figure 5.16. Contours of the turbulent kinetic energy in (a,b) upstream, (c,d) midplane, and (e,f) downstream cross-sectional planes show the effect of rotational Coriolis forces (right) on the flow as compared to the stationary case with no rotation (left).

Though the geometry and flow conditions are different between the experiments and calculations, these comparisons show that the LES calculations at the least predict reasonable turbulence quantities, as shown by adequate comparisons with measured values.

Table 5.2. Maximum Turbulent Kinetic Energy in Bend Midplane

Author	Method	Ribs	Re (Ro)	Components	TKE_{max} (2D)
Son et al. [2002]	PIV	90º ribs on one wall; $e/D_h = 0.125$	30,000 (0.00)	streamwise / spanwise	15%
Sewall and Tafti [2005]	LES	90º ribs on both walls; $e/D_h = 0.100$	20,000 (0.00)	streamwise / spanwise	27%
Liou et al. [2002]	LDV	90º ribs on both walls; $e/D_h = 0.136$	10,000 (0.15)	Spanwise / cross-stream	28%
Present Study	LES	90º ribs on both walls; $e/D_h = 0.100$	20,000 (0.30)	Spanwise / cross-stream	30%

In the midplane of the bend, profile comparisons show a quantitative view of Coriolis effects. Profiles at two vertical locations are compared in each plot of Figure 5.17: $y = 0.125$, which is between the centerline and the trailing wall and $y = 0.875$, which is between the centerline and the leading wall. A comparison of the turbulent kinetic energy in Figure 5.17(a) shows that, overall, rotation acts to attenuate turbulence near the leading side while altering it very little near the trailing side. One exception on the trailing side is found in the region of the vertical shear layer, between $x = 3.3$ and 3.5, where the shear layer is directed at a steeper angle downstream in the rotating case. Because of the bend, the quantity u_{rms} represents the cross-stream fluctuations in this figure. Rotation shows no effect on these fluctuations near the trailing wall, but on the leading wall the signal is greatly attenuated, especially outside of the separated flow region. Rotation is shown to decrease the vertical fluctuations in a similar manner, as shown in Figure 5.17(c). The fourth plot, that of w_{rms}, which is now the streamwise fluctuations, shows a sharp

increase in the vertical shear layer peak fluctuation near the trailing wall. The peak turbulence is attenuated near the leading wall, along with the other turbulence quantities. Essentially, Coriolis effects showed the most significant changes in attenuating turbulence on the flow outside of the separation zone, while creating very little change to the turbulence quantities within the recirculating zone. The vertical shear layer created by flow separation from the vertical wall was shifted in both shape and magnitude, as the peak turbulence was shifted towards the dividing wall near the trailing wall, and the fluctuations were increased on the trailing side and attenuated on the leading side. In Figure 5.17(d), a comparison with the stationary LDV measurements of Sewall et al. (2005) and the LES calculation at the same location shows that the streamwise turbulence is predicted well.

It has been observed in past studies the level of turbulence is increased as flow moves through a 180º bend. To quantify this increase, the turbulent kinetic energy was area-averaged at each streamwise (x) location in the upstream and downstream ducts. The same cross-sectional area was considered through the ducts all the way to the back wall. Figure 5.18 shows that the turbulent kinetic energy in the downstream duct increases by a factor of three over the upstream duct in both the stationary and rotating cases, with the strongest turbulence encountered immediately downstream of the first rib in the downstream duct. With rotation, the turbulence is slightly higher in the upstream duct, but it is lower than the stationary turbulence in the downstream duct.

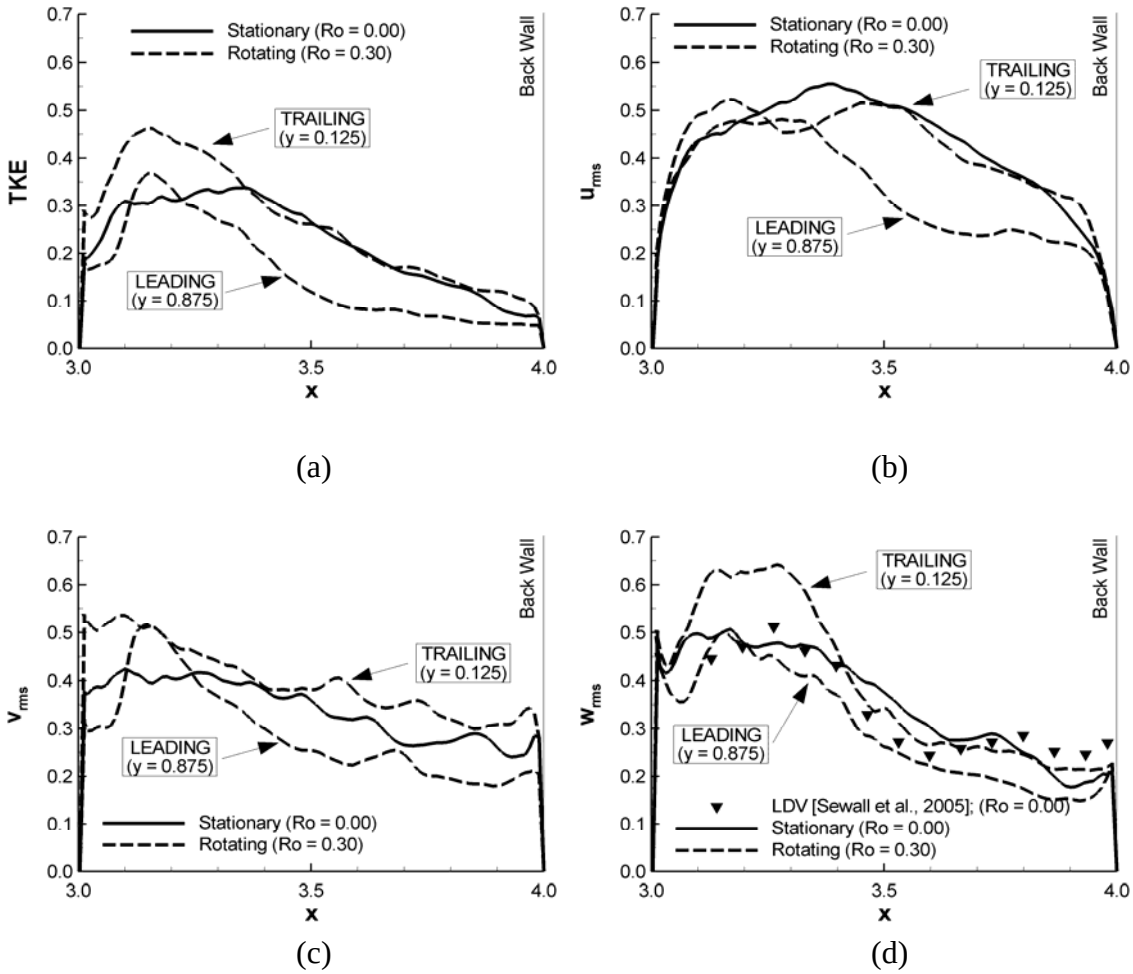

Figure 5.17. Horizontal plots of the turbulence quantities in the midplane of the bend show the attenuation of turbulence near the leading wall in all quantities. In addition, the peak of (d) w_{rms} near the trailing wall is greatly increased due to rotation and is shifted towards the dividing wall as rotation acts to skew the trailing wall turbulence towards the dividing wall.

The most dramatic difference brought about by rotation is found downstream of the first rib at the inlet of the downstream duct, where the trailing wall turbulence is strongly attenuated by the action of Coriolis forces, while there is a sharp increase in leading wall turbulence. Coming out of the bend, in spite of the effect of Coriolis forces, the mean turbulence is higher in the stationary duct. However, the difference between the rotating and stationary duct reduces significantly past the second rib in the downstream duct.

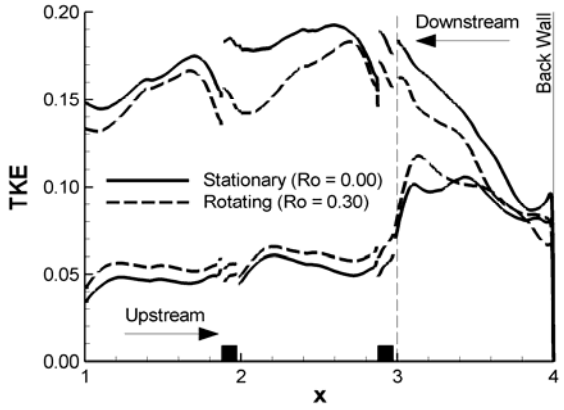

Figure 5.18. Area-averaged turbulent kinetic energy in the upstream and downstream ducts shows that the rotating case has higher turbulence in the upstream leg, while the stationary case shows higher turbulence in the downstream leg of the duct.

5.09 Heat Transfer Augmentation in the 180º Bend

Contours of the heat transfer augmentation on the ribbed walls are shown in Figure 5.19 The leading and trailing walls of the stationary duct are the same, and they are shown in Figure 5.19(a), while the leading wall of the rotating duct is shown as Figure 5.19(c) and the trailing wall as Figure 5.19(e). Comparisons with the mass transfer experiments of Kim et al. (2004) are also shown in Figure 5.19(b,d,e). The measurements were taken as similar flow conditions (Re = 10,000; Ro = 0.20), and the rib heights were 60% as large as those in the present study. Consequently, the spacing between the ribs is smaller, as it is determined by the rib height. Given these differences in geometry and flow conditions, and considering the fact that the bend geometry is slightly different, the qualitative comparisons are excellent. In the stationary duct, peak heat transfer regions are observed downstream of the last upstream rib, along the back wall, and along the outside downstream wall. In the rotating cases, high heat transfer regions in the bend on the leading and trailing walls are similar. From these comparisons it is reasonable to assume that the LES calculations are highly capable of reproducing the local heat transfer effects

in the bend. In the upstream section, a typical shift in heat transfer is observed, as the trailing wall heat transfer is increased and the leading wall heat transfer is decreased. Within the bend, the high heat transfer region near the back wall is elongated towards the downstream side of the bend, while the rotating high heat transfer region is confined to the upstream side. With rotation, the regions of high heat transfer are localized to an area immediately downstream of the last upstream rib, with low heat transfer augmentation on the downstream side of the bend. In the downstream section of the duct, leading wall heat transfer augmentation is strongly enhanced, especially near the outside wall, where local heat transfer augmentation values reach as high as 8.1. The sharp peak in heat transfer is a result of an extremely high turbulent kinetic energy immediately downstream of the first rib. Heat transfer augmentation on this wall remains high downstream. Downstream trailing wall heat transfer augmentation shows its highest values along the inside wall of the duct. The heat transfer values are lower than those found on the leading wall or in the stationary duct.

A series of local heat transfer augmentation values along six lines, three upstream and three downstream of the bend, are shown in Figure 5.20. The “centerline” is drawn through the centerline of the ribbed wall, the “inner line” is drawn between the centerline and the inside wall, and the “outer line” is drawn between the centerline and the outer wall. In addition to the values from the stationary and rotating leading and trailing walls, mass transfer measurements in a stationary duct performed by Han (1984) are also included in the figure. The mass transfer measurements compare very well with the stationary calculations with the exception of the outer line along the downstream duct, but this is an expected result because the thickness of the experimental dividing wall was ½ of that used in the calculations, which induced stronger flow separation within the bend and resulted in higher heat transfer augmentation along the outer line.

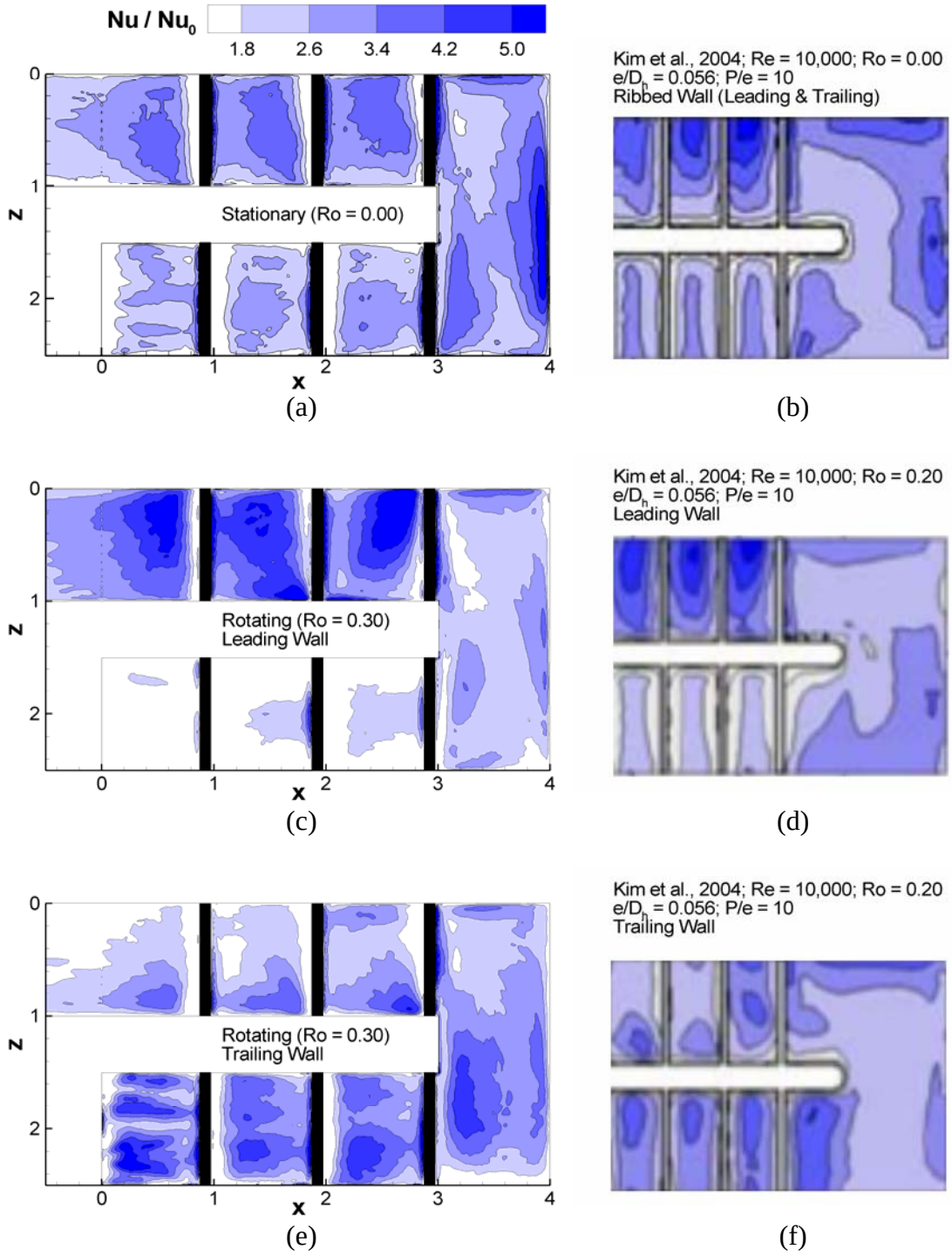

Figure 5.19. The ribbed wall heat transfer augmentation on the (a) stationary duct, (c) leading wall, and (e) trailing wall show comparisons with the mass transfer experiments of Kim et al. (2004) on the (b) stationary walls, (d) rotating leading wall, and (e) rotating trailing wall.

The turning effect upstream is also overemphasized by the calculations, as the upstream inner line comparison in Figure 5.20(a) shows a lower predicted heat transfer augmentation.

The general trend of the rotating calculations is that the upstream duct has a higher value of heat transfer augmentation on the trailing wall and a lower value on the leading wall and the downstream duct shows the opposite, with higher heat transfer augmentation on the leading wall. This is an expected effect based on the cross-stream influence of the Coriolis effects on the fluid momentum. In the upstream side of the bend, the trailing wall maintains its high heat transfer augmentation from the centerline in towards the bend, but the outside line actually shows lower or identical heat transfer to the stationary case. Rotation induces a weaker streamwise momentum towards the back wall in the upstream duct, and this allows for fluid to be more easily swept downstream through the bend, thus decreasing the outside line heat transfer and making it equal to that in the stationary case. In the downstream side of the duct, the stationary case shows a much higher heat transfer augmentation along the back wall, as the slower moving fluid in the rotating case is more easily forced into the downstream duct and does not maintain the high heat transfer peak along that wall. Downstream of the first rib on the outside line, a sharp peak in heat transfer on the leading side results from a strong Coriolis effect on the increased volume of fluid that is swept downstream.

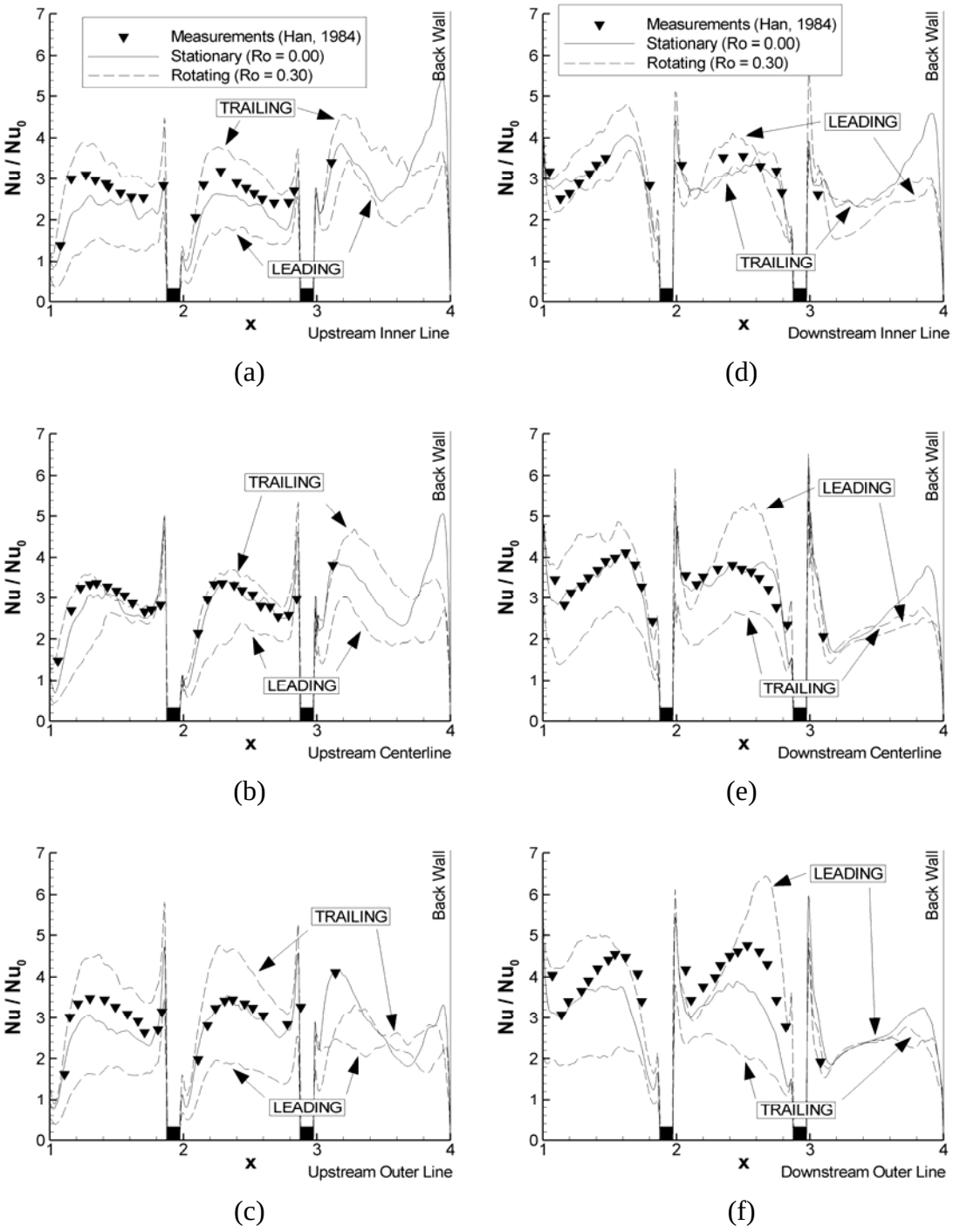

Figure 5.20. Local heat transfer augmentations compare well with J.C. Han in the stationary case, and the rotating cases show the asymmetry between the leading and trailing walls.

Figure 5.21 shows augmentation contours on the back wall and the dividing wall heat transfer, which reflects the Coriolis effects seen earlier on the mainstream flow impinging on the back wall. The large heat transfer region resulting from mainstream flow impingement from the upstream duct is shifted towards the leading wall and has a lower heat transfer value in the rotating case. The overall heat transfer augmentation on the back wall is decreased when rotation acts on the flow. On the downstream side of the duct, heat transfer augmentation is mostly symmetric between the leading and trailing walls in both cases. Along the inside dividing walls, rotation acts to diminish the high heat transfer regions near the ribbed walls seen in the stationary case due to the shear layers from the ribs. Slightly higher heat transfer is observed on the trailing side due to a higher turbulent kinetic energy in that region.

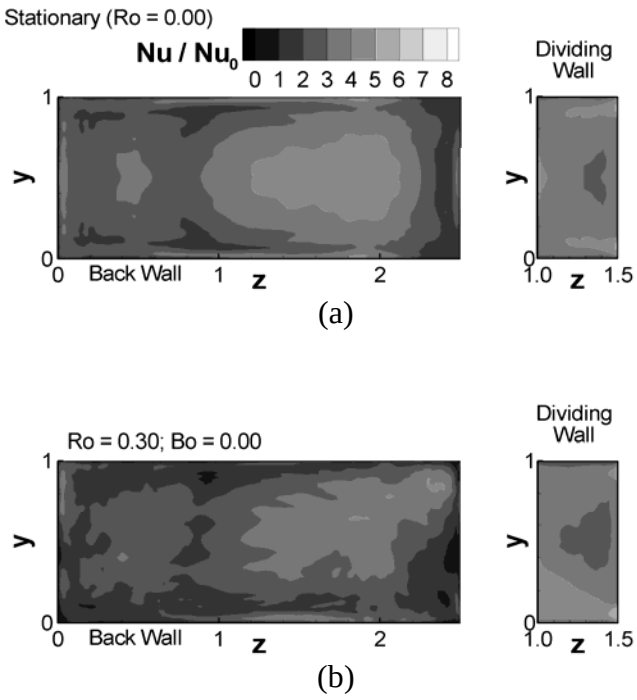

Figure 5.21. Heat transfer augmentation on the back wall and tip of the dividing wall in (a) the stationary duct and (b) the rotating duct show that rotation actually acts to decrease the heat transfer on the large impingement region on the back wall, while shifting the impingement region towards the leading wall.

Ribbed wall heat transfer augmentation averaged by sections is shown in Figure 5.22, corresponding to the section divisions shown in part (c) of the figure. As is expected from the presence of Coriolis effects, the highest heat transfer augmentation in the upstream side of the duct is found on the trailing wall, while the highest heat transfer in the downstream duct appears on the leading wall. In the bend, the leading wall heat transfer is decreased due to significantly attenuated turbulence, but the trailing wall heat transfer is similar to that found in the stationary case. The side walls have identical heat transfer values in the upstream duct. The outside walls in the bend show higher heat transfer in the stationary case than in the rotating case due to stronger flow impingement. Downstream of the bend, the inside wall heat transfer augmentation is higher with rotation.

An area-weighted average of heat transfer augmentation over each of the sections in the bend is plotted in Figure 5.23 for the stationary and rotating cases. Upstream of the bend, both the stationary and rotating calculations show the same results in the average. This indicates that the average heat transfer between the leading and trailing walls is approximately equal to the ribbed wall heat transfer in the stationary calculation, as the side wall heat transfer was shown to be similar between the two cases. The attenuation of turbulence along the leading side of the bend reduced the heat transfer augmentation on the leading wall of the bend, while the trailing wall heat transfer was similar in both cases. Because of this decrease, the overall averaged heat transfer in the rotating case is approximately 15% less than in the stationary case. Downstream of the bend, the leading wall and side wall heat transfer were significantly increased by rotation. The trailing wall heat transfer decreased, but the overall average shows an increase in the heat transfer because of the increase on the other three walls.

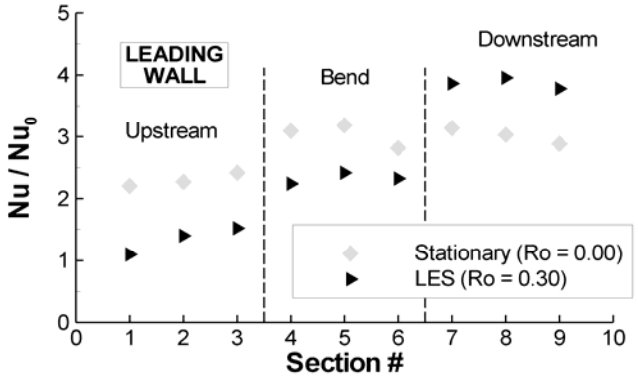

(a)

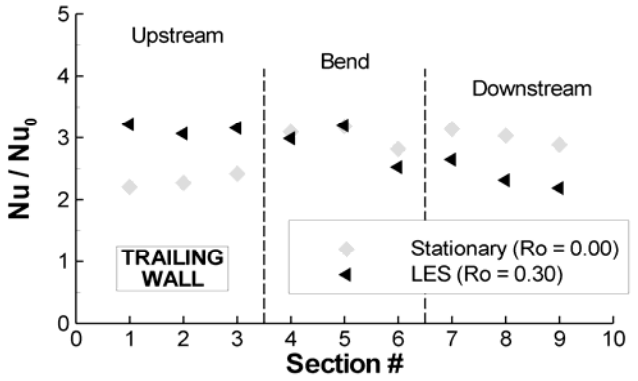

(b)

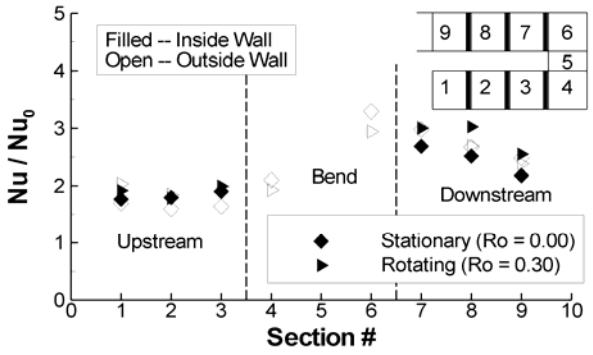

(c)

Figure 5.22. Group averaged heat transfer augmentation on the (a) leading, (b) trailing, and (c) side walls shows the increased heat transfer on the trailing side of the upstream duct and the leading side of the downstream duct. With the exception of the downstream outside wall, side wall heat transfer is generally higher in the presence of rotation.

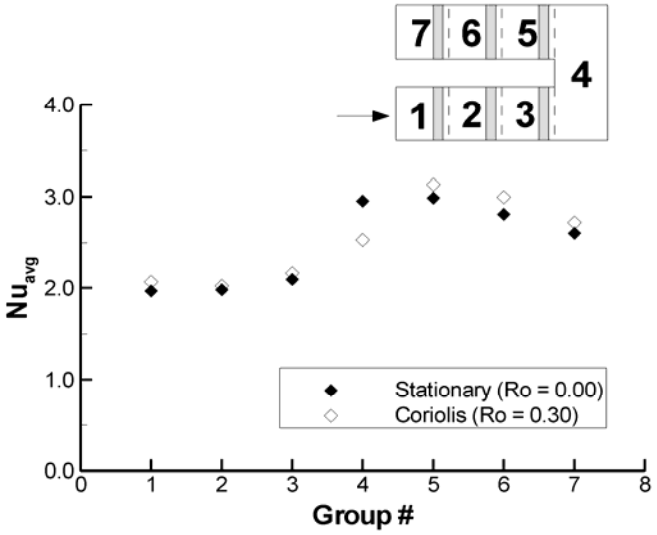

Figure 5.23. The area-averaged heat transfer augmentation over each section of the bend shows that Coriolis forces decrease the overall heat transfer augmentation in the bend while increasing the augmentation downstream of the bend.

5.10 Friction Factor

Pressure drop measurements in a rotating duct were obtained by Prabhu and Vedula (2003) in a study comparing configurations with 60º and 90º ribs with and without rotation. The geometry was similar to that used in the current study, with rib height ratios of e/D_h = 0.1 and P/e = 10. Three different dividing wall thicknesses were compared, and that of W/D = 0.37 matched most closely with the present value of W/D = 0.5. The Reynolds number in the study was 10,000, and the rotation number was 0.38, which compares with the present parameters of Re = 20,000 and Ro = 0.30. The nondimensional pressure drop between two local point measurements was reported in terms of the mainstream fluid dynamic pressure head according to following formula:

$$K = \frac{P_Y - P_{in}}{\frac{1}{2}\rho V^2}, \tag{11}$$

where P_y is the pressure at a given streamwise location. Pressure drop comparisons were made between this study and the LES calculations across 180º bend, from a local point two ribs upstream of the bend to a point two ribs downstream of the bend. In the stationary case, Prabhu and Vedula reported a K value of 2.99 across the bend, while the LES calculations resulted in a higher K value of 3.39. Local comparisons showed this difference to occur mostly as a result of a higher pressure drop across the last rib in the upstream leg of the duct in the calculations.

In the rotating case, leading wall pressure taps produced a much lower K value, 1.56 in the experiments and 1.43 in the calculations. However, the trailing wall K value in the calculations was found to be 4.34 (this quantity was not measured in the experiments), and the significant difference between the leading and trailing wall pressure drops clearly emphasizes the importance of obtaining pressure measurements on both the leading and trailing walls for a more accurate representation of pressure losses in a rotating duct.

The friction factor experiences a decrease with rotation as compared to the stationary case. In Figure 5.24, the friction factor calculated from a series of area averaged pressure drops is shown for the stationary and rotating cases. The friction factor in Group 1, corresponding to the pressure drop across a rib upstream of the bend, has a value of approximately 10 in both cases, which corresponds to the fully developed friction factor in a ribbed duct. The friction factor increases across the last rib, as shown in Group 2, and the rotating friction factor in Group 3 actually decreases, while that in the stationary case remains equivalent to the friction factor across the last rib. the lower pressure drop across the bend in Group 3 is due to more efficient turning in the rotating case with less impingement on the back wall. Across the first rib in the downstream duct, the friction factor augmentation in the rotating case is twice that of the stationary case, but then the rotating case experiences a larger pressure recovery in Group 5, as

indicated by the negative friction factor shown in the figure. Two pressure tap locations shown in the diagram of Figure 5.24 were used by Sewall et al. (2005) to compare the overall friction factor across the bend between the experimental measurements and the calculations and yielded a measured friction factor augmentation of 22.84, which is 1% less than the calculated value of 23.08. The same calculation in the rotating duct yields a value of 20.91, which is a smaller friction factor augmentation, despite the extremely large pressure drop across the first rib in the downstream duct. The distribution of pressure in the 180º bend is shown here to be quite different between the two cases, though the overall friction factors across the bend are similar with and without rotation.

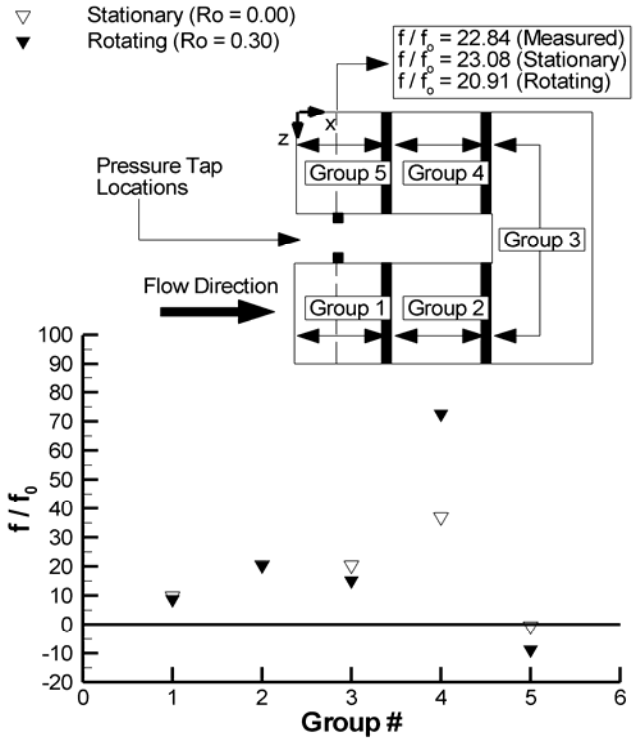

Figure 5.24. A comparison of the friction factor between the stationary and rotating cases shows a decrease in the bend due to rotation, but a sharp increase in pressure drop across the first rib downstream of the bend. A comparison of overall friction factors shows the rotating duct to have only a slightly smaller friction factor in the bend overall.

5.11 Summary and Conclusions

The time-averaged fluid flow, turbulence, and heat transfer augmentation have all been studied in a 180° bend region of a ribbed gas turbine blade internal cooling duct, and comparisons were made between a stationary duct and a duct with a constant rotation rate of Ro = 0.30. General expected trends of higher heat transfer along the trailing wall in the upstream duct and the leading wall in the downstream duct were reproduced, but many less understood effects within the bend itself are explored, as well.

Rotation decreased the trailing wall streamwise momentum entering the bend and increased the heat transfer on the leading side of the back wall through stronger flow impingement. Kinetic energy coming out of the bend was increased by an approximate factor of three in both the stationary and rotating ducts. Immediately downstream of the first rib after the bend, the destabilizing effect of Coriolis forces at the leading wall was evidenced by a large increase in turbulent kinetic energy, with a corresponding attenuation at the trailing wall. An unexpected result was that the magnitude of turbulent kinetic energy coming out of the bend was not affected greatly by rotation and cross-sectional averages were slightly less than the stationary bend.

Rotation induced considerable asymmetries in heat transfer augmentation at all surfaces in the bend and downstream of it. The highest level of heat transfer was found at the leading outer wall immediately after the first rib downstream of the bend. High augmentation regions were also observed at the inner side of the trailing wall after the bend. Area-averaged heat transfer augmentation values showed similar values between the stationary and rotating cases upstream of the bend. However, within the bend the heat transfer in the rotating case was 15% less than that in the stationary case, but Coriolis forces did result in a higher heat transfer augmentation downstream of the bend because of the augmentation on the leading wall and side walls. Overall, the friction factor across the bend was about two times the values encountered in the

fully-developed section of the duct. It was found to decrease slightly in the presence of rotation, and the predicted values compared well with experiments.

Chapter 6. Rotating Developing Flow and 180º Bends with Coriolis Effects and Centrifugal Buoyancy Forces[1]

Gas turbine blades operate at extremely high temperatures, with differences between the metal wall temperatures and cooling temperatures reaching several hundred degrees Kelvin. In a rapidly rotating duct, the differences in heat transfer between the fluid near the pressure side and suction side walls creates significant differences in fluid temperatures, and thus fluid densities, which vary the effect of centrifugal buoyancy forces acting on the fluid within the ducts. With these buoyancy forces present, it is extremely important to capture the physics correctly in predicting the turbulence and heat transfer within the ducts because of the significant variations that occur due to these effects. This chapter presents the calculation results of rotating ducts with both Coriolis and centrifugal buoyancy forces and consists of two sections. The first discusses the effects of buoyancy in the developing flow region with three different buoyancy parameters and their comparison with a zero buoyancy case, and the second discusses the results of calculations in the 180º bend with two different buoyancy parameters and their comparison with a zero buoyancy case.

6.01 Mean Flow in the Developing Flow Region

In general, as the buoyancy parameter is increased from Bo = 0.00 through Bo = 0.65, overall friction factor increases by a factor of two; leading wall heat transfer augmentation decreases when the buoyancy parameter is increased from Bo = 0.00 to Bo = 0.25 but increases after that; and trailing wall heat transfer increases monotonically with the increase in buoyancy parameter.

[1] Reproduced in part with permission from ASME

A significant change takes place in the size of the recirculation regions behind leading wall ribs and the reattachment length while little to no change occurs at the trailing wall.

Rotation induced Coriolis forces have two significant effects on the flow and heat transfer. The first effect is the destabilization and augmentation of turbulence at the trailing side of the duct together with stabilization and attenuation on the leading side. Another effect of Coriolis forces is the generation of secondary flow cells in the cross-section of the duct, which develop strong upwash and/or downwash regions. Centrifugal buoyancy can either complement or oppose the effect of Coriolis forces. Through the action of Coriolis forces, fluid in the vicinity of the trailing duct wall is cooler than at the leading wall for radially outward flow. To first order, the higher density exposes the fluid at the trailing wall to a larger centrifugal force than at the leading side of the duct and complements the effect of Coriolis forces. If the flow is radially inward, the leading wall of the duct will have cooler fluid temperatures in its vicinity than the trailing wall by the action of Coriolis forces. In this case, the centrifugal buoyancy body force is larger at the leading wall but opposes the action of Coriolis forces because of its outward direction.

A comparison of the mean velocity profiles across a vertical line between the eighth and ninth ribs in the symmetry plane of the duct is shown in Figure 6.1. In the rotating case with no buoyancy effects (Bo = 0.00), the peak velocity is skewed towards the leading wall, but as Bo increases and the reverse flow region at the leading wall gains strength, the maximum velocity is pushed towards the trailing wall to compensate for the reversed flow.

The change in the recirculation zones downstream of the ribs is another important characteristic of buoyancy changes. The effect of rotation has a stabilizing and destabilizing effect on the leading and trailing walls, respectively.

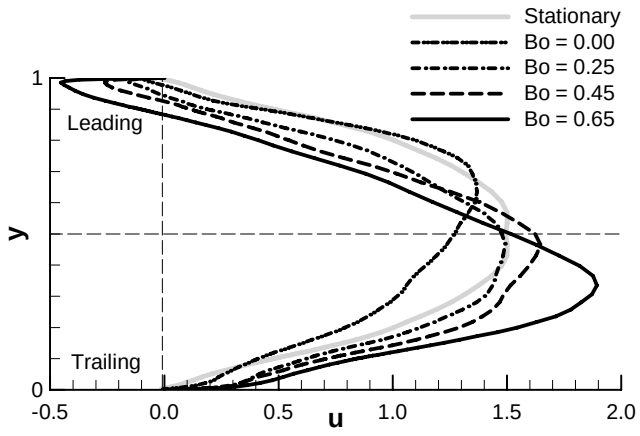

Figure 6.1. The mean velocity profiles along a vertical line between Ribs 8 & 9 in the symmetry plane show the effect of buoyancy on the streamwise velocity. Increasing the buoyancy parameter causes the profile to shift towards the trailing wall.

As fluid is forced away from the leading wall, the turbulence along that wall is decreased while the turbulence along the trailing wall is increased. As the buoyancy parameter increases, the trailing wall reattachment lengths approach a constant value of approximately 4.0 rib heights from the rib center. On the leading side, the only case in which flow reattaches to the wall downstream of every rib is at Bo = 0.00. At Bo= 0.25, the recirculation regions which form behind and in front of each rib start merging together as shown in Figure 6.2. At the two highest buoyancy parameters, a near-continuous recirculating zone extends throughout the cooling duct at the leading wall, which gathers strength as the flow moves into the duct. On the other hand, at the trailing wall, the recirculation zones do not experience large changes with the increase in buoyancy. These observations agree with the fully developed calculations of Abdel-Wahab and Tafti (2004); at low buoyancy parameters (Bo < 0.3), they reported an increase in the recirculation regions at the leading wall with no or little change at the trailing wall.

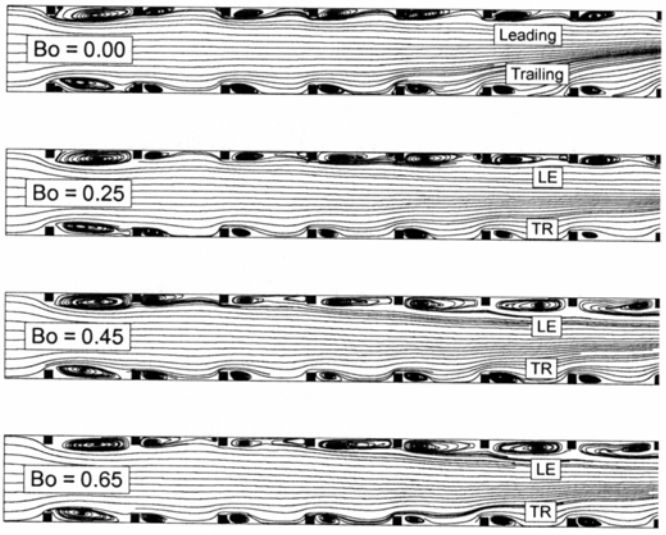

Figure 6.2. Streamlines in the symmetry plane of the ducts for buoyancy parameters of 0.00, 0.25, 0.45, and 0.65 show the increase in the sizes of the leading wall recirculation zones with the increase in buoyancy parameter, while the trailing wall recirculation zones maintain similar sizes.

A close-up of the streamlines on the leading wall between the seventh and eight ribs is shown in Figure 6.3. In the case with no buoyancy, flow reattaches to the leading wall between the two ribs, but with Bo = 0.25, the recirculation zone behind Rib 7 and the recirculation zone upstream of Rib 8 bridge together, not allowing any flow to attach to the leading wall. In the two highest buoyancy cases, the two zones merge into a single large recirculating zone. The vertical size of the recirculation zones is also important to note. In Figure 6.3(a), the recirculation zones are entirely below the shear layers formed above the ribs. When Bo = 0.25, the recirculation zone begins to enlarge, stretching towards the mainstream. Once the two recirculation zones merge, the size becomes much larger. When Bo = 0.45 (Figure 6.3(c)), the height of the recirculation zone is more than twice the height of the ribs, affecting channel flow at y = 0.8 that was not directly affected by recirculation zones at lower buoyancy parameters. At the highest buoyancy parameter, Bo = 0.65, the recirculation zone is approximately 2.5 times larger than the rib height.

More critical to the heat transfer is a close examination of the streamlines. At Bo=0.0 (Figure 6.3(a)), fluid from the center of the duct (free-stream) is directed towards the leading wall in the reattachment region. This is usually the region where heat transfer augmentation is higher than the rest of the leading wall surface. At Bo=0.25, the merging of the two recirculation regions blocks free-stream fluid from reaching the vicinity of the wall. However, an important change takes place in the structure of the recirculating zone as the buoyancy parameter increases further. At high buoyancy, as the recirculating zones get bigger, they draw in fluid from the center of the duct to the wall just upstream of the rib. This can be clearly observed in the streamline pattern upstream of the rib. As will be shown later this has consequences on heat transfer augmentation.

6.02 Turbulence in the Developing Flow Region

In addition to drawing in fluid from the duct center, the recirculating regions at the leading wall at the higher buoyancy parameters are highly energetic and unsteady compared to their low buoyancy counterparts. A vertical profile of turbulent kinetic energy between Rib 7 and Rib 8 in Figure 6.4 shows the increased turbulence near the trailing wall. The turbulence level of the fluid near the wall reaches magnitudes of 11%, 17%, 22%, and 26% for buoyancy parameters of 0.00, 0.25, 0.45, and 0.65, respectively. The turbulent kinetic energy of the fluid near the leading wall does not increase significantly, remaining at values less than 4%, indicating that turbulence near the wall is not a major contributor to the heat transfer. In the separated shear layer at the trailing wall, the turbulence reaches as high as 30%. The unexpected trend is in the increase in turbulent kinetic energy at $y = 0.7$, near the leading side of the duct.

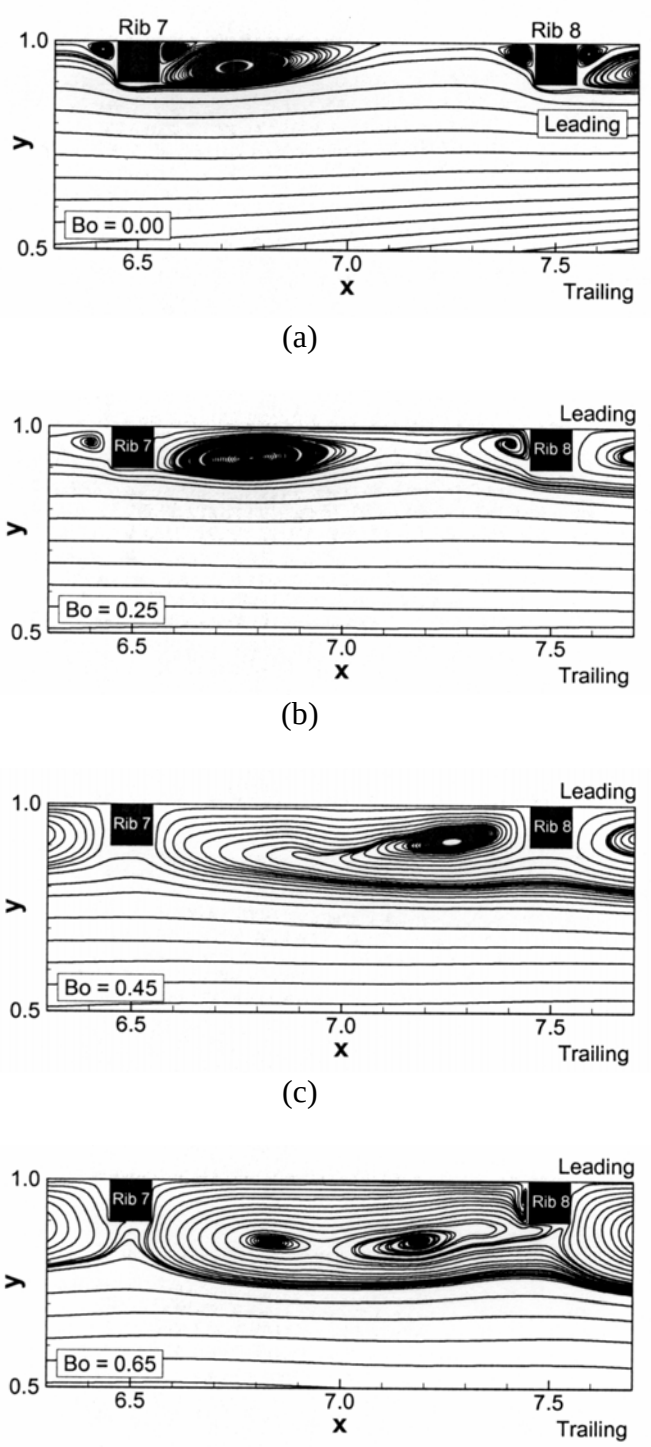

Figure 6.3. Close-up views of the leading wall recirculating zones for all four cases show the change from reattaching flow for Bo = 0.00 to no reattachment when Bo = 0.65. Eventually the two recirculation zones merge to form a single large recirculation zone between the two ribs.

This is a result of an energetic shear layer forming between the growing recirculation zones and the mainstream flow. In the two cases with low buoyancy (Bo = 0.00 & 0.25), the peak is at rib height with a magnitude of 8%, but in the high buoyancy cases (Bo = 0.45 & 0.65) TKE increases to a value of 22% at Bo=0.65, with the peak being closer to the channel center.

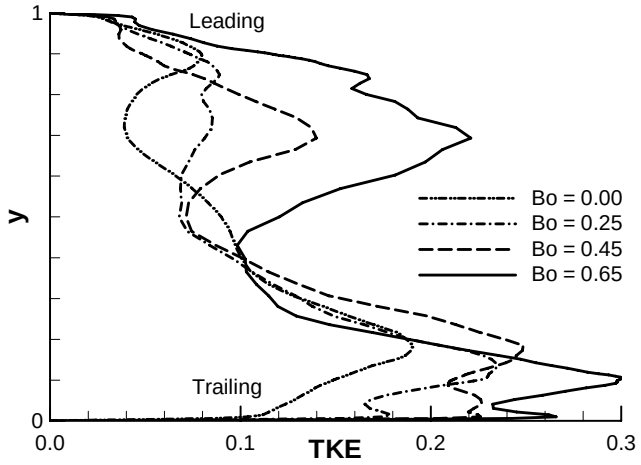

Figure 6.4. A vertical profile of turbulent kinetic energy in the symmetry plane (z = 0.5) directly between Rib 7 and Rib 8 shows the increase of turbulence on both the leading and trailing sides of the duct with an increase in buoyancy. The peak turbulence on the leading side occurs at the interface between the recirculation zones and streamwise flow, not at the rib height, as on the trailing side.

Figure 6.5 shows the normal turbulent stresses in the symmetry plane at a vertical location of y = 0.75 (¼ of the channel height away from the leading wall). A steady increase in turbulence is observed with an increase in buoyancy in all cases. In the low buoyancy cases (Bo = 0.00 & 0.25), the smooth curves indicate that the shear from the ribs does not reach this height in the duct. With high buoyancy (Bo = 0.45 & Bo = 0.65), however, the high turbulence results from the shear layer between the recirculation zones and mainstream flow.

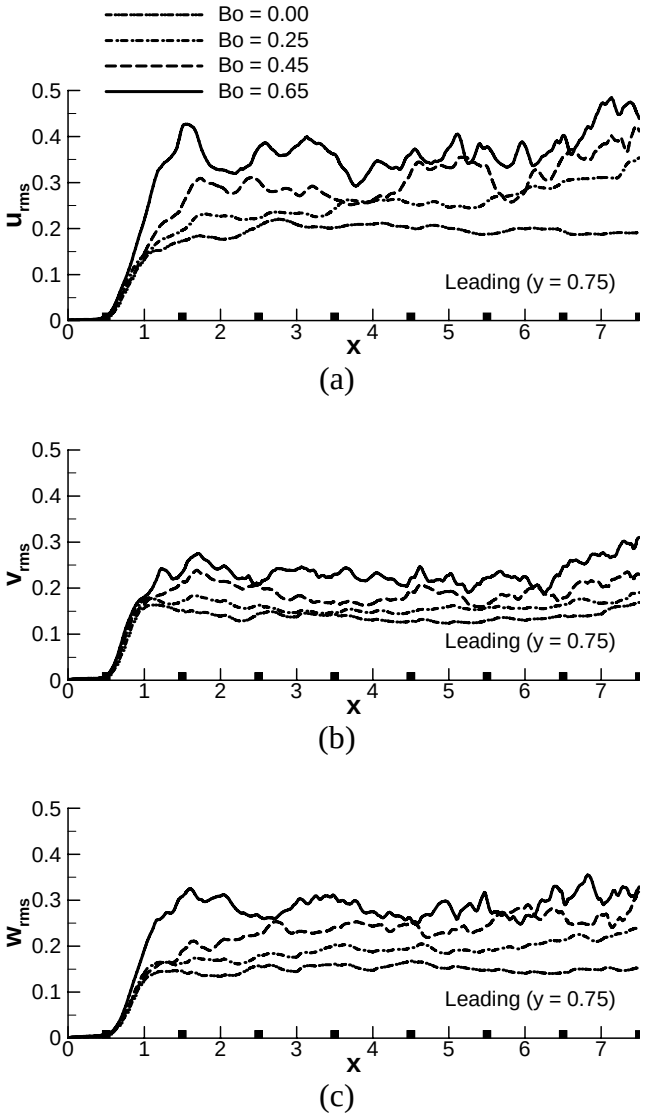

Figure 6.5. Individual turbulence quantities near the leading side show the increase in turbulence corresponding to an increase in buoyancy. The curves also become more jagged as the flow becomes more turbulent.

6.03 Heat Transfer in the Developing Flow Region

Figure 6.6 shows heat transfer augmentation contours on the leading wall for the four buoyancy parameters. The recirculation zones between the ribs have a significant effect on the mainstream flow. In the first two cases (Bo = 0.00 & 0.25), streamlines injected at rib height simply pass over the ribs, while in the higher buoyancy cases (Bo = 0.45 & 0.65), much of the

flow is entrained into the recirculation zone, which increases the heat transfer augmentation immediately upstream of the ribs because of impingement from the cooler mainstream fluid.

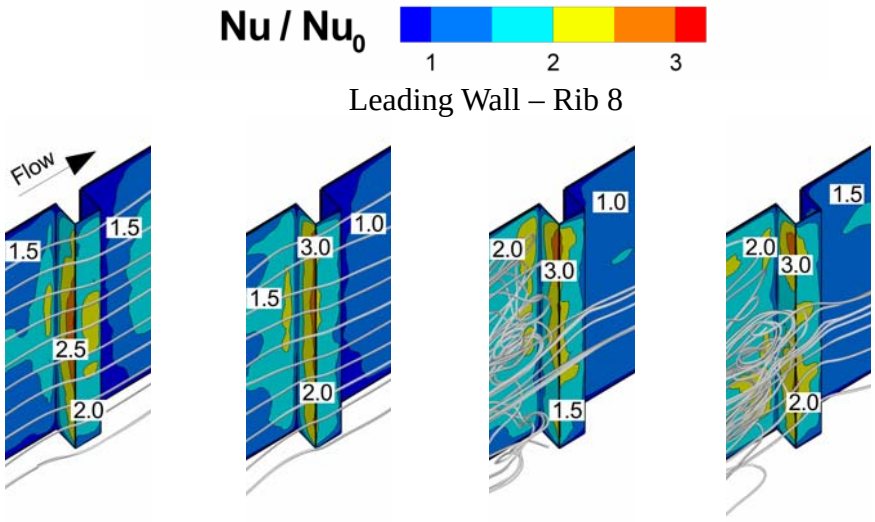

Figure 6.6. Streamlines injected upstream of Rib 8 in the four buoyancy cases of (a) Bo = 0.00, (b) Bo = 0.25, (c) Bo = 0.45, and (d) Bo = 0.65 show the different effects the recirculation zones have on the mainstream flow. The heat transfer augmentation (contours) shows the consistently increasing heat transfer upstream of the rib, and the mainstream flow is entrained in the recirculation zones beyond Bo = 0.45.

In Figure 6.7, the heat transfer augmentation contours on the leading wall are shown for the four different buoyancy parameters. In all cases, the heat transfer is highest near the duct inlet and decreases downstream. In the case with no buoyancy, the peak heat transfer augmentation is observed directly between two ribs and is the result of reattachment of the separated flow from the ribs. As the buoyancy parameter is increased and the flow fails to reattach, the heat transfer augmentation decreases in this area. Conversely, as the recirculation zones upstream and downstream of the ribs begin to merge, a region of high heat transfer augmentation immediately upstream of the ribs begins to grow as mainstream flow is entrained into the recirculation zones.

At Bo=0.00 & 0.25, there is a steady decrease in augmentation as the flow moves into the duct. As the buoyancy parameter increases further and the recirculation zones become large and extend all the way through the duct, the separated shear layer now impinges on the downstream rib and is redirected towards the wall. The combined effect of impingement, high turbulent fluctuations, and cold fluid from the center of the duct steadily increases the augmentation ratio in this region.

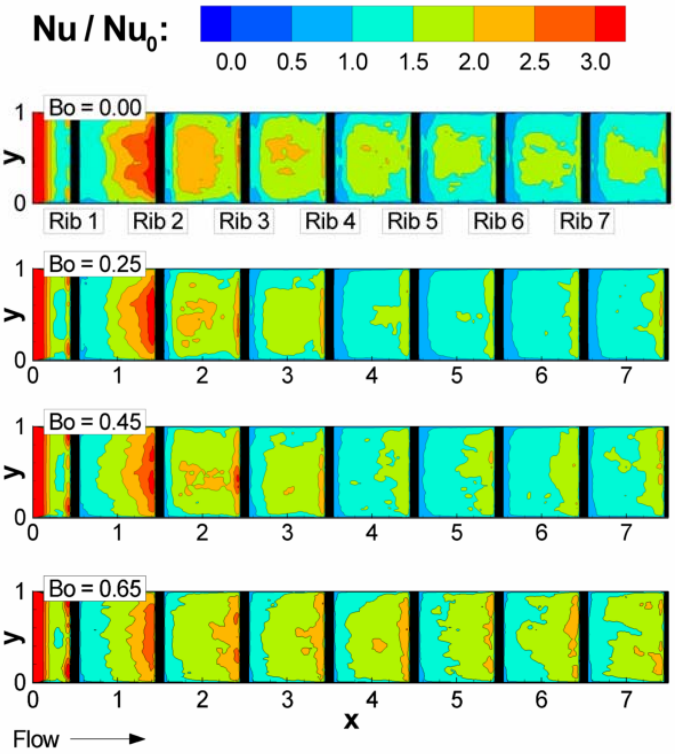

Figure 6.7. Heat transfer augmentation contours on the leading wall show the shift in peak heat transfer from an area between the ribs to the area immediately upstream of the ribs, resulting in an initial decrease in overall heat transfer, followed by an increase.

The rib-averaged values of heat transfer are shown for both the leading and trailing walls in Figure 6.8(a), and a close-up of the values on the leading wall is plotted in Figure 6.8(b). On the trailing side, the heat transfer shows a consistent increase as flow moves through the duct and as

the buoyancy parameter is increased. The leading wall heat transfer shows a decrease in heat transfer between the case with no buoyancy and that with a buoyancy parameter of 0.25. At the higher buoyancy parameters, however, the heat transfer augmentation on the leading wall increases. The increase in heat transfer augmentation is largest between the two highest buoyancy parameters (Bo = 0.45 & 0.65).

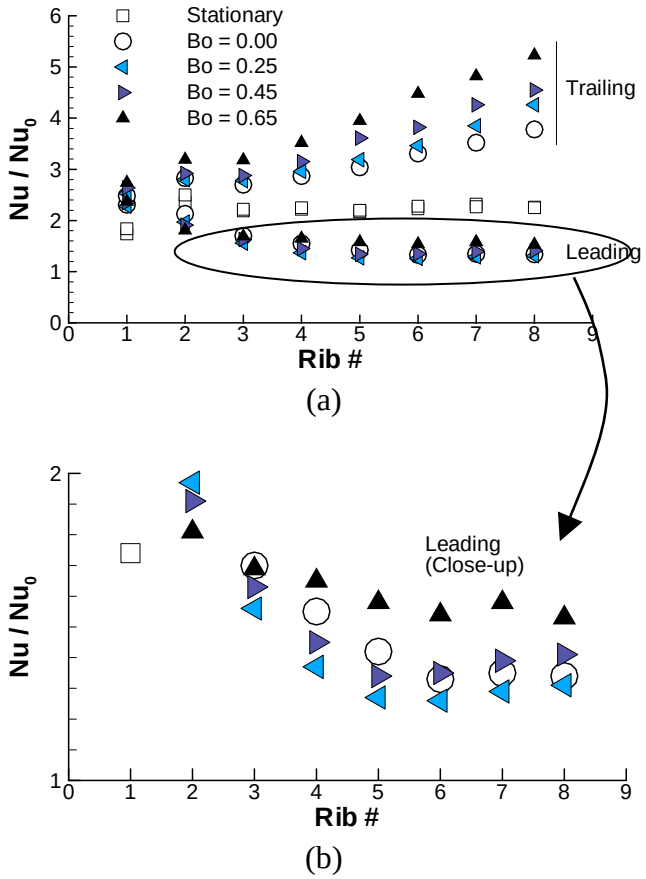

Figure 6.8. The rib-averaged heat transfer augmentation on (a) the leading and trailing walls and (b) a close-up of the leading wall heat transfer shows the consistent increase in trailing wall heat transfer with buoyancy and initial decrease in leading wall heat transfer at the low buoyancy parameters, followed by an increase.

In Figure 6.9, the rib-average heat transfer is plotted for the smooth side walls. In this case, no change is shown in the side wall heat transfer over the first rib because that region is dominated solely by Coriolis forces. Buoyancy effects begin to take effect at and beyond the second rib. The heat transfer increases steadily as flow moves through the duct and as the buoyancy parameter is increased.

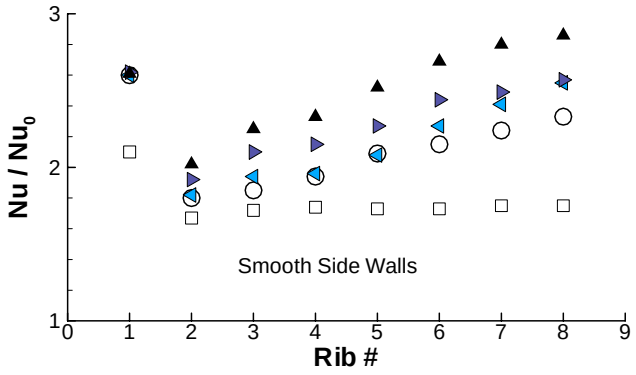

Figure 6.9. Side wall heat transfer augmentation shows an increase in heat transfer augmentation corresponding to the increase in the buoyancy parameter and streamwise position. This is primarily a result of stronger secondary flows induced by buoyancy forces.

To compare with Wagner's (1992) fully developed results, the average heat transfer augmentation over Ribs 7 & 8 was used. This comparison is shown in Figure 6.10. The test section in Wagner's experiments was similar to those of the present study, and a number of previous experiments in stationary (Sewall et al., 2005; Han, 1988; Fann et al., 1994) and rotating (Taslim et al., 1991) ducts have shown only a weak dependence on Reynolds number (Re = 25,000 in the experiments) when the normalized heat transfer is considered. In addition to the experiments, previous LES computations are included from a fully developed stationary calculation (Tafti, 2005) and a fully developed rotating calculation with varying buoyancy effects

(Abdel-Wahab and Tafti, 2004). The other experimental studies showing a shift in heat transfer trends due to changes in buoyancy are not shown because (El-Husayni et al., 1994) has angled ribs and therefore very different flow properties and (Chang and Morris, 2003) only has five ribs and would not compare well with data from the Rib 7 & Rib 8 (current study) or Ribs 8 – 11 (Wagner et al., 1992). In the fully developed rotating calculations (Abdel-Wahab and Tafti, 2004), the highest buoyancy parameter used was near Bo = 0.3, which was not high enough to capture the heat transfer increase between two calculations at higher buoyancy parameters.

At buoyancy parameters smaller than 0.3, the average heat transfer augmentation changed very little, decreasing slightly, with increases in buoyancy. At Bo > 0.3, however, the heat transfer augmentation increased steadily. This increase is larger than the initial decrease observed at the low buoyancy parameters, quickly surpassing the initial heat transfer at Bo = 0.00, resulting only from Coriolis forces.

6.04 Friction Factor in the Developing Flow Region

Friction factors are calculated for each individual rib by calculating the area averaged pressure drop across a pitch surrounding the rib (Figure 6.11). The calculation of the friction factor does not include the effects of centrifugal pumping, which would depend on the radius from the rotation axis. When this effect is not included the friction factor increases with the buoyancy parameter. The large positive and negative values at Ribs 1 and 2 are due to entrance effects and the large recirculation regions which form behind Rib 1 and the subsequent pressure recovery at Rib 2. Abdel-Wahab and Tafti (2004) noted that the form drag on the trailing wall accounted for about two-thirds of the overall pressure losses in the duct.

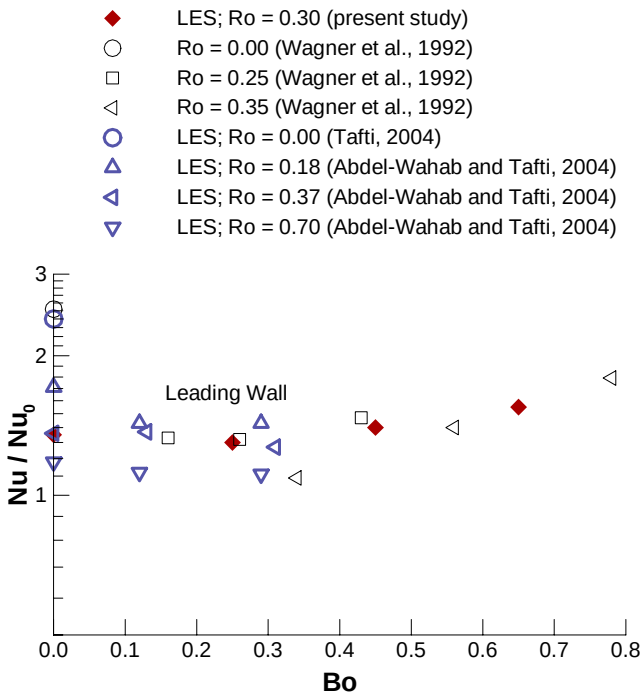

Figure 6.10. The fully developed heat transfer augmentation is compared with previous LES calculations (Tafti, 2005; Abdel-Wahab, 2004) and the experiments of Wagner et al. (1992). The agreement with experiments is very good, and both the experiments and calculations show the trend of decreasing heat transfer up to a buoyancy parameter of 0.3, followed by an increase at higher buoyancy parameters.

Since the flow structures remain fairly constant on this side of the duct, most of the increase in the friction factor is expected to come from the increase in form and friction drag at the leading wall as the recirculating regions become larger and stronger with the increase in buoyancy.

The results are consistent with an LES study by Abdel-Wahab and Tafti(2004), which showed an increase in friction factor with an increase in buoyancy at three different rotation numbers (Ro = 0.18, 0.35, & 0.70) and three different buoyancy parameters for each rotation number (Bo = 0.00, 0.12, & 0.30). They are also consistent with what has been reported in (Murata and Mochizuki, 2004), where an increase in buoyancy brought about an increase in friction factor in

the first pass of a straight ribbed duct at Re = 5,000 and low buoyancy parameters (Bo = 0.00, 0.15, 0.23, and 0.34).

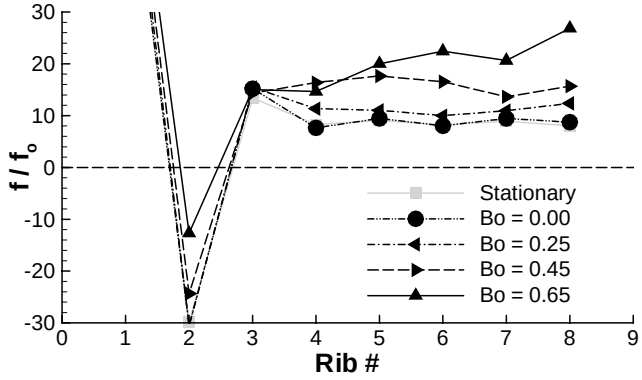

Figure 6.11. The friction factor augmentation for the stationary ribbed case and the four buoyancy cases shows an increase in friction as buoyancy increases, where the highest buoyancy parameter reaches values approximately twice those of the zero buoyancy case.

6.05 Mean Flow in the 180^o Bend

Comparisons in this section are made among four cases. The first is a stationary case with no rotation, while the case 2 is a rotating case with only Coriolis effects and no centrifugal buoyancy. The last two cases, case 3 and case 4 both have Coriolis and buoyancy forces included in the calculations, with case 3 being considered as the "low buoyancy" case and case 4 considered as the "high buoyancy case." The previous chapter described Coriolis effects as they relate to flow in the bend. The most significant results were that rotation improved flow turning in the bend, thus reducing impingement heat transfer on the back wall and downstream outside wall. In both cases, averaged turbulent kinetic energy was increased in the bend. However, with rotation, the increase in turbulence was not as high as it was in the stationary case. The focus of

this section will be to explain the effect of buoyancy forces, and comparisons with the zero buoyancy and stationary cases will be presented where relevant.

A comparison of all four cases is shown through a series of streamline plots at the mid-height of the duct in Figure 6.12. Increasing the buoyancy parameter shifts the separation vortex at the tip of the dividing wall towards the trailing wall. A further increase in buoyancy also causes this structure to separate from the dividing wall, as shown in Figure 6.12(d), where the vortex has separated from the wall and moved to the middle of the flow, between the dividing wall and back wall, decreasing the flow area and accelerating the mainstream flow around the outside of the bend. Due to this accelerated flow, the vortex in the downstream corner of the bend completely disappears in the high buoyancy case.

The streamwise velocity in the bend is compared between the cases with buoyancy effects at three locations in the bend in Figure 6.13. The first plane, labeled "upstream" is immediately downstream of the last rib in the upstream duct and shows the streamwise velocity, u, entering the bend. The midplane streamwise velocity, w, shows regions of recirculation back towards the upstream side of the bend, and the downstream plane shows the distribution of velocity exiting the bend. In all three cases, the positive value represents flow in the streamwise direction, while the negative value indicates recirculation. Upstream of the bend, buoyancy significantly skews the velocity profile towards the trailing wall, as was shown in earlier calculations in Sewall and Tafti (2004). This high velocity is shown in Figure 6.13(b), where the peak velocity entering the bend is shifted towards the trailing rib and has a larger magnitude than that in the low buoyancy case.

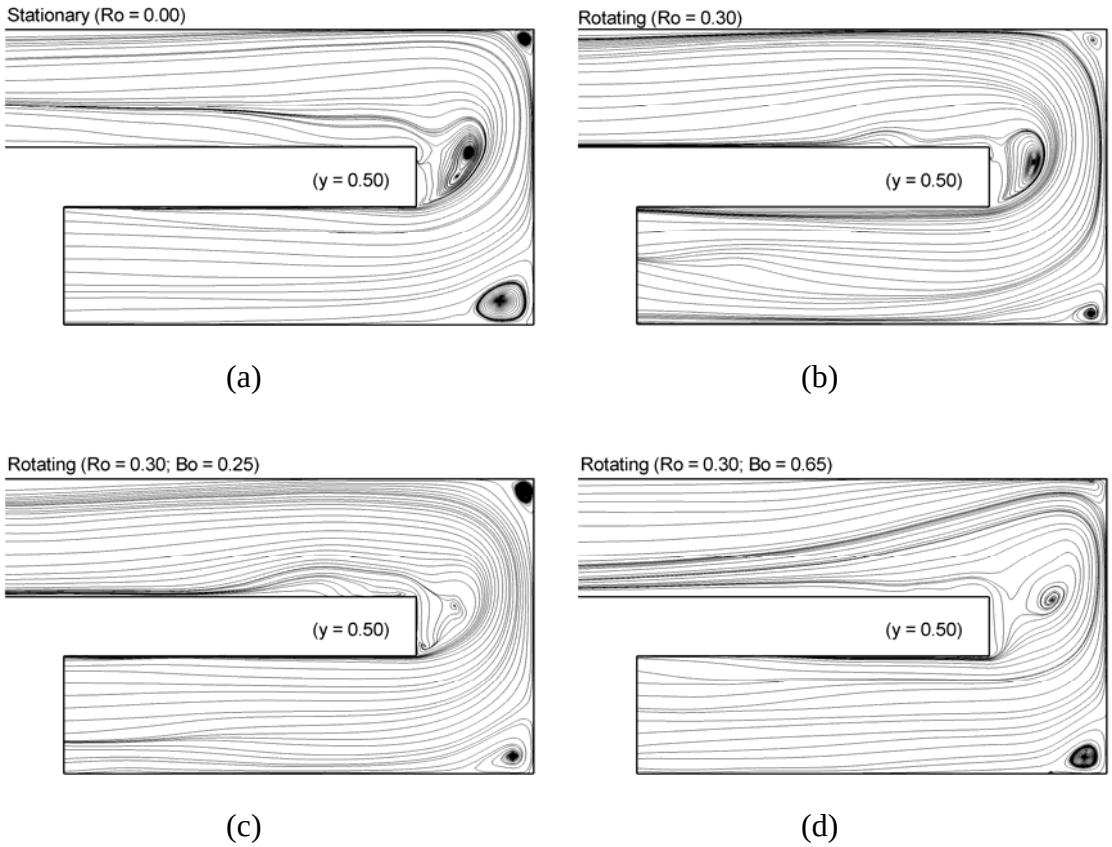

Figure 6.12. A comparison of streamlines at the mid-height of the duct (y = 0.5) among difference buoyancy numbers shows that increasing the buoyancy number increases the size of the vortex at the diving wall until it separates away from the wall and moves into the mainstream flow, accelerating the flow and eliminating the downstream recirculation zone.

In the midplane, shown in Figure 6.13(c) and (d), the dark circular region represents the recirculation of separated flow from the vertical dividing wall. With low buoyancy, the bubble is formed on the trailing side near the dividing wall, but increasing the buoyancy parameter causes the bubble to separate completely from the dividing wall and move upwards in the middle of the duct towards the leading wall. In both of these cases, the recirculation bubble stretches past the horizontal midpoint of the duct (x = 3.5), forcing the mainstream flow further towards the back

wall. The peak streamwise velocity in the midplane for both cases is shown near the back wall on the leading and trailing sides.

Downstream, the peak velocity regions are concentrated near the outside wall. The low buoyancy case has the same velocity profile at the mid-height as the stationary calculation. Contour values show that increasing buoyancy increases the streamwise velocity along the horizontal line at the mid-height, but the velocity is also decreased along the inside half of the trailing wall.

Figure 6.14 shows a comparison of the secondary flows in the bend. The stationary duct, Figure 6.14(a), shows the familiar Dean vortices commonly found in a 180º bend, both with smooth walls and with ribs. Coriolis effects are shown in Figure 6.14(b) to decrease the magnitude of spanwise velocity directed towards the back wall. A second characteristic of the Coriolis effects is the shift in vertical stagnation, where the vertical velocity is zero along the back wall. In the stationary case, it is at the midpoint of the back wall because of symmetry, and with rotation the stagnation point was moved towards the leading wall (y = 0.61). This point is moved towards the trailing wall when buoyancy effects are considered. Buoyancy also changes the size and location of the circulation zones. Figure 6.14(c) shows a much stronger leading wall vortex, which increases impingement on the leading side of the dividing wall and decreases impingement on the trailing side. The stagnation point on the back wall is very close to the trailing wall in this case (y = 0.08), and in the high buoyancy case the stagnation point moves closer to the center of the duct again (y = 0.33) because the trailing wall vortex strengthens and shifts towards the back wall. The secondary motion in the high buoyancy case is dominated by the large vortex near the center of the midplane.

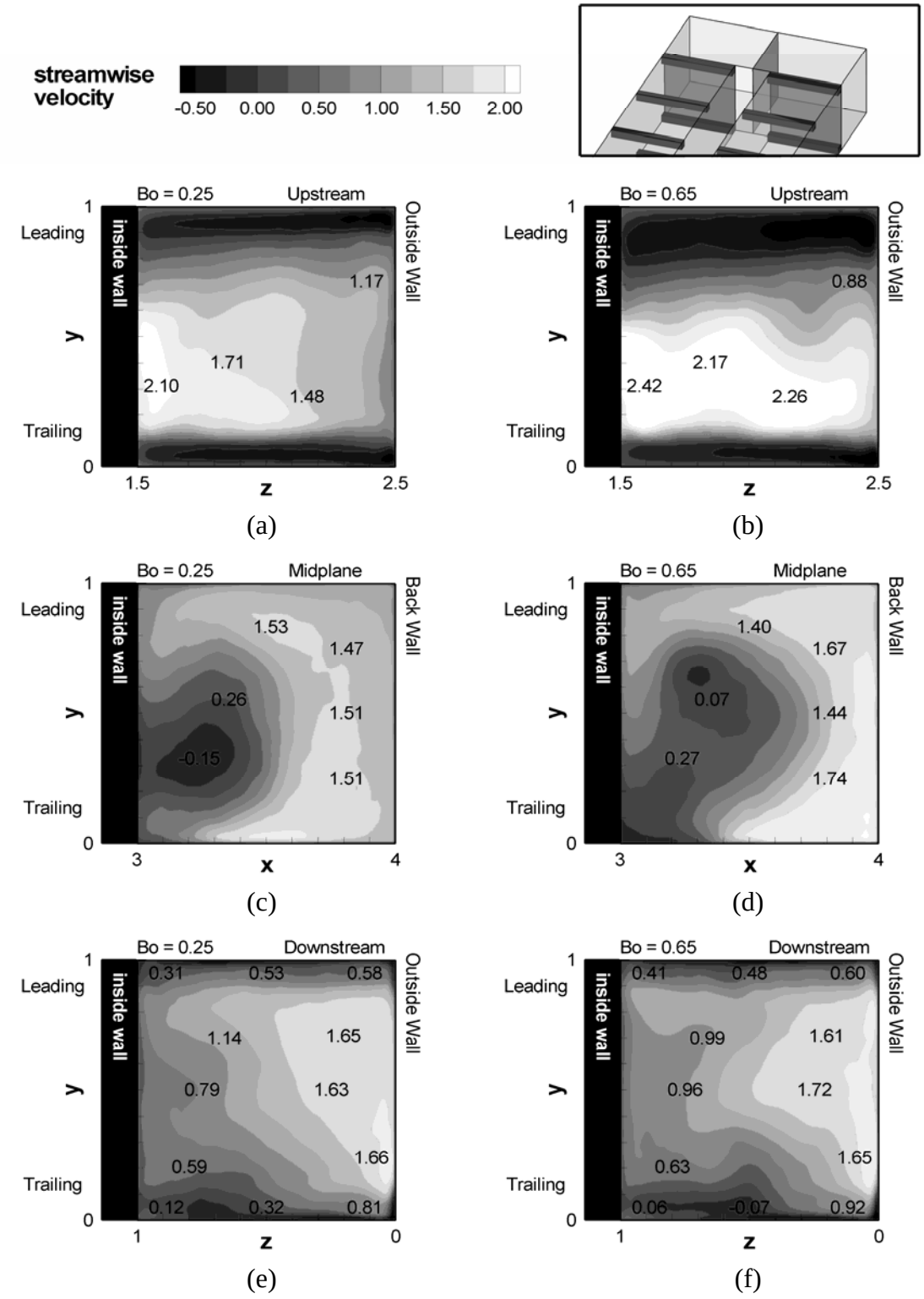

Figure 6.13. The streamwise velocity in three different cross-sections in the bend is compared between the low buoyancy case (left) and the high buoyancy case (right). The separated recirculation vortex is clearly seen at the midplane of the bend in the high buoyancy case.

As shown in Figure 6.14(d), the large vortex increases the magnitude of the velocity directed towards all four walls, which would be expected to increase the heat transfer augmentation on the walls.

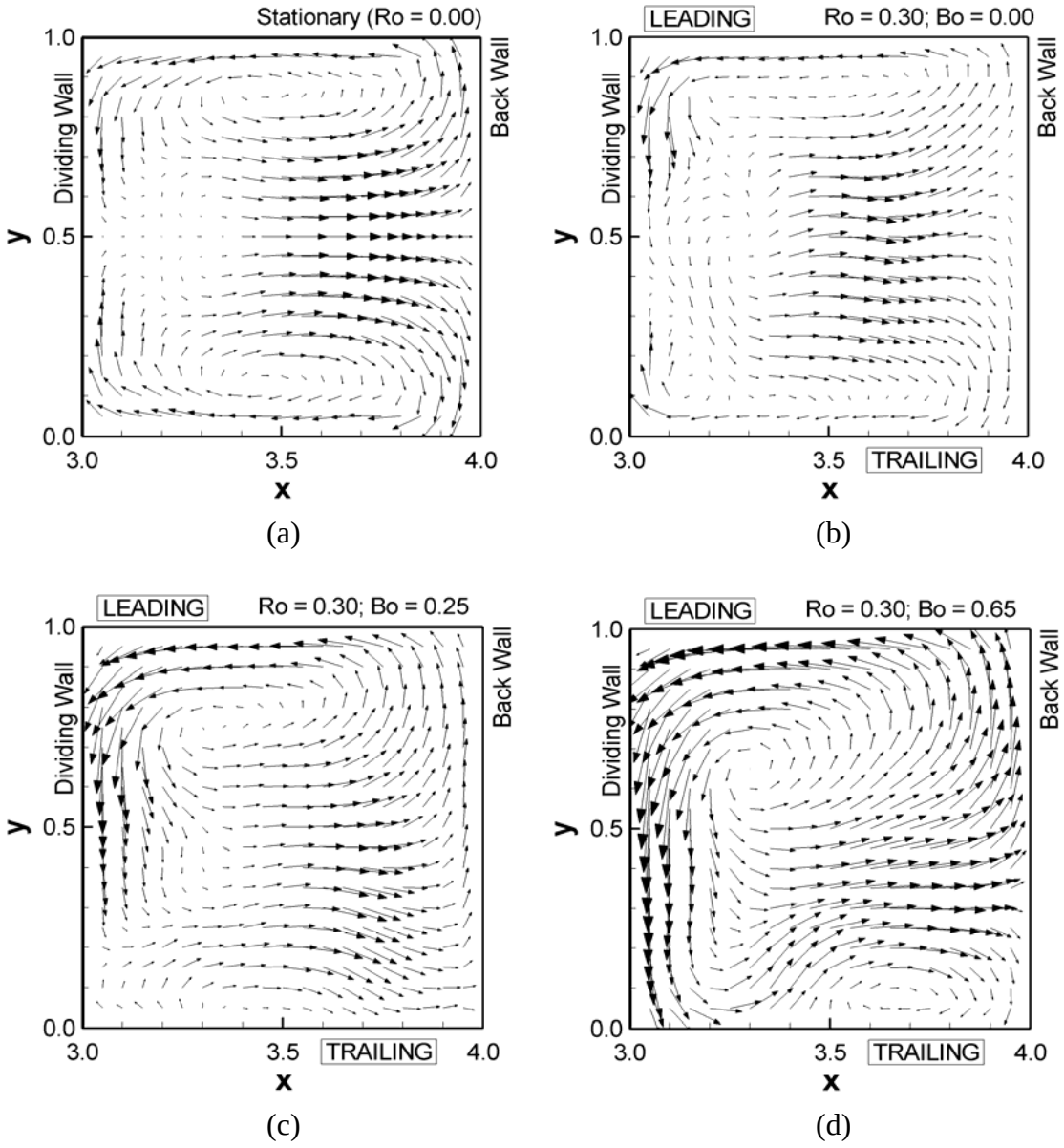

Figure 6.14. Velocity vectors in the midplane of the bend are compared among the (a) stationary case, (b) rotating case with Coriolis effects, (c) rotating case with low buoyancy, and (d) rotating case with high buoyancy. Increasing buoyancy enlarges the leading wall vortex and shifts it towards the dividing wall.

A quantitative comparison of the secondary flows in the bend midplane is plotted in Figure 6.15, where a series of horizontal velocity profiles is compared among the four cases near the leading and trailing walls, about 1 rib height away from each wall (y = 0.125 and 0.875). The spanwise velocity, u (which is the streamwise velocity upstream), shows the shift of the large vortex in towards the leading wall with increased buoyancy, as evidenced by the increased velocity directed towards the dividing wall. On the leading wall, buoyancy increases the magnitude of the profile in the negative direction, which describes a strong spanwise motion towards the dividing wall. Both the stationary and zero buoyancy rotation cases show minimal values of spanwise velocity along this line because the vortices in these cases are smaller and the profile passes directly through their centers. Near the trailing wall, an increase in velocity directed towards the back wall shows that the trailing wall vortex is compressed towards the trailing wall. As a result, the spanwise profile at y = 0.125 increases as the vortex center moves below that line. The peak spanwise velocity in the low buoyancy case is near the back wall, where the enlarged leading wall vortex and small trailing wall vortex direct the maximum spanwise velocity to this location. The peak spanwise velocity in the high buoyancy case is located near the dividing wall, where the more dominant leading wall vortex has further decreased the flow area, accelerating fluid directed towards the back wall.

Figure 6.15(b) shows the vertical component of velocity near the leading and trailing walls. Though few differences are observed near the leading wall, the trailing side high buoyancy case shows a region of strong impingement on the trailing wall, followed by a strong upwash region where fluid is ejected back towards the centerline. The plot of spanwise velocity, u, showed that buoyancy caused fluid to be swept across the trailing wall towards the back wall.

The streamwise flow, shown in Figure 6.15(c), also shows few differences near the leading wall, though the large vortex near the leading wall in the high buoyancy case does accelerate the flow slightly. The low trailing wall streamwise velocity near the dividing wall indicates that the flow is almost entirely directed in the spanwise and cross-stream directions. As stated earlier, the enlarged vortex decreases the flow area and accelerates the flow along the outside wall in the high buoyancy case.

Whereas turbulence is usually responsible for high heat transfer, flow impingement due to secondary flows and convective mean velocity was found by Liou et al. (2000) to be primarily responsible for the heat transfer augmentation on the back wall of the bend and the downstream outside wall. Therefore, the streamwise velocity directed towards the back wall of the bend is shown in Figure 6.16 for all four cases in a plane located 1 rib height away from the wall (x = 3.9). With no rotation, the impingement region is symmetric about the mid-height, but with rotation, Coriolis effects skew the velocity profile towards the leading wall, resulting in a peak impingement closer to the leading wall. The increased trailing wall momentum due to buoyancy causes the velocity profile to be shifted back towards the trailing wall in Figure 6.16(c), but the velocity magnitude is small and concentrated near the trailing wall corner. Neither the rotating case nor the low buoyancy case shows impingement velocities as strong as those in the stationary case. With a much higher buoyancy parameter, streamwise momentum entering the bend is highly concentrated near the trailing wall, and the large secondary flow vortex in the bend impedes flow turning. The result is a highly concentrated streamwise velocity (w) directed towards the back wall, with a peak value that is 20% higher than the peak velocity in the stationary case and nearly 50% higher than the other two rotating cases. The flow is then swept downstream along the back wall at a much higher velocity than in the other cases.

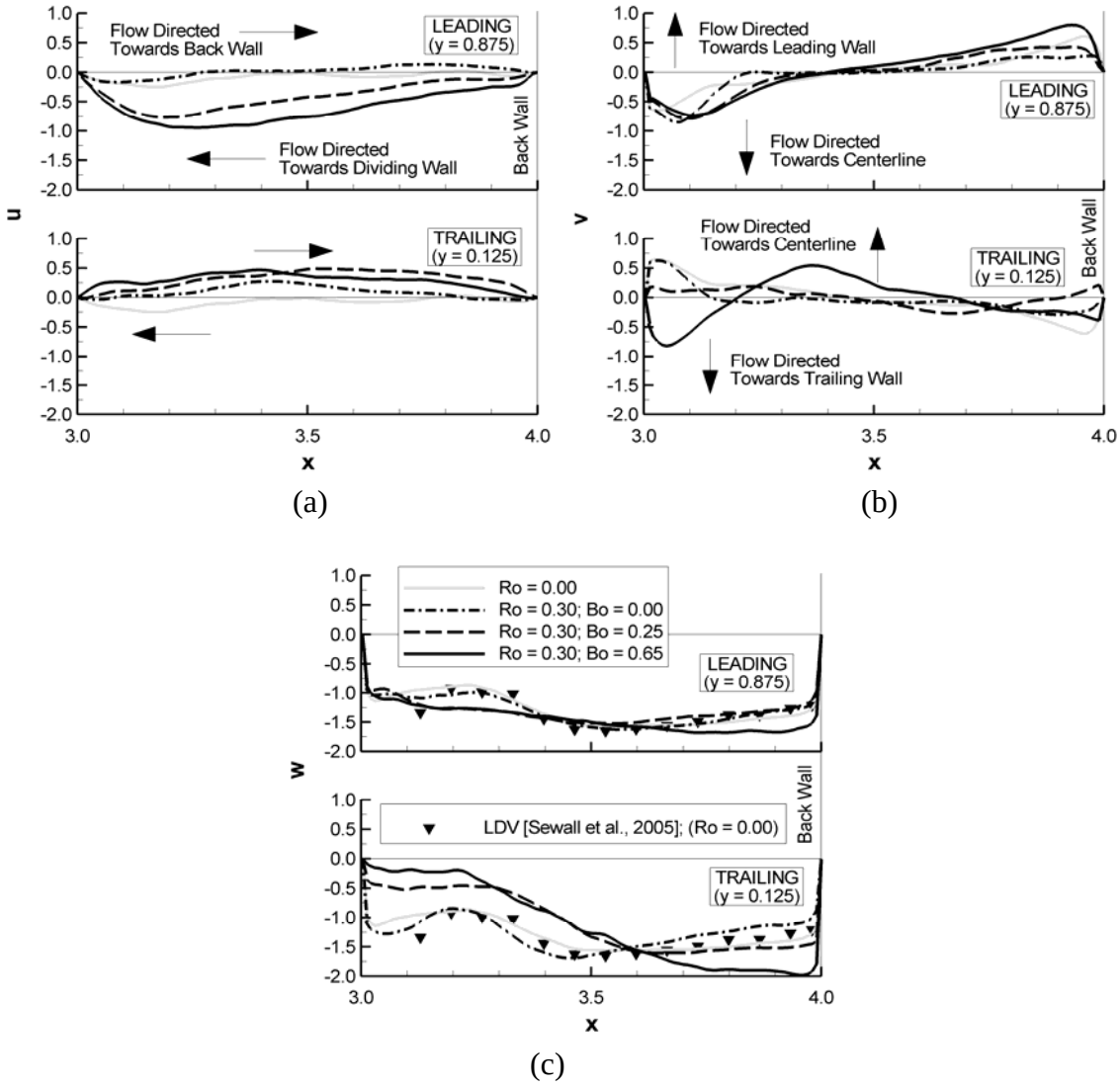

Figure 6.15. The three velocity components along a horizontal line near the leading and trailing walls of the midplane show the velocity shifts that take place with buoyancy in the flow. At Bo = 0.65, an enlarged vortex near the leading wall increases impingement flow on the walls and accelerates mainstream flow around it.

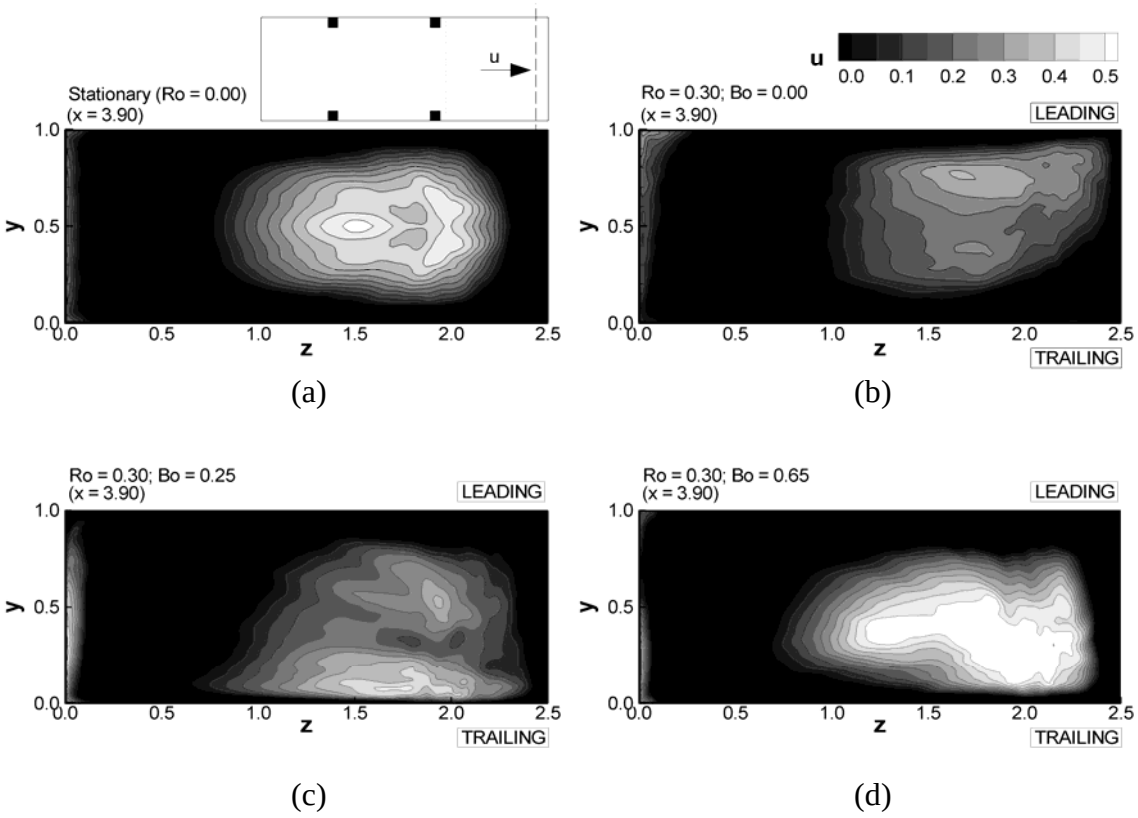

Figure 6.16. The upstream duct streamwise velocity, u, is shown 1 rib height upstream of the back wall in the bend (x = 3.9) for all four cases and shows the impingement on the back wall for each case.

6.06 Turbulent Quantities in the 180º Bend

Turbulent kinetic energy in three planes in the bend is shown through a series of contour plots in Figure 6.17, in which the low and high buoyancy cases are compared. The turbulence entering the bend is higher along the trailing wall than the leading wall due to turbulence destabilization from Coriolis and buoyancy effects, and the magnitude of turbulence is higher in the high buoyancy case than in the low buoyancy case. Leading wall turbulence is higher in the high buoyancy case because of increased shear between the mainstream flow and the

recirculation zones that are formed from the separated flow between the ribs (Sewall and Tafti, 2004).

In the midplane, a large region of high turbulence, reaching values over 60%, is observed at the mid-height near the dividing wall. Based on the secondary flow vectors in Figure 6.14, this region corresponds to a strengthened downwash region formed from enlargement of the leading wall vortex. At high buoyancy, where the recirculation zone has stretched to the middle of the duct, the turbulence is found to be more uniform in the center of the duct, with lower values near the walls.

In both cases, the outlet of the bend at the third plane (bottom of Figure 6.17) shows higher turbulence along the inside wall. The low buoyancy case shows a circular region of high turbulence (TKE = 41%) near the leading wall along the outside that is not present in the high buoyancy case (TKE = 14%), and this is most likely not observed in the high buoyancy case because of the increased momentum along the outside of the duct, decreasing the fluctuations along the outside wall. Exiting the bend, the turbulence between the two cases is similar, with the exception of the area near the leading wall, where turbulence in the low buoyancy case is higher near the inside wall and a high turbulence region at high buoyancy has moved closer to the middle of the duct.

Turbulence quantities are shown quantitatively in the midplane of the duct for all four cases to illustrate the differences of buoyancy effects on the leading and trailing walls. The plots are illustrated in Figure 6.18. For each value plotted, two profiles are shown. The top profile is plotted along a line near the leading wall (y = 0.875), and the bottom profile represents a line near the trailing wall (y = 0.125). The overall turbulent kinetic energy is attenuated with Coriolis effects on the leading wall, as Figure 6.18(a) shows.

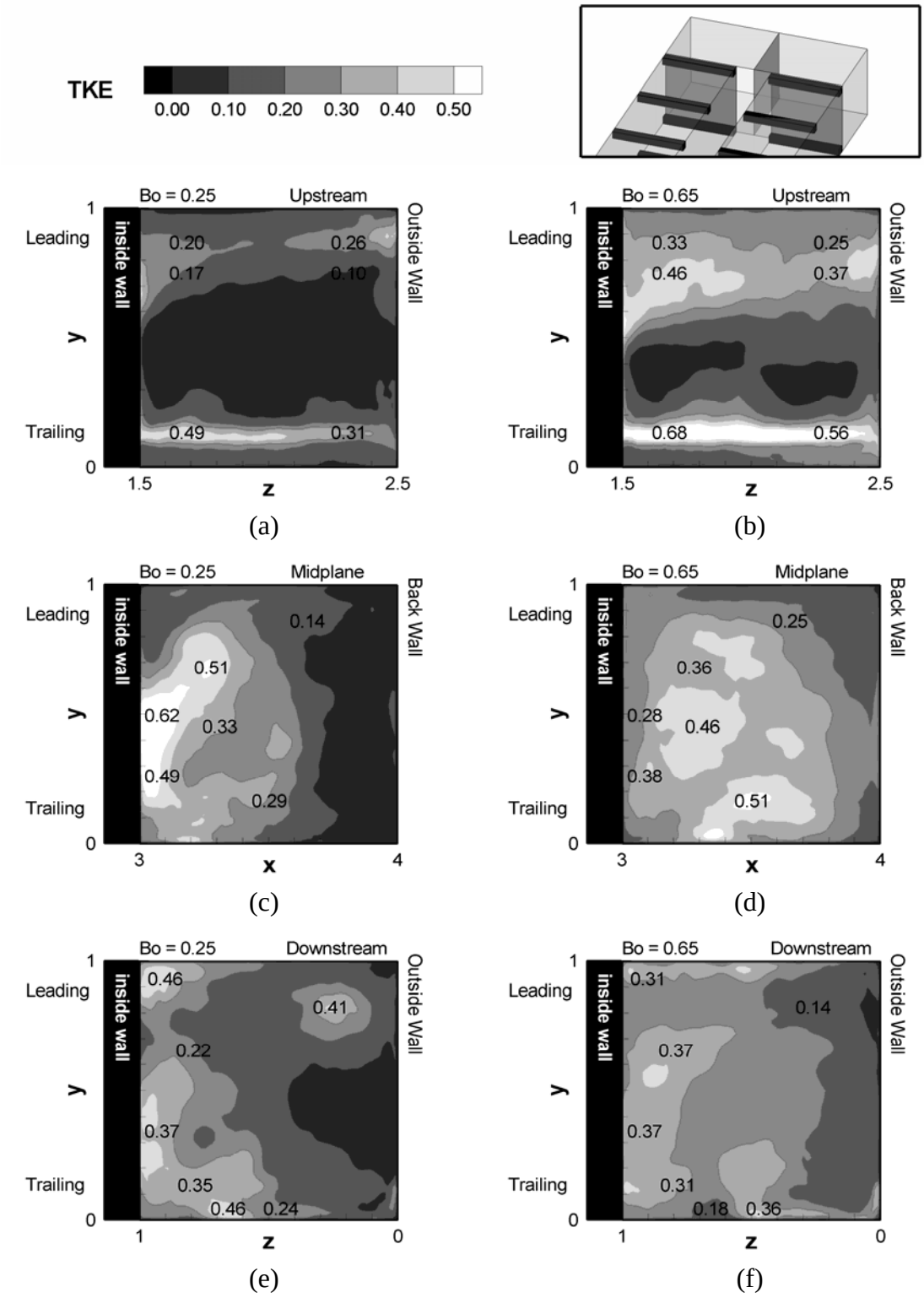

Figure 6.17. Turbulent kinetic energy in three cross-sections of the bend shows the differences between the low (left) and high (right) buoyancy cases. It is interesting to note that the peak turbulence in the midplane is found in the low buoyancy case, not the high buoyancy case.

With buoyancy, however, turbulence is increased back to a level very similar to that in the stationary case. On the trailing side, Coriolis effects increase turbulence near the dividing wall. With high buoyancy, the profile lies along a shear layer between the large secondary vortex and a smaller vortex in the trailing wall corner. The vertical fluctuations are attenuated by Coriolis forces near the leading wall but increased by buoyancy. Though low buoyancy does not affect the profile, a dramatic increase is found with high buoyancy because of the presence of the shear layer. Vertical fluctuations are strengthened in all cases along the trailing wall. Finally, the streamwise fluctuations are plotted in Figure 6.18(d). Stationary streamwise fluctuations are compared with the measurements of Sewall et al., (2005) and show good agreement between measurements and calculations. As observed with the vertical fluctuations, the streamwise fluctuations are attenuated by Coriolis effects near the leading wall, but increasing the buoyancy parameter strengthens them. Along the trailing wall, Coriolis effects strengthen the streamwise fluctuations near the dividing wall, while buoyancy forces attenuate them. Near the back wall, however, buoyancy is found to significantly increase the streamwise turbulence.

Area-averaged turbulent kinetic energy is plotted for all four cases along the upstream and downstream ducts in Figure 6.19. Area-averaging is continued to the back wall of the bend using the same cross-sectional area as that in the upstream duct, and the same is true for the downstream side of the duct. Upstream of the duct, turbulent kinetic energy is increased significantly because of the strong destabilization effect of Coriolis and buoyancy forces along the trailing wall. With the high buoyancy parameter, especially, the turbulence is significantly increased in the bend, reaching a peak of 33% at the inlet. Downstream, however, a comparison between the stationary and zero buoyancy cases reveals that turbulence is actually attenuated, mostly due to leading wall attenuation downstream of the bend.

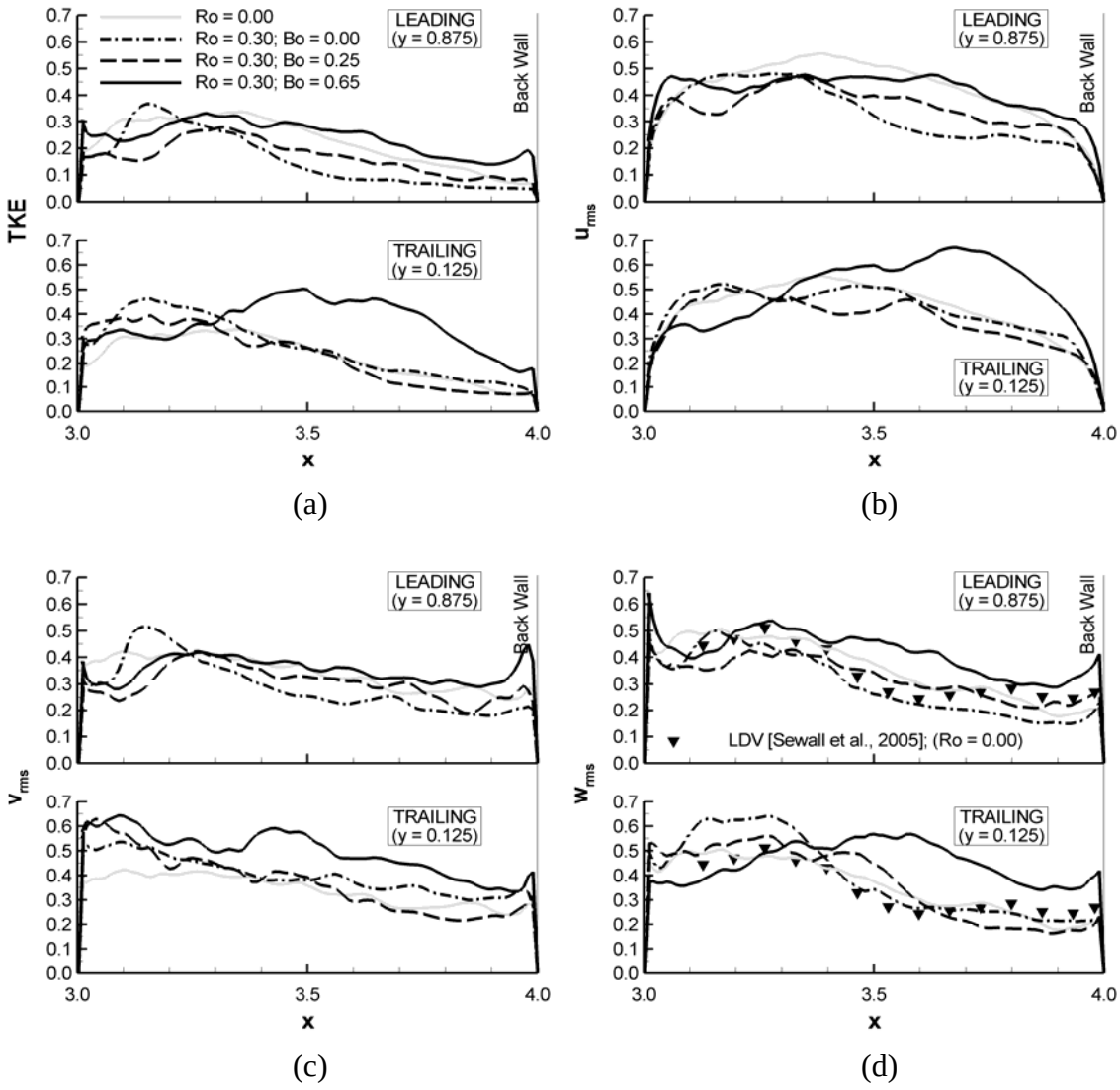

Figure 6.18. Profiles of turbulence in the midplane of the bend show the differences among all four cases. Comparisons of turbulence magnitude between the leading (top) and trailing (bottom) wall are best made by comparing the rotating cases to the gray stationary line, which is the same in both the leading and trailing cases.

With increased buoyancy, however, turbulence is increased downstream of the bend. It is high, initially, reaching over 25%, but it quickly decreases after the second rib to values between 10 and 20%.

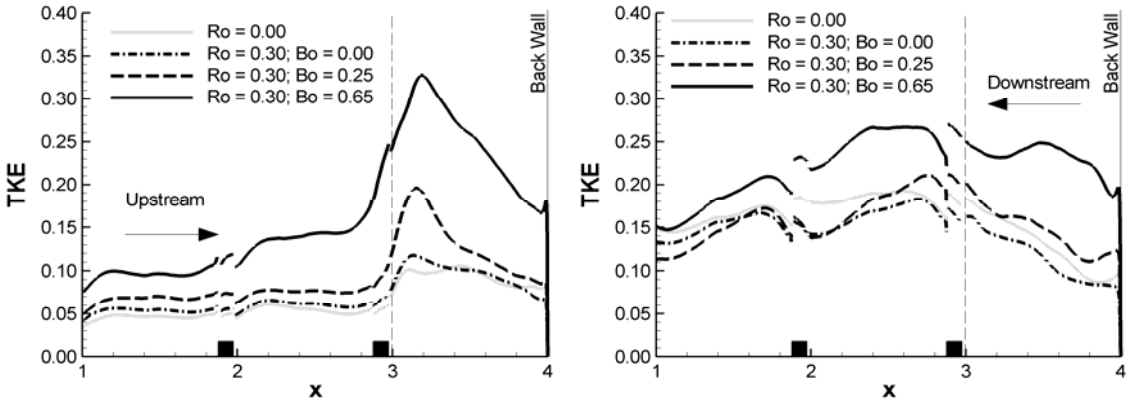

Figure 6.19. The area-averaged turbulent kinetic energy is compared among all four cases across the bend. Coriolis effects are found to decrease the overall turbulence, but buoyancy forces cause a sharp increase, especially at the entrance to the bend and the entrance to the downstream duct.

6.07 Heat Transfer Augmentation

A comparison of heat transfer augmentation contours is shown in Figure 6.20. It is important to note that the boundary conditions are different between the first two cases and last two cases. The stationary and zero buoyancy cases have a constant temperature boundary condition, while a uniform heat flux boundary condition is applied to the buoyancy calculations. The flow is unaffected by the difference, but the heat transfer augmentation has been found to be higher with the uniform heat flux boundary condition in some locations with high turbulence, occasionally reaching values 20% higher than the constant temperature boundary conditions in the average (Chapter 5, Figures 8 & 9). Because of this difference, only qualitative comparisons are shown between the zero buoyancy case and buoyancy calculations.

Upstream of the bend, leading wall heat transfer is decreased by Coriolis effects (when compared with the stationary case) and again with low buoyancy. Between the Coriolis results and buoyancy results, it is shown that increasing buoyancy on the leading wall increases heat

transfer downstream of the ribs (from values below 1 to those above 1). Also, upstream of the ribs, an increase in heat transfer due to enlarged recirculation zones was shown in the developing flow calculations (Sewall and Tafti, 2004). The same effects are present in these buoyancy cases but do not show up in Figure 6.20 because of the range of scales presented. The trailing wall experiences a consistent increase with both Coriolis effects and buoyancy forces, with the high buoyancy trailing wall reaching extremely high augmentation ratios over 9.0 in a few locations. Within the bend, Coriolis effects decrease the heat transfer along the back wall by weakening the secondary flow impingement. With the changes in secondary flows following an increase in buoyancy, the heat transfer is increased in the bend. On the leading wall, impingement is significantly strengthened due to stronger secondary flows, and that is reflected in the higher heat transfer augmentation near the back wall. On the trailing wall, a large region of high heat transfer is shown at the entrance to the bend as a result of high trailing wall turbulence upstream. Secondary flow impingement is responsible for the high trailing wall heat transfer near the dividing wall. Secondary flows also increase leading wall heat transfer augmentation near the back wall. Downstream of the bend, the leading wall shows an interesting trend. Coriolis effects shift mainstream momentum towards the leading wall, increasing the heat transfer on the wall with a high maximum value immediately downstream of the first rib at the inlet near the outside wall. With a low buoyancy parameter this heat transfer is increased slightly, but increasing the buoyancy much higher results in a much lower heat transfer augmentation, as shown in Figure 6.20(f). This is due to the opposing centrifugal buoyancy force, which acts against the flow in radially inward flow. On the trailing side, very little change is observed with increased buoyancy downstream, where the heat transfer augmentation is higher along the inside wall.

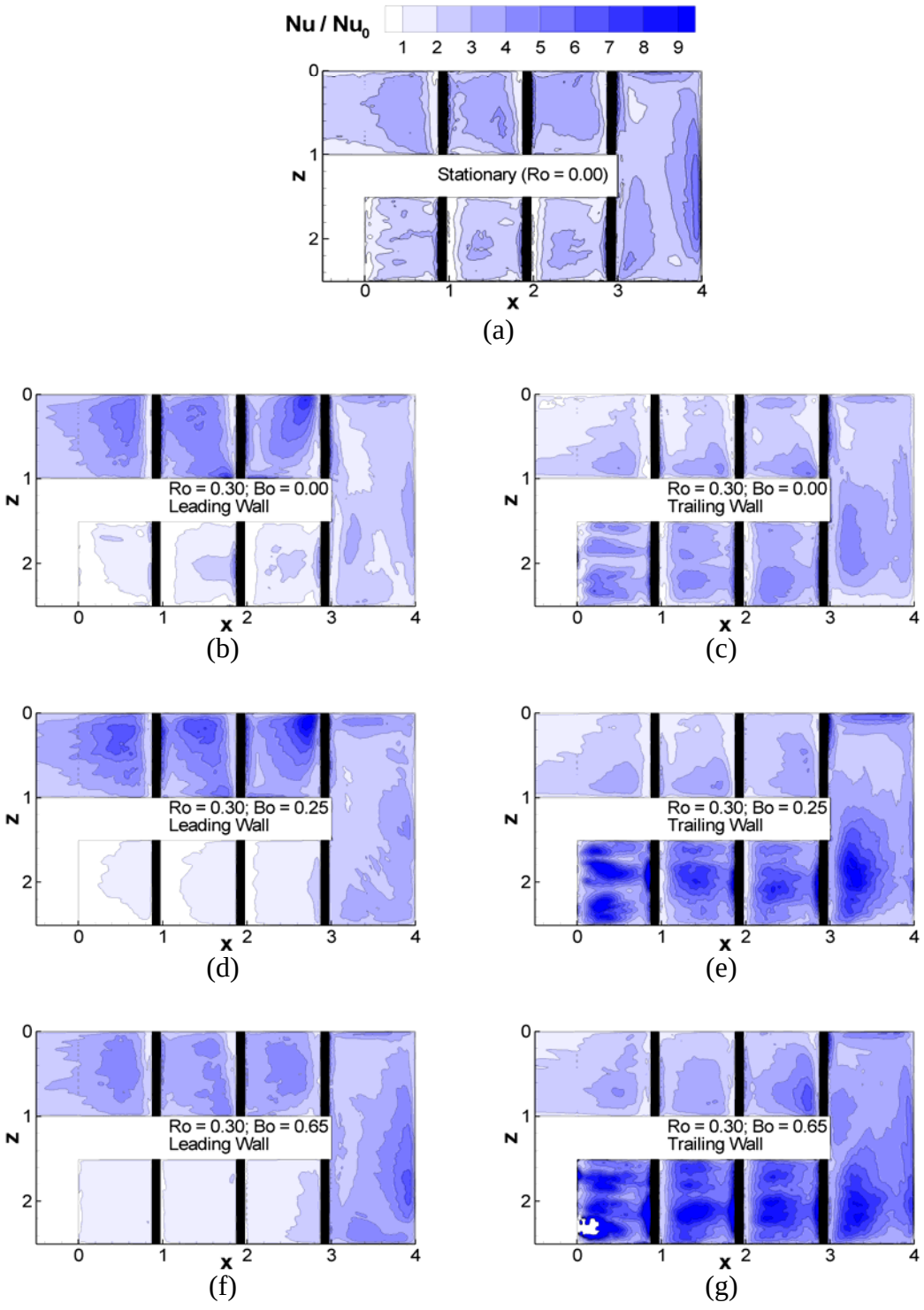

Figure 6.20. Heat transfer contours on the leading (left) and trailing (right) walls for each of the four cases shows that increasing buoyancy increases heat transfer augmentation on the trailing walls upstream and has little effect downstream. On the leading wall, increasing buoyancy eventually decreases heat transfer augmentation.

Heat Transfer augmentation on the back wall and dividing wall of each case is shown in Figure 6.21. With buoyancy, the heat transfer augmentation is highest near the trailing wall and has much higher magnitudes than the first two cases. A comparison of the dividing wall in the two cases shows that the highest heat transfer in the low buoyancy case is observed in a small area near the trailing wall, and conversely the highest heat transfer for the high buoyancy case is on the 75% of the wall on the leading side. The secondary flows undergo a dramatic change between the two cases, and this change is reflected in the differences in heat transfer on these two surfaces. On the downstream side, all four cases show a thin region of high heat transfer in the corner due to recirculating flow, though this region is extremely small in the zero buoyancy case and the high buoyancy case.

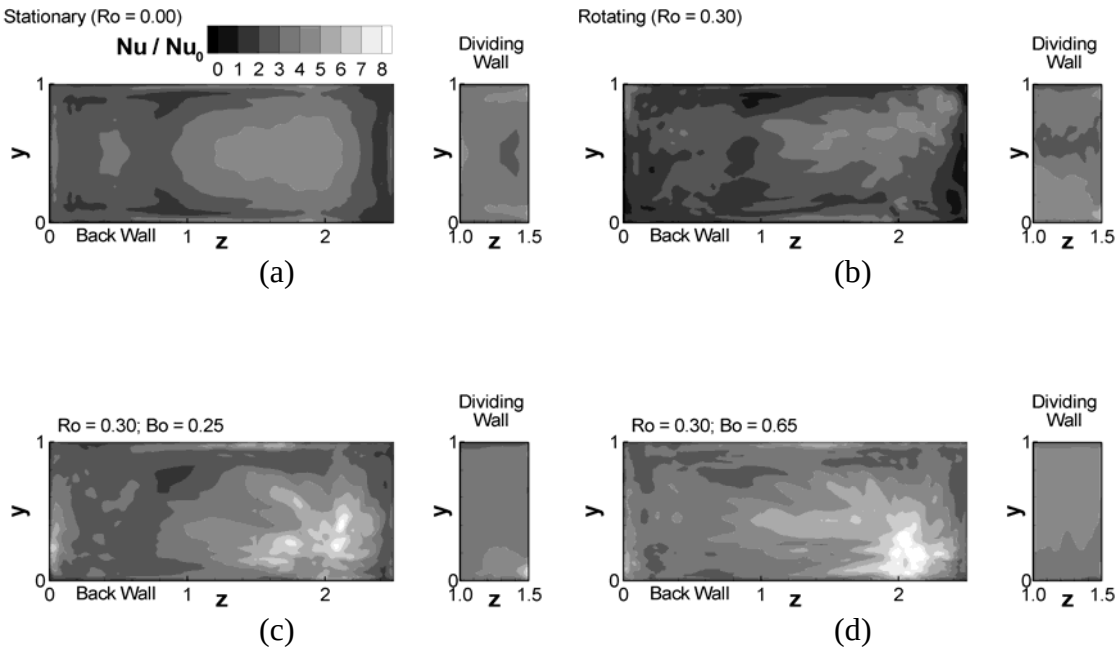

Figure 6.21. The heat transfer augmentation on the back wall and dividing wall is compared among all four cases. Buoyancy shifts the peak heat transfer towards the trailing side, as shown earlier in Figure 6.16.

Figure 6.22 shows the rib-averaged heat transfer augmentation in the upstream and downstream sections of the duct. Upstream of the duct, the trailing wall heat transfer shows an obvious increase with buoyancy. Increasing buoyancy on the upstream leading wall results in an initial decrease, followed by an increase. This effect was explored in more detail in the developing flow region by Sewall and Tafti (2005). The trailing wall experiences an increase with buoyancy across the entire bend, whereas the leading wall heat transfer also decreases initially, followed by an increase with buoyancy. Downstream, the leading wall heat transfer increases initially, but with a further increase in buoyancy the heat transfer declines. The trailing wall heat transfer decreases initially with low buoyancy but increases in the high buoyancy case.

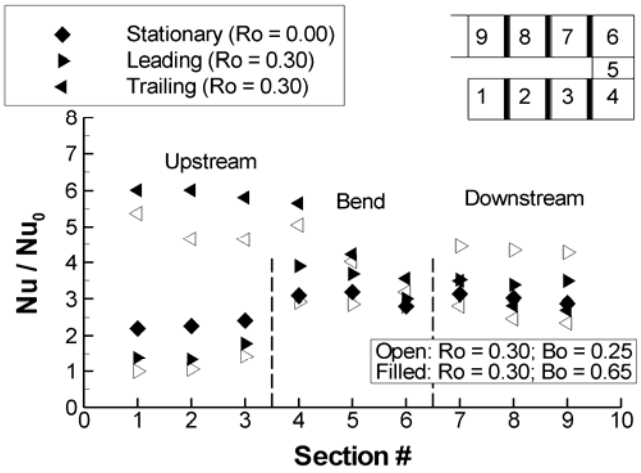

Figure 6.22. The heat transfer augmentation between the stationary case and two buoyancy cases shows the increases with buoyancy upstream on both walls but a decrease on the leading wall downstream, along with a trailing wall increase.

At each ribbed section, the area-averaged heat transfer augmentation across all sides is shown in Figure 6.23. Upstream of the bend, the stationary and zero buoyancy cases show the same heat transfer augmentation, and the low buoyancy case results in a heat transfer augmentation

that is approximately 30% greater than that of the first two cases. Increasing buoyancy further results in a heat transfer augmentation that is an additional 25% higher than the low buoyancy case. A similar trend is observed in the bend, where the high buoyancy case produces an averaged heat transfer of 4.02. Downstream, the low buoyancy case actually produces the maximum heat transfer augmentation, which is approximately 9% higher than the high buoyancy case at the maximum difference (Group 6). Heat transfer contours presented earlier in Figure 6.20 show that, downstream of the duct, the high buoyancy case produces a similar trailing wall heat transfer augmentation as the low buoyancy case but a much lower heat transfer on the leading wall, which explains the lower heat transfer in the downstream duct.

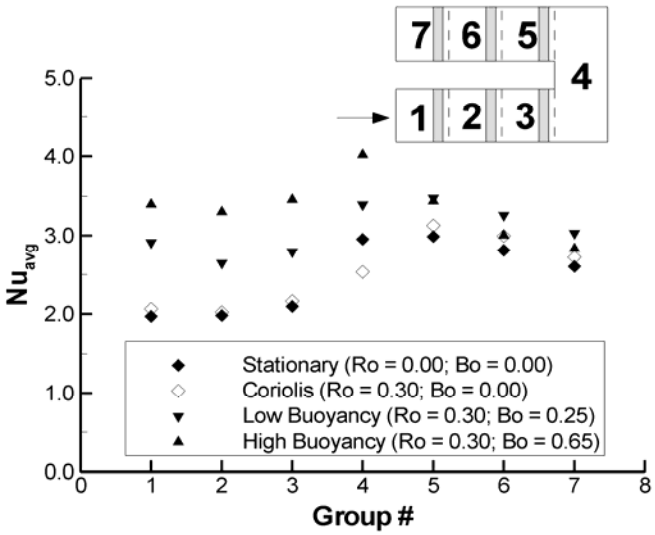

Figure 6.23. The area-averaged heat transfer augmentation across each section in the bend shows the overall increase in heat transfer due to buoyancy upstream. Downstream of the bend, however, all four cases show similar heat transfer augmentation values, with the low buoyancy case producing the highest values.

6.08 Friction Factor in the 180º Bend

The friction factor augmentation across the bend is listed in Table 6.1. The friction factor is calculate from the difference between the area-averaged pressure between two locations that are shown in Figure 6.24. It has been shown previously that the stationary calculation and the experimentally measured values show excellent agreement. The Coriolis effects were shown in the previous chapter (Figure 11) to improve turning by shifting the recirculation zone at the tip of the dividing wall. The decreased resistance to the flow results in a lower friction factor augmentation. The resistance is further decreased at low buoyancy because the recirculation zone is further condensed and shifted towards the trailing wall, resulting in even better flow turning. With a high buoyancy parameter, however, a dramatic shift occurs. The recirculation zone separates from the inside wall and moves up into the mainstream flow, dramatically reducing the flow area and producing a strong impingement region on the wall from the increased flow resistance. As a result of this change, the friction factor augmentation is increased dramatically in the high buoyancy case, reaching a value more than 40% greater than the low buoyancy friction factor augmentation.

Table 6.1. 180º Bend Friction Factor Comparison

Case	f / f_o
Stationary (Experiments)	22.84
Stationary (Calculations	23.08
Coriolis (Bo = 0.00)	20.91
Low Buoyancy (Bo = 0.25)	19.47
High Buoyancy (Bo = 0.65)	27.26

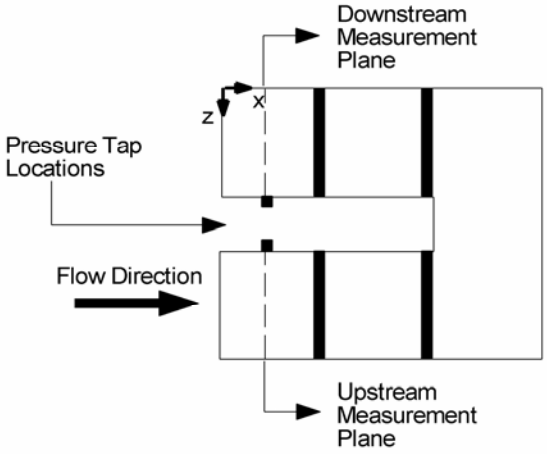

Figure 6.24. The friction factor is measured between two area-averaged planes, one located two rib-heights upstream of the bend, and the other located two rib-heights downstream of the bend.

6.09 Summary and Conclusions

The effect of centrifugal buoyancy has been observed in the developing flow and 180º bend domains in this chapter. The following conclusions are drawn from the results obtained in the developing flow domain:

a) Trailing wall heat transfer augmentation increased throughout the developing flow region with a corresponding increase in buoyancy.

b) On the leading wall, the heat transfer augmentation decreased when the buoyancy parameter was varied from zero to Bo = 0.25 but increased when the buoyancy parameter was increased beyond Bo = 0.25.

c) The LES calculations showed at low buoyancy parameters the growth of the separated region behind each rib was responsible for the decrease in heat transfer augmentation. However, as the separated region spanned the full pitch between ribs with an increase in buoyancy parameter, it led to entrainment of fluid from the mainstream of the duct into the separated shear layer which was redirected by the rib downstream into the vicinity of the leading wall. The combined effect of an increase in turbulent fluctuations in the shear layer separating the recirculating region from the mainstream flow, increased entrainment of mainstream fluid and subsequent redirection and impingement leads to an overall increase in heat transfer augmentation at the leading wall as the buoyancy parameter increases above 0.3.

d) It is noted that in spite of the Boussinesq approximation, the high resolution LES calculations are capable of accurately predicting the subtle changes in heat transfer resulting from changes in buoyancy.

e) Friction factors were found to increase monotonically with buoyancy and the increase is attributed mostly to the increased form drag losses at the leading wall.

In the 180º bend, the effects of buoyancy were also studied in their relationship to the stationary and rotating (with no buoyancy) cases. Special attention was paid to the effects of buoyancy on the mean flow, since that, and not necessarily turbulence, has been described as the most important factor in determining the regions of peak heat transfer in the bend (Liou et al., 2000). In the 180º bend, the following conclusions are drawn:

a) Low buoyancy shifts the recirculation zone at the tip of the dividing wall towards the trailing wall, while strengthening the secondary flow vortex on the leading side, increasing flow impingement on the inside of the dividing wall and shifting back wall impingement to a point along the trailing edge of the back wall.

b) High buoyancy shifts the recirculation zone away from the dividing wall and up into the mainstream flow, where an extremely strong vortex increases flow impingement on the dividing wall and on the inside part of the trailing wall. Mainstream flow is forced around the outside of this bubble and is strongly accelerated along the outside of the bend.

c) Coriolis effects shift the mainstream flow impingement on the back wall of the bend towards the leading side and decrease its magnitude. Low buoyancy causes the impingement flow to be shifted towards the leading wall, and high buoyancy greatly increases the impingement flow velocity due to resistance of flow around the bend.

d) Area-averaged turbulent kinetic energy is increased across the bend in all cases, with the highest buoyancy producing the highest turbulence, but high buoyancy actually decreases the peak values of turbulence in the midplane of the bend by dispersing it throughout the cross-section, while the low buoyancy case produces a high peak turbulence near the dividing wall.

e) In the bend, the high buoyancy also results in higher heat transfer, but downstream the leading wall heat transfer is lower in the high buoyancy case than in the low buoyancy case, though trailing wall heat transfer continues to be higher at high buoyancy.

f) The area-averaged heat transfer augmentation over each group shows that increasing buoyancy results in a similar increase in heat transfer upstream, but downstream the high buoyancy parameter produces a lower heat transfer augmentation than in the low buoyancy case because of decreased leading wall heat transfer.

g) Rotation is found to decrease overall friction factor across the bend, but the high buoyancy case shows a dramatic increase in friction to a value 40% higher than the low buoyancy case. This is attributed to greater flow resistance because of the strengthened vortex that has shifted to the center of the bend at high buoyancy.

Chapter 7. A Variable Property Algorithm for Calculating Unsteady Flows with Large Property Variations

The formulation for the implementation of centrifugal buoyancy forces in this project relies on the Boussinesq approximation to calculate the density variations based on a linear relationship with temperature. Because the incompressible Navier-Stokes equations are solved, this relationship is needed to approximate the changes in density resulting from temperature variations in the flow. The relationship between temperature and density is accurately described by the ideal gas law, and the Boussinesq approximation accurately reproduces this relationship for small temperature variations. As the differences in temperature become large, however, the Boussinesq approximation is no longer sufficient and the density must be calculated as a dependent variable. This additional variable and additional equation of state (the ideal gas law, in this case) complicates the calculation because the momentum and energy equations can no longer be de-coupled and must be solved simultaneously. In this chapter, an algorithm is presented for predicting unsteady flows in the presence of large temperature differences. This chapter presents the algorithm and the validation against two cases, Rayleigh-Bénard convection and Poiseuille-Bénard channel flow. Implementing this algorithm into a parallel solver such as GenIDLEST would allow for the calculation of rotating turbine blades without having to make the assumptions inherent in using the Boussinesq approximation.

One of the largest obstacles to overcome is the significant difference in time scales between the convective velocity in high temperature flows and the acoustic wave speed. Hence, whereas incompressible flow algorithms are not valid, compressible flow algorithms, which account for changes in density with pressure and temperature through a representative gas law, become ill-conditioned in the limit of very low Mach numbers. Hence, a low Mach number approximation

is commonly used to separate the low magnitude acoustic pressure waves from large scale pressure effects, as defined by Rehm and Baum (1978) and later by McMurtry et al. (1985). In ideal gases, this approximation relates the density to the temperature and a spatially-independent thermodynamic pressure, while ignoring the effect of small pressure fluctuations on the density.

7.01 Literature Review

A number of algorithms have been developed with the purpose of predicting these flows. A study by Chenoweth and Paolucci (1986) used an explicit fractional step algorithm to solve the time-dependent Navier-Stokes equation using the low Mach number approximation to filter out the effect of acoustic wave propagation. In the algorithm an ordinary differential equation was solved for the gradient of a thermodynamic pressure, which was time dependent but constant in space, and a Poisson equation for the first order pressure was solved to obtain an intermediate pressure and solved a second time to correct the pressure after advancing the momentum equations. A stability map was produced over a range of aspect ratios and Rayleigh numbers through a series of calculations.

Merkle and Choi (1987) developed a set of low Mach number equations discretized with an Euler implicit scheme in time. The equations included an artificial time derivative of pressure in the energy equation to represent pseudoacoustic waves with a speed on the same order as the particle velocity, eliminating the acoustic CFL constraint, and the system produced steady state solutions using standard block tridiagonal matrix procedures. Adding a buoyancy source term to the equations was found to cause instabilities at low Froude numbers, where the flow velocity does not necessarily dominate the gravitational body force, but because the cases of interest were at a higher Mach number than those typically found in low Froude number cases, the instability did not cause significant problems.

Mahalingam et al. (1990) solved the time-dependent low Mach number equations with a predictor corrector method in which the momentum and energy equations were time-advanced, allowing for the density to be obtained through the ideal gas law, followed by the solution of a Poisson equation for pressure. The updated velocities were then obtained based on the updated values of density and pressure. Fuel and oxidizer equations were also advanced along with the energy equation to represent the chemistry. The zeroth order pressure resulting from the low Mach number equations was set to a constant because an open flow was considered. The algorithm was used to study various parameters in jet diffusion flames, including both steady laminar flames and flames in the presence of time-dependent forced disturbances. Comparisons were made between nonreacting simulations, nonbuoyant reacting simulations, and buoyant reacting simulations.

An algorithm was presented by Bell and Marcus (1992) to solve the time-dependent variable density equations using an explicit predictor-corrector scheme. In the predictor step, the velocity and density were time advanced. The corrector step decomposed these results into a discrete gradient of a scalar potential (which corresponded to the new approximation to the pressure gradient) and a divergence-free vector field (which corresponded to an update for the velocity) using a discrete Galerkin approach and solved the resulting system of equations with a conjugate gradient algorithm. The density variations considered in this study were a result of either small temperature differences handled by the Boussinesq approximation or the acceleration of a high-density fluid into a low-density fluid by the effect of gravity (Rayleigh-Taylor instability). Density variations resulting from large temperature differences were not considered in this approach.

Pember et al. (1997) developed an adaptive method for modeling unsteady low Mach number reacting flow using a projection method. The low Mach number approximation was implemented in such a way that the first order pressure in a Mach number series expansion of pressure was used in the momentum equations, but the pressure work term was not included in the energy equation. Instead, a pressure relaxation term based on the pressure work term was added to the numerical representation of the divergence constraint. This relaxation term was necessary because a sequential solution approach could not simultaneously conserve mass and satisfy the equation of state. Solutions for reacting flow of methane-air flames, both steady and flickering, were calculated as examples.

Darbandi and Schneider (1998) introduced an analogy-based extension from incompressible to compressible flows. By changing the dependent variables from Cartesian velocities and modified pressure to the momentum flux components and actual pressure and treating the source terms properly, an algorithm was developed to treat both compressible and incompressible cases. The focus of the study was on the incompressible limit of compressible flows, and validation studies of driven cavity flow, channel entrance flow, and high speed flow through a converging-diverging nozzle showed good agreement with experiments. No mention was made of large temperature differences or the presence of a gravitational body force term.

Mary et al. (2000) used an approximate Newton method based on artificial compressibility to avoid the acoustic CFL limitation. A steady problem was solved at each time step, and the unsteady solution was calculated using a dual time stepping scheme in which the steady problem was solved in pseudo-time using a first order implicit method for fast convergence. The flowfield was advanced in physical time using a high order temporal scheme. Preconditioning was used to make the algorithm fast and efficient, and the most time-consuming step was found

to be the solution of the steady problems in pseudo-time. Strong temperature variations were also shown to decrease the efficiency of the algorithm in low Mach number cases.

Sato et al. (2002) used the SIMPLE algorithm with fully implicit time-stepping to simulate the unsteady behavior of buoyancy diffusion flames. The low Mach number approximation was used in the formulation, and a single-step chemical reaction was included, as well. Various strengths of the gravitational effect were simulated, and the results were used to study the unsteady motions and oscillatory frequency of a flickering flame.

Wall et al. (2002) developed an iterative technique for time-accurate solution of low frequency pressure waves of interest in studying acoustic instabilities in combustors. They used an iterative semi-implicit method based on the fractional-step algorithm. By treating pressure implicitly and filtering it to smooth high frequency waves, they were able to use acoustic CFL numbers much greater than unity for the propagation of small-amplitude acoustic waves in a periodic domain, in a one-dimensional model combustor, and in an LES study of a nonreacting co-axial combustor.

The objective of this chapter is to develop and validate an algorithm capable of time-accurate resolution of low Mach number flows with large temperature variations using the framework of a fractional-step algorithm used for incompressible flows. A fully-implicit iterative algorithm based on the solution of a Helmholtz equation for pressure is developed for this purpose, in which density dependence on both pressure and temperature is introduced through an equation of state. Comparisons with experimental, analytical, and benchmark numerical studies show the algorithm to be accurate in predicting flow and heat transfer in steady Rayleigh-Bénard convection in an enclosure with large temperature differences and in a time-dependent Poiseuille-Bénard channel flow with unsteady longitudinal convective instabilities in the duct.

7.02 Governing Equations

The conservation of mass, momentum, and energy and the ideal gas equation of state are described by the following time-dependent, variable property equations (boldface letters represent vector quantities):

$$\frac{\partial \rho}{\partial t} + \nabla \bullet (\rho \boldsymbol{u}) = 0\,, \tag{1}$$

$$\frac{\partial (\rho \boldsymbol{u})}{\partial t} = -\nabla \bullet (\rho \boldsymbol{u}\boldsymbol{u}) - \nabla P + \nabla \bullet \left(\mu\left(\nabla \boldsymbol{u} + \nabla \boldsymbol{u}^T\right) - \frac{2}{3}\mu(\nabla \bullet \boldsymbol{u})\boldsymbol{I} \right) + \rho g \hat{\boldsymbol{y}}\,, \tag{2}$$

$$\frac{\partial (\rho c_p T)}{\partial t} = -\nabla \bullet (\rho c_p \boldsymbol{u} T) + \nabla \bullet (k \nabla T) + \left(\frac{\partial P}{\partial t} + \boldsymbol{u} \bullet \nabla P \right) + \Phi\,, \tag{3}$$

where $\Phi = \left[\mu\left(\nabla \boldsymbol{u} + (\nabla \boldsymbol{u})^T\right) - \frac{2}{3}\mu(\nabla \cdot \boldsymbol{u})\boldsymbol{I} \right] : \nabla \boldsymbol{u}$ is the viscous-dissipation term, and

$$\rho = \frac{P}{RT}\,, \tag{4}$$

where g is the magnitude of gravitational acceleration defined as 9.81 m/s^2, $\hat{\boldsymbol{y}}$ is the directional vector of gravity, and R is the ideal gas constant defined as R = 287 J/kg·K. The flow and property variables are nondimensionalized as follows (an asterisk denotes nondimensional quantities):

$$\rho^* = \frac{\rho}{\rho_{ref}} \qquad \mu^* = \frac{\mu}{\mu_{ref}} \qquad k^* = \frac{k}{k_{ref}} \qquad c_p^* = \frac{c_p}{c_{p\_ref}}$$

$$\boldsymbol{x}^* = \frac{\boldsymbol{x}}{L} \qquad \boldsymbol{u}^* = \frac{\boldsymbol{u}}{U_{ref}} \qquad t^* = \frac{t U_{ref}}{L} \qquad P^* = \frac{P - P_{ref}}{\rho_{ref} U_{ref}^{\ 2}}$$

$$T^* = \frac{T - T_{ref}}{T_o}\,,$$

where L is some reference length scale and U_{ref} is a reference velocity that is specified in forced convection cases or calculated in the case of natural convection (this is discussed later). The

reference temperature, T_{ref}, is a basis for calculating all initial property values and is typically (but not always) set to the same value as T_o, which is a characteristic temperature that is described as the mean of the hot and cold wall temperatures ($T_o = (T_H + T_C) / 2$). While the dynamic viscosity μ/μ_{ref} and thermal conductivity k/k_{ref} variations with temperature are represented by Sutherland's law for gases, it is assumed that the specific heat c_p/c_{p_ref} is unity, or that the specific heat is constant at the reference temperature. This is a valid assumption for most gases and liquids. For example, viscosity and conductivity for air in the temperature range 240 K to 960 K vary ±54% about the reference value, whereas c_p only varies ±7%. Hence in all the development that follows, it is assume that $c_p/c_{p\_ref} = 1$ without loss of generality. The non-dimensional equations are written as[1]:

$$\frac{\partial \rho}{\partial t} + \nabla \bullet (\rho \boldsymbol{u}) = 0, \tag{5}$$

$$\frac{\partial (\rho \boldsymbol{u})}{\partial t} = -\nabla \bullet (\rho \boldsymbol{u}\boldsymbol{u}) - \nabla P + \frac{1}{\mathrm{Re}} \nabla \bullet \left(\mu \left(\nabla \boldsymbol{u} + \nabla \boldsymbol{u}^T \right) - \frac{2}{3} \mu (\nabla \bullet \boldsymbol{u}) \boldsymbol{I} \right) + \frac{\mathrm{Ra}}{\mathrm{Re}^2 \cdot \mathrm{Pr}} \frac{\rho}{(T_H - T_C)} \hat{\boldsymbol{y}}, \tag{6}$$

$$\frac{\partial (\rho T)}{\partial t} = -\nabla \bullet (\rho \boldsymbol{u} T) + \frac{1}{\mathrm{Re} \cdot \mathrm{Pr}} \nabla \bullet (k \nabla T) + \mathrm{Ec} \left(\frac{\partial P}{\partial t} + \boldsymbol{u} \bullet \nabla P \right) + \frac{\mathrm{Ec}}{\mathrm{Re}} \Phi, \tag{7}$$

$$\rho = \frac{\rho_{ref} {U_{ref}}^2 P + P_{ref}}{R \cdot \rho_{ref} (T \cdot T_o + T_{ref})}, \tag{8}$$

where T_H and T_C are nondimensional temperatures, and

$$\mathrm{Re} = \frac{\rho_{ref} U_{ref} L}{\mu_{ref}}, \ \mathrm{Pr} = \frac{\mu_{ref} c_{p\_ref}}{k_{ref}}, \ \mathrm{Ra} = \frac{g\beta (T_H - T_C) L^3}{\alpha_{ref} \nu_{ref}}, \text{ and } \mathrm{Ec} = \frac{\beta {U_{ref}}^2}{c_{p\_ref}}.$$

[1] The asterisk has been dropped for clarity, and from this point forward all terms, both in the equations and in the results, are given in their non-dimensional form unless noted otherwise.

The thermal expansion coefficient β is approximated as $1/T_o$. The reference velocity, U_{ref}, depends on the dominating convection force. In forced convection cases, the reference velocity is specified from the driving flow, implemented as a dimensional velocity that is chosen to produce the desired Reynolds number. In the absence of forced convection (pure natural convection), a temperature difference is specified and the reference velocity is calculated from the characteristic length and the temperature difference, as defined by the following (dimensional) equation:

$$U_{ref} = \sqrt{g \cdot L \cdot \beta \cdot (T_H - T_C)}, \tag{9}$$

where β is the coefficient of thermal expansion, and T_H and T_C are the dimensional hot and cold wall temperatures, respectively. In this case, a large temperature difference would induce a large reference velocity, while a small temperature difference would induce a small reference velocity.

In Eq. (6), the nondimensional coefficient of the gravitational body force term, $Ra/(Re^2 \cdot Pr)$, determines the gravitational effect on the flowfield. This quantity is also known as the Froude number, which is the ratio of the inertial force to the gravitational force. In pure natural convection, this term has a value of unity because the reference velocity (Eq. (9)), when substituted into the Reynolds number, causes the nondimensional terms to divide out, resulting in a coefficient of unity. In pure forced convection, Re >> Ra, and the coefficient would be negligible, but in mixed convection, both a temperature variation and reference velocity would be specified. In this case, both the temperature difference and reference velocity determine the relative importance of natural versus forced convection.

Since the development in this paper is primarily targeted towards low speed flows, some simplifying assumptions can be made. The Eckert number in the non-dimensional energy equation (Eq. (7)) can be expressed as:

$$\mathrm{Ec} = \mathrm{Ma}^2(\gamma - 1). \tag{10}$$

In a low speed regime, both the Eckert number ($O(10^{-6})$) and Mach number ($O(10^{-3})$) show that the pressure work term in Eq. (7) has little effect on energy conservation. Also, neglecting the viscous dissipation term in Eq. (7) results in the following simplified form of the energy equation:

$$\frac{\partial(\rho T)}{\partial t} = -\nabla \bullet (\rho \boldsymbol{u} T) + \frac{1}{\mathrm{Re} \cdot \mathrm{Pr}} \nabla \bullet (k \nabla T), \tag{11}$$

In all cases presented in this study, the working fluid is air, though any functional relationships with temperature could be defined for the physical properties. In the presence of large temperature variations, the variations in density are determined by the ideal gas law (Eq. (8)). The dynamic viscosity and thermal conductivity variations are determined by Sutherland's Law:

$$\frac{\mu}{\mu_{ref}} = \left(\frac{T}{T_{ref}}\right)^{3/2} \frac{T_{ref} + S_\mu}{T + S_\mu} \tag{12}$$

$$\frac{k}{k_{ref}} = \left(\frac{T}{T_{ref}}\right)^{3/2} \frac{T_{ref} + S_k}{T + S_k}, \tag{13}$$

where μ_{ref} and k_{ref} are the viscosity and thermal conductivity at some reference temperature, T_{ref}, and S_μ and S_k are the Sutherland constants for air and have values of 110.4K and 194K, respectively. The specific heat is assumed constant at the reference temperature and is determined by a functional form as outlined by Çengel and Boles (1998):

$$c_{p\_ref} = (1/M) \cdot (a + bT_{ref} + cT_{ref}^2 + dT_{ref}^3) \tag{14}$$

where M is the molar mass of air, the constants a,b,c, and d are curve fit constants and have values of 28.11, 1.967×10^{-3}, 4.802×10^{-6}, and -1.966×10^{-9}, respectively. The equations for

viscosity and thermal conductivity are valid for temperature ranges from 167K to 1900K (1971). The curve fit for specific heat is valid from 273K to 1800K, but the curve fit is only used at the reference temperature, which is well within the given range.

7.03 Numerical Algorithm

The analysis uses a finite volume formulation with second order central differencing for spatial discretization. Time stepping is accomplished with an implicit iterative Crank-Nicolson fractional step algorithm, the basic steps of which are shown in Figure 7.1. The core of the algorithm is based on the fractional-step algorithm used for incompressible constant density flows and is characterized by a de-coupled non-linear iterative procedure at each time step to resolve the coupled set of non-linear equations. Both the effect of temperature and pressure changes are incorporated into the calculated density, whereas only the temperature dependence is considered for other properties. In the case of isothermal flows, the algorithm defaults to a non-linear iterative fractional-step algorithm, which only resolves the non-linearity in the momentum equations. Throughout the inner iterations (described by iteration variable k), more accurate intermediate values for the dependent variables are sought, which produce a time-accurate solution at each time step (described by iteration variable n). The discretized equations are solved on a non-staggered grid. The dependent variables, pressure (P), Cartesian velocities ($\boldsymbol{u}$), temperature (T), and density (ρ) are solved and stored at the cell center, whereas cell face mass fluxes ($\boldsymbol{C}$) are stored and calculated at the cell faces to emulate a staggered grid arrangement (Tafti, 2001).

1. **Begin with velocities, temperature, density and pressure from the previous time step $(n\Delta t)$ or previous inner iteration (*k-1)***
2. **Advance energy equation to update temperature (T^k)**
3. **Calculate an intermediate density ($\widetilde{\rho}^k$) using the temperature in step 2 and the ideal gas law**
4. **Advance momentum equations to calculate intermediate velocities ($\widetilde{\boldsymbol{u}}^k$) and cell face fluxes ($\widetilde{\boldsymbol{C}}^k = \widetilde{\rho}^k \widetilde{\boldsymbol{u}}^k$)**
5. **Solve a Helmholtz pressure correction equation (P') to solve for an updated pressure (P^k).**
6. **Update density (ρ^k) with corrected pressure using the ideal gas law.**
7. **Update cell face fluxes and velocities using the corrected pressure ($\boldsymbol{u}^k, \boldsymbol{C}^k$)**
8. **Check for convergence. If converged then proceed to next time step. If not converged then proceed to step 1.**

Figure 7.1. The steps in the solution algorithm for advancing a time step are similar to those of the fractional step algorithm used in GenIDLEST but with more steps included to account for an additional equation of state.

The following steps outline the exact solution procedure in the algorithm.

Step1 -- In this step, the inner loop is initialized. The working variables are set to the variables from the previous time step (if k=1) or previous inner iteration (k-1). The following initializations are imposed if k=1

$$\rho^{k-1} = \rho^n;\ \boldsymbol{u}^{k-1} = \boldsymbol{u}^n;\ T^{k-1} = T^n;\ P^{k-1} = P^n;\ \boldsymbol{C}^{k-1} = \boldsymbol{C}^n;\ \mu^{k-1} = \mu^n;\ k^{k-1} = k^n.$$

Step 2 – Calculate Intermediate Temperature

The energy equation is advanced implicitly based on the temperature at the previous time step and the current inner iteration. The physical properties and convective fluxes in the current inner iteration terms are taken from the previous inner iteration (k-*1*).

$$T^k + \frac{1}{2}\frac{\Delta t}{\rho^{k-1}}\nabla\bullet\left(\boldsymbol{C}^{k-1}T^k\right) - \frac{1}{2}\frac{\Delta t}{\rho^{k-1}}\frac{1}{\mathrm{Re}\cdot\mathrm{Pr}}\nabla\bullet\left(k^{k-1}\nabla T^k\right) =$$

$$\frac{\rho^n}{\rho^{k-1}} T^n - \frac{1}{2}\frac{\Delta t}{\rho^{k-1}} \nabla \bullet \left(\boldsymbol{C}^n T^n \right) + \frac{1}{2}\frac{\Delta t}{\rho^{k-1}} \frac{1}{\mathrm{Re} \cdot \mathrm{Pr}} \nabla \bullet \left(k^n \nabla T^n \right) \tag{15}$$

where $\boldsymbol{C}^0 = \boldsymbol{C}^n$, $\rho^0 = \rho^n$, $T^0 = T^n$, and $k^0 = k^n$.

Boundary conditions are applied as a specified temperature for the hot and cold surfaces and Neumann or zero gradient conditions for other surfaces.

Step 3 – Calculate Intermediate Density

The density is updated to an intermediate value using the ideal gas law to incorporate the change in temperature from the solution of the energy equation.

$$\tilde{\rho}^k = \frac{\rho_{ref} {U_{ref}}^2 P^{k-1} + P_{ref}}{\rho_{ref} R\left(T^k \cdot T_o + T_{ref} \right)}, \text{ where } P^0 = P^n \tag{16}$$

Step 4 – Calculate Intermediate Velocities

The intermediate velocities are calculated using a Crank-Nicolson formulation for the convection terms and part of the diffusion terms which are amenable to a simple three-point stencil in one dimension. Additional terms in the stress tensor are advanced explicitly as source terms with values from the previous inner iteration. In addition, the pressure term and the *y*-momentum gravitational body force term are also included in the source terms with values from the previous inner iteration.

$$\begin{aligned} \tilde{\boldsymbol{u}}^k + \frac{1}{2}\frac{\Delta t}{\tilde{\rho}^k} \nabla \bullet \left(\boldsymbol{C}^{k-1} \tilde{\boldsymbol{u}}^k \right) - \frac{1}{2}\frac{\Delta t}{\tilde{\rho}^k} \frac{1}{\mathrm{Re}} \nabla \bullet \left(\mu^{k-1} \nabla \tilde{\boldsymbol{u}}^k \right) = \\ \frac{\rho^n}{\tilde{\rho}^k} \boldsymbol{u}^n - \frac{1}{2}\frac{\Delta t}{\tilde{\rho}^k} \nabla \bullet \left(\boldsymbol{C}^n \boldsymbol{u}^n \right) - \frac{\Delta t}{\tilde{\rho}^k} \nabla P^{k-1} + \frac{1}{2}\frac{\Delta t}{\tilde{\rho}^k} \frac{1}{\mathrm{Re}} \nabla \bullet \left(\mu^n \nabla \boldsymbol{u}^n \right) \\ + \frac{\Delta t}{\tilde{\rho}^k} \frac{1}{\mathrm{Re}} \nabla \bullet \left[\left(\mu^{k-1} \left(\nabla \boldsymbol{u}^{k-1} \right)^T \right) - \frac{2}{3} \left(\mu^{k-1} \nabla \bullet \boldsymbol{u}^{k-1} \right) \boldsymbol{I} \right] \\ + \frac{\Delta t}{\tilde{\rho}^k} \frac{\mathrm{Ra}}{\mathrm{Re}^2 \mathrm{Pr}} \frac{\tilde{\rho}^k}{\left(T_H - T_C \right)} \hat{\boldsymbol{y}}, \end{aligned} \tag{17}$$

where $\boldsymbol{u}^0 = \boldsymbol{u}^n$, and $P^0 = P^n$.

No slip boundary conditions are applied on all surfaces. The Conjugate Gradient (CG) method is used to solve the momentum equations. Typically only a couple of iterations are needed to relax the residue by one order of magnitude.

At the end of the momentum steps, the cell face fluxes are updated by interpolating the nodal density and velocities:

$$\widetilde{\boldsymbol{C}}^{k} = \widetilde{\rho}^{k}\widetilde{\boldsymbol{u}}^{k} . \tag{18}$$

At the end of this step, the velocity and density fields do not satisfy the conservation of mass.

Step 5 – Formulate and Solve a Helmholtz Pressure Correction Equation

The pressure correction equation is formulated from the momentum and continuity equations by requiring that the updated cell face fluxes ($\boldsymbol{C}^{k} = \rho^{k}\boldsymbol{u}^{k}$) and ρ^{k} and $\boldsymbol{u}^{k}$ satisfy the discrete continuity equation and the updated momentum equations:

$$\frac{\rho^{k} - \rho^{n}}{\Delta t} + \nabla \bullet \left(\boldsymbol{C}^{k}\right) = 0 \quad \& \tag{19}$$

$$\begin{aligned}\frac{\rho^{k}\boldsymbol{u}^{k} - \rho^{n}\boldsymbol{u}^{n}}{\Delta t} + \frac{1}{2}\nabla \bullet \left(\boldsymbol{C}^{k-1}\boldsymbol{u}^{k}\right) - \frac{1}{2}\frac{1}{\mathrm{Re}}\nabla \bullet \left(\mu^{k-1}\nabla\boldsymbol{u}^{k}\right) = \\ -\frac{1}{2}\nabla \bullet \left(\boldsymbol{C}^{n}\boldsymbol{u}^{n}\right) - \nabla P^{k} + \frac{1}{2}\frac{1}{\mathrm{Re}}\nabla \bullet \left(\mu^{n}\nabla\boldsymbol{u}^{n}\right) \\ + \frac{1}{\mathrm{Re}}\nabla \bullet \left[\left(\mu^{k-1}\left(\nabla\boldsymbol{u}^{k-1}\right)^{T}\right) - \frac{2}{3}\left(\mu^{k-1}\nabla \bullet \boldsymbol{u}^{k-1}\right)\boldsymbol{I}\right] \\ + \frac{\mathrm{Ra}}{\mathrm{Re}^{2}\mathrm{Pr}}\frac{\widetilde{\rho}^{k}}{\left(T_{H} - T_{C}\right)}\hat{\boldsymbol{y}}\end{aligned} \tag{20}$$

The velocity correction obtained by subtracting Eq. (20) from the intermediate momentum equation (Eq. (15)) can be expressed in terms of a pressure correction and additional terms which result from the implicit treatment of the convection and diffusion terms.

$$\rho^k \boldsymbol{u}^k - \tilde{\rho}^k \tilde{\boldsymbol{u}}^k = -\Delta t\left(\nabla P^k - \nabla P^{k-1}\right) - \frac{1}{2}\Delta t\left(\nabla \bullet \left(\boldsymbol{C}^{k-1}\left(\boldsymbol{u}^k - \tilde{\boldsymbol{u}}^k\right)\right)\right) + \frac{1}{2}\frac{1}{\mathrm{Re}}\Delta t\left(\nabla \bullet \left(\mu^{k\text{-}1}\nabla\left(\boldsymbol{u}^k - \tilde{\boldsymbol{u}}^k\right)\right)\right) \tag{21}$$

The additional terms in the form of convective and diffusive fluxes of the velocity correction, if retained, couple the resulting pressure correction equation to the velocity correction necessitating a coupled solution of the two. This situation can be avoided by either neglecting the terms altogether or lagging them by one inner iteration at (*k*-1). Both options result in the same final solution, since at convergence both the pressure and velocity correction tend to zero. Both options were implemented and it was found that lagging the terms by one inner iteration resulted in about 10% faster convergence at the cost of more storage. For the sake of clarity, these terms are not included in the development that follows. Hence Eq. (21) is represented as:

$$\rho^k \boldsymbol{u}^k - \tilde{\rho}^k \tilde{\boldsymbol{u}}^k = -\Delta t\left(\nabla P'\right), \tag{22}$$

where *P'* is the pressure correction. Taking the divergence of Eq. (22) and substituting it into the continuity equation (Eq. (19)), results in the following form

$$\frac{\rho^k - \rho^n}{\Delta t} + \nabla \bullet \left(\tilde{\boldsymbol{C}}^k\right) - \Delta t \nabla^2 P' = 0 \tag{23}$$

Further, the density ρ^k in Eq. (23) is expressed in terms of the pressure and temperature by the ideal gas law as:

$$\rho^k = \frac{\rho_{ref} {U_{ref}}^2 P^{k-1} + \rho_{ref} {U_{ref}}^2 P' + P_{ref}}{\rho_{ref} R\left(T^k \cdot T_o + T_{ref}\right)} = \tilde{\rho}^k + \frac{\rho_{ref} {U_{ref}}^2 P'}{\rho_{ref} R\left(T^k \cdot T_o + T_{ref}\right)} \tag{24}$$

where ρ^k is expressed in terms of the updated pressure P^k, which includes the pressure correction. This can also be expressed as a density correction to the intermediate density as a result of the change in pressure. Substituting the ideal gas law into the equation and rearranging the terms produces a Helmholtz pressure equation,

$$\nabla^2 P' - \frac{\rho_{ref} {U_{ref}}^2}{\Delta t^2 \rho_{ref} R\left(T^k \cdot T_o + T_{ref}\right)} P' = \frac{\widetilde{\rho}^k - \rho^n}{\Delta t^2} + \frac{1}{\Delta t} \nabla \bullet \left(\widetilde{\boldsymbol{C}}^k\right) \tag{25}$$

Because the pressure equation is directly formulated at the cell faces, the Laplace operator is of a compact form. The Helmholtz term in Eq. (25) fortifies the diagonal of the system matrix and adds stability to the iterative procedure, enhancing convergence. Its magnitude increases as the dependence of density on pressure increases and as the time step decreases ($\Delta t < 1$). In the limit of isothermal flow, the Helmholtz equation retains its form but behaves much like the pressure Poisson equation for incompressible constant density flow with some preconditioning to fortify the diagonal term. In this case, density retains its relationship to the pressure. The Helmholtz equation is also solved iteratively by using a Conjugate Gradient Method. A zero gradient condition is applied at all boundaries. Like any other decoupled iterative algorithm, at each visit to the pressure equation, it is only necessary to relax the pressure field toward a final solution. In order to do that as efficiently as possible the following rules are established for pressure convergence, at which point the pressure solution is considered adequate and the calculation continues to the next step:

1. If the residue drops by 10^{-1} and the current residue is less than 10^{-4}
2. If the residual drops below 10^{-6}
3. If the solver iterates through the set maximum number of iterations.

This set of rules essentially keeps the pressure residue between 10^{-4} and 10^{-6}, although it could become much less, especially in steady state cases.

In all cases, the initial pressure field is set to a reference pressure, as is the initial temperature field. In confined closed domains with heat addition at the boundaries and large temperature changes over the course of the calculation, the pressure will maintain the relationship with temperature as defined by the equation of state. If the temperature changes significantly from the

initial temperature field, the pressure will change correspondingly. On the other hand, in open domains, the pressure is made to maintain the initial reference pressure at an appropriate location by setting the pressure correction to zero at that location, as is done in fully-incompressible flow solvers. Unlike most low Mach number algorithms, in which the thermodynamic pressure is only a function of time and evolves based on a global energy conservation, the pressure in the current algorithm is not uniform over the domain but can exhibit local variations based on the density and velocity fields[2].

Step 6 – Update Density

Once the pressure has been updated to $P^k = P^{k-1} + P'$, a new density is calculated based on the updated pressure.

$$\rho^k = \frac{P^k}{RT^k} = \frac{\left(P^{k-1} + P'\right)}{RT^k} = \frac{\rho_{ref} {U_{ref}}^2 P^k + P_{ref}}{\rho_{ref} R\left(T^k \cdot T_o + T_{ref}\right)} = \widetilde{\rho}^k + \frac{\rho_{ref} {U_{ref}}^2}{\rho_{ref} R\left(T^k \cdot T_o + T_{ref}\right)} P' \tag{26}$$

Hence the density is first updated based only on temperature changes (Eq. (16)) and is then corrected to account for changes in the thermodynamic pressure.

Step 7 – Update Cell face fluxes and Nodal Velocities

In this step, the cell face fluxes and the nodal velocities are updated using the calculated gradient of the pressure correction field. The cell face fluxes are updated as:

$$\boldsymbol{C}^k = \widetilde{\boldsymbol{C}}^k - \Delta t \nabla P' \tag{27}$$

using a compact gradient operator. To update the nodal velocities, however, the pressure must be interpolated onto the faces to calculate the gradient in Eq. (28):

$$\rho^k \boldsymbol{u}^k = \widetilde{\rho}^k \widetilde{\boldsymbol{u}}^k - \Delta t\left(\nabla P'\right) \tag{28}$$

[2] For steady state flows, the spatial variation of dimensional pressure is much smaller than the mean value of pressure in the domain.

Since the density at the nodes is known, it follows to calculate the nodal velocities from Eq. (28) as follows:

$$\boldsymbol{u}^k = \frac{\tilde{\rho}^k \tilde{\boldsymbol{u}}^k}{\rho^k} - \frac{\Delta t}{\rho^k}\left(\nabla P'\right) \tag{29}$$

Step 8 – Check for Convergence

The state of convergence is estimated by checking the average $\mathbf{L_2}$ norm of the change in the dependent variable from iteration *k-1* to *k* as $\|\boldsymbol{\phi}^k - \boldsymbol{\phi}^{k-1}\| \leq 1 \times 10^{-5}$, where $\phi = \boldsymbol{u}$, ρ and T. Typically, mass residues are of order 1×10^{-6} or smaller at convergence. If all dependent variables satisfy this criterion then the calculation moves to the next time step. If the change is larger than the tolerance, then the inner iterative loop is repeated once again.

7.04 Calculation Results

A number of test cases are presented in this section for validation of the algorithm and its ability to predict both steady and unsteady flows. Two main flow types are considered: Rayleigh-Bénard convection, which is flow in a rectangular enclosure with two opposite walls at different temperatures, and Poiseuille-Bénard flow, which is low-speed channel flow with the bottom wall heated and top wall cooled.

To facilitate comparison with previous studies, a nondimensional temperature difference ratio is defined. This parameter is a measure of the difference in temperature between the two walls and the reference temperature, defined by the following equation in dimensional and nondimensional form:

$$\epsilon = \frac{T_H^* - T_C^*}{T_H^* + T_C^*} \text{ (dimensional) } \& \ \epsilon = \frac{1}{2}\left(T_H - T_C\right) \text{ (nondimensional).} \tag{30}$$

This parameter is used as an input, and the hot and cold temperatures are calculated symmetrically about the average temperature:

$$T_H^* = T_o^*(1+\epsilon) \;\&\; T_C^* = T_o^*(1-\epsilon). \tag{31}$$

Rayleigh-Bénard Convection

In a case presented as a numerical benchmark study by Davis (1983), a square enclosure with the left wall heated to some temperature T_H, the right wall kept constant at some temperature T_C, and thermally insulated top and bottom walls was presented as a test case for comparing computational results with each other. Figure 7.2 describes the domain and the boundary conditions implemented on the domain. Four Rayleigh numbers, all of which lie in the Boussinesq regime, were compared in the study: Ra = 10^3, 10^4, 10^5, and 10^6. All of these produce steady-state results, and comparisons are made with reported values of velocity, streamfunction, temperature, vorticity, and heat transfer. Adequate comparison with the quantities in this study shows that the algorithm is capable of reproducing results in the Boussinesq regime, which creates a baseline for comparisons with higher temperature cases as well as unsteady calculation results.

A non-uniform grid of size 161 × 161 was used in the calculation. Initially the temperature in the domain was set to the average of the hot and cold temperatures with zero velocities. A series of tests showed the maximum allowable time step to be 0.057, which yielded a viscous stability number ($\nu\Delta t(1/\Delta x^2+1/\Delta y^2)$) of 8.5, a convective CFL number ($\Delta t / (\Delta x/u + \Delta y/v)$) of 2.6, and an acoustic CFL number, which is based on the speed of sound instead of the convective velocity, of 5555. Each linear system was relaxed to a residual of 1.0×10^{-6} before continuing.

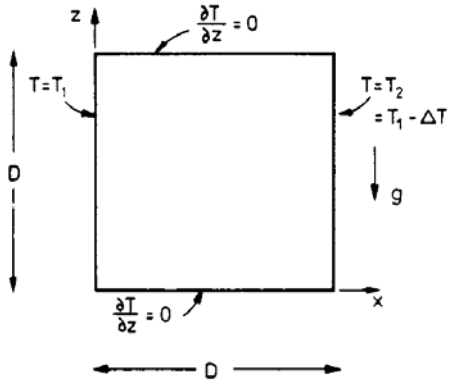

Figure 7.2. A square cavity with differentially heated vertical side walls and adiabatic top and bottom walls is used to validate the variable density calculation results in the steady Boussinesq regime.

A steady state was assumed to be reached when the change in the L2 norm of the velocities reached a tolerance below 1.0×10^{-5} and the density and temperature reached a tolerance below 1.0×10^{-6}. A steady state solution was reached in approximately 100 time units, but each calculation was run to 200 time units to ensure a steady state solution.

Comparisons of calculation results among three calculations at $Ra = 10^6$ are given in Table 7.1. The first calculation listed is that of Davis, and it serves as the benchmark for this study. The second is a calculation with the incompressible code GenIDLEST (Tafti, 2001), which has been extensively validated in calculations of louvered fin heat exchangers (Zhang and Tafti, 2003) and gas turbine blade internal cooling ducts (Tafti, 2005), and the third calculation is the present variable property formulation. The first two calculation results were obtained from incompressible codes using the Boussinesq approximation to account for density changes due to heating. The grid size used by Davis was 81×81, and the grid size used by GenIDLEST was 96×96. Both grid sizes were simulated with the variable property algorithm and showed negligible differences in the results. The quantities compared in the table include the magnitude of the streamfunction ($|\Psi|$), the maximum horizontal (u) and vertical (w) velocities, and average,

maximum, and minimum Nusselt numbers. The locations are also given in terms of the horizontal position (x) and the vertical position (z).

Table 7.1. Velocity and Heat Transfer Comparisons with Davis (1983) at Ra = 10^6

Quantity	Davis	GenIDLEST	Variable Density Algorithm
$\lvert\Psi_{mid}\rvert$	16.530	---	16.340
$\lvert\Psi_{max}\rvert$	16.961	---	16.381
x	0.1510	---	0.1450
z	0.5430	---	0.5376
u_{max}	65.330	64.933	64.892
z	0.8510	0.8539	0.8407
w_{max}	216.750	212.908	217.711
x	0.0387	0.0416	0.0251
Nu_{avg}	8.928	9.030	9.006
Nu_{max}	18.076	18.443	18.702
z	0.0456	0.0310	0.0310
Nu_{min}	1.005	1.021	0.974
z	1.0000	1.0000	1.0000

Additional comparisons at Ra = 10^6 show the algorithm's ability to reproduce quantities throughout the domain, not just minima, maxima, and averages. A comparison of the nondimensional temperature ($T^* = (T-T_C)/(T_H-T_C)$) contours is shown in Figure 7.3. The scales on each comparison are identical for exact comparison, and the variable density algorithm is shown to reproduce the previous calculated results exactly. Additional comparisons of velocity components, streamfunction, and vorticity also showed excellent agreement.

Rayleigh-Bénard convection in enclosures with a significantly large temperature difference between the two walls cannot be accurately simulated with the Boussinesq approximation. Variable properties must be used to accurately calculate the flow and heat transfer characteristics because inertial mass can no longer be neglected.

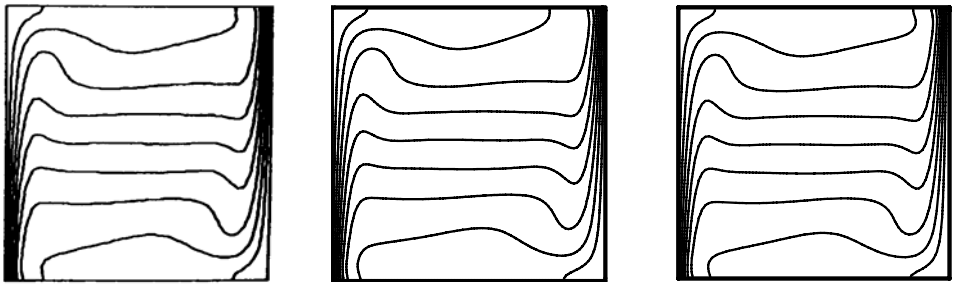

Davis (1983) (a) | GenIDLEST (b) | Present Study (c)

Figure 7.3. Temperature contour comparisons among (a) Davis (1983), (b) GenIDLEST (middle), and (c) the variable density algorithm at Ra = 10^6 show the capability of the algorithm to predict low temperature results.

Heuveline (2003) presented a high-order finite element simulation of the heat transfer in a square enclosure (same geometry as Davis) with Rayleigh numbers of 10^6 and 10^7 with large temperature differences. The algorithm used the low Mach number approximation to compute steady flows for the two Rayleigh numbers. The temperatures and length scales used to obtain the same temperature differences and Rayleigh numbers as those of Heuveline are shown in Table 7.2.

Table 7.2. Input Parameters Used for Comparisons with Heuveline (2003)

Ra	ϵ	T_{ref}	T_C	T_H	L
10^6	0.01	300 K	297 K	303 K	0.12105 m
10^6	0.60	600 K	240 K	960 K	0.06863 m
10^7	0.60	600 K	240 K	960 K	0.14784 m

This case was more computationally demanding because of the large density variations. The maximum allowable time step was found to be 0.035, which yielded a viscous stability number of 14, a convective CFL of 2.1 and an acoustic CFL of 5500. The number of iterations required

for convergence was more than an order of magnitude larger than the low temperature difference case.

In Figure 7.4, the Nusselt number distribution at the hot and cold walls for the different Rayleigh numbers is compared with that of the present study. Figure 7.4(a) shows a comparison with the low temperature results at Ra = 10^5. Under these conditions, the heat transfer curves are symmetric on the hot and cold walls. Figure 7.4(b) shows the high temperature differences at larger Rayleigh numbers (Ra = 10^6 & 10^7). In Heuveline's and many previous studies with variable properties, the local Prandtl number and specific heat are assumed constant. The viscosity is determined by Sutherland's law, and the variation of thermal conductivity varies at the same rate to keep the Prandtl number constant. In the present study, the local Prandtl number is not assumed to be constant, and all property variations are calculated from constitutive relationships. However, in the comparison with Heuveline the Prandtl number is held constant to obtain an adequate comparison. The value of the Prandtl number used by Heuveline was 0.71, while that used in the present study was calculated directly from the property values at the reference temperature at 600K and came out to a value of 0.686. The overall comparison is very good, with some minor differences in the predicted maxima on the hot and cold walls at Ra = 10^6.

Figure 7.5 shows the time evolution of dimensional pressure for three different high Rayleigh number cases. Figure 7.5(a) shows a case in which the initial field is at the same temperature as the cold wall, 300K, and the hot wall has a temperature of 500K. As the flow develops, the pressure maintains the relationship determined by the ideal gas law. The dimensional pressure is initially at a pressure of 101kPa, and as the temperature rises and the density decreases, the pressure approaches a steady state value of approximately 177kPa.

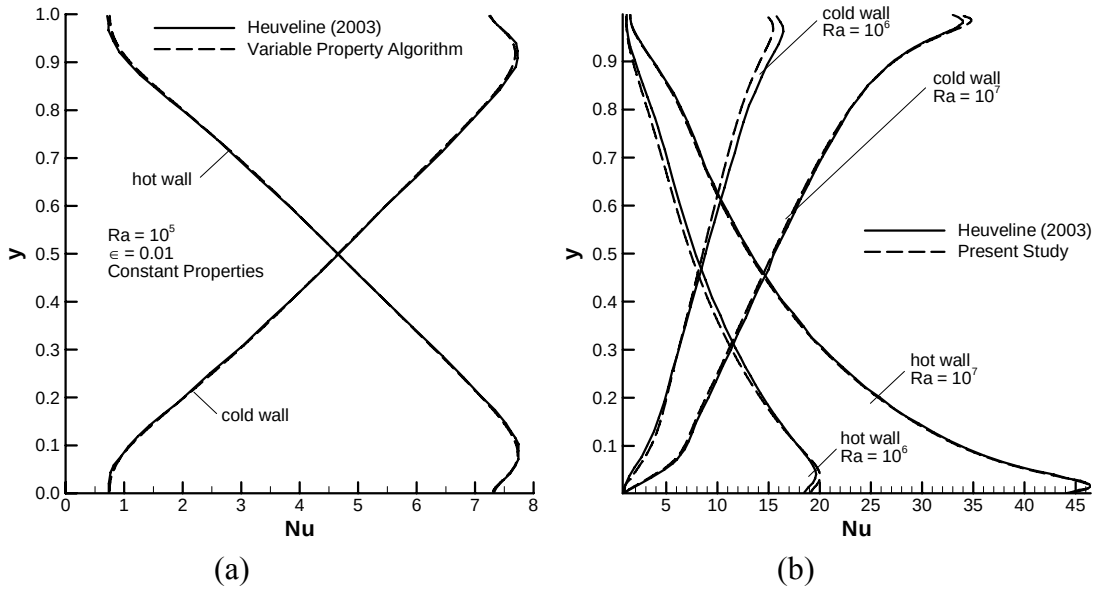

Figure 7.4. A comparison with the high-order (a) low temperature and (b) high temperature results of Heuveline (2003) shows good agreement between the two calculations.

In Figure 7.5(b), the initial field is also at rest at an initial pressure of 101kPa, but the initial temperature is at 600K, which is the mean value of the hot and cold walls, which have temperatures of 960K and 240K, respectively. As the temperature and density fields develop, the pressure again maintains the ideal gas law relationship and reaches a steady state value of approximately 92% of the reference pressure. This number compares well with the steady state thermodynamic pressure predicted by Vierendeels et al. (2001) and Heuveline (2003), in a comparison shown in Table 7.3. It is important to note that the value shown by Vierendeels comes from the pressure averaged over the domain, while the pressure given by Heuveline is the thermodynamic pressure which is assumed constant over the domain as a result of the low Mach number approximation. The pressure ratio from the present study is a local pressure measurement at the mid-height of the domain that is found to be a good representative of the

overall pressure. Despite these differences, the values of steady state pressure compare quite well with each other.

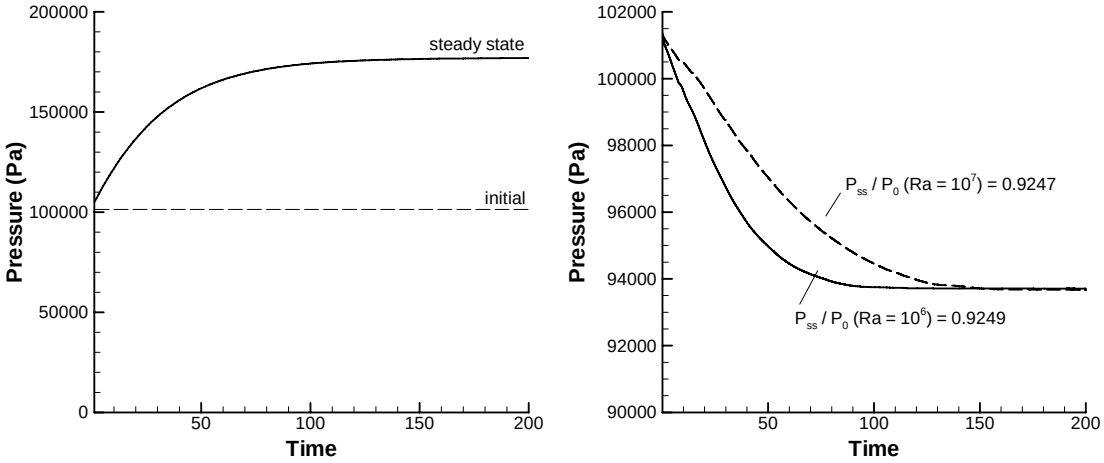

Figure 7.5. The area-averaged pressure from (a) a calculation with an initial temperature field equal to the cold wall temperature and (b) the initial temperature equal to the mean temperature shows the evolution of pressure with time. When the initial temperature is equal to the average of the two wall temperatures, the steady state pressure is found to be approximately 92% of the reference pressure.

Table 7.3. Steady State Pressure Ratio Comparison

Ra	Vierendeels et al. (2001)	Heuveline (2003)	Present Study
10^6	0.9245	0.9244	0.9225 (-0.2%)
10^7	0.9226	0.9226	0.9191 (-0.4%)

Table 7.4 shows a series of comparisons of point and average values of those high temperature Rayleigh-Bénard cases shown in Figure 7.4(b) with the benchmark numerical study of Vierendeels et al. (2003), in which steady state solutions were calculated on a stretched grid with a resolution of 1024 × 1024. The Prandtl number in the study was set to a value of 0.71,

and the local Prandtl number was held constant, forcing the thermal conductivity to vary at the same rate as dynamic viscosity. To compare with this study, the same variation of thermal conductivity was implemented into the calculation in the present study, and a calculation with a grid size of 160 × 160 was used to produce results for comparison. Comparisons of maximum, minimum, middle, and average values of Nusselt number are given on both the left (hot) and right (cold) walls. In addition, the steady state pressure is compared, along with minimum and maximum velocities and local maxima of the streamfunction and their locations as defined by Vierendeels. The reference velocity of Vierendeels varies from that of the present study by a factor of the square root of the Prandtl number, so the results of Vierendeels have been adjusted to those of the present study. Overall the comparisons agree very well with the high resolution benchmark calculations.

Another case in which high temperature differences are often encountered is in tall vertical slots with differential heating. A study by Chenoweth and Paolucci (1985) reported analytical solutions of the equations of motion for steady state high aspect ratio vertical slots with closed ends. The absence of end effects and the presence of one-dimensional flow (horizontal flow=0) were assumed to allow for the calculation of the analytical solution. A normalized vertical velocity was presented for a number of different temperature ratios.

For comparison purposes, a high-aspect-ratio calculation with the variable property algorithm was used to reproduce the analytical results. The calculation domain, grid coordinates, and boundary conditions were the same as those shown in Figure 7.2, except the aspect ratio of the enclosure (W:H), which was 1:16.

Table 7.4a. Comparison of the Benchmark Calculation of Vierendeels (2003) with Values from the Present Study at Ra = 10^6

Ra = 10^6			
Quantity	**Vierendeels (2003)**	**Present Study**	**% Difference**
Hot Wall			
Nu_{max}	20.270	20.271	(0.0%)
Nu_{min}	1.067	1.069	(+0.2%)
Nu_{mid}	7.459	7.447	(-0.2%)
Nu_{avg}	8.687	8.681	(-0.1%)
Cold Wall			
Nu_{max}	15.519	15.626	(+0.7%)
Nu_{min}	0.758	0.758	(0.0%)
Nu_{mid}	8.637	8.633	(-0.1%)
Nu_{avg}	8.687	8.681	(-0.1%)
$P_{steady\ state} / P_{ref}$	0.9245	0.9225	(-0.2%)
Midline Velocities			
v_{max} (y = 0.5)	0.2699	0.2738	(+1.4%)
v_{min} (y = 0.5)	-0.2529	-0.2552	(+0.1%)
u_{max} (x = 0.5)	0.1005	0.1041	(+3.6%)
u_{min} (x = 0.5)	-0.0672	-0.0681	(+1.3%)
Streamfunction			
Ψ_{mid} (0.5000,0.5000)	0.0186	0.0188	(+1.0%)
Ψ_{max1} (0.8688,0.3926)	0.0198	0.0200	(+1.0%)
Ψ_{max2} (0.2081,0.6477)	0.0195	0.0197	(+1.0%)
Ψ_{max3} (0.8880,0.1458)	0.0179	0.0182	(+1.7%)

Table 7.4b. Comparison of the Benchmark Calculation of Vierendeels (2003) with Values from the Present Study at Ra = 10^7

Ra = 10^7			
Quantity	**Vierendeels (2003)**	**Present Study**	**(160 × 160 Grid)**
Hot Wall			
Nu_{max}	46.379	47.010	(+1.4%)
Nu_{min}	1.454	1.462	(+0.6%)
Nu_{mid}	13.188	13.202	(+0.1%)
Nu_{avg}	16.241	16.295	(+0.3%)
Cold Wall			
Nu_{max}	34.269	35.200	(+2.7%)
Nu_{min}	1.089	1.091	(+0.2%)
Nu_{mid}	15.512	15.523	(+0.1%)
Nu_{avg}	16.240	16.295	(+0.3%)
$P_{steady\ state} / P_{ref}$	0.9226	0.9191	(-0.4%)
Midline Velocities			
v_{max} (y = 0.5)	0.2721	0.2767	(+1.7%)
v_{min} (y = 0.5)	-0.2537	-0.2548	(+0.4%)
u_{max} (x = 0.5)	0.0631	0.0649	(+2.9%)
u_{min} (x = 0.5)	-0.0432	-0.0439	(+1.6%)
Streamfunction			
Ψ_{mid} (0.5000,0.5000)	0.0126	0.0108	(-14.3%)
Ψ_{max1} (0.0989,0.5016)	0.0111	0.0112	(+0.9%)
Ψ_{max2} (0.1639,0.8211)	0.0102	0.0104	(+2.0%)
Ψ_{max3} (0.2798,0.4556)	0.0108	0.0109	(+0.9%)
Ψ_{max4} (0.8009,0.0419)	-0.0001	-0.0001	(0.0%)
Ψ_{max5} (0.8040,0.4301)	0.0109	0.0110	(+0.9%)
Ψ_{max6} (0.8807,0.1765)	0.0078	0.0079	(+1.3%)
Ψ_{max7} (0.9207,0.0793)	0.0093	0.0094	(+1.1%)
Ψ_{max8} (0.9256,0.3909)	0.0112	0.0113	(+0.9%)

The fully developed region was determined to be in a large section at the mid-height of the enclosure, where the horizontal velocity was nearly zero and no changes were observed in the vertical velocity profile over a range of about 20% of the enclosure. The grid size of the calculation was 60 × 960, and the dimensional calculation inputs are shown in Table 7.5.

Table 7.5. Calculation Inputs for Comparison with Chenoweth and Paolucci (1985).

ϵ	T_{ref}	T_H	T_C	L	Ra
0.005	600 K	603 K	597 K	0.00800 m	13
0.200	600 K	720 K	480 K	0.00800 m	528
0.400	600 K	840 K	360 K	0.00800 m	1056
0.600	600 K	960 K	240 K	0.00686 m	999

A non-dimensional time step of 0.01 was used for the calculation, which resulted in a viscous stability number of 5, a maximum convective CFL of 0.21 and an acoustic CFL of 410. In this case the pressure equation was relaxed at each inner iteration to a residual of 1.0×10^{-5} while the tolerance for estimating a steady state solution was set to 1.0×10^{-6} for velocity changes and 1.0×10^{-7} for density and temperature changes.

A comparison of the analytical results of Chenoweth and Paolucci (1985) and the calculated results, which are scaled by a factor of Ra/12 to match the analytical results, is shown in Figure 7.6. In the case with the smallest temperature difference ($\epsilon = 0.005$), the vertical velocity profile is completely symmetric because the velocities are influenced almost entirely by the temperature differences. However, as the temperature difference increases, a break in symmetry comes as a result of property variations across the domain. Despite the fact that the total heat flow at the hot and cold walls is equal, the heat flux distribution on the hot and cold walls becomes increasingly

nonuniform for increasing temperature differences (1985). As a result, an asymmetry develops in the velocity profile and is predicted well by the variable property algorithm.

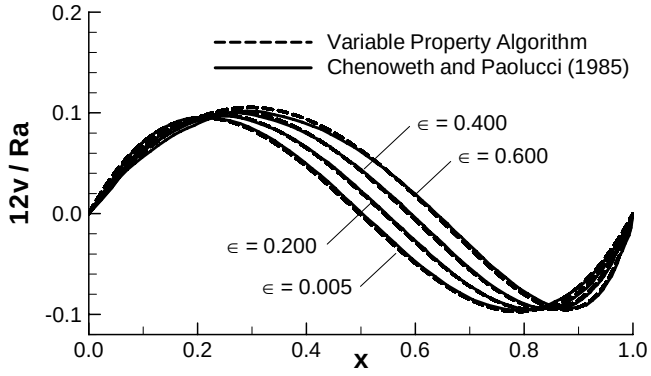

Figure 7.6. Comparisons with the analytical results of Chenoweth and Paolucci (1985) show excellent agreement. The hot wall is at $x = 0.0$, and the cold wall is at $x = 1.0$.

Poiseuille-Bénard Flow

A common internal flow used for validating unsteady codes is that of channel flow between two infinite parallel plates. In this case, a comparison is made with experiments at low Reynolds number in which the bottom plate is heated to a constant temperature that is greater than that of the top plate. The Reynolds number and Rayleigh number both play an important role in the flow characteristics, as they determine the proportion of forced convection effects to natural convection in the flow. A diagram of the calculation domain and boundary conditions is shown in Figure 7.7.

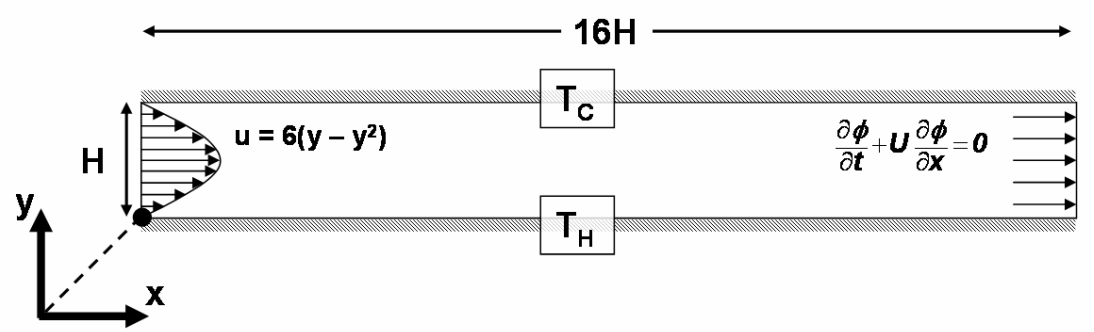

Figure 7.7. The Poiseuille-Bénard domain has a laminar fully developed profile at the inlet and a convective outflow boundary condition. The bottom wall is heated and the top wall is cooled.

A flow visualization study by Yu et al. (2003) showed the onset of longitudinal instabilities in a heated channel flow by using smoke visualization. In one case, in which Re = 5 and Ra = 4,000, seven time frames 1.23 seconds apart were reported. To compare with the measurements, a calculation matching the same Reynolds number and Rayleigh number was used to produce an unsteady set of time frames. A grid dependence study was conducted to determine the minimum grid spacing needed to adequately capture the unsteady motions. In Figure 7.8, a comparison of the time history of streamwise velocity and temperature at the mid-height of the channel and four channel heights downstream of the inlet shows the effect of grid size on the unsteady flow characteristics. The grid spacing is uniform in the streamwise direction and is concentrated near the walls in the vertical direction. Five different grids are compared in the figure, the grid size of 481 × 61 was considered adequate for the study, given that the two larger grids were more expensive computationally and did not produce significantly more accurate results.

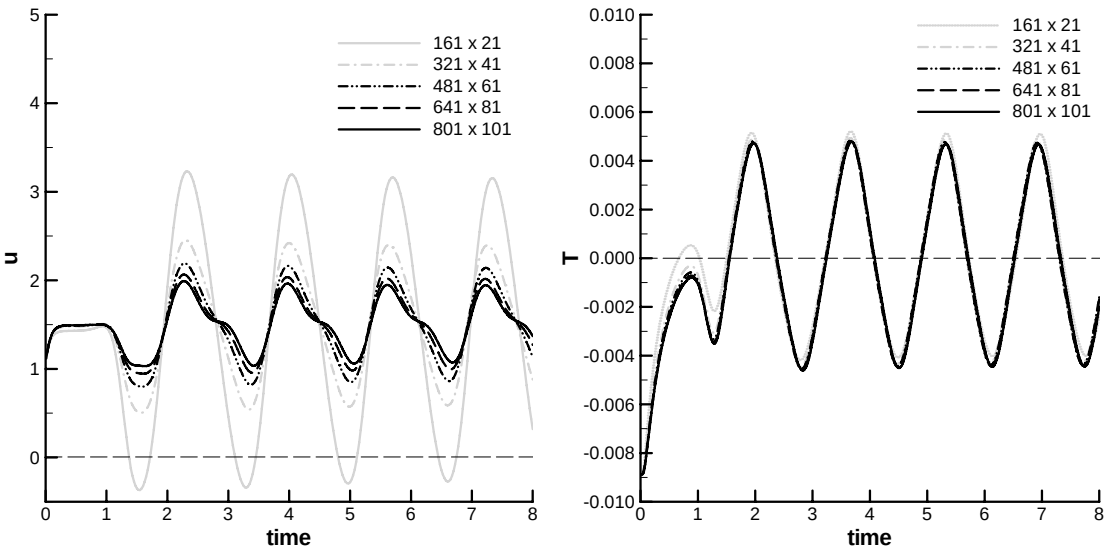

(a) (b)

Figure 7.8. A comparison of three different grid sizes shows that the finer two grids produce similar results, though the highest resolution shows a slight improvement.

The magnitude of the streamfunction from the calculation and the smoke visualization photographs of Yu et al. are compared in Figure 7.9. As seen in the comparison, the size, shape, and convective velocity of the vortex patterns are identical. Also, the formation of a new convective roll at the location where heating begins (but with hydrodynamically fully developed flow) is similar in both cases.

An incompressible flow calculation by Evans and Paolucci (1990) employed the SIMPLER method to calculate the unsteady flow and heat transfer in a heated channel by using the Boussinesq approximation. The calculations were first order accurate in time but used a time step small enough to capture the physics accurately. Richardson extrapolation was used in both space and time to produce converged results for validating unsteady algorithms in buoyant flows. The Reynolds number used in the calculation was 10, and the Prandtl number was 2/3. The Froude number ($Re^2 \cdot Pr / Ra$) was set to 1/150, resulting in a Rayleigh number of 10,000.

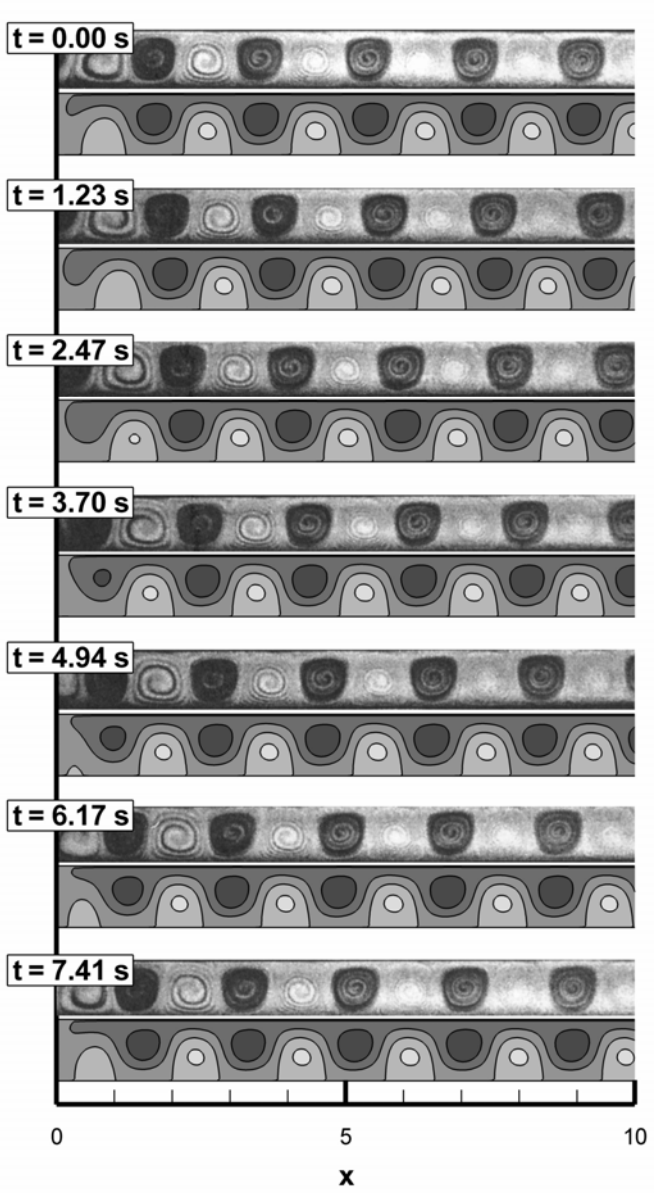

Figure 7.9. A comparison with the unsteady flow measurements of Yu et al. (1997) and the magnitude of the streamfunction from the calculation shows the time-accuracy of the calculation.

The calculation domain was 20 channel heights long, and unsteady results were presented at a time when the temperature at the mid-height of the duct five hydraulic diameters downstream of the inlet reached a minimum.

A heated channel flow calculation was used to compare with the benchmark study by matching the nondimensional numbers. The Mach number in the calculations was 1.0×10^{-5}. The grid used was 16 channel heights long and consisted of 61 grid points in the vertical direction clustered near the walls and 721 evenly spaced grid points in the streamwise direction. A time step of 0.001 was used for accurate time-resolution. The maximum convective CFL number reached in this case was 0.33.

A series of comparisons between the calculations and the benchmark solutions of Evans and Paolucci (1985) is shown in Figure 7.10. Two locations are compared, one at $x = 5$ (five channel heights downstream of the entrance) and the other at $x = 10$. Because the wavelength was underpredicted by 1.8% (1.421 instead of 1.447), the calculation data is actually shown at $x = 4.95$ & 9.93 instead of $x = 5.00$ & 10.00. The time frame shown is that point at which the temperature at the mid-height of the duct and five channel heights downstream of the inlet is a minimum. Figure 7.10(a) shows this to occur when the vertical velocity is at a strong negative value and flow is directed towards the bottom wall at $x = 5$, while a strong positive vertical velocity shows flow directed towards the top wall at $x = 10$. The streamfunction (Figure 7.10(b)) shows the increased fluid motion near the top wall as compared to the bottom wall. In the temperature comparison in Figure 7.10(c), the temperature used by Evans and Paolucci is nondimensionalized differently than that in the present study, and the comparison is reported as a temperature normalized by the difference between the hot and cold wall temperatures instead of the mean temperature. The temperature profile in Figure 7.10(c) shows the steep gradient near the hot wall as opposed to the more shallow change near the cool wall on top.

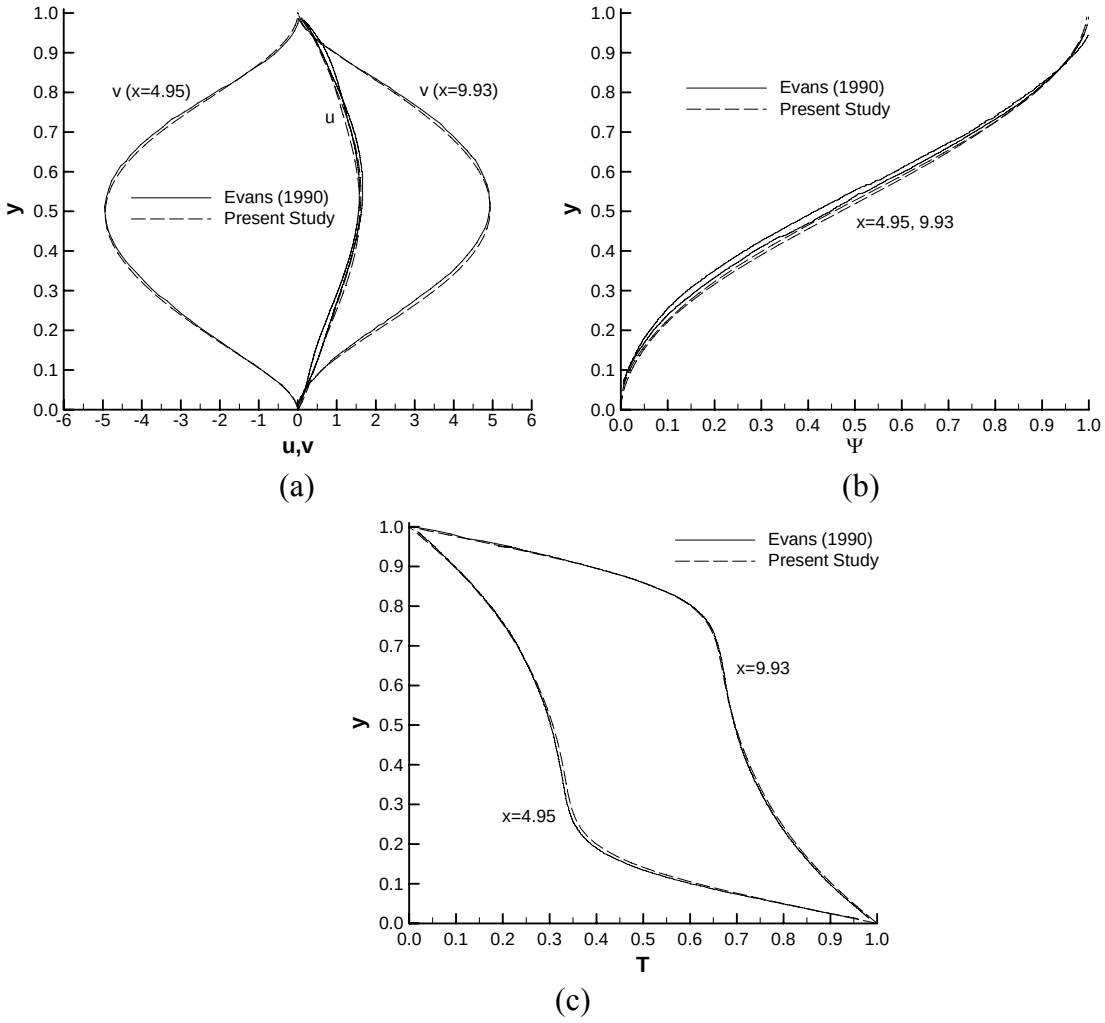

Figure 7.10. A comparison between an unsteady calculation and the calculations of Evans and Paolucci (1990) of (a) the streamwise and vertical velocities, (b) the streamfunction, and (c), the temperature show the ability of the algorithm to capture unsteady flows.

Figure 7.11 shows the time evolution of the centerline temperature five channel heights downstream of the entrance for one period. The initial time was set to $t = 4.592$ to correspond with the initial value of the temperature reported by Evans and Paolucci (1990). The agreement between the two calculations shows that the present algorithm accurately predicts the temporal behavior of the temperature. The temporal period of oscillation was predicted by the highest resolution calculation of Evans and Paolucci to be 1.306, which is 3.7% greater than that

predicted by the present study, which is 1.260. The difference is not visible in the comparison in Figure 7.11, however.

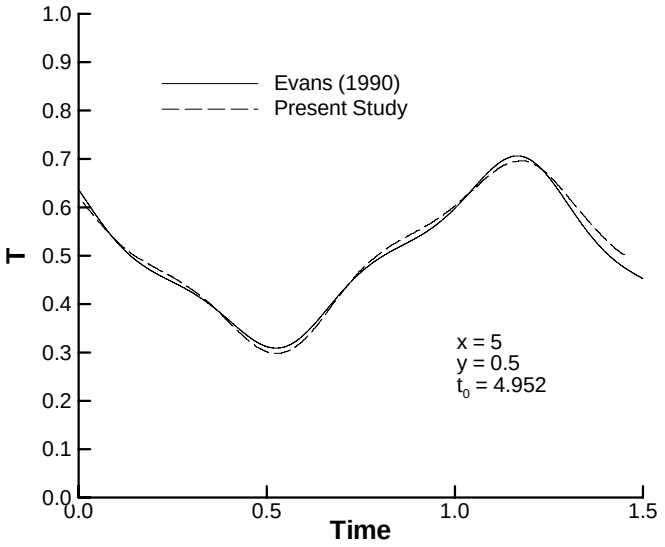

Figure 7.11. A time period of temperature at the midheight of the duct is predicted well by the variable property algorithm, as shown by the comparison with the calculations of Evans and Paolucci (1990).

7.05 Summary and Conclusions

A low speed algorithm is developed for time-accurate calculations of both forced and natural convection with large temperature gradients. The non-linear coupled set of equations with property variations is resolved by an implicit iterative procedure at each time step. The momentum and energy equations are integrated in time using an implicit Crank-Nicolson method, and a Helmholtz equation for pressure is solved at each inner iteration. Unlike most low Mach number approximations, the full pressure field is calculated. Density dependency on both local temperature and pressure is resolved through an equation of state, whereas dynamic viscosity and thermal conductivity are only dependent on temperature.

The stability and accuracy of the algorithm is validated in Rayleigh-Bénard convection with large temperature differences and in Poiseuille-Bénard flow in a heated parallel plate channel. In both cases, steady and unsteady solutions show excellent comparisons with previous benchmark numerical studies, analytical solutions, and experimental measurements.

Chapter 8. Summary and Conclusions

LES calculations of flow and heat transfer have been presented for three different flow conditions: stationary, rotating with Coriolis effects, and rotation with Coriolis and centrifugal buoyancy forces. Two domains have been studied in this project, the first of which is the developing flow domain, where the onset of secondary flows, the development length, the high and low heat transfer regions, and the effects of rotation have been discussed. In the 180^o bend, calculation results have explored the impact of the bend on the flow in the downstream duct. The impact of rotation on the separated vortex in the bend has been discussed, and the changes in turbulence and heat transfer have been related to flow structures, as well. The following conclusions from this project have been drawn from the three different flow regimes:

8.01 Stationary Ducts

In stationary ducts, the primary mechanism of heat transfer augmentation is the generation of unsteady vortical structures in separated shear layers on ribs and at rib junctions with the ribbed and smooth walls. The unsteady vorticity, which continuously replenishes and mixes fluid in wall boundary layers, manifests itself in the mean as increased turbulent intensity in boundary layers. While secondary flows in the duct cross-section and the 180^o bend have a large impact on heat transfer, they do not have as large an impact on frictional losses, which are dominated by form losses.

Among the major flow features predicted with accuracy are shear layer transition at the entrance of the duct; the distribution of mean and turbulent quantities in the developing, fully developed, and 180^o bend; the development of secondary flows in the duct cross-section and the

180º bend; and friction and heat transfer augmentation. In all different aspects, it is found that LES produces the correct physics both qualitatively and quantitatively to within 10-15%.

Two comparisons with different inlet conditions showed that the exact nature of the hydrodynamic inlet conditions does not have a big impact on the friction and heat transfer augmentation downstream of the second rib. Similar trends were found in the calculations after the third rib, with the exception of the heat transfer at the center of the smooth wall, which takes a longer time to develop and had a slightly higher value in the calculation with the fully developed turbulent inlet.

The flow development length was a primary consideration in the developing flow calculations, and it was found that the mean flow velocities reach a near fully developed state by the fourth or fifth rib downstream of the entrance to the duct. Turbulence was found to be nearly fully developed in the vicinity of the ribbed wall by the third or fourth rib, however, it was not fully developed at the center of the duct until approximately 10 ribs downstream of the inlet. The development of mean flow and turbulence has a direct effect on the development of the heat transfer coefficient. Heat transfer coefficients at the ribbed wall reach a fully developed state after the third rib, reflecting the short development length of flow and turbulence along the ribbed wall. The smooth wall, on the other hand, exhibits fully developed augmentation ratios in the vicinity of the ribbed wall but lower augmentation ratios at the center of the channel. Hence, the smooth wall shows a slight but steady increasing trend in the surface averaged heat transfer augmentation up to the sixth rib in the calculation. However, it is within 10% of its fully developed value.

The friction factor exhibits a very large value across the first rib, reflecting a very large pressure drop. A pressure recovery occurs across the second rib, however, and the following ribs

settle into consistent pressure drops with values similar to the fully developed values. Because the pressure drop has been determined to be caused primarily from form drag, the friction factor develops quickly, within a few ribs, as opposed to some heat transfer characteristics, such as the side wall heat transfer, which is dependent on secondary flows and takes longer to develop.

Subtle characteristics of mean flow and turbulent quantities have a long development length. However, from a design engineer's perspective, the friction and heat transfer in the stationary ribbed duct are to within 10% of their fully developed values after the third rib.

In the stationary 180° bend region, a number of well-documented mean flow characteristics are observed. A pair of counter-rotating Dean vortices in the midplane of the bend are observed from a vector plot of the spanwise and cross-stream velocities. A large recirculation zone at the tip of the dividing wall is also shown to obstruct flow in the bend and accelerate it around the bubble along the back wall. A third characteristic of flow in the bend is a pair of vertical vortices found in the upstream and downstream corners of the bend.

The friction factor across the bend, including the two ribs upstream and two ribs downstream of the bend, compares extremely well with the friction factor measured from static pressure taps along the smooth wall of the bend. Overall, the value of the friction factor across the bend is approximately 2 ½ times larger than the fully developed friction factor in a straight ribbed duct.

A comparison of two calculations, one with a rib in the bend and one without a rib, shows that adding a rib to the bend increases the friction factor by 82%, while it only increases the heat transfer by 20%. Though the tradeoff is significant, it may still be advisable to place a rib in the bend if the 20% increase in heat transfer is worth the pressure loss incurred by doing so.

Comparisons with a number of flow and heat transfer measurements have proven LES to be a robust, reliable, and accurate prediction tool for flow and heat transfer characteristics in the

developing flow and 180° bend regions of internal cooling ducts. It predicts all the major flow features accurately, particularly secondary flows, which commonly used RANS two-equation eddy-viscosity models cannot reproduce. Presently, the computational expense of LES prevents it from being used in a design setting. However, the exponential increase in raw computing power is making LES more and more accessible for such purposes. Calculations such as those presented in Chapter 4 can be used as an establish benchmark for the rotating calculations.

8.02 Rotating ducts with Coriolis Effects

The time-averaged fluid flow, turbulence, and heat transfer augmentation have all been studied in the developing flow and 180° bend regions. Comparisons were made between a stationary duct and a duct with a constant rotation rate of Ro = 0.30.

In the developing flow, Coriolis forces were observed immediately through a shift in the size and shape of the recirculation zones downstream of the first rib. Turbulent kinetic energy was also increased immediately along the trailing wall, while the leading wall turbulence was attenuated immediately. Downstream, Coriolis effects shifted the velocity profile towards the leading wall, while a horizontal velocity profile showed that the maximum velocity was shifted away from the center towards the side walls.

Secondary flows in the rotating duct developed in shape and structure by the fourth rib. However, the strength of the secondary flows continued to increase up to the eighth rib. Secondary flows are stronger with rotation because of the cross-stream forces acting on the mean velocity, and this has implications on the mainstream velocity and on side wall heat transfer augmentation.

Heat transfer augmentation is enhanced on the trailing wall by Coriolis forces, which destabilize turbulence along the trailing wall and force cooler mainstream fluid towards the

trailing wall, both of which increase heat transfer. On the leading wall, turbulence is attenuated, and the fluid is drawn away from the wall, increasing the leading wall temperature and decreasing the heat transfer augmentation.

In the 180° bend, general expected trends of higher heat transfer along the trailing wall in the upstream duct and the leading wall in the downstream duct were continued as expected from the developing flow calculations. Within the bend, however, many less understood effects were explored, as well.

Rotation decreased the trailing wall streamwise momentum entering the bend and increased the heat transfer on the leading side of the back wall through stronger flow impingement. Turbulent kinetic energy coming out of the bend was increased by an approximate factor of three in both the stationary and rotating ducts. Immediately downstream of the first rib after the bend, the destabilizing effect of Coriolis forces at the leading wall was evidenced by a large increase in turbulent kinetic energy, with a corresponding attenuation at the trailing wall. An unexpected result was that the magnitude of turbulent kinetic energy coming out of the bend was not affected greatly by rotation and cross-sectional averages were slightly less than the stationary bend.

Rotation induced considerable asymmetries in heat transfer augmentation at all surfaces in the bend and downstream of it. The highest level of heat transfer was found at the leading outer wall immediately after the first rib downstream of the bend. High augmentation regions were also observed at the inner side of the trailing wall after the bend. Area-averaged heat transfer augmentation values showed similar values between the stationary and rotating cases upstream of the bend. However, within the bend the heat transfer in the rotating case was 15% less than that in the stationary case, but Coriolis forces did result in a higher heat transfer augmentation downstream of the bend because of the augmentation on the leading wall and side walls.

Overall, the friction factor across the bend was about two times the values encountered in the fully-developed section of the duct. It was found to decrease slightly in the presence of rotation, and the predicted values compared well with experiments.

8.03 Rotating Duct with Centrifugal Buoyancy Forces

The effect of centrifugal buoyancy has been observed in the developing flow and 180º bend domains. These results represent the best reproduction of realistic engine conditions in the project, where both Coriolis effects and centrifugal buoyancy forces act upon the fluid and impact the mainstream flow velocity and turbulence, which in turn are reflected by changes in the heat transfer augmentation.

In the developing flow, trailing wall turbulence and heat transfer augmentation were found to increase throughout the domain with an increase in the buoyancy parameter. The increase in wall-averaged heat transfer augmentation became greater as flow moved farther downstream of the inlet.

On the leading wall, the heat transfer augmentation decreased when the buoyancy parameter was varied from zero to Bo = 0.25. When the buoyancy parameter was increased beyond Bo = 0.25, however, the leading wall heat transfer increased. The LES calculations showed that at low buoyancy parameters the growth of the separated region behind each rib was responsible for the decrease in heat transfer augmentation. However, as the separated region spanned the full pitch between ribs with an increase in buoyancy parameter, it led to entrainment of fluid from the mainstream of the duct into the separated shear layer which was redirected by the rib downstream into the vicinity of the leading wall. The combined effect of an increase in turbulent fluctuations in the shear layer separating the recirculating region from the mainstream flow, increased entrainment of mainstream fluid, and subsequent redirection and impingement led to

an overall increase in heat transfer augmentation at the leading wall as the buoyancy parameter increased above 0.3.

In all calculations involving the buoyancy parameter, the Boussinesq approximation was used to linearly relate temperature differences to density variations in the buoyancy parameter. Despite this approximation, the LES calculations have proven to be capable of accurately predicting the subtle changes in heat transfer resulting from changes in buoyancy.

As the buoyancy parameter was increased, the leading wall recirculation zones increased in size, resulting in a greater form drag on the leading wall ribs. The friction factors in the bend were found to increase monotonically with buoyancy and this increase is attributed primarily to these increased form drag losses at the leading wall.

In the 180º bend, the effects of buoyancy were also studied in their relationship to the stationary and rotating (with no buoyancy) cases. Special attention was paid to the effects of buoyancy on the mean flow, since that, and not necessarily turbulence, has been described as the most important factor in determining the regions of peak heat transfer in the bend (Liou et al., 2000).

With a low buoyancy parameter, the velocity profile of the developing flow entering the bend is shifted towards the trailing wall, resulting in back wall flow impingement on the trailing side. The recirculation zone at the tip of the dividing wall is shifted towards the trailing wall. The mainstream flow experiences less resistance to flow downstream, resulting in a weakened back wall impingement. The secondary vortex near the leading wall in the midplane of the bend increases in size and strength, increasing flow impingement on the inside of the dividing wall.

With high buoyancy, the recirculation zone is greatly strengthened and shifts away from the dividing wall and up into the mainstream flow, where an extremely strong vortex increases flow

impingement on the dividing wall and on the inside part of the trailing wall. Mainstream flow is forced around the outside of this bubble and is strongly accelerated along the outside of the bend. Because of the increased size of the vortex, however, the mainstream flow experiences greater resistance to progressing downstream, producing very strong impingement on the back wall.

Coriolis effects shift the mainstream flow impingement on the back wall of the bend towards the leading side and decrease its magnitude. Low buoyancy causes the impingement flow to be shifted towards the trailing wall, and high buoyancy greatly increases the impingement flow velocity due to resistance of flow around the bend.

Area-averaged turbulent kinetic energy is increased across the bend in all cases, with the highest buoyancy producing the highest turbulence, but high buoyancy actually decreases the peak values of turbulence in the midplane of the bend by dispersing it throughout the cross-section, while the low buoyancy case produces a high peak turbulence near the dividing wall.

In the bend, the high buoyancy also results in higher heat transfer, but downstream the leading wall heat transfer is lower in the high buoyancy case than in the low buoyancy case, though trailing wall heat transfer continues to be higher at high buoyancy.

The area-averaged heat transfer augmentation over each group shows that increasing buoyancy results in a similar increase in heat transfer upstream, but downstream the high buoyancy parameter produces a lower heat transfer augmentation than in the low buoyancy case because of decreased leading wall heat transfer.

Rotation is found to decrease overall friction factor across the bend, but the high buoyancy case shows a dramatic increase in friction to a value 40% higher than the low buoyancy case. This is attributed to greater flow resistance because of the strengthened vortex that has shifted to the center of the bend at high buoyancy.

8.04 Development of a Variable Property Algorithm

A low speed algorithm is developed for time-accurate calculations of both forced and natural convection with large temperature gradients. The non-linear coupled set of equations with property variations is resolved by an implicit iterative procedure at each time step. The momentum and energy equations are integrated in time using an implicit Crank-Nicolson method, and a Helmholtz equation for pressure is solved at each inner iteration. Unlike most low Mach number approximations, the full pressure field is calculated. Density dependency on both local temperature and pressure is resolved through an equation of state, whereas dynamic viscosity and thermal conductivity are only dependent on temperature.

The stability and accuracy of the algorithm is validated in Rayleigh-Bénard convection with large temperature differences and in Poiseuille-Bénard flow in a heated parallel plate channel. In both cases, steady and unsteady solutions show excellent comparisons with previous benchmark numerical studies, analytical solutions, and experimental measurements.

8.05 Relevance to Gas Turbine Blade Design

From the standpoint of blade cooling design, a number of difficulties resulting from rotational effects have been described in this project. Coriolis forces augment turbulence on one wall and attenuate turbulence on an opposite wall, and centrifugal buoyancy forces have opposite effects with respect to flow direction. Both of these rotational effects cause a considerable imbalance in the heat transfer coefficients between the leading and trailing walls and between radially inward and radially outward flow directions. This proves to be especially problematic because the suction side heat transfer coefficients are often higher than the pressure side heat transfer, resulting in much higher leading wall temperatures. Typical internal cooling schemes in rotating ducts, such as the one presented in this project, produce increased heat transfer

augmentation on the trailing wall and decreased leading wall heat transfer, adding to the problems encountered due to the suction side wall temperature.

The detailed calculation results presented here are helpful in identifying the major flow structures that either enhance or decrease turbulence. It is well known that separation and the resulting turbulent shear layer increase heat transfer, but this effect is decreased on the leading wall as Coriolis effects draw momentum away from the ribs. Secondary flows force fluid along the side walls towards the leading walls, and increasing this effect, such as what occurs in the pressure driven secondary flows produced by 45º ribs, would counteract the Coriolis effects and help to redistribute the heat transfer augmentation among the leading and trailing walls. Other methods of generating turbulence in a low momentum fluid could also be considered as possibilities for increasing leading wall heat transfer augmentation. It has also been shown in fully developed calculations that the leading contributor of friction factor is form drag from the rib blockage (Abdel-Wahab and Tafti, 2004; Tafti, 2005), so avoiding the presence of large solid obstacles facing perpendicular to the flow direction would help decrease pressure losses.

The developing flow region showed that, even though flow and heat transfer effects developed quickly on the leading and trailing walls, rotation causes the side wall heat transfer development length to increase dramatically, often requiring more than 10 ribs (a significant portion of the channel length) to become completely fully developed because of the developing secondary flow magnitudes. The fully developed heat transfer augmentation should not be used as an approximation of side wall heat transfer in the developing flow region, especially in any cases where this is expected to be a significant contributor to overall heat transfer.

In the 180º bend, the separation zone at the tip of the dividing wall was found to influence the friction factor across the bend, the production of turbulence within the bend, and the degree of

impingement on the back wall (blade tip, for radially outward flow). Though the size of the recirculation zone contributes to the pressure drop, it also augments turbulence downstream of the bend and strengthens back wall impingement. Finding ways to control the size and shape of this recirculation zone (which is heavily dependent on rotation conditions) could aid a designer in controlling the balance between friction and heat transfer augmentation.

An in-depth knowledge of a ribbed duct flowfield can assist a cooling scheme designer in controlling the factors that augment heat transfer and decrease the losses. This project has shed light on the effects of rotation on the development of flow and heat transfer near the duct entrance. Additionally, some of the major contributors to overall heat transfer and friction in the duct are the 180º bends, and the dominating motions have been explored in that domain as well, especially in the presence of rotation. Understanding and controlling these major flow structures will assist in the development of new cooling schemes capable of cooling the future's advanced turbine blade designs.

Overall the calculation of large scale flows using LES calculations is still expensive and time-consuming. However, within a few years, the cost will quickly drop, as it always has. LES calculations are going to be a highly feasible alternative to RANS calculations for large-scale calculations, and this project was a step in that direction. The calculations have provided a clearer understanding of the relationship between flow, turbulence, and heat transfer augmentation in a rotating duct with 90º ribs, and they have provided the opportunity to explore the physics in an unprecedented framework of highly accurate, detailed calculations.

References

Chapter 2: Literature Review

Acharya, S., Dutta, S., Myrum, T.A., Baker, R.S., 1993, "Periodically Developed Flow and Heat Transfer in a Ribbed Duct," *International Journal of Heat and Mass Transfer*, **36**, pp. 2069-2082.

Ahn, J., Choi, Haecheon, C., Lee, J.S., 2004,"Large Eddy Simulation of Flow and Heat Transfer in a Channel Roughened by Square or Semicircle Ribs," Proceedings of the ASME Turbo Expo 2004, Vienna, Austria.

Al-Qahtani, M., Chen, H.C., Han, J.C., 2002, "A Numerical Study of Flow and Heat Transfer in Rotating Rectangular Channels (AR=4) with 45° Rib Turbulators by Reynolds Stress Turbulence Models," Proceedings of the ASME Turbo Expo, Amsterdam, The Netherlands, Paper no. GT-2002-30216.

Al-Qahtani, M., Jang, Y.J., Chen, H.C., Han, J.C., 2002, "Prediction of Flow and Heat Transfer in Rotating Two-Pass Rectangular Channels with 45° Rib Turbulators," *ASME Journal of Turbomachinery*, **124**, pp. 242-250.

Arts, T., Rau, G., Çakan, M., Vialonga, J., Fernandez, D., Tarnowski, F., Laroche, E., 1997, "Experimental and Numerical Investigation on Flow and Heat Transfer in Large-Scale, Turbine Cooling, Representative, Rib-Roughened Channels," Proceedings of Institution of Mechanical Engineers, **211**, pp. 263-272.

Astarita, T., Cardone, G., 2000, "Thermofluidynamic Analysis of the Flow in a Sharp 180° Turn Channel," *Experimental Thermal and Fluid Science*, **20**, pp. 188-200.

Astarita, T., Cardone, G., Carlomagno, G.M., 2002, "Convective Heat Transfer in Ribbed Channels with a 180° Turn," *Experiments in Fluids*, **33**, pp. 90-100.

Astarita, T., Cardone, G., 2003, "Convective Heat Transfer in a Square Channel with Angled Ribs on Two Opposite Walls," *Experiments in Fluids*, **34**, pp. 625-634.

Azad, G.S., Uddin, M.J., Han, J.C., Moon, H.K., Glezer, B., 2002, "Heat Transfer in a Two-Pass Rectangular Rotating Channel with 45° Angled Rib Turbulators," *ASME Journal of Turbomachinery*, **124**, pp. 251-259.

Baughn, J.W., Yan, X., 1992, "Local Heat Tranfer Mesuarements in Square Ducts with Transverse Ribs," ASME HTD, **202,** pp. 1-7.

Besserman, D.L., Tanrikut, S., 1992, "Comparison of Heat Transfer Measurements With Computations for Turbulent Flow Around a 180° Bend," *ASME Journal of Turbomachinery*, **114**, pp. 865-871.

Bo, T., Iacovides, H., Launder, B.E., 1995, "Developing Buoyancy-Modified Turbulent Flow in Ducts Rotating in Orthogonal Mode," *ASME Journal of Turbomachinery*, **117**, pp. 474-484.

Bonhoff, B., Tomm, U., Johnson, B.V., 1997, "Heat Transfer Predictions for Rotating U-Shaped Coolant Channels with Skewed Ribs and with Smooth Walls," Proceedings of the International Gas Turbine and Aeroengine Congress and Exhibition, Orlando, Florida, Paper no. 97-GT-162.

Bons, J.P., Kerrebrock, J.L., 1998, "Complementary Velocity and Heat Transfer Measurements in a Rotating Cooling Passage with Smooth Walls," Proceedings of the ASME International Gas Turbine and Aeroengine Congress and Exhibition, Stockholm, Sweden, Paper no. 98-GT-484.

Braun, H., Neumann, H., Mitra, N.K., 1999, "Experimental and Numerical Investigation of Turbulent Heat Transfer in a Channel with Periodically Arranged Rib Roughness Elements," *Experimental Thermal and Fluid Science*, **19**, pp. 67-76.

Cardone, G., Astarita, T., Carlomagno, G.M., 1998, "Wall Heat Transfer in Static and Rotating 180° Turn Channels by Quantitative Infrared Thermography," *International Journal of Thermal Sciences*, **37**, pp. 644-652.

Casarsa, L., Çakan, M., Arts, T., 2002, "Characterization of the Velocity and Heat Transfer Fields in an Internal Cooling Channel with High Blockage Ratio," Proceedings of the ASME Turbo Expo, Amsterdam, The Netherlands, Paper no. GT-2002-30207.

Chandra, P.R., Han, J.C., Lau, S.C., 1988, "Effect of Rib Angle on Local Heat/Mass Transfer Distribution in a Two-Pass Rib-Roughened Channel," *ASME Journal of Turbomachinery*, **110**, pp. 233-241.

Chang, S.W., Morris, W.D., 1998, "A Comparative Study of Heat Transfer Between Rotating Circular Smooth-Walled and Square Rib-Roughened Ducts with Cooling Application for Gas Turbine Rotor Blades," *JSME International Journal*, **2**, pp. 302-315.

Chang, S.W., Morris, W.D., 2003, "Heat Transfer in a Radially Aligned Square Duct Fitted with In-line Transverse Ribs," *International Journal of Thermal Sciences*, **42**, pp. 267-282.

Chanteloup, D., Juaneda, Y., Bölcs, A., 2002, "Combined 3D Flow and Heat Transfer Measurements in a 2-Pass Internal Coolant Passage of Gas Turbine Airfoils," Proceedings of the ASME Turbo Expo, Amsterdam, The Netherlands, Paper no. GT-2002-30214.

Chen, Y., Nikitopoulos, D.E., Hibbs, R., Acharya, S., Myrum, T.A., 2000, "Detailed Mass Transfer Distribution in a Ribbed Coolant Passage with a 180° Bend," *International Journal of Heat and Mass Transfer,"* **43**, pp. 1479-1492.

Choi, D., Prasad, D., Wang, M., Pierce, C., 2000, "Evaulation of an Industrial CFD Code for LES Applications," Center for Turbulence Research, Proceedings of the Summer Program, pp. 221-228.

Cui, J., Patel, V., Lin, C.-L., 2003, "Large-Eddy Simulation of Turbulent Flow in a Channel with Rib Roughness," *International Journal of Heat and Fluid Flow*, **24**, pp. 372-388.
Dutta, S., Andrews, M.J., Han, J.C., 1993, "Simulation of Turbulent Heat Transfer in a Rotating Duct," *Journal of Thermophysics***, 9**, 381-382.

Dutta, S., Zhang, X., Khan, J.A., Bell, D., 1999, "Adverse and Favorable Mixed Convection Heat Transfer in a Two-Side Heated Square Channel," *Experimental Thermal and Fluid Science*, **18**, pp. 314-322.

Ekkad, S.V., Han, J.C., 1997, "Detailed Heat Transfer Distributions in Two-Pass Square Channels with Rib Turbulators," *International Journal of Heat and Mass Transfer*, **40**, pp. 2525-2537.

Ekkad, S.K., Pamula, G.P., Shantiniketanam, M., 2000, "Detailed Heat Transfer Measurements Inside Straight and Tapered Two-Pass Channels with Rib Turbulators," *Experimental Thermal and Fluid Science*, **22**, pp. 155-163.

Elfert, M., 1994, "The Effect of Rotation and Buoyancy on Flow Development in a Rotating Circular Coolant Channel with Radially Inward Flow," *Experimental Thermal and Fluid Science*, **9**, pp. 206-214.

El-Husayni, H.A., Taslim, M.E., Kercher, D.M., 1992, "Experimental Heat Transfer Investigation of Stationary and Orthogonally Rotating Asymmetric and Symmetric Heated Smooth and Turbulated Channels," *ASME Journal of Turbomachinery*, **116**, pp. 124-132.

Fann, S., Yang, W.J., Zhang, N., 1994, "Local Heat Transfer in a Rotating Serpentine Passage with Rib-Roughened Surfaces," *International Journal of Heat and Mass Transfer*, **37**, pp. 217-228.

Feiz, A.A., Ould-Rouis, M., Lauriat, G., Large Eddy Simulation of Turbulent Flow in a Rotating Pipe," *International Journal of Heat and Fluid Flow*, **24**, pp. 412-420.

Gu, X., Wu, H.W., Schock, H.J., Shih, T.I-P., 2002, "Two-Equation Versus Reynolds-Stress Modeling in Predicting Flow and Heat Transfer in a Smooth U-Duct With and Without Rotation," Proceedings of the ASME Turbo Expo, Amsterdam, The Netherlands, pp. 1-10, Paper no. GT-2002-30616.

Han, J.C., Glicksman, L.R., Rohsenow, W.M., 1978, "An Investigation of Heat Transfer and Friction for Rib-Roughened Surfaces," *International Journal of Heat and Mass Transfer*, **21**, pp. 1143-1156.

Han, J.C., 1984, "Heat Transfer and Friction in Channels with Two Opposite Rib-Roughened Walls," *ASME Journal of Heat Transfer*, **106**, pp. 774-781.

Han, J.C., Chandra, P.R., Lau, S.C., 1988, "Local Heat/Mass Transfer Distributions Around Sharp 180° Turns in Two-Pass Smooth and Rib-Roughened Channels," *ASME Journal of Heat Transfer*, **110**, pp. 91-98.

Han, J.C., Park, J.S., 1988, "Developing Heat Transfer in Rectangular Channels with Rib Turbulators," *International Journal of Heat and Mass Transfer*, **31**, pp.183-195.

Han, J.C., 1988, "Heat Transfer and Friction Characteristics in Rectangular Channels with Rib Turbulators," *ASME Journal of Heat Transfer*, **110**, pp. 321-328.

Hébrard, J., Métais, O., Slinas-Vasquez, M., 2004, "Large-Eddy Simulation of Turbulent Duct Flow: Heating and Curvature Effects," *International Journal of Heat and Fluid Flow*, **25**, pp. 569-580.

Hibbs, R.G., Acharya, S., Chen, Y., Nikitopoulos, D.E., 1996, "Heat/Mass Transfer Distribution in a Rotating, Two-Pass Channel with Smooth and Ribbed Walls," Proceedings of the ASME HTD, **324**, pp.123-136.

Hirota, M., Yokosawa, H., Fujita, H., 1992, "Turbulence Kinetic Energy in Turbulent Flows through Square Ducts with Rib-Roughened Wall," *International Journal of Heat and Fluid Flow***, 13**, pp. 22-29.

Hsieh, S.S., Chiang, M.H., Chen, P.J., 1997, "Velocity Measurements and Local Heat Transfer in a Rotating Ribbed Two-Pass Square Channel with Uneven wall Heat Flux," Proceedings of the ASME International Gas Turbine and Aeroengine Congress and Exhibition, Orlando, Florida, Paper no. 97-GT-160.

Iaccarino, G., Ooi, A., Pettersson Reif, B.A., Durbin, P., 1999, "RANS Simulations of Rotating Flows," *Center for Turbulence Research Annual Research Briefs*, pp. 257- 266.

Iacovides, H., Launder, B.E., 1991, "Parametric and Numerical Study of Fully Developed Flow and Heat Transfer in Rotating Rectangular Ducts," *ASME Journal of Turbomachinery*, **113**, pp. 331-338.

Iacovides, H., 1998, "Computation of Flow and Heat Transfer through Rotating Ribbed Passages," *International Journal of Heat and Fluid Flow*, **19**, pp. 393-400.

Iacovides, H., Raisee, M., 2001, "Computation of Flow and Heat Transfer in Two-Dimensional Rib-Roughened Passages, Using Low-Reynolds-Number- Turbulence Models," *International Journal of Numerical Methods for Heat and Fluid Flow*, **11**, pp. 138-155.

Iacovides, H., Jackson, D.C., Kelemenis, G., Launder, B.E., Yuan, Y.M, 2001, "Flow and Heat Transfer in a Rotating U-Bend with 45° Ribs," *International Journal of Heat and Fluid Flow*, **22**, pp. 308-314.

Islam, M.S., Haga, K., Kaminaga, M., Hino, R., Monde, M., 2002, "Experimental Analysis of Turbulent Flow Structure in a Fully Developed Rib-Roughened Rectangular Channel with PIV," *Experiments in Fluids*, **33**, pp. 296-306.

Jang, Y.J., Chen, H.C., Han, J.C., 2001, "Flow and Heat Transfer in a Rotating Square Channel with 45° Angled Ribs by Reynolds Stress Turbulence Model," *ASME Journal of Turbomachinery*, **123**, pp. 124-132.

Jia, R., Saidi, A., Sundén, B., 2002, "Heat Transfer Enhancement in Square Ducts with V-Shaped Ribs of Various Angles," Proceedings of the ASME Turbo Expo, Amsterdam, The Netherlands, Paper no. GT-2002-30209.

Johnson, A.R., Morris, W.D., 1983, "Experimental Investigation of the Effect of Entry Conditions and Rotation on Flow Resistance in Circular Tubes Rotating about a Parallel Axis," *International Journal of Heat and Fluid Flow*, **5**, pp. 121-127.

Jordan, S.A., 2003, "The Turbulent Character and Pressure Loss Produced by Periodic Symmetric Ribs in a Circular Duct," *International Journal of Heat and Fluid Flow*, **24**, pp. 795-806.

Kajishima, T., Miyake, Y., 1992, "A Discussion on Eddy Viscosity Models on the Basis of the Large Eddy Simulation of Turbulent Flow in a Square Duct," *Computers Fluids*, **21**, pp. 151-161.

Korotky, G.J., Taslim, M.E., 1998, "Rib Heat Transfer Coefficient Measurements in a Rib-Roughened Square Passage," *ASME Journal of Turbomachinery*, **120**, pp. 376-385.

Lau, S.C., McMillin, R.D., Han, J.C., 1991, "Heat Transfer Characteristics of Turbulent Flow in a Square Channel with Angled Discrete Ribs," *ASME Journal of Turbomachinery*, **113**, pp. 367-374.

Lau, S.C., McMillin, R.D., Han, J.C., 1991, "Turbulent Heat Transfer and Friction in a Square Channel with Discrete Rib Turbulators," *ASME Journal of Turbomachinery*, **113**, pp. 360-366.

Lin, Y.L., Shih, T.I.-P., Stephens, M.A., Chyu, M.K., 2001, "A Numerical Study of Flow and Heat Transfer in a Smooth and Ribbed U-Duct With and Without Rotation," *ASME Journal of Heat Transfer*, **123**, pp. 219-231.

Liou, T.M., Hwang, J.J., 1992, "Developing Heat Transfer and Friction in a Ribbed Rectangular Duct with Flow Separation at Inlet," *ASME Journal of Heat Transfer*, **114**, pp. 565-573.

Liou, T.M., Hwang, J.J., 1992, "Turbulent Heat Transfer Augmentation and Friction in Periodic Fully Developed Channel Flows," *ASME Journal of Heat Transfer*, **114**, pp. 56-64.

Liou, T.M., Wu, Y.Y., Chang, Y., 1993, "LDV Measurements of Periodic Fully Developed Main and Secondary Flows in a Channel with Rib-Disturbed Walls," *ASME Journal of Fluids Engineering*, **115**, pp.109-114.

Liou, T.M., Hwang, J.J., Chen, S.H., 1993, "Simulation and Measurement of Enhanced Turbulent Heat Transfer in a Channel With Periodic Ribs on One Principal Wall," *International Journal of Heat and Mass Transfer*, **36**, pp. 507-517.

Liou, T.M., Tzeng, Y.Y., Chen, C.C., 1999, "Fluid Flow in a 180° Sharp Turning Duct With Different Divider Thicknesses," *ASME Journal of Turbomachinery*, **121**, pp. 569-576.

Liou, T.M., Chen, C.C., Tzeng, Y.Y., Tsai, T.W., 2000, "Non-Intrusive Measurements of Near-Wall Fluid Flow and Surface Heat Transfer in a Serpentine Passage," *International Journal of Heat and Mass Transfer*, **43,** pp. 3233-3244.

Liou, T.M., Chen, M.Y., Tsai, M.H., 2002, "Fluid Flow and Heat Transfer in a Rotating Two-Pass Square Duct With In-Line 90° Ribs," *ASME Journal of Turbomachinery*, **124**, pp. 260-268.

Lokai, V.I., Limanskii, A.S., 1975, "Influence of Rotation on Heat Transfer in Radial Cooling Channels of Turbine Blades," *Izvestiya VUZ. Aviatsionnaya Tekhnika*, **18**, pp. 69-72.

Lokai, V.I., Gunchenko, E.I., 1979, "Heat Transfer Over the Initial Section of Turbine Blade Cooling Channels Under Conditions of Rotation," *Thermal Engineering*, **26**, pp. 93-95.

Mahmood, G.I., Ligrani, P.M., Won, S.Y., 2002, "Spatially-resolved Heat Transfer and Flow Structure in a Rectangular Channel with 45° Angled Rib Turbulators," Proceedings of the ASME Turbo Expo, Amsterdam, The Netherlands, Paper no. GT-2002-30215.

Metzger, D.E., Sahm, M.K., 1986, "Heat Transfer Around Sharp 180° Turns in Smooth Rectangular Channels," *ASME Journal of Heat Transfer*, **108**, pp. 500-506.

Mochizuki, S., Takamura, J., Yamawaki, S.,Yang, W.J., 1994, "Heat Transfer in Serpentine Flow Passages With Rotation," *ASME Journal of Turbomachinery*, **116**, pp. 133-140.

Mochizuki, S., Murata, A., Fukunaga, M., 1997, "Effects of Rib Arrangements on Pressure Drop and Heat Transfer in a Rib-Roughened Channel with a Sharp 180° Turn," *ASME Journal of Turbomachinery*, **119**, pp. 610-616.

Mochizuki, S., Murata, A., Shibata, R., Wen-Jei, Y., 1999, "Detailed Measurements of Local Heat Transfer Coefficients in Turbulent Flow Through Smooth and Rib-Roughened Serpentine Passages with a 180° Sharp Bend," *International Journal of Heat and Mass Transfer*, **42**, pp. 1925-1934.

Murata, A., Mochizuki, S., 1999, "Effect of Cross-Sectional Aspect Ratio on Turbulent Heat Transfer in an Orthogonally Rotating Rectangular Smooth Duct," *International Journal of Heat and Mass Transfer*, **42**, pp. 3803-3814.

Murata, A., Mochizuki, S., 2000, "Large Eddy Simulation with a Dynamic Subgrid-Scale Model of Turbulent Heat Transfer in an Orthogonally Rotating Rectangular Duct with Transverse Rib Turbulators," *International Journal of Heat and Mass Transfer*, **43**, pp. 1243-1259.

Murata, A., Mochizuki, S., 2001, "Comparison between Laminar and Turbulent Heat Transfer in a Stationary Square Duct with Transverse or Angled Rib Turbulators," *International Journal of Heat and Mass Transfer*, **44**, pp. 1127-1141.

Murata, A., Mochizuki, S., 2001, "Effect of Centrifugal Buoyancy on Turbulent Heat Transfer in an Orthogonally Rotating Square Duct with Transverse or Angled Rib Turbulators," *International Journal of Heat and Mass Transfer*, **44**, pp. 2739-2750.

Murata, A., Mochizuki, S., 2004, "Large Eddy Simulation of Turbulent Heat Transfer in a Rotating Two-Pass Smooth Square Channel with Sharp 180º Turns," *International Journal of Heat and Mass Transfer*, **47**, pp. 683-698.

Murata, A., Mochizuki, S., 2004, "Centrifugal Buoyancy Effects on Turbulent Heat Transfer in a Rotating Two-Pass Smooth Square Channel with Sharp 180-deg Turns," *International Journal of Heat and Mass Transfer*, **47**, pp. 3215-3231.

Murata, A., Mochizuki, S., 2004, "Effect of Rib Orientation and Channel Rotation on Turbulent Heat Transfer in a Two-Pass Square Channel with Sharp 180º Turns Investigated by Using Large Eddy Simulation," *International Journal of Heat and Mass Transfer*, **47**, pp. 2599-2618.

Murata, A., Mochizuki, S., 2004, "Aiding and Opposing Contributions of Centrifugal Buoyancy on Turbulent Heat Transfer in a Two-Pass Transverse- or Angled-Rib-Roughened Channel with Sharp 180º Turns," *International Journal of Heat and Mass Transfer*, **47**, pp. 3721-3743.

Nikitopoulos, D.E., Eliades, V., Acharya, S., 2000, "Heat Transfer Enhancements in Rotating Two-Pass Coolant Channels with Profiled Ribs: Part 2 – Detailed Measurements," Proceedings of the ASME Turbo Expo, Munich, Germany, Paper no. 2000-GT-0226.

Nilsen, P.J., Andersson, H.I., 1994, "Developing Turbulent Flow in a Rotating Channel," *International Journal of Heat and Fluid Flow*," **15**, pp. 100-103.

Okita, Y., Iacovides, H., 2003, "Comparisons of High-Reynolds-Number EVM and DSM Models in the Prediction of Heat and Fluid Flow of Turbine Blade Cooling Passages," *ASME Journal of Turbomachinery*, **425**, pp. 585-597.

Ooi, A., Petterson Reif, B.A., Iaccarino, G., Durbin, P.A., 2000, "Evaluation of RANS Models for Rotating Flows," Proceedings of Center for Turbulence Research Summer Program, pp. 229-239.

Ooi, A., Iaccarino, G., Durbin, P.A., Behnia, M., 2002, "Reynolds Averaged Simulation of Flow and Heat Transfer in Ribbed Ducts," *International Journal of Heat and Fluid Flow*, pp. 750-757.

Pallares, J., Davidson, L., 2000, "Large-Eddy Simulations of Turbulent Flow in a Rotating Square Duct," *Physics of Fluids*, **12**, pp. 2878-2898.

Pallares, J., Davidson, L., 2002, "Large-Eddy Simulations of Turbulent Heat Transfer in Stationary and Rotating Square Ducts," *Physics of Fluids*, **14**, pp. 2804-2816.

Park, C.W., Lau, S.C., Kukreja, R.T., 1997, "Heat/Mass Transfer in a Rotating Two-Pass Channel with Transverse Ribs," *Journal of Thermophysics and Heat Transfer*, **12**, pp. 80-86.

Park, C.W., Kukreja, R.T., Lau, S.C., 1997, "Effect of Rib Size on Heat (Mass) Transfer Distribution in a Rotation Channel," Proceedings of the ASME Asia Congress and Exhibition, pp. 1-10, Paper no. 97-AA-126.

Park, C.W., Lau, S.C., Kukreja, R.T., 1998, "Heat (Mass) Transfer in a Rotating Channel with Ribs of Various Sizes on Two Walls," *Journal of Thermophysics*, **12**, pp. 152-154.

Park, C.W., Lau, S.C., 1998, "Effect of Channel Orientation of Local Heat (Mass) Transfer Distributions in a Rotating Two-Pass Square Channel With Smooth Walls," *ASME Journal of Heat Transfer*, **120**, pp. 624-632.

Parsons, J.A., Han, J.C., Zhang, Y., 1994, "Wall Heating Effect on Local Heat Transfer in a Rotating Two-Pass Square Channel with 90° Rib Turbulators," *International Journal of Heat and Mass Transfer*, **37**, pp. 1411-1420.

Parsons, J.A., Han, J.C., Zhang, Y., 1995, "Effect of Model Orientation and Wall Heating Condition on Local Heat Transfer in a Rotating Two-Pass Square Channel with Rib Turbulators," *International Journal of Heat and Mass Transfer*, **38**, pp. 1151-1159.

Prakash, C., Zerkle, R., 1992, "Prediction of Turbulent Flow and Heat Transfer in a Radially Rotating Square Duct," *ASME Journal of Turbomachinery***, 114**, pp. 835-846.

Prakash, C., Zerkle, R., 1995, "Prediction of Turbulent Flow and Heat Transfer in a Ribbed Rectangular Duct With and Without Rotation," *ASME Journal of Turbomachinery*, **117**, pp. 255-264.

Rau, G., Çakan, M., Moeller, D., Arts, T., 1998, "The Effect of Periodic Ribs on the Local Aerodynamic and Heat Transfer Performance of a Straight Cooling Channel," *ASME Journal of Turbomachinery*, **120**, pp. 368-375.

Saha, A.K., Acharya, S., 2003, "Flow and Heat Transfer in an Internally Ribbed Duct with Rotation: An Assessment of LES and URANS," Proceedings of the ASME Turbo Expo 2003, Atlanta, Georgia.

Saidi, A., Sundén, B., 2001, "On Prediction of Thermal-Hydraulic Characteristics of Square-Sectioned Ribbed Cooling Ducts," *ASME Journal of Turbomachinery*, **123**, pp. 614-620.

Satoh, H., Hishida, K., Maeda, M., Takahashi, K., 1987, "Turbulent Flow Characteristics Around Three Dimensional Ribs for Enhancement of Heat Transfer," Proceedings of the ASME-JSME Thermal Engineering Joint Conference, Honolulu, Hawaii, HTD, **5**, pp. 225-231.

Sato, H., Hishida, K., Maeda, M., 1989, "Turbulent Flow Characteristics in a Rectangular Channel with Repeated Rib Roughness," Proceedings of the National Heat Transfer Conference, HTD, **107**, pp. 191-196.

Schabacker, J., Bölcs, A., Johnson, B.V., 1998, "PIV Investigation of the Flow Characteristics in an Internal Coolant Passage with Two Ducts Connected by a Sharp 180° Bend," Proceedings of the ASME International Gas Turbine and Aeroengine Congress and Exhibition, Stockholm, Sweden, pp. 1-11, Paper no. 98-GT-544.

Servouze, Y., Sturgis, J.C., 2003, "Heat Transfer and Flow Field Measurements in a Rib-Roughened Branch of a Rotating Two-Pass Duct," Proceedings of the ASME Turbo Expo, Atlanta, Georgia, pp. 1-12, Paper no. GT2003-38048.

Sleiti, A.K., Kapat, J.S., 2004, "Comparison Between EVM and RSM Turbulence Models in Predicting Flow and Heat Transfer in Rib-Roughened Channels," Proceedings of the ASME Heat Transfer/Fluids Engineering Summer Conference, Charlotte, North Carolina, pp. 1-12, Paper no. HT-FED04-56250.

Son, S.Y., Kihm, K.D., Han, J.C., 2002, "PIV Flow Measurements for Heat Transfer Characterization in Two-Pass Square Channels with Smooth and 90° Ribbed Walls," *International Journal of Heat and Mass Transfer*, **45**, pp. 4809-4822.

Soong, C.W., Yan, W.M., 1999, "Development of Secondary Flow and Convective Heat Transfer in Isothermal / Iso-flux Rectangular Ducts Rotating about a Parallel Axis," *International Journal of Heat and Mass Transfer*, **42**, pp. 497-510.

Sparrow, E.M., Cur, N., 1982, "Turbulent Heat Transfer in a Symmetrically or Asymmetrically Heated Flat Rectangular Duct With Flow Separation at Inlet," *ASME Journal of Heat Transfer*, **104**, pp. 82-89.

Sparrow, E.M., Tao, W.Q., 1983, "Enhanced Heat Transfer in a Flat Rectangular Duct With Streamwise-Periodic Disturbances at One Principal Wall," *ASME Journal of Heat Transfer*, **105,** pp. 851-861.

Sparrow, E.M., Tao, W.Q., 1984, "Symmetric vs. Asymmetric Periodic Disturbances at the Walls of a Heated Flow Passage," *International Journal of Heat and Mass Transfer*, **27**, pp. 2133-2144.

Su, G., Teng, S., Chen, H.C., Han, J.C., 2003, "Computation of Flow and Heat Transfer in Rotating Rectangular Channels (AR=4) With V-Shaped Ribs by a Reynolds Stress Turbulence Model," Proceedings of the ASME Turbo Expo, Atlanta, Georgia, pp. 1-10, Paper no. GT2003-38348.

Sugawara, K., Yoshikawa, H., Ota, T., 2004, "LES of Turbulent Separated Flow and Heat Transfer in a Symmetric Expansion Plane Channel," Proceedings of the ASME Heat Transfer/Fluids Engineering Summer Conference, Charlotte, North Carolina, Paper no. HT-FED04-56139.

Takahashi, T., Watanabe, K., 2004, "Large Eddy Simulation of Flow and Heat Transfer in a Rectangular Channel with Crossed Angled Ribs," Proceedings of the ASME Turbo Expo 2004, Vienna, Austria.

Taslim, M.E., Rahman, A., Spring, S.D., 1991, "An Experimental Investigation of Heat Transfer Coefficients in a Spanwise Rotating Channel with Two Opposite Rib-Roughened Walls," *ASME Journal of Turbomachinery*, **113**, pp. 75-82.

Taslim, M.E., Wadsworth, C.M., 1997, "An Experimental Investigation of the Rib Surface-Averaged Heat Transfer Coefficient in a Rib-Roughened Square Passage," *ASME Journal of Turbomachinery*, **381**, pp.381-389.

Tse, D.G.N., Steuber, G.D., 1997, "Flow in a Rotating Square Serpentine Coolant Passage with Skewed Trips," Proceedings of the ASME International Gas Turbine and Aeroengine Congress and Exhibition, Orlando, Florida, Paper no. 97-GT-529.

Tyagi, M., Acharya, S., 2004, “Large Eddy Simluations of Flow and Heat Transfer in Rotating Ribbed Duct Flows,” Proceedings of the ASME Turbo Expo 2004, Vienna, Austria.

Xu, H., Pollard, A., 2001, “Large Eddy Simulation of Turbulent Flow in a Square Annular Duct,” *Physics of Fluids*, **13**, pp. 3321-3337.

Wagner, J.H., Johnson, B.V., Hajek, T.J., 1991, “Heat Transfer in Rotating Passages with Smooth Walls and Radial Outward Flow,” *ASME Journal of Turbomachinery*, **113**, pp. 42-51.

Wagner, J.H., Johnson, B.V., Kopper, F.C., 1991, “Heat Transfer in Rotating Serpentine Passages with Smooth Walls,” *ASME Journal of Turbomachinery*, **113**, pp. 321-330.

Wagner, J.H., Johnson, B.V., Graziani, R.A., Yeh, F.C., 1992, “Heat Transfer in Rotating Passages with Trips Normal to the Flow,” *ASME Journal of Turbomachinery*, **114**, pp. 847-857.

Wang, L.B., Tao, W.Q., Wang, Q.W., Wong, T.T., 2001, “Experimental Study of Developing Turbulent Flow and Heat Transfer in ribbed Convergent/Divergent Square Ducts,” *International Journal of Heat and Fluid Flow*, **22**, pp.603-613.

Watanabe, K., Takahashi, T., 2002, “LES Simulation and Experimental Measurement of Fully Developed Ribbed Channel Flow and Heat Transfer,” Proceedings of the ASME Turbo Expo 2002, Amsterdam, The Netherlands.

Yan, W.M., Soong, C.Y., 1995, “Simultaneously Developing Mixed Convection in Radially Rotating Rectangular Ducts,” *International Journal of Heat and Mass Transfer*, **38**, pp. 665-677.

Yang, K.-S., Ferziger, J.H., 1993, “Large-Eddy Simulation of Turbulent Obstacle Flow Using a Dynamic Subgrid-Scale Model,” *AIAA Journal*, **31**, pp. 1406-1413.

Zhao, C.Y., Tao, W.Q., 1997, “A Three Dimensional Investigation of Turbulent Flow and Heat Transfer Around Sharp 180° Turns in Two-Pass Rib-Roughened Channels,” *International Communications of Heat and Mass Transfer*, **24**, pp. 587-596.

Chapter 3: Computational Methodology

Abdel-Wahab, S., Tafti, D.K., 2004, “Large Eddy Simulation of Flow and Heat Transfer in a 90º Ribbed Duct with Rotation - Effect of Coriolis Forces,” Proceedings of the ASME Turbo Expo 2004, Vienna, Austria, ASME Paper No. GT2004-53796.

Abdel-Wahab, S., Tafti, D.K., 2004, “Large Eddy Simulation of Flow and Heat Transfer in a 90º Ribbed Duct with Rotation – Effect of Coriolis and Centrifugal Buoyancy Forces,” Proceedings of the ASME Turbo Expo 2004, Vienna, Austria, ASME Paper No. GT2004-53799.

Abdel-Wahab, S., Tafti, D.K., 2004, “Large Eddy Simulation Simulation of Flow and Heat Transfer in a 90 deg Ribbed Duct with Rotation: Effect of Coriolis and Centrifugal Buoyancy Forces,” *ASME Journal of Turbomachinery*, **126**, pp. 627-636.

Germano, M., Piomelli, U., Moin, P., Cabot, W.H., 1991, “A dynamic subgrid-scale eddy viscosity model,” *Physics of Fluids A*, **3**-7, pp. 1760-1765.

Han, J.C. and Park, J.S., Developing heat transfer in rectangular channels with rib turbulators, *Int. J. Heat Mass Transfer*, Vol. 31, No. 1, pp.183-195, 1988.

Incropera, F.P., and DeWitt, D.P., 2002, *Fundamentals of Heat and Mass Transfer*, fifth edition, John Wiley and Sons, New York.

Lilly, D.K., A Proposed Modification of the Germano Subgrid-Scale Eddy Viscosity Model, *Phys. Fluids A*, 4-3, pp. 633-635, 1992.

Liou, T.-M. and Hwang, J.-J., Developing Heat Transfer and Friction in a Ribbed Rectangular Duct With Flow Separation at Inlet, *Journal of Heat Transfer*, Vol. 114, 1992.

Moin, P., Squires, K., Cabot, W., Lee, S., A Dynamic Sub-Grid-Scale Model for Compressible Turbulence and Scalar Transport, *Phys. Fluids A*, 3-11, pp. 2746-2757, 1991.

Najjar, F.M. and Tafti, D.K., Study of Discrete Test Filters and Finite Difference Approximations for the Dynamic Subgrid-Scale Stress Model, *Phys. Fluids*, Vol. 8, pp. 1076-1088, 1996.

Tafti, D.K., GenIDLEST – A Scalable Parallel Computational Tool for Simulating Complex Turbulent Flows, Proceedings of the ASME Fluids Engineering Division, FED, Vol. 256, ASME-IMECE, New York, 2001.

Tafti, D.K., 2005, “Evaluating the Role of Subgrid Stress Modeling in a Ribbed Duct for the Internal Cooling of Turbine Blades,” *International Journal of Heat and Fluid Flow*, **26**, pp. 92-104.

Chapter 4: Stationary Developing Flow and 180º Bends

Abdel-Wahab, S., Tafti, D.K., 2004, "Large Eddy Simulation of Flow and Heat Transfer in a Staggered 45º Ribbed Duct," Proceedings of the ASME Turbo Expo 2004, Vienna, Austria, ASME Paper No. GT2004-53800.

Al-Qahtani, M., Jang, Y.-J., Chen, H.-C., Han, J.-C., 2002, "Prediction of Flow and Heat Transfer in Rotating Two-Pass Rectangular Channels With 45-deg Rib Turbulators," *ASME Journal of Turbomachinery*, **124**, pp. 242-250.

Al-Qahtani, M., Chen, H.-C., Han, J.-C., 2002, "A Numerical Study of Flow and Heat Transfer in Rotating Rectangular Channels (AR=4) With 45º Rib Turbulators by Reynolds Stress Turbulence Model," Proceedings of the ASME Turbo Expo 2002, Amsterdam, The Netherlands, ASME Paper No. GT-2002-30216.

Arts, T., Rau, G., Çakan, M., Vialonga, J., Fernandez, D., Tarnowski, F., Laroche, E., 1997, "Experimental and Numerical Investigation on Flow and Heat Transfer in Large-Scale, Turbine Cooling, Representative, Rib-Roughened Channels," Proceedings of the Institution of Mechanical Engineers (ImechE), **211**, Part A, pp. 263-272.

Astarita, T., Cardone, G., Carlomagno, G.M., 2002, "Convective Heat Transfer in Ribbed Channels With a 180º Turn," *Experiments in Fluids*, **33**, pp. 90-100.

Astarita, T., Cardone, G., 2003, "Convective Heat Transfer in a Square Channel With Angled Ribs on Two Opposite Walls," *Experiments in Fluids*, **34**, pp. 625-634.

Besserman, D.L., Tanrikut, S., 1992, "Comparison of Heat Transfer Measurements With Computations for Turbulent Flow Around a 180 deg Bend," *ASME Journal of Turbomachinery*, **114**, pp. 865-871.

Bonhoff, B., Tomm, U., Johnson, B.V., Jennions, I., 1997, "Heat Transfer Predictions for Rotating U-Shaped Coolant Channels With Skewed Ribs and With Smooth Walls," Proceedings of the International Gas Turbine & Aeroengine Congress & Exhibition, Orlando, Florida, USA, Paper No. 97-GT-162.

Bonhoff, B., Parneix, S., Leusch, J., Johnson, B.V., Schabacker, J., Bölcs, A., 1999, "Experimental and Numerical Study of Developed Flow and Heat Transfer in Coolant Channels With 45 Degree Ribs," *International Journal of Heat and Fluid Flow*, **20**, pp. 311-319.

Fann, S., Yang, W.-J., Zhang, N., 1994, "Local Heat Transfer in a Rotating Serpentine Passage With Rib-Roughened Surfaces," *International Journal of Heat and Mass Transfer*, **37**(2), pp. 217-228.

Gu, X., Wu, H.-W., Schock, H.J., Shih, T.I.-P., 2002, "Two-Equation Versus Reynolds-Stress Modeling in Predicting Flow and Heat Transfer in a Smooth U-Duct with and without Rotation," Proceedings of the ASME Turbo Expo 2002, Amsterdam, The Netherlands, ASME Paper No. GT-2002-30616.

Han, J.C., Chandra, P.R., Lau, S.C., 1988, "Local Heat/Mass Transfer Distributions Around Sharp 180 deg Turns in Two-Pass Smooth and Rib-Roughened Channels," *ASME Journal of Heat Transfer*, **110**, pp. 91-98.

Han, J.C., Park, J.S., 1988, "Developing Heat Transfer in Rectangular Channels With Rib Turbulators," *International Journal of Heat and Mass Transfer*, **31**(1), pp. 183-195.

Iacovides, H., Kelemenis, G., Raisee, M., 2003, "Flow and Heat Transfer in Straight Cooling Passages With Inclined Ribs on Opposite Walls: an Experimental and Computational Study," *Experimental Thermal and Fluid Science*, **27**, pp. 283-294.

Incropera, F.P., DeWitt, D.P., 2002, *Fundamentals of Heat and Mass Transfer*, fifth edition, John Wiley and Sons, New York.

Islam, M.S., Haga, K., Kaminaga, M., Hino, R., Monde, M., 2002, "Experimental Analysis of Turbulent Flow Structure in a Fully Developed Rib-Roughened Rectangular Channel with PIV," *Experiments in Fluids*, **33**, pp. 296-306.

Jang, Y.-J., Chen, H.-C., Han, J.-C., 2001, "Flow and Heat Transfer in a Rotating Square Channel With 45 deg Angled Ribs by Reynolds Stress Turbulence Model," *ASME Journal of Turbomachinery*, **123**, pp. 124-132.

Lin, Y.-L., Shih, T.I.-P., Stephens, M.A., Chyu, M.K., 2001, "A Numerical Study of Flow and Heat Transfer in a Smooth and Ribbed U-Duct With and Without Rotation," *ASME Journal of Heat Transfer*, **123**, pp. 219-232.

Liou, T.-M., Hwang, J.-J., 1992, "Developing Heat Transfer and Friction in a Ribbed Rectangular Duct With Flow Separation at Inlet," *ASME Journal of Heat Transfer*, **114**, pp. 565-573.

Liou, T.-M., Tzeng, Y.-Y., Chen, C.-C., 1999, "Fluid Flow in a 180 deg Sharp Turning Duct With Different Divider Thicknesses," *ASME Journal of Turbomachinery*, **121**, pp. 569-576.

Moffat, R.J., 1988, "Describing the Uncertainties in Experimental Results," *Experimental Thermal Fluid Science*, **1**, pp. 3-17.

Ooi, A., Iaccarino, G., Durbin, P.A., Behnia, M., 2002, "Reynolds Averaged Simulation of Flow and Heat Transfer in Ribbed Ducts," *International Journal of Heat and Fluid Flow*, **23**, pp. 750-757.

Prakash, C., Zerkle, R., 1995, "Prediction of Turbulent Flow and Heat Transfer in a Ribbed Rectangular Duct With and Without Rotation," *ASME Journal of Turbomachinery*, **117**, pp. 255-264.

Rau, G., Çakan, M., Moeller, D., Arts, T., 1998, "The Effect of Periodic Ribs on the Local Aerodynamic and Heat Transfer Performance of a Straight Cooling Channel," *ASME Journal of Turbomachinery*, **120**, pp. 368-375.

Saidi, A., Sundén, B., 2001, "On Prediction of Thermal-Hydraulic Characteristics of Square-Sectioned Ribbed Cooling Ducts," *ASME Journal of Turbomachinery*, **123**, pp. 614-620.

Schabacker, J., Bölcs, B.V., Johnson, B.V., 1998, "PIV Investigation of the Flow Characteristics in an Internal Coolant Passage with Two Ducts Connected by a Sharp 180º Bend," Proceedings of the International Gas Turbine & Aeroengine Congress & Exhibition, Stockholm, Sweden, ASME Paper No. 98-GT-544.

Sewall, E.A., Tafti, D.K., 2004, "Large Eddy Simulation of the Developing Region of a Stationary Ribbed Internal Turbine Blade Cooling Channel," Proceedings of the ASME Turbo Expo 2004, Vienna, Austria, ASME Paper No. GT2004-53832.

Shih, T.I.-P., Lin, Y.-L., Stephens, M.A., Chyu, M.K., 1998, "Flow and Heat Transfer in a Ribbed U-Duct under Typical Engine Conditions," Proceedings of the International Gas Turbine & Aeroengine Congress & Exhibition, Stockholm, Sweden, Paper No. 98-GT-213.

Sleiti, A.K., Kapat, J.S., 2004, "Comparison Between EVM and RSM Turbulence Models in Predicting Flow and Heat Transfer in Rib-Roughened Channels," Proceedings of the 2004 ASME Heat Transfer/Fluids Engineering Summer Conference, Charlotte, North Carolina, USA, ASME Paper No. HT-FED04-56250.

Son, S.Y., Kihm, K.D., Han, J.-C., 2002, "PIV Flow Measurements for Heat Transfer Characterization on Two-Pass Square Channels With Smooth and 90º Ribbed Walls," *International Journal of Heat and Mass Transfer*, **45**, pp. 4809-4822.

Tafti, D.K., 2005, "Evaluating the Role of Subgrid Stress Modeling in a Ribbed Duct for the Internal Cooling of Turbine Blades," *International Journal of Heat and Fluid Flow*, **26**, pp. 92-104.

Chapter 5: Rotating Developing Flow and 180º Bends with Coriolis Effects

Abdel-Wahab, S., Tafti, D.K., 2004, "Large Eddy Simulation Simulation of Flow and Heat Transfer in a 90 deg Ribbed Duct with Rotation: Effect of Coriolis and Centrifugal Buoyancy Forces," *ASME Journal of Turbomachinery*, **126**, pp. 627-636.

Hibbs, R.G., Acharya, S., Chen, Y., Nikitopoulos, D.E., "Heat/mass transfer distribution in a rotating, two-pass channel with smooth and ribbed walls," ASME Heat Transfer Division, Vol. 324, No. 2, 1996, pp. 123-136.

Kim, K.M., Kim, Y.Y., Rhee, D.H., Cho, H.H., 2004, "An Investigation of Duct Aspect Ratio Effects on Heat/Mass Transfer in a Rotating Duct with 90º Ribs," Proceedings of ASME Turbo Expo 2004, Vienna, Austria, ASME Paper No. GT2004-53533.
Han, J.C., Chandra, P.R., Lau, S.C., 1988, "Local Heat/Mass Transfer Distributions Around Sharp 180 deg Turns in Two-Pass Smooth and Rib-Roughened Channels," *ASME Journal of Heat Transfer*, **110**, pp. 91-98.

Liou, T.-M., Chen, C.-C., Tzeng, Y.-Y., Tsai, T.-W., 2000, "Non-intrusive Measurements of New-Wall Fluid Flow and Surface Heat Transfer in a Serpentine Passage," *International Journal of Heat and Mass Transfer*, **43**, pp. 3233-3244.

Liou, T.-M., Chen, M.-Y., Tsai, M.-H., "Fluid Flow and Heat Transfer in a Rotating Two=Pass Square Duct With In-Line 90-deg Ribs," *ASME Journal of Turbomachinery*, Vol. 124, April 2002, pp. 260-268.

Prabhu, S.V., Vedula, R.P., 2003, "Pressure Drop Characteristics in a Rib Roughened Rotating Square Duct with a Sharp 180º Bend," *Journal of Enhanced Heat Transfer*, **10**, pp. 363-377.

Schabacker, J., Bölcs, B.V., 1998, "PIV Investigation of the Flow Characteristics in an Internal Coolant Passage with Two Ducts Connected by a Sharp 180º Bend," Proceedings of the International Gas Turbine & Aeroengine Congress & Exhibition, Stockholm, Sweden, 1998, ASME Paper No. 98-GT-544.

Sewall, E.A., Tafti, D.K., 2004, "Large Eddy Simulation of the Developing Region of a Stationary Ribbed Internal Turbine Blade Cooling Channel," Proceedings of the ASME Turbo Expo 2004, Vienna, Austria, ASME Paper No. GT2004-53832.

Sewall, E.A., Tafti, D.K., Graham, A.B., Thole, K.A., 2005, "Experimental Validation of Large Eddy Simulations of Flow and Heat Transfer in a Stationary Ribbed Duct," *International Journal of Heat and Fluid Flow*, In Press.

Son, S.Y., Kihm, K.D., Han, J.-C., 2002, "PIV Flow Measurements for Heat Transfer Characterization in Two-Pass Square Channels with Smooth and 90º Ribbed Walls," *International Journal of Heat and Mass Transfer*, **45**, pp. 4809-4822.

Tafti, D.K., 2005, "Evaluating the Role of Subgrid Stress Modeling in a Ribbed Duct for the Internal Cooling of Turbine Blades," *International Journal of Heat and Fluid Flow*, **26**, pp. 92-104.

Chapter 6: Rotating Developing Flow and 180º Bends with Coriolis Effects and Centrifugal Buoyancy Forces

Abdel-Wahab, S., Tafti, D.K., 2004, "Large Eddy Simulation Simulation of Flow and Heat Transfer in a 90 deg Ribbed Duct with Rotation: Effect of Coriolis and Centrifugal Buoyancy Forces," *ASME Journal of Turbomachinery*, **126**, pp. 627-636.

Chang, S.W., Morris, W.D., 2003, "Heat Transfer in a Radially Aligned Square Duct Fitted with In-line Transverse Ribs," *International Journal of Thermal Sciences*, **42**, pp. 267-282.

Han, J.C., 1988, "Heat Transfer and Friction Characteristics in Rectangular Channels with Rib Turbulators," *ASME Journal of Heat Transfer*, **110**, pp. 321-328.

El-Husayni, H.A., Taslim, M.E., Kercher, D.M., 1994, "Experimental Heat Transfer Investigation of Stationary and Orthogonally Rotating Asymmetric and Symmetric Heated Smooth and Turbulated Channels," *ASME Journal of Turbomachinery*, **116**, pp. 124-132.

Fann, S., Yang, W.-J., Zhang, N., 1994, "Local Heat Transfer in a Rotating Serpentine Passage With Rib-Roughened Surfaces," *International Journal of Heat and Mass Transfer*, **37**(2), pp. 217-228.

Liou, T.-M., Chen, C.-C., Tzeng, Y.-Y., Tsai, T.-W., 2000, "Non-intrusive Measurements of New-Wall Fluid Flow and Surface Heat Transfer in a Serpentine Passage," *International Journal of Heat and Mass Transfer*, **43**, pp. 3233-3244.

Murata, A., Mochizuki, S., 2004, "Aiding and Opposing Contributions of Centrifugal Buoyancy on Turbulent Heat Transfer in a Two-Pass Transverse- or Angled-Rib-Roughened Channel with Sharp 180º Turns," *International Journal of Heat and Mass Transfer*, **47**, pp. 3721-3743.

Sewall, E.A., Tafti, D.K., Graham, A.B., Thole, K.A., 2005, "Experimental Validation of Large Eddy Simulations of Flow and Heat Transfer in a Stationary Ribbed Duct," *International Journal of Heat and Fluid Flow*, In Press.

Tafti, D.K., 2005, "Evaluating the Role of Subgrid Stress Modeling in a Ribbed Duct for the Internal Cooling of Turbine Blades," *International Journal of Heat and Fluid Flow*, **26**, pp. 92-104.

Taslim, M.E., Rahman, A., Spring, S.D., 1991, "An Experimental Investigation of Heat Transfer Coefficients in a Spanwise Rotating Channel with Two Opposite Rib-Roughened Walls," *ASME Journal of Turbomachinery*, **113**, pp. 75-82.

Wagner, J.H., Johnson, B.V., Graziani, R.A., Yeh, F.C., 1992, "Heat Transfer in Rotating Passages with Trips Normal to the Flow," *ASME Journal of Turbomachinery*, **114**, pp. 847-857.

Chapter 7: A Variable Property Algorithm for Calculating Unsteady Flows with Large Property Variations

Bell, J.B., Marcus, D.L., 1992, "A Second-Order Projection Method for Variable-Density Flows," *Journal of Computational Physics*, **101**, pp. 334-348.

Çengel, Y.A., Boles, M.A., Thermodynamics, An Engineering Approach, McGraw-Hill, Boston, Massachusetts, 1998.

Chenoweth, D.R., Paolucci, S., 1985, "Gas Flow in Vertical Slots with Large Horizontal Temperature Differences," *Physics of Fluids*, **28**, pp. 2365-2374.

Chenoweth, D.R., Paolucci, S., 1986, "Natural Convection in an Enclosed Vertical Air Layer with Large Horizontal Temperature Differences," *Journal of Fluid Mechanics*, **169**, pp. 173-210.

Darbandi, M., Schneider, G.E., 1998, "Analogy-Based Method for Solving Compressible and Incompressible Flows," *Journal of Thermophysics and Heat Transfer*, **12**, pp. 239-247.

Davis, G.D.V., 1983, "Natural Convection of Air in a Square Cavity: A Bench Mark Numerical Solution," *International Journal for Numerical Methods in Fluids*, **3**, pp. 249-264.

Evans, G., Paolucci, S., 1990, "The Thermoconvective Instability of Plane Poiseuille Flow Heated from Below: A Proposed Benchmark Solution for Open Boundary Flows," *International Journal for Numerical Methods in Fluids*, **11**, pp. 1001-1013.

Heuveline, V., 2003, "On higher-order mixed FEM for low Mach number flows: application to a natural convection benchmark problem," *International Journal for Numerical Methods in Fluids*, **41**, pp. 1339-1356.

Mahalingam, S., Cantwell, B.J., Ferziger, J.H., 1990, "Full Numerical Simulation of Coflowing, Axisymmetric Jet Diffusion Flames," *Physics of Fluids A*, **2**, pp. 720-728.

Mary, I., Sagaut, P., Deville, M., 2000, "An Algorithm for Low Mach Number Unsteady Flows," *Computers & Fluids*, **29**, pp. 119-147.

McMurtry, P.A., Jou, W.-H., Riley, J.J., Metcalfe, W., 1985, "Direct Numerical Simulations of a Reacting Mixing Layer with Chemical Heat Release," Proceedings of the AIAA 23rd Aerospace Sciences Meeting, Paper No. AIAA-85-0143.

Merkle, C.L., Choi, Y.-H., 1987," Computation of Low-Speed Flow with Heat Addition," *AIAA Journal*, **25**, pp. 831-838.

Pember, R.B., Howell, L.H., Bell, J.B., Colella, P., Crutchfield, W.Y., Fiveland, W.A., Jesse, J.P., 1997, "An Adaptive Projection Method for the Modeling of Unsteady Low-Mach Number Combustion," Proceedings of the Western States Section of the Combustion Institute, 1997 Fall Meeting, Diamond Bar, CA, Paper No. WSS/CI 97F-125.

Rehm, R.G., Baum, H.R., 1978, "The Equations of Motion for Thermally Driven Buoyant Flows," *Journal of Research of the National Bureau of Standards*, **83**, pp. 297-308.

Sato, H., Kushida, G., Amagai, K., Arai, M., 2002, "Numerical Analysis of the Gravitational Effect on the Buoyancy-Driven Fluctuations in Diffusion Flames," *Proceedings of the Combustion Institute*, **29**, pp. 1671-1678.

Tafti, D.K., 2001, "GenIDLEST – A Scalable Parallel Computational Tool for Simulating Complex Turbulent Flows," Proceedings of the ASME Fluids Engineering Division, FED, ASME-IMECE, November 2001, New York, Vol. 256.

Tafti, D.K., 2005, "Evaluating the Role of Subgrid Stress Modeling in a Ribbed Duct for the Internal Cooling of Turbine Blades," *International Journal of Heat & Fluid Flow*, **26**, pp. 92-104.

Vierendeels, J., Merci, B., Dick, E., 2001, "Numerical Study of Natural Convective Heat Transfer with Large Temperature Differences," *International Journal of Numerical Methods for Heat & Fluid Flow*, **11**, pp. 329-341.

Vierendeels, J., Merci, B., Dick, E., 2003, "Benchmark Solutions for the Natural Convective Heat Transfer Problem in a Square Cavity with Large Horizontal Temperature Differences," *International Journal of Numerical Methods for Heat & Fluid Flow*, **13**, pp. 1057-1078.

Wall, C., Pierce, C.D., Moin, P., 2002, "A Semi-Implicit Method for Resolution of Acoustic Waves in Low Mach Number Flows," *Journal of Computational Physics*, **181**, pp. 545-563.

White, F.M., *Viscous Fluid Flow*, McGraw-Hill, New York, 1971.

Yu, C.H., Chang, M.Y., Lin, T.F., 1997, "Structures of Moving Transverse and Mixed Rolls in Mixed Convection of Air in a Horizontal Plane Channel," *International Journal of Heat & Mass Transfer*, **40**, pp. 333-346.

Zhang, X., Tafti, D.K., 2003, "Flow Efficiency in Multi-Louvered Fins," *International Journal of Heat and Mass Transfer*, **46**, 1737-1750.

Chapter 8: Summary and Conclusions

Abdel-Wahab, S., Tafti, D.K., 2004, "Large Eddy Simulation Simulation of Flow and Heat Transfer in a 90 deg Ribbed Duct with Rotation: Effect of Coriolis and Centrifugal Buoyancy Forces," *ASME Journal of Turbomachinery*, **126**, pp. 627-636.

Tafti, D.K., 2005, "Evaluating the Role of Subgrid Stress Modeling in a Ribbed Duct for the Internal Cooling of Turbine Blades," *International Journal of Heat & Fluid Flow*, **26**, pp. 92-104.

Appendix A. Project Publications

Table A.1 outlines the publications produced as part of the project. Currently, 14 conference papers and 6 journal papers have been published from this work. They include the Masters Work of Samer Abdel-Wahab in fully developed rotating ducts, the Ph.D. work of Aroon Viswanathan in DES studies, and my work in LES of the developing flow and 180º bend regions. All papers were overseen and co-authored by D.K. Tafti.

Table A.1. Publications resulting from the Project "Enhanced Prediction Techniques Based on Time-Accurate Simulations for Turbine Blade Internal Cooling"

Paper	Calculation Details	Publication Year
Tafti, D.K., 2003, "Large Eddy Simulations of Heat Transfer in a Ribbed Channel for Internal Cooling of Turbine Blades," Proceedings of ASME/IGTI Turbo Expo, Atlanta, Georgia, 2003, ASME Paper No. GT2003-38122.	Fully Developed Stationary LES	2003
Tafti, D.K., 2005, "Evaluating the Role of Subgrid Stress Modeling in a Ribbed Duct for the Internal Cooling of Turbine Blades," *International Journal of Heat and Fluid Flow*, **26**, pp. 92-104.	Fully Developed Stationary LES	2005
Abdel-Wahab, S., Tafti, D.K., 2004, "Large Eddy Simulation of Flow and Heat Transfer in a 90º Ribbed Duct with Rotation – Effect of Coriolis Forces," Proceedings of ASME Turbo Expo 2004, Vienna, Austria, ASME Paper No. GT2004-53796.	Fully Developed Coriolis Forces LES	2004
Abdel-Wahab, S., Tafti, D.K., 2004, "Large Eddy Simulation of Flow and Heat Transfer in a 90º Ribbed Duct with Rotation – Effect of Buoyancy Forces," Proceedings of ASME Turbo Expo 2004, Vienna, Austria, ASME Paper No. GT2004-53799.	Fully Developed Buoyancy Forces LES	2004
Abdel-Wahab, S., Tafti, D.K., 2004, "Large Eddy Simulation of Flow and Heat Transfer in a Staggered 45º Ribbed Duct," Proceedings of ASME Turbo Expo 2004, Vienna, Austria, ASME Paper No. GT2004-53800.	Fully Developed Stationary 45º Ribs LES	2004
Abdel-Wahab, S., Tafti, D.K., 2005, "Large Eddy Simulation of Flow and Heat Transfer in a 90 deg Ribbed Duct With Rotation: Effect of Coriolis and Centrifugal Buoyancy Forces," *ASME Journal of Turbomachinery*, **126**, pp. 627-636.	Fully Developed Buoyancy Forces LES	2005
Graham, A., Sewall, E., Thole, K.A., 2004, "Flowfield Measurements in a Ribbed Channel Relevant to Internal Turbine Blade Cooling," Proceedings of ASME Turbo Expo 2004, June 14-17, Vienna, Austria, ASME Paper No. GT2004-53361.	Fully Developed Experiments	2004
Sewall, E.A., Tafti, D.K., 2004, "Large Eddy Simulation of the Developing Region of a Stationary Ribbed Internal Turbine Blade Cooling Channel," Proceedings of ASME Turbo Expo 2004, Vienna, Austria, ASME Paper No. GT2004-53832.	Developing Flow Stationary LES	2004

Paper	Calculation Details	Publication Year
Sewall, E.A., Tafti, D.K., 2004, "Large Eddy Simulation of the Developing Region of a Rotating Ribbed Internal Turbine Blade Cooling Channel," Proceedings of the ASME Turbo Expo 2004, Vienna, Austria, ASME Paper No. GT2004-53833.	Developing Flow Coriolis LES	2004
Sewall, E.A., Tafti, D.K., Graham, A.B., Thole, K.A., 2005, "Experimental Validation of Large Eddy Simulations of Flow and Heat Transfer in a Stationary Ribbed Duct," *International Journal of Heat and Fluid Flow*, In Press.	Dev., F.D., 180º Stationary Experiments LES	2005
Sewall, E.A., Tafti, D.K., 2005, "Large Eddy Simulation of Flow and Heat Transfer in the Developing Flow Region of a Rotating Gas Turbine Blade Internal Cooling Duct with Coriolis and Buoyancy Forces," Proceedings of ASME Turbo Expo 2005, Reno-Tahoe, Nevada, 2005, ASME Paper No. GT2005-68519.	Developing Flow Buoyancy Forces LES	2005
Sewall, E.A., Tafti, D.K., 2005, "Large Eddy Simulation of Flow and Heat Transfer in the 180º Bend Region of a Stationary Ribbed Gas Turbine Internal Cooling Duct," Proceedings of ASME Turbo Expo 2005, Reno-Tahoe, Nevada, 2005, ASME Paper No. GT2005-68518.	180º Bend Stationary LES	2005
Sewall, E.A., Tafti, D.K., 2005, "Large-Eddy Simulation of Flow and Heat Transfer in the 180-Deg Bend Region of a Stationary Gas Turbine Blade Ribbed Internal Cooling Duct," ASME Journal of Turbomachinery, **128**, pp. 1-9.	180º Bend Stationary LES	2005
Viswanathan, A.K., Tafti, D.K., 2004, "Detached Eddy Simulation of Turbulent Flow and Heat Transfer in a Ribbed Duct," Proceedings of Heat Transfer/Fluids Engineering Summer Conference ASME, Charlotte, North Carolina, ASME Paper No. HT-FED2004-56152.	Fully Developed Stationary DES	2004
Viswanathan, A.K., Tafti, D.K., 2005, "Detached Eddy Simulation of Turbulent Flow and Heat Transfer in a Ribbed Duct," *ASME Journal of Fluids Engineering*, **127**, pp. 888-896.	Fully Developed Stationary DES	2005
Viswanathan, A.K., Tafti, D.K., Abdel-Wahab, S., 2005, "Large Eddy Simulation of Flow and Heat Transfer in an Internal Cooling Duct with High Blockage Ratio 45º Staggered Ribs," Proceedings of ASME Turbo Expo 2005, Reno-Tahoe, Nevada, ASME Paper No. GT2005-68086.	Fully Developed Stationary 45º Ribs LES	2005
Viswanathan, A.K., Tafti, D.K., 2005, "Large Eddy Simulation in a Duct with Rounded Skewed Ribs," Proceedings of ASME Turbo Expo 2005, Reno-Tahoe, Nevada, ASME Paper No. GT2005-68117.	Fully Developed Stationary Rounded Ribs LES	2005
Viswanathan, A.K., Tafti, D.K., 2005, "Detached Eddy Simulation of Flow and Heat Transfer in a Stationary Internal Cooling Duct with Skewed Ribs," Proceedings of ASME Turbo Expo 2005, Reno-Tahoe, Nevada, ASME Paper No. GT2005-68818.	Fully Developed Stationary 45º Ribs DES	2005
Viswanathan, A.K., Tafti, D.K., 2005, "A Comparative Study of DES and URANS in a Two-Pass Internal Cooling Duct with Normal Ribs," Proceedings of the 2005 ASME International Mechanical Engineering Congress and Exposition, Orlando, Florida, ASME Paper No. IMECE2005-79288.	2-Pass Duct Stationary DES	2005
Viswanathan, A.K., Tafti, D.K., 2005, "Detached Eddy Simulation of Turbulent Flow and Heat Transfer in a Two-Pass Internal Cooling Duct," *International Journal of Heat and Fluid Flow*, In Press.	2-Pass Duct Stationary DES	2005

Appendix B. Complete Derivation of Rotational Source Terms

The source terms for rotation, including the Coriolis and centrifugal buoyancy terms, are derived for the LES calculations from the dynamics equations describing a moving particle rotating about a central axis. The Coriolis and centrifugal acceleration terms are used to calculate the forces on the fluid due to rotation, which are implemented into the momentum conservation equations as source terms. These source terms are implemented into the governing equations solved by GenIDLEST to allow the calculation to take into account the effects of rotation on the fluid flow in a duct.

The objective of this appendix is to describe the derivation of the rotational source terms, starting with the dynamic equations in a rotating frame of reference, and their implementation into the rotating duct calculations. Once the terms are described, the implementation into the conservation equations in the context of GenIDLEST and the assumptions made, are discussed. The Coriolis and centrifugal buoyancy forces are added separately as individual inputs, allowing them to be considered separately to understand their individual effects.

B.01 Acceleration of a Fluid Particle

This derivation borrows heavily from the textbook of David Morris entitled *Heat Transfer and Fluid Flow in Rotating Coolant Channels* (Research Studies Press, New York, 1981). The premise is to consider a particle moving away from a central location. At the same time, the particle's frame of reference is rotating about that same location. The equations describing the Coriolis and centrifugal forces are derived from this situation, which is illustrated in Figure B.1.

Rotation about the *z*-axis, as shown in the figure, is the only direction considered in this project, although the initial derivation applies for an arbitrary rotational axis.

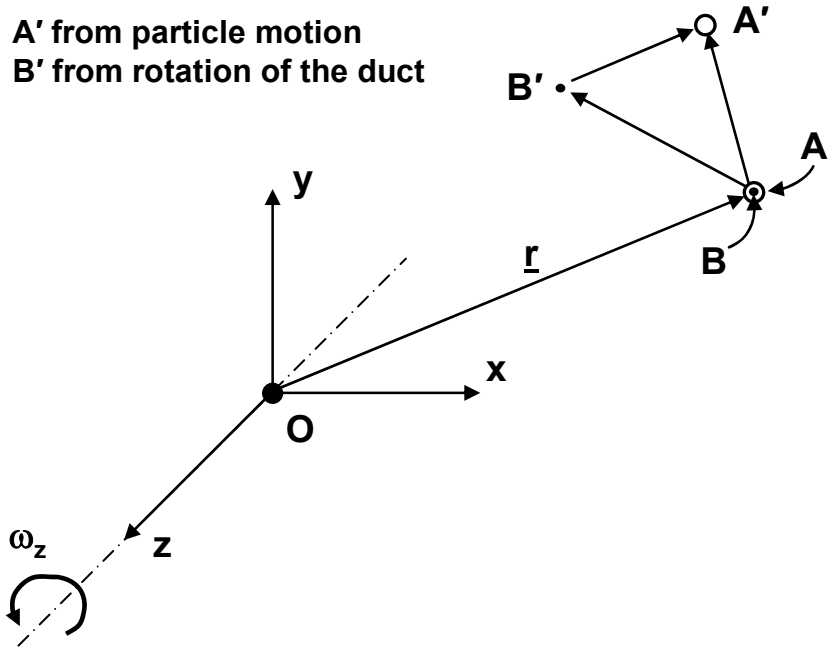

Figure B.1. The motion of flow through a rotating duct is described by a fluid particle moving away from the axis of rotation while both the particle and its initial location are rotating about the *z*-axis.

Consider a particle, A, that is located at point B, is moving in space. At some instant in time, t, the particle has a position vector, **r**, with respect to an inertial rectangular Cartesian frame of reference, OXYZ. After an interval of time, δt, particle A has moved to position A', whereas the original position, point B, which is fixed relative to the rotating frame, has moved to B'. This motion is described by the following equation:

$$AA' = BB' + B'A', \tag{1}$$

Where AA' represents the change in position of the particle in space over the time interval δt, B'A' represents the change in position of the particle relative to the rotating frame over the same

time interval, and BB' represents the change in position of the point coincident with the particle at time t that is fixed relative to the rotating frame.

Because the radius of the particles initial location (point B) is the same as the radius of point B', the path BB' may be expressed as the vector product of the angular displacement, $\boldsymbol{\omega}\delta t$, of the point B and the position vector **r**:

$$BB' = (\boldsymbol{\omega} \times \mathbf{r})\, \delta t. \tag{2}$$

The velocity vector, **v**, of particle A in space may be expressed in terms of the particle path, AA', and the path of the fixed point, BB':

$$\mathbf{v} = \lim_{\delta t \to 0}\left[\frac{AA'}{\delta t}\right] = \lim_{\delta t \to 0}\left[\frac{B'A'}{\delta t}\right] + (\boldsymbol{\omega} \times \mathbf{r}). \tag{3}$$

This equation may be expressed in terms of time derivatives in the following form:

$$\mathbf{v} = \frac{d}{dt}\mathbf{r} = \frac{\partial}{\partial t}\mathbf{r} + (\boldsymbol{\omega} \times \mathbf{r}), \tag{4}$$

where the derivative d/dt refers to time-wise differentiation with respect to any fixed reference frame having its origin at O and the partial derivative $\partial/\partial t$ refers to the rate of change relative to the rotating frame of reference with its origin at O. Equation (4) can be extended to vectors other than **r** as an operator:

$$\frac{d}{dt} = \left(\frac{\partial}{\partial t} + \boldsymbol{\omega} \times\right). \tag{5}$$

Using this identity, the acceleration of particle A may be derived by using the operator above on the particle velocity vector, **v**:

$$\mathbf{a} = \frac{d}{dt}\mathbf{v} = \frac{\partial}{\partial t}\mathbf{v} + (\boldsymbol{\omega} \times \mathbf{v}), \tag{6}$$

which can be expanded in terms of the angular velocity vector and particle position by using Eq. (4):

$$\mathbf{a} = \frac{d^2}{dt^2}\mathbf{r} + 2\left[\omega \times \frac{\partial \mathbf{r}}{\partial t}\right] + \left[\frac{\partial \boldsymbol{\omega}}{\partial t} \times \mathbf{r}\right] + \boldsymbol{\omega} \times (\boldsymbol{\omega} \times \mathbf{r}). \tag{7}$$

Equation (7) consists of four terms used to describe the acceleration of fluid particle A with respect to an inertial frame of reference. These terms are described individually in Table B.1.

Table B.1. Individual Terms Describing the Acceleration of Particle A

Term	Title	Description
$d^2\mathbf{r}/dt^2$	Particle Acceration	Acceleration of the fluid particle with respect to the inertial frame of reference
$2(\boldsymbol{\omega} \times \partial\mathbf{r}/\partial t)$	Coriolis Acceleration	Acceleration of the particle in a direction perpendicular to the flow direction and rotational axis
$(\boldsymbol{\omega} \times \boldsymbol{\omega} \times \mathbf{r})$	Centripetal Acceretation	Acceleration of the particle in the flow direction of that particle
$(\partial\boldsymbol{\omega}/\partial t \times \mathbf{r})$	Non-uniform Acceleration	Particle acceleration for a non-uniform rotation rate

B.02 Rotation in a 180º Bend

The above derivation is for a general case of rotation. In this project, the mainstream flow direction of both the developing flow and 180° bend ducts is perpendicular to the axis of rotation, and the inlet is some fixed distance, r_0, from the rotational axis, which is labeled Point O' in Figure B.2, which describes the present flow arrangement.

The position, velocity, and rotation vectors are given in terms of the inertial frame of reference corresponding to the coordinate system shown in Figure B.2:

$$\mathbf{r} = (r_0 + x)\,\mathbf{i} + \mathbf{y}\,\mathbf{j} + z\,\mathbf{k} \tag{8}$$

$$\mathbf{u} = \frac{\partial \boldsymbol{r}}{\partial t} = u\,\mathbf{i} + \mathbf{v}\,\mathbf{j} + w\,\mathbf{k} \tag{9}$$

$$\boldsymbol{\omega} = \omega_z\,\mathbf{k}. \tag{10}$$

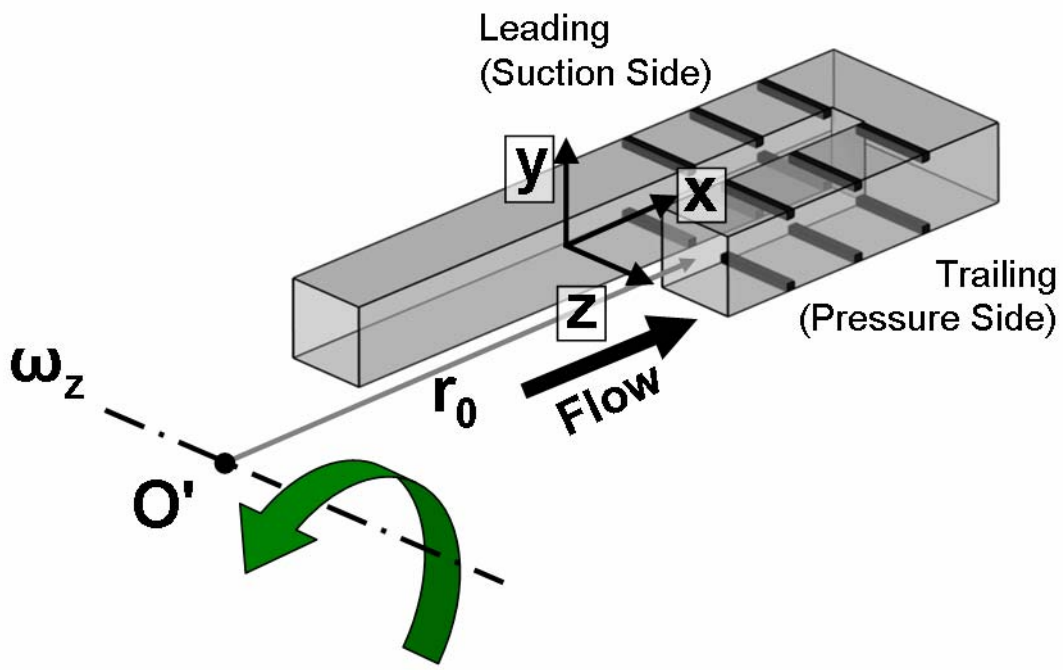

Figure B.2. For all calculations in this project, the streamwise direction is the *x*-axis and rotation occurs about the *z*-axis, which is orthogonal to the primary flow direction.

Substituting Eqs (8) – (10) into Eq. (7) results in the following form, which is specific to rotation in a duct perpendicular to the rotational axis:

$$\boldsymbol{a} = \left(\frac{\partial u}{\partial t} - 2\omega_z v - \omega_z{}^2\left(r_0 + x\right)\right)\boldsymbol{i} + \left(\frac{\partial v}{\partial t} + 2\omega_z u - \omega_z{}^2 y\right)\boldsymbol{j} + \left(\frac{\partial w}{\partial t}\right)\boldsymbol{k}\,, \tag{11}$$

where $-2\omega_z v\,\mathbf{i} + 2\,\omega_z u\,\mathbf{j}$ is the Coriolis acceleration vector and $-\omega_z^2(r_0 + x)\,\mathbf{i} - \omega_z^2 y\,\mathbf{j}$ is the *centrifugal* acceleration vector.

In the Navier-Stokes equations, the non-inertial effects of rotation are modeled as body forces in an inertial reference frame. To obtain a force per unit volume, which is implemented into the momentum equations, the Coriolis and centrifugal acceleration terms must be multiplied by the density of the cell. Because the assumption was stated earlier that the flow is incompressible, the density remains constant throughout the calculation. However, variations of

temperature in an actual flowfield produce density differences that are not negligible when acted upon by centrifugal forces. These "centrifugal buoyancy" forces either aid or oppose the rotational centrifugal forces acting on the fluid, depending on whether the fluid density is higher or lower than the reference density, respectively. The Coriolis and centrifugal buoyancy forces implemented into the momentum equations are listed as follows:

$$F_x = 2\rho\omega_z v + \rho\omega_z{}^2(r_0 + x) \text{ (x-momentum)} \tag{12}$$

$$F_y = -2\rho\omega_z u + \rho\omega_z{}^2 y \text{ (y-momentum)} \tag{13}$$

These terms are the source terms (per unit volume) implemented into the momentum equations to represent the presence of Coriolis forces and centrifugal buoyancy forces. Note that the signs are opposite those of Eq. (11) because the terms are moved to the RHS of the equation as source terms.

B.03 Implementation of Centrifugal Buoyancy

Table B.2 defines the dimensional and non-dimensional temperatures used in this derivation. In this section, all quantities with a star are dimensional.

Table B.2. Dimensional and Non-dimensional temperatures

Temperature	Description
T^*	Dimensional fluid temperature
T_{in}^*	Dimensional domain inlet temperature
T_0^*	Arbitrary dimensional reference temperature
T_{ref}^*	Dimensional mixed-mean reference temperature
T_w^*	Dimensional wall temperature
θ	Non-dimensional fluid temperature
θ_{ref}	Non-dimensional reference temperature

In typical rotating channel studies, the non-dimensional inlet rotation radius, r_0, is typically on the order of 50 hydraulic diameters. In this case, the value is two orders of magnitude (O(2))

larger than the *y*-coordinate. As a result, centrifugal buoyancy in the *y*-direction is ignored and only the *x*-direction buoyancy is considered. The buoyancy term implemented as a source term in the *x*-momentum equation, is described by the following equation:

$$\rho^* \omega_z^{*2} \left(r_0^* + x^* \right) = \left(\rho_0^* + \Delta\rho^* \right) \omega_z^{*2} \left(r_0^* + x^* \right), \tag{14}$$

where $\Delta\rho^*$ is the deviation from the reference density, ρ_0^*. Because density is assumed constant for all other terms (including the Coriolis force), ρ_0^* is divided out of the momentum equation, with the exception of the centrifugal buoyancy term:

$$\frac{\left(\rho_0^* + \Delta\rho^* \right)}{\rho_0^*} \omega_z^{*2} \left(r_0^* + x^* \right) = \left(1 + \frac{\Delta\rho^*}{\rho_0^*} \right) \omega_z^* \left(r_0^* + x^* \right). \tag{15}$$

The Boussinesq approximation is used to calculate density variations based on a linear relationship with temperature. This approximation assumes no thermal inertia is added to the convection terms in the momentum equations via density variations. Also, temperature variations are assumed to be small because density differences, which are described by the ideal gas law when air is the working fluid, are no longer accurately described by the linear Boussinesq approximation when the temperature difference are extremely large. The Boussinesq approximation is described by the following relationship between the density variation and temperatures:

$$\frac{\Delta\rho^*}{\rho_0^*} = -\beta^* (T^* - T_o^*), \tag{16}$$

where β^* is the volumetric thermal expansion coefficient, which for ideal gases is equal to the inverse of the reference temperature: $1 / T_o^*$. When applying the Boussinesq approximation, the buoyancy parameter takes the following form:

$$\mathrm{Bo}^* = \left(1 - \beta^* (T^* - T_o^*) \right) \omega_z^{*2} \left(r_0^* + x^* \right) = \omega_z^{*2} \left(r_0^* + x^* \right) - \beta^* (T^* - T_o^*) \omega_z^{*2} \left(r_0^* + x^* \right). \tag{17}$$

The first term on the RHS of Eq. (17) is the mean centrifugal force and is combined with the mean pressure gradient term. Therefore, the resulting centrifugal buoyancy term takes the following form:

$$\mathrm{Bo}^* = -\beta^*(T^* - T_o^*)\omega_z^{*2}\left(r_0^* + x^*\right). \tag{18}$$

B.04 Non-dimensionalization – Uniform Heat Flux

Expanding the buoyancy parameter, Eq. (18), with $\frac{U_b^{*2} \cdot D_h^{*2}}{U_b^{*2} \cdot D_h^{*2}}$ to back out non-dimensional parameters results in the following term:

$$\mathrm{Bo}^* = -\beta^*(T^* - T_o^*)Ro^2 r \cdot \frac{U_b^{*2}}{D_h^*}, \tag{19}$$

where Ro is the rotation number, defined by $\mathrm{Ro} = \frac{\omega_z^* D_h^*}{U_b^*}$, and r is the non-dimensional rotation radius, defined by $\frac{r^*}{D_h^*}$. The term $\frac{U_b^{*2}}{D_h^*}$ divides out of the momentum equation due to the non-dimensionalization of the other terms in the equation. Additionally, the arbitrary reference temperature, T_o^*, can be replaced by the mixed-mean temperature, T_{ref}^*, and the thermal expansion coefficient, β^*, is equivalent to $1/T_{ref}^*$. Implementing these changes to the buoyancy term results in the following form:

$$\mathrm{Bo} = -\frac{(T^* - T_{ref}^*)}{T_{ref}^*} Ro^2 r\,. \tag{20}$$

With a uniform heat flux boundary condition applied to the walls, the non-dimensional temperature is given by:

$$\theta = \frac{T^* - T_{in}^*}{\frac{q''^* D_h^*}{k^*}}. \tag{21}$$

Manipulating Eq. (20) into a form consistent with Eq. (21) produces the following:

$$\mathrm{Bo} = -\left(\frac{\left(T^* - T_{in}^*\right)}{\frac{q''^* D_h^*}{k^*}} - \frac{\left(T_{ref}^* - T_{in}^*\right)}{\frac{q''^* D_h^*}{k^*}} \right) \frac{q''^* D_h^*}{k^*} \frac{1}{T_{ref}^*} Ro^2 r . \tag{22}$$

The dimensional thermal expansion coefficient, β^*, is equal to the inverse of the dimensional reference temperature, $1/T_{ref}^*$. Therefore, the non-dimensional thermal expansion coefficient, β, is equal to $\frac{q''^* D_h^*}{k^*} / T_{ref}^*$. Substituting this and the non-dimensional temperatures into Eq. (22) results in the final form of the centrifugal buoyancy source term:

$$\mathrm{Bo} = -\beta\left(\theta - \theta_{ref}\right) Ro^2 r . \tag{23}$$

For implementing this source term into GenIDLEST, the Richardson number is defined as:

$$\mathrm{Ri} = -\beta Ro^2 r . \tag{24}$$

However, since the rotation radius, r, varies with streamwise location, a coefficient of Ri / r is defined in GenIDLEST as the buoyancy input.

Because the temperature difference is included in the formulation, the buoyancy parameter cannot be calculated a priori. The calculated buoyancy parameter must be calculated from the value input as Ri / r, the non-dimensional rotation radius, and an average non-dimensional temperature difference, which is the inverse of the average Nusselt number:

$$\mathrm{Bo}_{\mathrm{avg}} = \left(\frac{\mathrm{Ri}}{r}\right) \cdot r \overline{\left(\theta - \theta_{ref}\right)} = \left(\frac{\mathrm{Ri}}{r}\right) \cdot r \cdot \left(\frac{1}{\overline{\mathrm{Nu}}}\right). \tag{25}$$

There are two assumptions implicit in the treatment of the buoyancy term. The first is that β is a constant in spite of its dependence on T_{ref}^*, which increases in the streamwise direction and that the Reynolds number, $\mathrm{Re} = \frac{\rho_0^* D_h^* U_b^*}{\mu^*}$, is constant throughout the calculation. Since ρ_0 is tied to T_{ref}, the Reynolds number should change with the streamwise direction. Currently, there is no feedback to Re, and it is assumed to be constant.

B.05 Buoyancy Parameter in Developing Flow Calculations

To specify the buoyancy parameters in the calculations, the Richardson number was chosen to match the density ratios of Wagner et al. (1992). To differentiate the buoyancy parameters, values of Ri/r were chosen as Ri/r = 0.70, 1.40, and 2.25 for the low, medium, and high buoyancy cases, respectively. Table B.3 shows the Nusselt number augmentation averaged over each ribbed section in the developing flow calculations for use in calculating the buoyancy parameter. The resulting buoyancy parameter is also calculated

Table B.3. Developing Flow Buoyancy Parameters from the LES Calculations

Rib #	Buoyancy 1 (Ri/r=0.7)		Buoyancy 2 (Ri/r=1.4)		Buoyancy 3 (Ri/r=2.25)	
	Nu	Bo	Nu	Bo	Nu	Bo
1	137.77	0.2159	140.68	0.4230	142.26	0.6722
2	114.85	0.2651	118.56	0.5137	123.93	0.7898
3	112.82	0.2761	118.95	0.5238	128.70	0.7780
4	114.13	0.2791	122.43	0.5203	134.69	0.7601
5	119.49	0.2724	130.01	0.5007	143.25	0.7304
6	126.71	0.2624	137.13	0.4849	154.27	0.6928
7	135.81	0.2500	146.70	0.4628	163.37	0.6680
8	145.11	0.2388	152.90	0.4532	170.09	0.6548
Avg	125.84	0.2575	133.42	0.4853	145.07	0.7183

The experiments of Wagner present two forms of the density ratio, which is then used to calculate the buoyancy parameter through the following equation:

$$\mathrm{Bo} = \frac{\Delta\rho}{\rho}\mathrm{Ro}^2(\bar{r}), \tag{26}$$

where $\Delta\rho/\rho$ is the density ratio, Ro is the rotation number, and $\bar{r}$ is the average rotation radius of the duct, which has a value of 49. The two density ratios specified are $(\Delta\rho/\rho)_i$, which is the ratio at the inlet, and $\Delta\rho/\rho$, which is the local density ratio. In the experiments, $\Delta\rho/\rho$ is significantly less than the inlet ratio because it is calculated from the temperature difference, which decreases downstream of the inlet because of the constant temperature boundary conditions. In the calculations, a constant density ratio is assumed, which prevents the buoyancy parameter from decreasing significantly downstream of the inlet.

A comparison is made between the average heat transfer augmentation results of Wagner et al. (1992) in the developing region and the developing flow calculations in Figure 6.10. In this figure, the downstream section of the first pass of the duct in the experiments is compared to the downstream ribs (Ribs 7 & 8) in the developing flow calculations. The buoyancy parameter used in the experiments is calculated by Eq. (26) using the local density ratio. For the calculations, the buoyancy parameter used is an averaged over Ribs 7 & 8, which has values of 0.24, 0.46, and 0.66 (referred to in the text as 0.25, 0.45, and 0.65), for the low, medium, and high buoyancy parameters, respectively. Based on a non-dimensional rotation radius of 50 (radius between Ribs 7 & 8), the corresponding density ratios of the calculations are 0.05, 0.10, and 0.15, which are slightly less than the *inlet* density ratios specified by Wagner as 0.07, 0.12, and 0.23.

References

Morris, D.W., *Heat Transfer and Fluid Flow in Rotating Coolant Channels*, Research Studies Press, New York, 1981.

Wagner, J.H., Johnson, B.V., Graziani, R.A., Yeh, F.C., 1992, "Heat Transfer in Rotating Passages with Trips Normal to the Flow," *ASME Journal of Turbomachinery,* **114**, pp. 847-857.

Appendix C. Creation and Implementation of Time Dependent Inlet Boundary Conditions

In an unsteady calculation with a turbulent inlet boundary condition, time-dependent velocity and temperature profiles have to be specified. Synthetic boundary conditions with all the characteristics of the "real" flow are often difficult in complex situations such as the one encountered at the inlet to the 180º bend. Hence, it is necessary to use calculated profiles from and "auxiliary" calculation. To provide the inlet frames for the 180º bend calculation, the developing flow calculations are used to provide inlet frames. For example, the inlet conditions for the 180º bend calculated are extracted from the stationary developing flow calculation and so on.

There are two counteracting requirements in choosing the number of inlet frames. One is the requirement that the first and last frames are uncorrelated such that no significant artificial modes are introduced, which is counteracted by the requirement that a significant perturbation not be introduced at the inlet in transitioning from the last to the first frame. This is balanced by assuming that the correlation between the first and last frame is small but then transitioning from the last frame to the first frame by using interpolated frames. There is also the issue of the cost, either in terms of memory usage if all frames are stored in memory during the calculation, or conversely the cost of I/O when each frame is read in when needed. Overall, the goal is to use the fewest number of frames that approximate the "real" characteristics of the turbulent flow in space and time. The following paragraphs describe the process and some best practices for generating the inlet frames, checking their validity, and implementing them in a parallel multi-block environment of GenIDLEST.

C.01 Frame Extraction

The developing flow calculation is used to extract a set of i-planes (perpendicular to the streamwise direction) for the 180º bend. In this case each 180º bend calculation is started from a corresponding developing flow calculation downstream of the eighth rib because of the outflow extension downstream of the ninth rib. As the flow in the 180º bend would pass three ribs before reaching the bend, the entire channel length would be eleven ribs. To extract the frames, a subroutine is added to GenIDLEST to write the temperature and velocities at a certain i-index number (in this case, i = 68) to a file for each block in Group 8 (the group containing the eighth rib). The file written out is called bc.b**BBB**.**TTTT**, where **BBB** indicates the block number and **TTTT** indicates the iteration number (e.g. bc.b225.0001 for block 225 and iteration number 1).

To determine the number of frames required, a comparison of contour plots of the mean velocities, mean temperature, and turbulent kinetic energy is made between the time averaged data (averaged over 10 to 20 time units) and the sets of frames averaged over 5,000 and 10,000 iterations. Because these sets of frames averaged over the short time will be repeated continuously, it is extremely important that the basic flow features desired at the inlet are found in these frames. For instance, the rotating developing flow calculations show region of high turbulence along the trailing wall, low turbulence along the leading wall, and a velocity profile that is skewed towards the leading or trailing wall (depending on the buoyancy parameter). These characteristics must be present in the time-average of the set of frames used for a good representation of the true physics.

An additional factor considered in determining the number of frames required is to calculate the autocorrelation to determine when each dependent variable was no longer correlated with itself in time. The autocorrelation was calculated from the following equation:

$$R_{\varphi}(\tau,\vec{x}) = \frac{\frac{1}{N}\left[\sum \varphi(t,\vec{x}) \cdot \varphi(t+\tau,\vec{x})\right]}{\overline{a}^2}, \tag{1}$$

where ϕ is the dependent variable used to calculate the autocorrelation. This value is calculated at each point in a single frame, and an area-weighted spatial average is calculated over the frame at each time step, τ:

$$\overline{R_{\varphi}(\tau)} = \frac{\sum_{j,k} R_{\varphi}(\tau,\vec{x}(j,k)) \cdot \Delta A_{j,k}}{\sum_{j,k} \Delta A_{j,k}}. \tag{2}$$

Ideally, a zero value of the autocorrelation is desired between the first and last frame, which would indicate the proper number of frames needed in the calculation.

It was determined that 5,000 frames (1/4 time unit based on a time step of 5×10^{-5}) was sufficient based on a comparison with the autocorrelation of 10,000 frames. The autocorrelation dropped below a value of approximately 0.3 at 5,000 frames and did not drop much lower with 10,000 frames, so it was deemed sufficient to only use 5,000 frames to save on memory. The autocorrelation plots for a set of 10,000 frames extracted from a stationary developing flow calculation and a high buoyancy developing flow calculation are shown in Figure C.1.

Computer memory must be considered with this problem because the number of frames that can be read into memory at one time is limited by the RAM on the compute node. Table C.1 outlines the memory required on a single processor containing two blocks at a 96^3 grid resolution. Each "slice," which is 1/32 of the total width, has a resolution of $98 \times 5 \times 1$, or 490 grid points. Two blocks on a processor requires 980 grid points per frame. Each grid point includes four 64-bit double precision floating point values to account for the velocities *u*, *v*, and *w*, and the temperature, *t*. Each processor requires approximately 150 MB to store the frames.

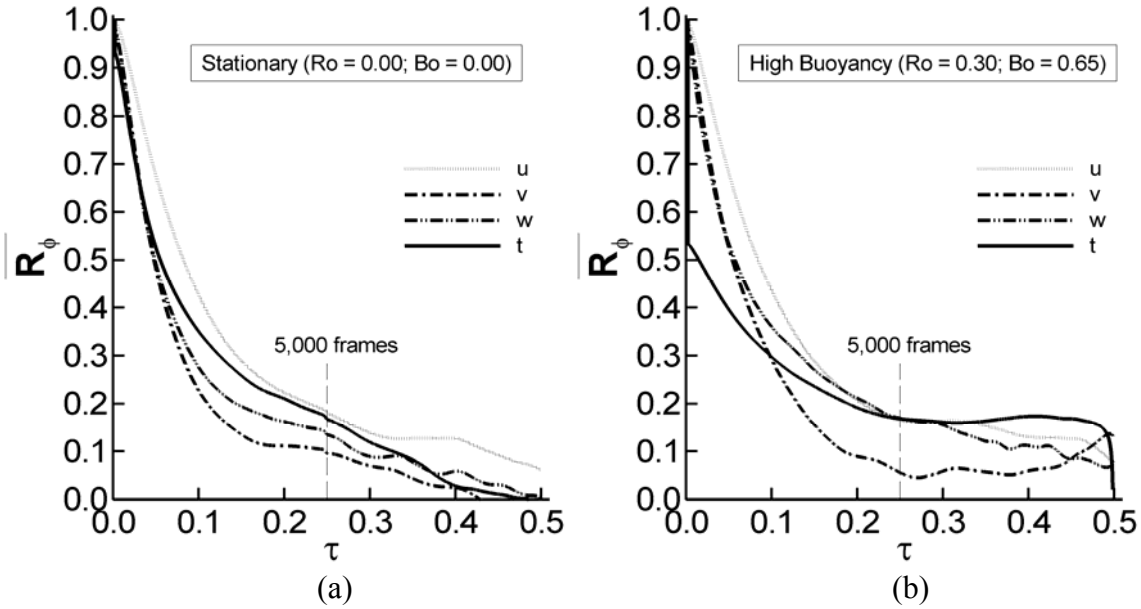

Figure C.1. The autocorrelation of extracted frames from (a) a stationary developing flow calculation and (b) a high buoyancy calculation shows that no significant differences in correlation between ½ time unit and ¼ time unit exists. Therefore, ¼ time unit was used to same on computational resources.

Table C.1. Memory Size for Inlet Boundary Conditions

Description	Size (Bytes)	Size (Mbytes)*
1 64-bit double precision floating point value	8	7.6×10^{-6}
4 values (*u*,*v*,*w*, and *t*)	32	30.5×10^{-6}
One "slice" (98 × 5 × 1)	15.68×10^{3}	15.0×10^{-3}
One processor (98 × 5 × 1 × 2)	31.36×10^{3}	29.9×10^{-3}
5,000 frames on one processor	156.80×10^{3}	149.5

*Using the conversion 1 MB = 2^{20} Bytes = 1,048,576 Bytes

C.02 Frame Processing

Once the frames have been extracted, the mean and turbulent quantities have been verified, and the autocorrelation has been calculated, the next step is to process the frames to match the conditions of the destination calculation (in this case, the 180º bend. This can involve such

processing as changing the non-dimensionalization, changing the flow angle or direction, changing the number of variables, or any other processing options. No processing was needed for the 180º bend, but some modifications could be made at this point.

One essential step in processing the frames is establishing a transition between the last frame and the first frame. Because this set of frames will be repeated once the last frame has been reached, it is important to have continuity between the final frame and the initial frame. If there is no transition, the flow will be artificially perturbed every ¼ time unit, resulting in "ringing" in the friction and heat transfer, and will never be able to settle down. To establish a transition, the final 200 frames in the set (4%, in this case) were overwritten by a linear fit at each grid point between the frame immediately before the first of the 200 and the first frame in the entire set. For 5,000 frames, this means that frames 4,801 through 5,000 were overwritten by a linear curve fit between frame 4,800 and frame 1. This transition changes the autocorrelation, as well. Now, the autocorrelation will go back to a value of unity because the last frame and the first frame are correlated. Figure C.2 shows a plot of the autocorrelation of the ¼ time unit set of frames after the transition has been applied.

Once the transition has been applied, the next step is to compile the frames into usable blocks that can be read by GenIDLEST, which is (or can be) set up to read a binary file for each block with the inlet boundary condition. Each binary file contains a three dimensional array for each flow variable, where the first two dimensions are the size of the two-dimensional domain and the third dimension is the frame number. The individual files are compiled into a file called bci1.b**BBB**, where **BBB** is the block number. Once these files have been created, they are tarred together into a single file and stored in the run directory in mass storage so it can be called along with the grid and restart files.

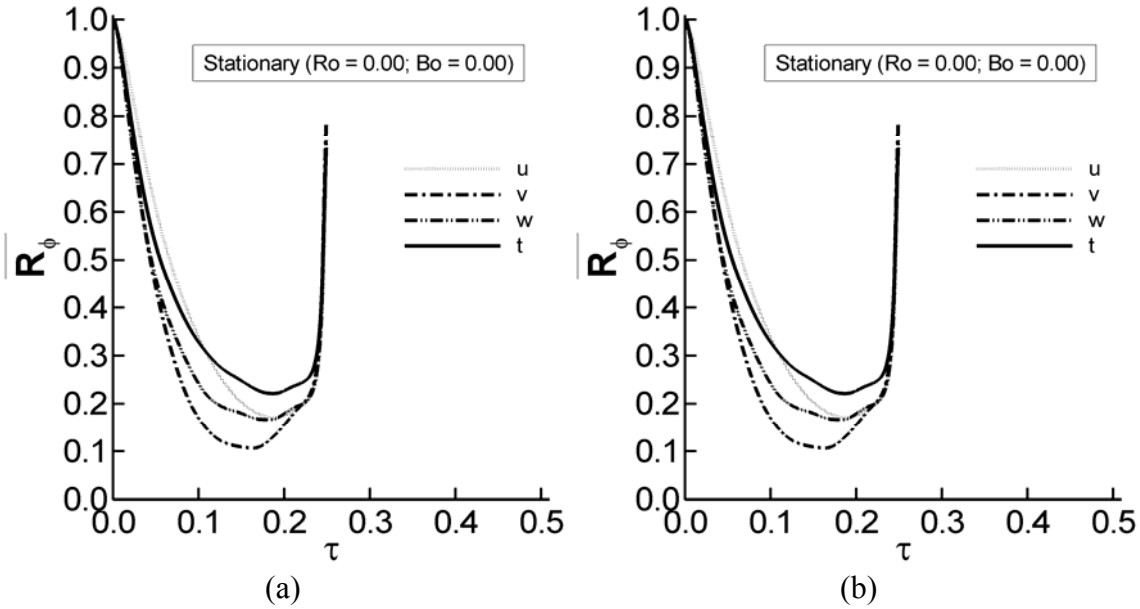

Figure C.2. The autocorrelation of the frames from the (a) stationary calculation and (b) high buoyancy calculation show the transition between the last 200 frames and the first frame brings the value of the autocorrelation back to a value of 1.

At the beginning of a calculation, GenIDLEST reads the entire set of frames (or the first set if multiple sets of frames are used). It will cycle through and implement a new boundary condition at each iteration. Once the counter reaches the maximum number of frames, it will read the next set of frames (if multiple sets are used) and reset the counter to read the first frame again. A restart file, gen.rest4.b**BBB**, is written at every location reading inlet frames and contains a single integer to keep track of which frame the calculation is on when it is restarted.

A few tips for working through the process for extracting and working with frames:

- With a large number of blocks and a large number of frames (e.g. 32 blocks multiplied by 10,000 frames = 320,000 files in a directory), name all executable and script files starting with an "`a_`", so if you want to see what files are in the directory aside from the frames, you can simply type "`ls a_* -l`" because `ls -l` will not work (too many files).

- Because there are so many files, it helps to perform frame operations in pieces. For instance, tarring the files for putting into mass store can be done by putting a set of commands in a script file, like the following:

```
#!/bin/csh
tar cvf frames.0.1000.tar bc.b*.0???
tar cvf frames.1.1000.tar bc.b*.1???
tar cvf frames.2.1000.tar bc.b*.2???
tar cvf frames.3.1000.tar bc.b*.3???
tar cvf frames.4.1000.tar bc.b*.4???
```

  This script file will tar 1000 frames at a time (the ? acts like a * for a single character). If you put this into a script file and then run the file instead of entering the commands one at a time, you won't have to keep going back and checking to see if it's done or not.

- When you write or modify subroutines to process frames, remember that the form of the frames remains the same. It is worth the extra time after you've finished to go back and archive the program files you've written so that next time you have to create a set of frames you can do it quickly without having to do any debugging.

- I have found it helpful to keep a Tecplot file with all of the autocorrelation information in it. I also have a Powerpoint file that contains the averaged contours of the restart files, 5,000 frames, and 10,000 frames. This information is helpful to have to back up the validity of your inlet conditions. It is helpful to have the information in an easily retrievable form.

- If the compiled frames file (e.g. bci1.5000.tar) is very large, it will get moved to the tape drive (AR) in mass storage within a day or two of non-use, so staging the file regularly (using the command "quote stage 0 bci1.5000.tar") to keep it in the disk drive (DK) would be helpful with a job in the queue waiting to run. Otherwise, the calculation will wait until it stages automatically at the beginning of a calculation, often taking hours to do so.

Appendix D. Large-Eddy Simuation of Flow and Heat Transfer in the 180-Deg Bend Region of a Stationary Gas Turbine Blade Ribbed Internal Cooling Duct[1]

Abstract

Large Eddy Simulation of the 180º bend in a stationary ribbed duct is presented. The domain studied includes three ribs upstream of the bend region and three ribs downstream of the bend with an outflow extension added to the end, using a total of 8.4 million cells. Two cases are compared to each other: one includes a rib in the bend and the other does not. The friction factor, mean flow, turbulence, and heat transfer are compared in the two cases to help explain the benefits and disadvantages of the wide number of flow effects seen in the bend, including flow separation at the tip of the dividing wall, counter-rotating Dean vortices, high heat transfer at areas of flow impingement, and flow separation at the upstream and downstream corners of the bend. Mean flow results show a region of separated flow at the tip of the dividing region in the case with no rib in the bend, but no separation region is observed in the case with a rib. A pair of counter-rotating Dean vortices in the middle of the bend is observed in both cases. Turbulent kinetic energy profiles show a 30% increase in the mid-plane of the bend when the rib is added. High gradients of heat transfer augmentation are observed on the back wall and downstream outside wall, where mean flow impingement occurs. This heat transfer is increased with the presence of a rib. Including a rib in the bend increases the friction factor in the bend by 80%, and it increases the heat transfer augmentation by approximately 20%, resulting in a tradeoff between pressure drop and heat transfer.

[1] Reproduced with permission from ASME

Large-Eddy Simulation of Flow and Heat Transfer in the 180-Deg Bend Region of a Stationary Gas Turbine Blade Ribbed Internal Cooling Duct

Evan A. Sewall
e-mail: esewall@vt.edu

Danesh K. Tafti

Mechanical Engineering Department,
Virginia Tech,
Blacksburg, VA 24061

Large-eddy simulation of the 180 deg bend in a stationary ribbed duct is presented. The domain studied includes three ribs upstream of the bend region and three ribs downstream of the bend with an outflow extension added to the end, using a total of 8.4 million cells. Two cases are compared to each other: one includes a rib in the bend and the other does not. The friction factor, mean flow, turbulence, and heat transfer are compared in the two cases to help explain the benefits and disadvantages of the wide number of flow effects seen in the bend, including flow separation at the tip of the dividing wall, counter-rotating Dean vortices, high heat transfer at areas of flow impingement, and flow separation at the upstream and downstream corners of the bend. Mean flow results show a region of separated flow at the tip of the dividing region in the case with no rib in the bend, but no separation region is observed in the case with a rib. A pair of counter-rotating Dean vortices in the middle of the bend is observed in both cases. Turbulent kinetic energy profiles show a 30% increase in the midplane of the bend when the rib is added. High gradients of heat transfer augmentation are observed on the back wall and downstream outside wall, where mean flow impingement occurs. This heat transfer is increased with the presence of a rib. Including a rib in the bend increases the friction factor in the bend by 80%, and it increases the heat transfer augmentation by approximately 20%, resulting in a trade-off between pressure drop and heat transfer.
[DOI: 10.1115/1.2098769]

Introduction

Flow inside cooling ducts in gas turbine blades is highly turbulent and is often complicated by the presence of ribs, which are placed in the ducts to increase turbulence and augment heat transfer. The 180-deg bends that connect two passages further complicate the flow by reversing its direction. Prediction of the flow through these cooling passages has been sought through the use of Reynolds averaged Navier–Stokes turbulence modeling for closure in the Navier–Stokes equations, but the lack of consistency and accuracy in these simulation methods brings about the motivation to use more detailed calculations, such as large-eddy simulations (LES), to predict the complicated flow. The added computational expense has proven to be worth the cost because of the significant increase in computational accuracy and reliability. The resources required have, up to this point, limited internal computational domains of ribbed ducts to those of fully developed periodic flows, but current supercomputers are capable of adequately resolving the large scales in these time-dependent calculations.

The goal of this paper is to present mean flow, turbulence, friction factor, and heat transfer results from two LES calculations of the 180-deg bend region of a ribbed internal cooling duct. The domain consists of three hydraulic diameters (three ribs) of the upstream pass, a bend region connecting the upstream and downstream passes, and three hydraulic diameters (three ribs) in the downstream leg. The duct cross section is square, ribs are attached to opposite walls in an in-line configuration, and a constant temperature boundary condition is applied on all walls and ribs. A comparison is made of a case with a rib in the bend and without a rib in the bend.

Previous Works. A heat transfer experiment by Metzger and Sahm [1] and a mass transfer experiment by Park and Lau [2] in smooth 180-deg bends both showed a steep increase in heat transfer, reaching a maximum value at the exit of the bend leading into the second pass. A PIV study by Schabacker and Bölcs in a 180 -deg bend region with smooth walls pointed out several large scale flow structures in the duct, including recirculation zones in the upstream and downstream corners, a large separation bubble hugging the inside wall downstream of the divider tip, and a set of counter-rotating vortices (Dean-type secondary motion) in a plane parallel to the dividing wall. The maximum value of turbulent kinetic energy in the bend was found in the shear layer between the separation bubble and downstream shear flow and had a magnitude of 28% [3]. A comparison of divider thicknesses in a smooth bend showed that the width of the divider has a significant effect on the size and location of the separation bubble at the tip of the dividing wall, as well as the shape of the counter-rotating Dean vortices. Peak values of turbulence are lower than those reported by Shabacker and Bölcs, falling closer to 20% [4]. A smooth channel study by Mochizuki et al. (1994) showed flow visualization of laminar flow in a bend region and found that the flow is highly three dimensional and significantly affected by the recirculation region in the upstream corner [5]. An infrared thermography study of the bend region in smooth ducts reported that bend effects do not reach more than 1 D_h upstream from the turn. The highest heat transfer occurred on the downstream part of the bend, immediately before flow entered the downstream leg. A

Contributed by the International Gas Turbine Institute (IGTI) of THE AMERICAN SOCIETY OF MECHANICAL ENGINEERS for publication in the ASME JOURNAL OF TURBOMACHINERY. Paper presented at the ASME Turbo Expo 2005: Land, Sea, and Air, Reno, NV, June 6–9, 2005, Paper No. GT2005-68518. Manuscript received by IGTI, October 1, 2004; final revision, February 1, 2005. IGTI Review Chair: K. C. Hall.

second peak in heat transfer was observed about 1.5 channel widths downstream of the bend, corresponding with reattachment of the separation bubble on the inside wall [6].

An attempt to calculate the flow characteristics around a 180-deg bend using a k-ε model was reported by Besserman and Tanrikut. This study showed that an advanced treatment of the boundary conditions was essential when the k-ε model was used [7]. Calculations of smooth U bends have been reported in several studies using more advanced models, including k-ω [8] and Reynolds-stress models [2,9].

A few experimental studies have reported flow measurements in 180-deg bends connecting ribbed ducts. PIV measurements by Son et al. [10] showed results for a bend with ribs on one wall, and LDV measurements by Liou et al. [11] focused primarily on the effects of rotation. Most other flow measurement studies focused on ducts with 45-deg ribs [12–15].

A wide number of heat transfer studies have been published on 180-deg bends with 90-deg ribs. In addition to the two mentioned in the previous paragraph, these studies include a 180-deg bend with one ribbed wall and a rib in the bend [16,17], one with ribs on opposite walls and no rib in the bend [18], another with ribs on opposite walls and no rib in the bend but with an aspect ratio of 2:1 [19], and one with two opposite rib roughened walls and no rib in the bend [20].

A computational study on a two-pass duct with 90-deg ribs was reported by Zhao and Tao [21]. They used a k-ε model with wall functions to simulate the flowfield and obtained reasonably good agreement between numerical and experimental results. More calculations of 180-deg bends have been reported of studies with 45-deg ribs [22–27].

Internal flow calculations using large-eddy simulations (LES) have rarely been used in domains other than periodic calculations of fully developed flow in ribbed ducts [28–40] because of the requirements in computational resources. Flow and pressure characteristics in smooth 90-deg pipe bends were explored by Teng et al. [41] and Rütten [42]. Recently, LES calculations have been extended to include developing flow in a ribbed duct [43,44], and a series of full two-pass channel calculations with smooth walls and 45- and 90-deg ribs was carried out by Murata and Mochizuki [45–48]. The bulk Reynolds number was less than 5,000 in these studies, which is less than $\frac{1}{4}$ of that used in the current study. No rib was included in the bend in these studies.

Objective. The objective of this study is to provide a detailed view of the flow and heat transfer in a stationary 180-deg bend connecting two ducts with in-line 90-deg ribs, using information from LES calculations and comparing them with experiments and previous findings. In this study, a comparison is made between a configuration with and without a rib in the bend, and the goal is to determine the benefit of increased heat transfer with the included rib over the friction factor penalty incurred. The comparison will be made in terms of the friction factor across the bend and the differences in the flowfield, turbulence, and heat transfer between the two cases.

Computational Model and Governing Equations

The computational domain used for studying the 180-deg bend region, shown in Fig. 1, extends from three ribs in the upstream leg to three ribs downstream and is followed by a smooth extension region. In Case 1, no rib is included in the bend, and in Case 2, a rib is included. The duct surfaces, as well as the ribs, are heated with a constant temperature boundary condition. The governing flow and energy equations are nondimensionalized by a characteristic length scale, given by the channel hydraulic diameter (D_h), a characteristic velocity scale, given by the channel bulk velocity ($\overline{u_{\text{in}}}$), and a characteristic temperature scale, given by ($T_s - T_{\text{in}}$).

The equations governing the flow are the time-dependent Navier–Stokes and energy equations in transformed coordinates,

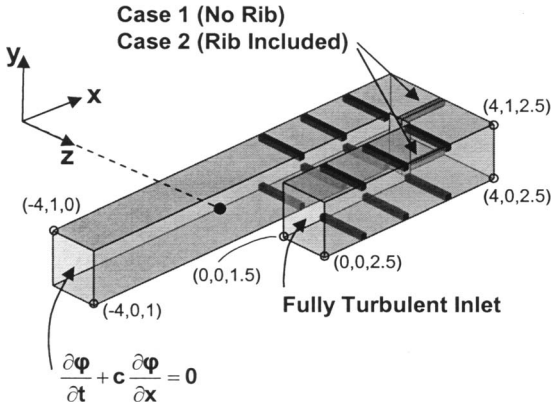

Fig. 1 The 180 deg bend domain consists of three ribs upstream and downstream of the bend. An extension region is included downstream to negate effects from the outflow boundary condition. The dividing wall is $\frac{1}{2}$ D_h in width, and the duct cross-sectional area is 1 D_h^2 throughout the bend. A comparison is made between having no rib in the bend (Case 1) and having a rib in the bend (Case 2).

$\boldsymbol{\xi} = \boldsymbol{\xi}(\mathbf{x})$. The equations, as well as all results presented in this paper, are given in terms of non-dimensional variables:

Continuity:

$$\frac{\partial}{\partial \xi_j}(\sqrt{g}\bar{U}^j) = 0, \tag{1}$$

Momentum:

$$\frac{\partial}{\partial t}(\sqrt{g}\bar{u}_i) + \frac{\partial}{\partial \xi_j}(\sqrt{g}\bar{U}^j\bar{u}_i) = -\frac{\partial}{\partial \xi_j}(\sqrt{g}(\mathbf{a}^j)_i\bar{p}), + \frac{\partial}{\partial \xi_j}\left(\left(\frac{1}{\text{Re}} + \frac{1}{\text{Re}_t}\right)\sqrt{g}g^{jk}\frac{\partial \bar{u}_i}{\partial \xi_k}\right) \tag{2}$$

and Energy:

$$\frac{\partial}{\partial t}(\sqrt{g}\bar{\theta}) + \frac{\partial}{\partial \xi_j}(\sqrt{g}\bar{U}^j\bar{\theta}) = \frac{\partial}{\partial \xi_j}\left(\left(\frac{1}{\text{PrRe}} + \frac{1}{\text{Pr}_t\text{Re}_t}\right)\sqrt{g}g^{jk}\frac{\partial \bar{\theta}}{\partial \xi_k}\right), \tag{3}$$

where $\mathbf{a}^i$ are the contravariant basis vectors (the notation $(\mathbf{a}^j)_k$ is used to denote the kth component of vector $\mathbf{a}^j$. $(\mathbf{a}^j)_k = \partial \xi_j / \partial x_k$), $\sqrt{g}$ is the Jacobian of the transformation, g^{ij} are the elements of the contravariant metric tensor, $\sqrt{g}U^j = \sqrt{g}(\mathbf{a}^j)_k u_k$ is the contravariant flux vector, u_i is the Cartesian velocity vector, and θ is the non-dimensional temperature. The overbar denotes grid filtered quantities with an implicit top-hat filter, $\bar{G}$.

The inverse of the non-dimensional eddy-viscosity, Re_t, is modeled as:

$$\frac{1}{\text{Re}_t} = C_s^2(\sqrt{g})^{2/3}|\bar{S}|, \tag{4}$$

where $|\bar{S}|$ is the magnitude of the strain rate tensor and the Smagorinsky constant C_s^2 is obtained via the Dynamic subgrid stress model [49]. The model is described in more detail in [50]. The turbulent Prandtl number used in the heat transfer model is $\text{Pr}_t = 0.5$.

The three boundary conditions imposed on the walls are the following:

$$\mathbf{u} = 0 \tag{5}$$

$$\nabla p \cdot \mathbf{n} = 0 \tag{6}$$

$$\theta_s = 1 \tag{7}$$

The inlet velocity and temperature boundary (identified as "Fully Turbulent Inlet" in Fig. 1) is represented by a series of time-dependent frames extracted from a location immediately downstream of the fifth rib in the developing flow calculation [28], giving the entire channel a length of eight ribs. The frames span a region of $\frac{1}{4}$ time unit and are repeated continuously. A comparison of the time average of the mean and turbulent quantities of the frames to that of the developing flow region from where they were extracted yielded a negligible difference. The autocorrelation spatially averaged across each frame settled to a value less than 0.2 for all quantities, and doubling the number of frames to span a region of $\frac{1}{2}$ time unit only decreased the autocorrelation to a value of 0.1. The time span of $\frac{1}{4}$ time unit was determined to be a sufficiently long time based on these criteria. The last 2% of frames in the set were linearly interpolated between the previous frame and the first frame to produce a smooth transition as the sequence of frames was repeated. A convective outflow boundary condition is used as shown in Fig. 1, where c is the convective flow velocity and is the same as the mean flow velocity.

The governing equations for momentum and energy are discretized with a conservative finite-volume formulation using a second-order central difference scheme on a non-staggered grid topology. The Cartesian velocities, pressure, and temperature are calculated and stored at the cell center, whereas contravariant fluxes are stored and calculated at the cell faces. For the time integration of the discretized continuity and momentum equations, a projection method is used. The temporal advancement is performed in two steps, a predictor step, which calculates an intermediate velocity field, and a corrector step, which calculates the updated velocity by satisfying discrete continuity. The energy equation is advanced in time by the predictor step. Details about the algorithm, functionality, and capabilities can be found in Tafti [51].

The computer program GenIDLEST (Generalized Incompressible Direct and Large-Eddy Simulations of Turbulence) used for these simulations has been applied to fully developed flow and heat transfer in a ribbed duct geometry [50], with rotation and buoyancy effects [52,53], and in a channel with 45-deg ribs [54]. It has also been applied to both stationary and rotating developing flow [28,44]. In all of these cases, it has been consistently established through comparison with experiments that predictions of mean flow, turbulent quantities, and heat transfer, are accurate to within ±10% of experiments and in some cases within experimental uncertainty.

Computational Details

The calculation domain presented in this paper is a 180-deg bend connecting two straight ribbed ducts. Each ribbed section has similar grid distribution as the 96^3 resolution periodic channel presented in Tafti [50]. A grid independence study between a periodic channel with 96^3 and 128^3 grid points showed no significant differences between the low and high resolution cases when the Dynamic Smagorinsky subgrid scale model is used. Both meshes predicted the local and mean heat transfer augmentations within experimental uncertainty on the ribbed and smooth walls. For this reason and because of the domain size, the 96^3 mesh is used for each rib. The total mesh size for this calculation is 8.4×10^6 computational cells.

The channel aspect ratio is 1:1, and the geometric ratios governing the rib placement are $e/D_h = 0.1$ and $P/e = 10$, which is typical in many computational and experimental studies. A constant temperature boundary condition is imposed on both the walls and the ribs, and the Reynolds number based on the inlet velocity, which is also the bulk fluid velocity, is 20,000. The Prandtl number in this study is 0.7.

The non-dimensional time step in the calculations is set to 5×10^{-5}. The diffusion terms are treated implicitly, and the average L_1 residual norm of global mass balance is converged to 1×10^{-8}, while the momentum and energy equations are converged to 1×10^{-7}. The calculations utilized 152 processors of an IA-64 Itanium Linux cluster. Each time step took about 0.5 μs/grid node of wall clock time.

Each calculation was initiated by assuming initial conditions similar to a fully developed channel and integrating in time until the flow reached a statistically stationary state. The time evolution of bulk quantities such as Nusselt number, wall heat flux, friction drag losses, and form drag losses were observed until all values reached a uniform state. Once stationary conditions were established, sampling to obtain mean and turbulent quantities was carried out for approximately 11.5 time units. Initial mean quantities were obtained by sampling over one time unit before obtaining turbulent statistical quantities. The sampling time was doubled by using the y symmetry of the duct and by presenting the averaged and turbulent quantities for $\frac{1}{2}$ of the duct cross section. The coordinate system used for reporting results is shown in Fig. 1.

The local Nusselt number as related to the *non-dimensional* heat flux and non-dimensional temperature is calculated as:

$$\mathrm{Nu} = \frac{q''}{\theta_s - \theta_{\mathrm{ref}}} \tag{8}$$

where q'' is the non-dimensional heat flux at the walls, $\theta_s = 1$ is the surface boundary condition, and θ_{ref} is the reference temperature defined as:

$$\theta_{\mathrm{ref}} = \frac{\int\int |u_1| \theta dA_x}{\int\int |u_1| dA_x}, \tag{9}$$

where θ is the non-dimensional temperature defined as:

$$\theta = \frac{T - T_{\mathrm{in}}}{T_s - T_{\mathrm{in}}}. \tag{10}$$

The surface-averaged Nusselt number is area weighted as:

$$\overline{\mathrm{Nu}} = \frac{\int\int_{\Omega} \mathrm{Nu} \cdot dS}{\int\int_{\Omega} dS}, \tag{11}$$

where S denotes the surface under consideration.

The Fanning friction factor is calculated in terms of the non-dimensional pressure gradient as:

$$f = -\frac{1}{2}\frac{\Delta p}{\Delta L}. \tag{12}$$

The reference value for the Nusselt number is obtained from the Dittus–Boelter correlation:

$$\mathrm{Nu}_0 = 0.023 \cdot \mathrm{Re}^{0.8} \cdot \mathrm{Pr}^{0.4} \tag{13}$$

and the reference value for the friction factor is [55]:

$$f_0 = 0.046 \cdot \mathrm{Re}^{-0.2}. \tag{14}$$

Results

Table 1 shows the friction factor and heat transfer augmentation in the ribbed sections and the bend. The section numbers correspond to the diagram above the table. The first value shown is the heat transfer augmentation or friction factor augmentation for Case 1, while the second value, in parentheses, represents Case 2. The third value is the percent change from Case 1 to Case 2. The

Table 1 Averaged heat transfer and friction in the bend

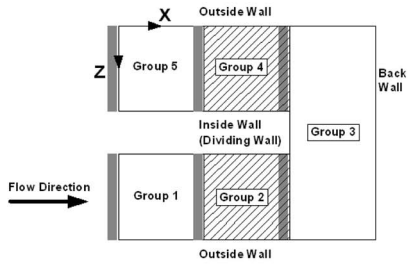

$Nu_o = 0.23\ Re^{0.8}\ Pr^{0.4}$

$f_o = 0.046\ Re^{-0.2}$

Section #	Nu / Nu$_o$ Ribbed Wall	Inside Wall	Outside Wall	f / f$_o$
Case 1 -- No Rib in Bend (Case 2 – Rib in Bend) % Change from Case 1 to Case 2				
1	2.27 (2.24) -1%	1.79 (1.77) -1%	1.59 (1.59) 0%	9.77 (9.85) +1%
2	2.42 (2.38) -2%	1.91 (1.87) -2%	1.64 (1.67) +2%	20.56 (20.96) +2%
3	3.03 (3.62) +19%			20.44 (37.22) +82%
4	3.12 (3.36) +8%	2.68 (3.26) +22%	2.97 (3.06) +3%	37.02 (35.84) -3%
5	3.02 (2.84) -6%	2.51 (2.56) +2%	2.66 (2.63) -1%	-0.55 (3.94) -716%
Dividing Wall = 3.60 Nu / Nu$_0$ (4.37) +21%			Back Wall = 2.94 Nu / Nu$_0$ (3.42) +16%	

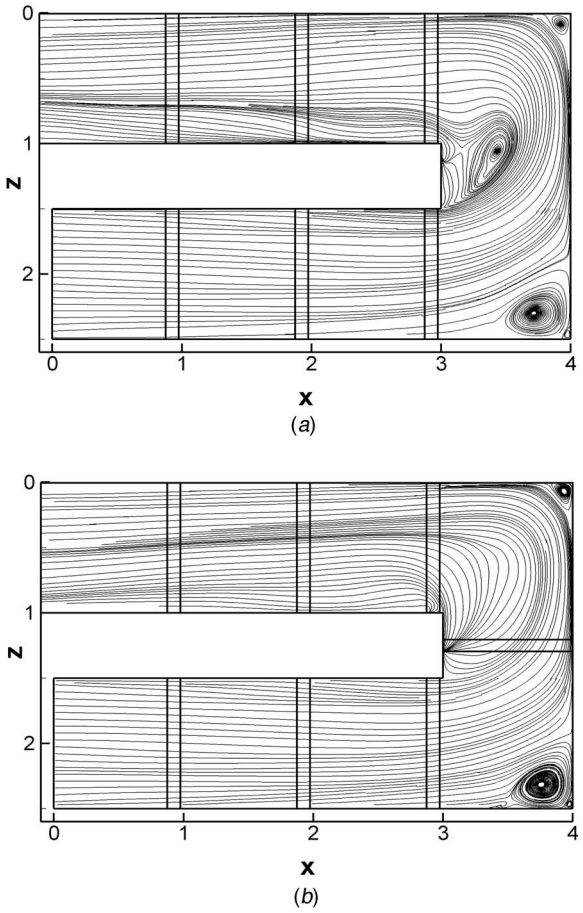

Fig. 2 The prominent features of the bend for (*a*) Case 1 and (*b*) Case 2 include separation at the end of the dividing wall and recirculation at the upstream and downstream corners, resulting in impingement of highly accelerated flow on the back wall and outside wall of the downstream leg.

table shows that the heat transfer augmentation is much higher in the downstream leg than in the upstream leg. The maximum heat transfer is found on the ribbed walls. In the upstream leg of the duct, the inside wall has a higher heat transfer augmentation than the outside wall in both cases, and in the downstream leg, the heat transfer augmentation on the outside wall is higher than the inside wall, but only in Case 1. In Case 2, the inside wall actually shows more heat transfer.

The heat transfer augmentation on the ribbed wall in the bend region is 19% higher in Case 2. The section immediately downstream of the bend is also a region of high heat transfer. In Case 1, the heat transfer peaks in this region. Downstream of the bend, the addition of the rib (Case 2) also significantly increases the heat transfer on the inside wall, in this case by 22%. The outside wall in the downstream leg of both cases experiences high heat transfer due to flow impingement. The friction factor is also much higher in the bend. The fully developed calculations show the area averaged friction factor augmentation to have a value of 8.6 across a single rib pitch. In this case, the value is slightly higher upstream of the bend (section 1) but has a significantly larger value across the entrance and exit ribs and the bend itself (sections 2–4). The last rib in the upstream leg leading into the bend (section 2) shows a friction factor augmentation about 2–3 times as large as that of the fully developed channel in both cases, and in the bend (section 3), the friction factor increases by a factor of 2 when the rib is added (Case 2).

A very large pressure drop is seen in both cases across the first rib in the downstream duct (section 4), with a value of more than four times that of the fully developed ribbed duct in both cases. It is interesting to note that the friction factor only changed significantly in the immediate vicinity of the rib in the bend. In Case 1, downstream of the bend a slight pressure recovery similar to that found in the calculation of the developing region [43,44] results in a negative friction factor, while in Case 2 only a small friction factor is shown.

A comparison of the basic flow effects in the 180-deg bend can be seen in streamlines plotted in the symmetry plane, as shown in Fig. 2. In both cases, a large recirculation zone is seen in the upstream corner of the bend, as well as a smaller zone in the downstream corner. High heat transfer augmentation results from flow impingement on the back and downstream outside walls due to redirection of the flow around the bend. In Case 1, a large recirculating bubble is observed at the tip of the dividing wall. This zone is not observed, however, in Case 2 because of the high acceleration in the streamwise direction as a result of the addition of the ribs. The recirculating zones in the corner and the separated flow at the divider tip have also been shown in the PIV study in [3] and the LDV study in [4].

Another feature of the mean flow is a pair of counter-rotating Dean vortices in the midplane of the bend, which is oriented par-

PROOF COPY [TURBO-05-1087] 008601JTM

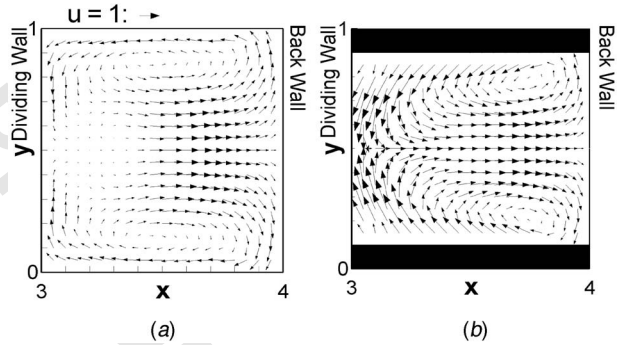

Fig. 3 A pair of counter-rotating Dean vortices at the midplane of (*a*) Case 1 and (*b*) Case 2 shows impingement on the back wall. Case 1 shows a low velocity in the recirculation bubble near the dividing wall.

allel to the dividing wall. The Dean vortices have been reported in many studies of flow through smooth 180-deg bends [3,4,7,9,10]. Vector plots of the Dean vortices are shown in Fig. 3 for both cases. In Case 1, the peak velocity is found near the back wall, with a low velocity seen in the region near the large recirculation bubble shown previously. In Case 2, however, the recirculation strength near the dividing wall is much stronger due to the high vertical velocity above the ribs. The horizontal velocity towards the back wall is similar to that of Case 1.

A comparison of the streamwise velocity and streamwise turbulence is shown in Fig. 4. Two vertical locations are considered: one at $\frac{1}{4}$ of the channel height (y=0.25) and the other at the midchannel height (y=0.50). The LDV data of Sewall et al. [56], which was taken in a duct with geometry and flow conditions exactly the same as Case 1, is also shown in the figure.

In the middle plane of the bend, the streamwise velocity is nominally negative, and positive values indicate backward flow. In Case 1, both experiments and computations show the presence of a recirculating region at the inner wall of the bend, whereas the presence of the rib in the bend prevents the separation and recirculation. Besides this effect, the ribs in the bend also tend to produce a more uniform flow in the bend particularly at y=0.25 near the ribbed wall. The comparisons of mean flow velocity show very good agreement with LDV data.

Streamwise turbulence comparisons show the highest turbulence near the inside wall, peaking at 55% in this case, and the lowest turbulence near the back wall, dipping below 15% in the figure. Towards the center of the duct, the turbulence in both cases is approximately equal. The measured values are in close agreement with the computations, although the measurements show a trajectory of the shear layer which is slightly closer to the inside wall of the bend. Because the measurement plane is directly on top of the ribs, the distributions of streamwise turbulence intensities are not very different between Case 1 and Case 2.

Turbulent kinetic energy in the midplane of the bend (Fig. 5) shows the effect of adding a rib in the bend. Unlike the distribution of streamwise intensities as shown in Fig. 4, the distribution of turbulent kinetic energy is strongly affected by the presence of the rib in the bend through the differences in cross-stream and spanwise fluctuations. In Case 1, turbulence as high as 35% from the shear layers on the ribs upstream of the bend is shown to be transported towards the center of the dividing wall by the action of the secondary Dean vortices. In Case 2, the turbulence is further augmented by the ribs in the bend and reaches over 45%. In a 180-deg bend connecting two smooth ducts, the turbulent kinetic energy peaks at 20% [3,4]. In Case 1, a vertical layer of relatively high turbulence (20% surrounded by 15%) indicates the presence of the shear layer formed from flow separation off of the dividing wall as flow enters the bend. In Case 2, the shear layer is

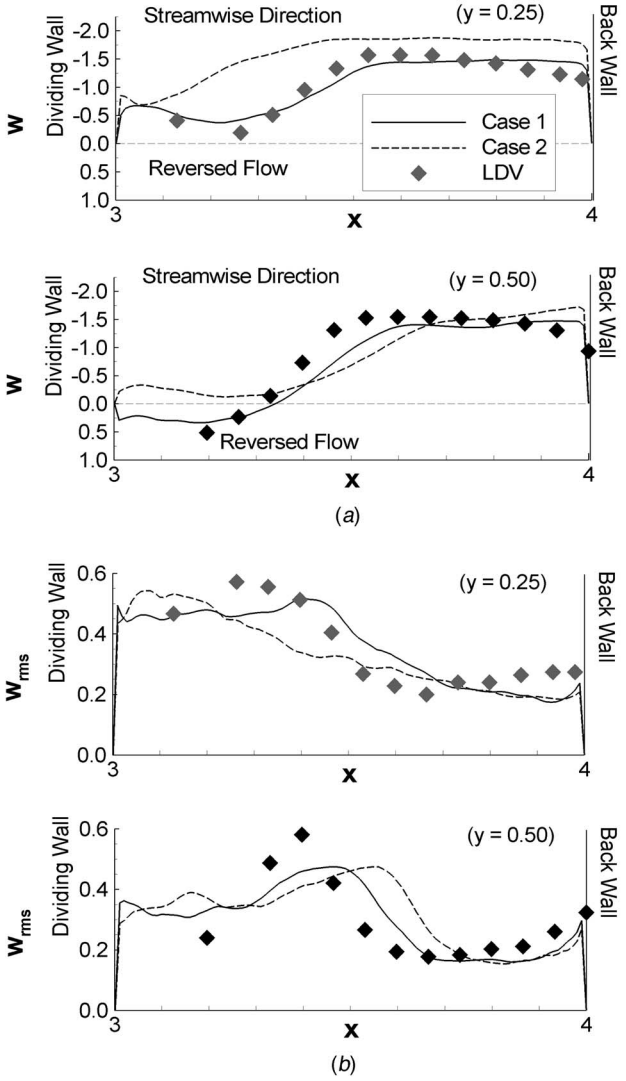

Fig. 4 The (*a*) streamwise velocity and (*b*) streamwise rms quantity are compared between Case 1 (solid line) and Case 2 (dashed line). The LDV measurements correspond to the calculations in Case 1.

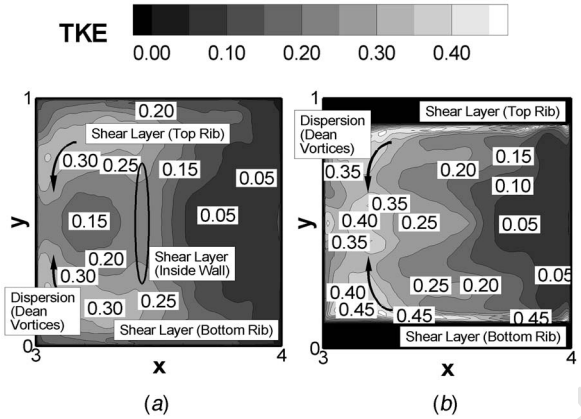

Fig. 5 Turbulent kinetic energy in the bend in (*a*) Case 1 and (*b*) Case 2 shows the combination of shear layers as well as transport of turbulence up along the inside wall from the motion of the Dean vortices.

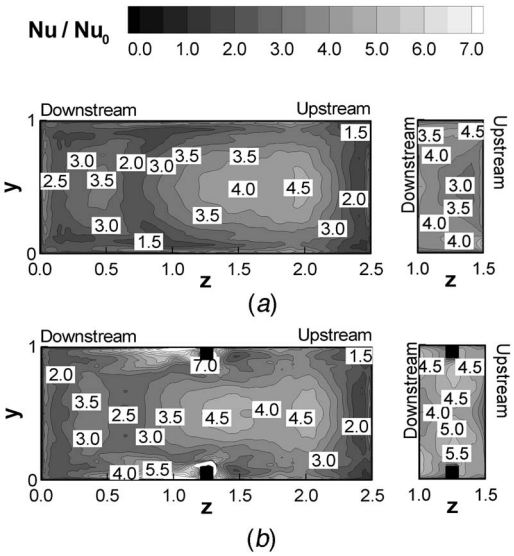

Fig. 6 Heat transfer augmentation on the back wall and tip of the dividing wall with (*a*) Case 1 and (*b*) Case 2 shows the difference in heat transfer augmentation near the top and bottom walls and the higher heat transfer augmentation on the tip of the dividing wall due to the presence of the rib.

not seen explicitly and the turbulence is much higher. In both cases, the turbulence near the back wall is very low, between 5% and 10%.

As a result of the mean and turbulent flow effects, the dividing wall and back wall of the bend show large gradients of heat transfer augmentation. Flow from the upstream duct impinges on the back wall, and due to the motion of the counter-rotating Dean vortices, the fluid is swept back towards the inside wall where it increases the heat transfer augmentation on the end of the dividing wall near the ribbed walls in both cases. These effects can be seen in Fig. 6. In both cases, the peak heat transfer augmentation on the center of the back wall has a value of 4.5, but in Case 2 the heat transfer near the ribs reaches over 7.0. The presence of the rib also increases the heat transfer augmentation on the dividing wall tip. The maximum augmentation in Case 2 reaches 5.5, while the maximum in Case 1 is only 4.0, which is 27% less than that of Case 2. The edges of the back wall show low heat transfer near the ribbed walls in Case 1 but show much higher heat transfer in the same area in Case 2.

Figure 7 shows a series of comparisons between the mass transfer experiments of Han et al. [20] at Re=30,000 and the LES calculations in the upstream and downstream legs of the duct. The rib size (e/D_h) and spacing (P/e) and in-line rib configuration with ribs on opposite walls are the same as those in the present study. A number of studies in the fully developed region of ribbed ducts have shown a very weak dependence of heat transfer augmentation ratios on Reynolds number (Re=30,000 in the experiments) that is certainly within experimental uncertainty [56–59]. In the study by Han et al. [20], averaged heat transfer augmentation values in the bend yielded essentially no difference between Reynolds numbers of 15,000 and 30,000. The experimental uncertainty was reported to be ±8%, and the calculated heat transfer augmentation is expected to be well within the range of the experimental values. A study of smooth 180-deg bends comparing divider thickness of $\frac{1}{2}\,D_h$ (calculations) and $\frac{1}{4}\,D_h$ (experiments) [4] concluded that a larger dividing wall thickness would decrease the turbulent kinetic energy downstream of the bend and reduce the heat transfer augmentation. However, in ribbed ducts the level of turbulence is much higher than that encountered in smooth

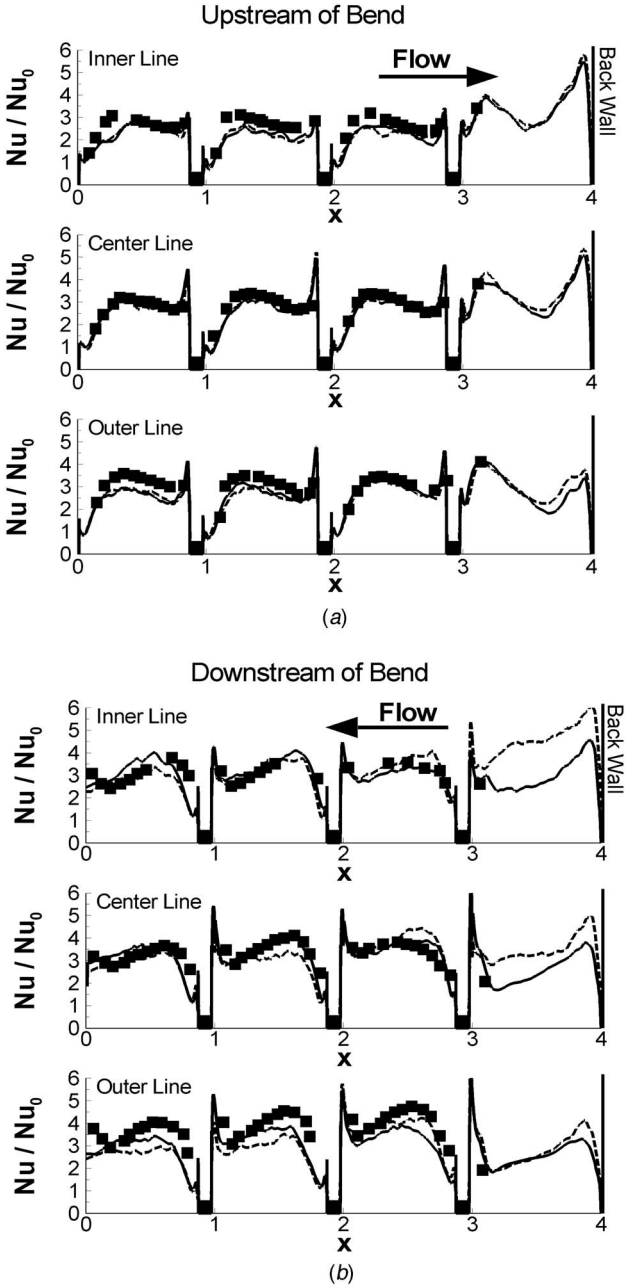

Fig. 7 Heat transfer comparisons with Han et al. [20] along an inner line, center line, and outer line in the (*a*) upstream leg and (*b*) downstream leg of the ribbed wall show good agreement between the mass transfer experiments and heat transfer results. The measurements of Han et al. did not have a rib in the bend (Case 1), and the dashed lines denote the LES calculations of Case 2.

ducts, and the effect of the thickness of the dividing wall may not have a large effect on the average heat transfer augmentation downstream of the bend.

The experimental measurements of Han et al. [20] were taken along three lines on the ribbed wall of the duct. The inner line was measured midway between the centerline and inside wall, and the outer line was measured midway between the centerline and outside wall. The first three plots show comparisons along the ribbed wall of the upstream side of the bend, where flow is in the $+x$ direction, and the last three are downstream of the bend, where flow is in the $-x$ direction. The upstream calculations [Fig. 7(*a*)]

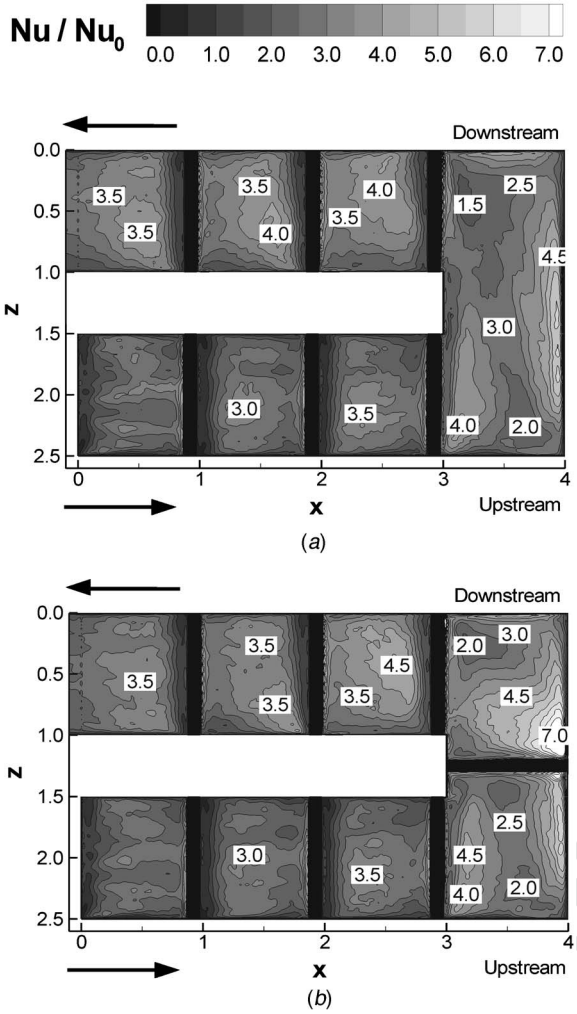

Fig. 8 The heat transfer augmentation on the ribbed wall in (*a*) Case 1 and (*b*) Case 2 shows the high heat transfer in the immediate vicinity of the rib and a slightly increased heat transfer augmentation downstream.

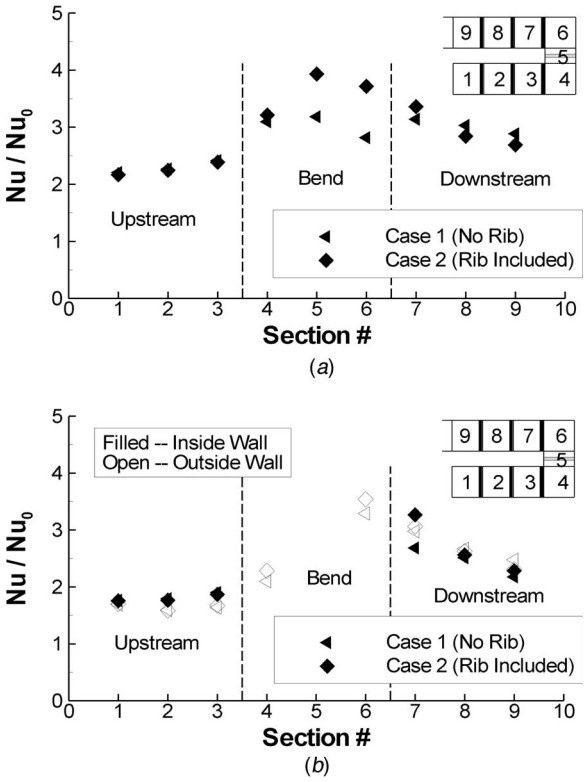

Fig. 9 Average heat transfer augmentation on (*a*) the ribbed walls and (*b*) the inside and outside walls shows the increase in heat transfer due to the rib.

show that the bend has relatively little effect on the upstream flow. An increase in heat transfer augmentation is seen downstream of the last rib, and a very high value can be seen in the corner at the back wall. Downstream of the bend [Fig. 7(*b*)], the heat transfer is shifted more towards the outside wall than it was upstream. Here, the outside line shows a much higher heat transfer augmentation than it did on the upstream side. Also, the inner two curves show a low heat transfer augmentation downstream of the first rib in the downstream leg, but this value is found to increase after the second rib. The only significant difference between the two LES cases is found on the downstream side of the bend, where the inclusion of the rib increases the heat transfer significantly.

Figure 8 shows the heat transfer augmentation on the ribbed wall of both cases. In the upstream section, the heat transfer augmentation is nearly identical in both cases. For Case 2, the peak heat transfer increases significantly along the back wall, as well as in the downstream half of the bend, where greater flow acceleration due to the added ribs causes stronger flow impingement on the outside wall than in Case 1. At the entrance to the second pass of the duct, the effect of the included rib is manifest through a higher peak heat transfer value in Case 2 in the reattachment region downstream of the first rib. Heat transfer downstream of the following ribs becomes similar between the two cases, indicating that the added rib in Case 2 only increases the heat transfer augmentation in the bend and immediately downstream.

Averaged heat transfer along the ribbed wall is shown in Fig. 9(*a*). The presence of the rib increases the bend heat transfer dramatically, but the increase in heat transfer is not seen past the entrance to the downstream leg. In the bend, the rib is shown to increase heat transfer augmentation by 20–30%. Figure 9(*b*) shows the sidewall heat transfer. The addition of the rib slightly increases the outside wall heat transfer on both the upstream and downstream sides, but in the downstream leg the rib increases the heat transfer on both the inside and outside walls. The inside wall is increased significantly, and it actually has a value larger than the outside wall in Case 2, as well.

Conclusions

Large eddy simulations are shown to be an effective prediction tool for highly turbulent flows in the 180-deg bend region of a ribbed duct. Two configurations were compared in this study, one without a rib in the bend and the other with a rib included in the bend, and the conclusions are as follows:

- Both cases showed a pair of counter-rotating Dean vortices in the midplane of the bend, while only Case 1 showed a large recirculation zone at the tip of the dividing wall.
- The friction factor increases by a factor of 2 across the last rib in the upstream leg of the bend in both cases. The friction factor is approximately four times as large as that of a straight ribbed duct across the first rib in the downstream leg.
- Upstream of the bend, the ribbed wall and smooth wall heat transfer are unaffected by the addition of the rib in the middle of the bend. In this region, however, the average heat transfer on the back wall increases by 16%, and the heat transfer on the tip of the divider wall increases by 21%. The ribbed wall also experiences a jump of nearly 20% when the rib is added in the bend.

PROOF COPY [TURBO-05-1087] 008601JTM

- Downstream of the bend, the heat transfer is about 8% higher on the ribbed wall in Case 2 (added rib), but it is also higher on the inside and outside walls. In addition, the inside wall has a higher heat transfer augmentation than the outside wall in Case 2, while the opposite is true in Case 1.
- Adding a rib to the bend increases the friction factor by 82%, while it only increases the heat transfer by 20%. Though the trade-off is significant, it may still be advisable to place a rib in the bend if the 20% increase in heat transfer is worth the pressure loss incurred by doing so.

Acknowledgments

This research was supported by the U.S. DOE, Office of Fossil Energy, National Energy Technology Laboratory. Any opinions, findings, conclusions, or recommendations expressed herein are those of the author and do not necessarily reflect the views of the DOE. This work was also supported by National Computational Science Alliance under MCA98N042N and utilized the Teragrid Linux cluster at the National Center for Supercomputing Applications.

Nomenclature

D_h = hydraulic diameter, characteristic length
e = rib height
f = fanning friction factor
k = thermal conductivity
ΔL = change in streamwise position between two pressure measurements
$\underline{\mathrm{Nu}}$ = local Nusselt number
$\overline{\mathrm{Nu}}$ = spatially averaged Nusselt number
P = rib pitch
p = non-dimensional pressure
Pr = Prandtl number ($=\mu C_p/K$)
q'' = non-dimensional heat flux on duct walls and ribs
Re = Reynolds number ($=\bar{u}_{\mathrm{in}} D_h/v$)
T = temperature, characteristic temperature is ($T_s - T_{\mathrm{in}}$)
TKE = turbulent kinetic energy described by: TKE $=(\overline{u'^2}+\overline{v'^2}+\overline{w'^2})/2\bar{u}_{\mathrm{in}}^2$
$\mathbf{u}$ = Cartesian velocity vector (u,v,w) or (u_1,u_2,u_3)
$\bar{u}_{\mathrm{in}}$ = inlet flow velocity/mean bulk flow velocity, characteristic velocity
$\mathbf{x}$ = physical coordinates (x,y,z) or (x_1,x_2,x_3)
Ω = heat transfer surface area
θ = non-dimensional temperature, $(T-T_{\mathrm{in}}/T_s-T_{\mathrm{in}})$
$\boldsymbol{\xi}$ = computational coordinates (ξ,η,ζ)

Subscripts

s = surface
in = inlet to calculation domain; average bulk velocity
rms = root mean square
t = turbulent Reynolds number and Prandtl number
0 = smooth duct

References

[1] Metzger, D. E., and Sahm, M. K., 1986, "Heat Transfer Around Sharp 180-deg Turns in Smooth Rectangular Channels," ASME J. Heat Transfer, **108**, pp. 500–506.
[2] Park, C. W., and Lau, S. C., 1998, "Effect of Channel Orientation of Local Heat (Mass) Transfer Distributions in a Rotating Two-Pass Square Channel With Smooth Walls," ASME J. Heat Transfer, **120**, pp. 624–632.
[3] Schabacker, J., and Bölcs, A., 1998, "PIV Investigation of the Flow Characteristics in an Internal Coolant Passage With Two Ducts Connected by a Sharp 180° Bend," *Proceedings of the International Gas Turbine & Aeroengine Congress & Exhibition*, Stockholm, Sweden, *ASME Paper No. 98-GT-544*.
[4] Liou, T.-M., Tzeng, Y.-Y., and Chen, C.-C., 1999, "Fluid Flow in a 180-deg Sharp Turning Duct With Different Divider Thicknesses," ASME J. Turbomach., **121**, pp. 569–576.
[5] Mochizuki, S., Takamura, J., Yamawaki, S., and Yang, W.-J., 1994, "Heat Transfer in Serpentine Flow Passages With Rotation," ASME J. Turbomach., **116**, pp. 133–140.
[6] Cardone, G., Astarita, T., and Carlomagno, G. M., 1998, "Wall Heat Transfer in Static and Rotating 180[d] Turn Channels by Quantitative Infrared Thermography," Rev. Gen. Therm., **37**, pp. 644–652.
[7] Besserman, D. L., and Tanrikut, S., 1992, "Comparison of Heat Transfer Measurements With Computations for Turbulent Flow Around a 180-deg Bend," ASME J. Turbomach., **114**, pp. 865–871.
[8] Song, B., and Amano, R. S., 2000, "Application of Non-Linear k-ω Model to the Turbulent Flow Inside a Sharp U-Bend," *Proceedings of the ASME Turbo Expo 2000*, Munich, Germany, *ASME Paper No. 2000-GT-0225*.
[9] Gu, X., Wu, H.-W., Schock, H. J., and Shih, T. I.-P., 2002, "Two-Equation Versus Reynolds-Stress Modeling in Predicting Flow and Heat Transfer in a Smooth U-Duct With and Without Rotation," *Proceedings of the ASME Turbo Expo 2002*, Amsterdam, The Netherlands, *ASME Paper No. GT-2002-30616*.
[10] Son, S. Y., Kihm, K. D., and Han, J.-C., 2002, "PIV Flow Measurements for Heat Transfer Characterization in Two-Pass Square Channels With Smooth and 90° Ribbed Walls," Int. J. Heat Mass Transfer, **45**, pp. 4809–4822.
[11] Liou, T.-M., Chen, M.-Y., and Tsai, M.-H., 2002, "Fluid Flow and Heat Transfer in a Rotating Two-Pass Square Duct With In-Line 90-deg Ribs," ASME J. Turbomach., **124**, pp. 260–268.
[12] Tse, D. G. N., and Steuber, G. D., 1997, "Flow in a Rotating Square Serpentine Coolant Passage With Skewed Trips," *Proceedings of the International Gas Turbine and Aeroengine Congress and Exhibition*, Orlando, Florida, *ASME Paper No. 97-GT-529*.
[13] Iacovides, H., Jackson, D. C., Kelemenis, G., Launder, B. E., and Yuan, Y.-M., 2001, "Flow and Heat Transfer in a Rotating U-Bend With 45° Ribs," Int. J. Heat Fluid Flow, **22**, pp. 308–314.
[14] Chanteloup, D., Juaneda, Y., and Bölcs, A., 2002, "Combined 3D Flow and Heat Transfer Measurements in a 2-Pass Internal Coolant Passage of Gas Turbine Airfoils," *Proceedings of the ASME Turbo Expo 2002*, Amsterdam, The Netherlands, *ASME Paper No. GT-2002-30214*.
[15] Servouse, Y., and Sturgis, J. C., 2003, "Heat Transfer and Flow Field Measurements in a Rib-Roughened Branch of a Rotating Two-Pass Duct," *Proceedings of the ASME Turbo Expo 2003*, Atlanta, Georgia, *ASME Paper No. GT2003-38048*.
[16] Ekkad, S. V., and Han, J.-C., 1997, "Detailed Heat Transfer Distributions in Two-Pass Square Channels With Rib Turbulators," Int. J. Heat Mass Transfer, **40**, pp. 2525–2537.
[17] Ekkad, S. V., Pamula, G., and Shantiniketanam, M., 2000, "Detailed Heat Transfer Measurements Inside Straight and Tapered Two-Pass Channels With Rib Turbulators," Exp. Therm. Fluid Sci., **22**, pp. 155–163.
[18] Chandra, P. R., Han, J. C., and Lau, S. C., 1988, "Effect of Rib Angle on Local Heat/Mass Transfer Distribution in a Two-Pass Rib-Roughened Channel," ASME J. Turbomach., **110**, pp. 233–241.
[19] Mochizuki, S., Murata, A., Shibata, R., and Yang, W.-J., 1999, "Detailed Measurements of Local Heat Transfer Coefficients in Turbulent Flow Through Smooth and Rib-Roughened Serpentine Passages With a 180° Sharp Bend," Int. J. Heat Mass Transfer, **42**, pp. 1925–1934.
[20] Han, J. C., Chandra, P. R., and Lau, S. C., 1988, "Local Heat/Mass Transfer Distributions Around Sharp 180 Deg Turns in Two-Pass Smooth and Rib-Roughened Channels," ASME J. Heat Transfer, **110**, pp. 91–98.
[21] Zhao, C. Y., and Tao, W. Q., 1997, "A Three Dimensional Investigation on Turbulent Flow and Heat Transfer Around Sharp 180-Deg Turns in Two-Pass Rib-Roughened Channels," Int. J. Heat Mass Transfer, **24**, pp. 587–596.
[22] Bonhoff, B., Tomm, U., Johnson, B. V., and Jennions, I., 1997, "Heat Transfer Predictions for Rotating U-Shaped Coolant Channels With Skewed Ribs and With Smooth Walls," *Proceedings of the International Gas Turbine & Aeroengine Congress & Exhibition*, Orlando, Florida, *ASME Paper No. 97-GT-162*.
[23] Stephens, M. A., and Shih, T. I.-P., 1997, "Computation of Compressible Flow and Heat Transfer in a Rotating Duct With Inclined Ribs and a 180-Degree Bend," *Proceedings of the International Gas Turbine & Aeroengine Congress & Exhibition*, Orlando, Florida, *ASME Paper No. 97-GT-192*.
[24] Shih, T. I.-P., Lin, Y.-L., Stephens, M. A., and Chyu, M. K., 1998, "Flow and Heat Transfer in a Ribbed U-Duct Under Typical Engine Conditions," *Proceedings of the International Gas Turbine & Aeroengine Congress & Exhibition*, Stockholm, Sweden, *ASME Paper No. 98-GT-213*.
[25] Jang, Y.-J., Chen, H.-C., and Han, J.-C., 2000, "Flow and Heat Transfer in a Rotating Square Channel With 45° Angled Ribs by Reynolds Stress Turbulence Model," *Proceedings of the ASME Turbo Expo 2000*, Munich, Germany, *ASME Paper No. 2000-GT-0229*.
[26] Lin, Y.-L., Shih, T. I.-P., Stephens, M. A., and Chyu, M. K., 2001, "A Numerical Study of Flow and Heat Transfer in a Smooth and Ribbed U-Duct With and Without Rotation," ASME J. Heat Transfer, **123**, pp. 219–232.
[27] Al-Qahtani, M., Jang, Y.-J., Chen, H.-C., and Han, J.-C., 2002, "Prediction of Flow and Heat Transfer in Rotating Two-Pass Rectangular Channels With 45 -Deg Rib Turbulators," ASME J. Turbomach., **124**, pp. 242–250.
[28] Ciofalo, M., and Collins, M. W., 1992, "Large-Eddy Simulation of Turbulent Flow and Heat Transfer in Plane and Rib-Roughened Channels," Int. J. Opt. Comput., **15**, pp. 453–489.
[29] Braun, H., Neumann, H., and Mitra, N. K., 1999, "Experimental and Numerical Investigation of Turbulent Heat Transfer in a Channel With Periodically

Arranged Rib Roughness Elements," Exp. Therm. Fluid Sci., **19**, pp. 67–76.
[30] Murata, A., and Mochizuki, S., 2000, "Large Eddy Simulation With a Dynamic Subgrid-Scale Model of Turbulent Heat Transfer in an Orthogonally Rotating Rectangular Duct With Transverse Rib Turbulators," Int. J. Heat Mass Transfer, **43**, pp. 1243–1259.
[31] Murata, A., and Mochizuki, S., 2001, "Comparison Between Laminar and Turbulent Heat Transfer in a Stationary Square Duct With Transverse or Angled Rib Turbulators," Int. J. Heat Mass Transfer, **44**, pp. 1127–1141.
[32] Murata, A., and Mochizuki, S., 2001, "Effect of Centrifugal Buoyancy on Turbulent Heat Transfer in an Orthogonally Rotating Square Duct With Transverse or Angled Rib Turbulators," Int. J. Heat Mass Transfer, **44**, pp. 2739–2750.
[33] Murata, A., and Mochizuki, S., 2003, "Effect of Cross-Sectional Aspect Ratio on Turbulent Heat Transfer in an Orthogonally Rotating Rectangular Duct With Angled Rib Turbulators," Int. J. Heat Mass Transfer, **46**, pp. 3119–3133.
[34] Jordan, S. A., 2003, "The Turbulent Character and Pressure Loss Produced by Periodic Symmetric Ribs in a Circular Duct," Int. J. Heat Fluid Flow, **24**, pp. 795–806.
[35] Cui, J., Patel, V., and Lin, C.-L., 2003, "Large-Eddy Simulation of Turbulent Flow in a Channel With Rib Roughness," Int. J. Heat Fluid Flow, **24**, pp. 372–388.
[36] Saha, A. K., and Acharya, S., 2003, "Flow and Heat Transfer in an Internally Ribbed Duct With Rotation: An Assessment of LES and URANS," *Proceedings of the ASME Turbo Expo 2003*, Atlanta, Georgia, *ASME Paper No. GT2003–38619*.
[37] Tyagi, M., and Acharya, S., 2004, "Large Eddy Simulations of Flow and Heat Transfer in Rotating Ribbed Duct Flows," *Proceedings of the ASME Turbo Expo 2004*, Vienna, Austria, *ASME Paper No. GT2004-53401*.
[38] Ahn, J., Choi, H., and Lee, J. S., 2004, "Large Eddy Simulation of Flow and Heat Transfer in a Channel Roughened by Square or Semicircle Ribs," *Proceedings of the ASME Turbo Expo 2004*, Vienna, Austria, *ASME Paper No. GT2004-53924*.
[39] Watanabe, K., and Takahashi, T., 2002, "LES Simulation and Experimental Measurement of Fully Developed Ribbed Channel Flow and Heat Transfer," *Proceedings of the ASME Turbo Expo 2002*, Amsterdam, The Netherlands, *ASME Paper No. GT-2002-30203*.
[40] Takahashi, T., and Watanabe, K., 2004, "Large Eddy Simulation of Flow and Heat Transfer in a Rectangular Channel With Crossed Angled Ribs," *Proceedings of the ASME Turbo Expo 2004*, Vienna, Austria, *ASME Paper No. GT2004-53673*.
[41] Tang, X.-L, Qian, Z.-D., Wu, Y.-L., Liu, S.-H., and Yang, F., 2004, "An Improved Dynamic Subgrid-Scale Stress Model," J. Hydrodynam., **16**, pp. 276–282.
[42] Rütten, F., Meinke, M., and Schröder, W., 2001, "Large-Eddy Simulations of 90° Pipe Bend Flows," J. Turbul., **2**, pp. 1–14.
[43] Sewall, E. A., and Tafti, D. K., 2004, "Large Eddy Simulation of the Developing Region of a Stationary Ribbed Internal Turbine Blade Cooling Channel," *Proceedings of the ASME Turbo Expo 2004*, Vienna, Austria, *ASME Paper No. GT2004-53832*.
[44] Sewall, E. A., and Tafti, D. K., 2004, "Large Eddy Simulation of the Developing Region of a Rotating Ribbed Internal Turbine Blade Cooling Channel," *Proceedings of the ASME Turbo Expo 2004*, Vienna, Austria, *ASME Paper No. GT2004-53833*.
[45] Murata, A., and Mochizuki, S., 2004, "Large Eddy Simulation of Turbulent Heat Transfer in a Rotating Two-Pass Smooth Square Channel With Sharp 180° Turns," Int. J. Heat Mass Transfer, **47**, pp. 683–698.
[46] Murata, A., and Mochizuki, S., 2004, "Effect of Rib Orientation and Channel Rotation on Turbulent Heat Transfer in a Two-Pass Square Channel With Sharp 180° Turns Investigated by Using Large Eddy Simulation," Int. J. Heat Mass Transfer, **47**, pp. 2599–2618.
[47] Murata, A., and Mochizuki, S., 2004, "Centrifugal Buoyancy Effect on Turbulent Heat Transfer in a Rotating Two-Pass Smooth Square Channel With Sharp 180-Deg Turns," Int. J. Heat Mass Transfer, **47**, pp. 3215–3221.
[48] Murata, A., and Mochizuki, S., 2004, "Aiding and Opposing Contributions of Centrifugal Buoyancy on Turbulent Heat Transfer in a Two-Pass Transverse- or Angled-Rib-Roughened Channel With Sharp 180° Turns," Int. J. Heat Mass Transfer, **47**, pp. 3721–3743.
[49] Germano, M., Piomelli, U., Moin, P., and Cabot, W. H., 1991, "A Dynamic Subgrid-Scale Eddy Viscosity Model," Phys. Fluids A, **3**, pp. 1760–1765.
[50] Tafti, D. K., 2005, "Evaluating the Role of Subgrid Stress Modeling in a Ribbed Duct for the Internal Cooling of Turbine Blades," Int. J. Heat Fluid Flow, **26**, pp. 92–104.
[51] Tafti, D. K., 2001, "GenIDLEST—A Scalable Parallel Computational Tool for Simulating Complex Turbulent Flows," *Proceedings of the ASME Fluids Engineering Division, FED*, ASME-IMECE, New York, p. 256.
[52] Abdel-Wahab, S., and Tafti, D. K., 2004, "Large Eddy Simulation of Flow and Heat Transfer in a 90° Ribbed Duct With Rotation—Effect of Coriolis Forces," *Proceedings of the ASME Turbo Expo 2004*, Vienna, Austria, *ASME Paper No. GT2004-53796*.
[53] Abdel-Wahab, S., and Tafti, D. K., 2004, "Large Eddy Simulation of Flow and Heat Transfer in a 90° Ribbed Duct With Rotation—Effect of Buoyancy Forces," *Proceedings of the ASME Turbo Expo 2004*, Vienna, Austria, *ASME Paper No. GT2004-53799*.
[54] Abdel-Wahab, S., and Tafti, D. K., 2004, "Large Eddy Simulation of Flow and Heat Transfer in a Staggered 45° Ribbed Duct," *Proceedings of the ASME Turbo Expo 2004*, Vienna, Austria, *ASME Paper No. GT2004-53800*.
[55] Incropera, F. P., and DeWitt, D. P., 2002, *Fundamentals of Heat and Mass Transfer*, 5th ed., Wiley, New York.
[56] Sewall, E. A., Tafti, D. K., Graham, A., and Thole, K. A., 2005, "Experimental Validation of Large Eddy Simulations of Flow and Heat Transfer in a Stationary Ribbed Duct," Int. J. Heat Fluid Flow (accepted).
[57] Han, J. C., 1988, "Heat Transfer and Friction Characteristics in Rectangular Channels With Rib Turbulators," ASME J. Heat Transfer, **110**, pp. 321–328.
[58] Fann, S., Yang, W.-J., and Zhang, N., 1994, "Local Heat Transfer in a Rotating Serpentine Passage With Rib-Roughened Surfaces," Int. J. Heat Mass Transfer, **37**, pp. 217–228.
[59] Taslim, M. E., and Wadsworth, C. M., 1997, "An Experimental Investigation of the Rib Surface-Averaged Heat Transfer Coefficient in a Rib-Roughened Square Passage," ASME J. Turbomach., **119**, pp. 381–389.

Vita

Evan Sewall was born and raised in Little Rock, AR. He graduated from high school in 1997 and completed a Bachelor of Engineering (B.E.) degree at John Brown University in Siloam Springs, AR, in May, 2001. The following Fall, Evan started in the Masters program at Virginia Tech and graduate with his M.S. degree in Mechanical Engineering in December, 2002. His Master's Thesis was entitled "Development of a Thermal Design Methodology for a Front-End DPS Power Supply." He started work immediately on his Ph.D. and is graduating with the degree in December, 2005. His dissertation is entitled "Large Eddy Simulations of Flow and Heat Transfer in the Developing and 180° Bend Region of Ribbed Gas Turbine Blade Internal Cooling Ducts with Rotation – Effect of Coriolis and Centrifugal Buoyancy Forces." He plans to start a career at GE Global Research in Niskayuna, NY, in January, 2006.

Currently the following references are a result of Evan's work:

Graham, A., Sewall, E., Thole, K.A., 2004, "Flowfield Measurements in a Ribbed Channel Relevant to Internal Turbine Blade Cooling," Proceedings of ASME Turbo Expo 2004, June 14-17, Vienna, Austria, ASME Paper No. GT2004-53361.

Sewall, E.A., Tafti, D.K., 2004, "Large Eddy Simulation of the Developing Region of a Stationary Ribbed Internal Turbine Blade Cooling Channel," Proceedings of ASME Turbo Expo 2004, Vienna, Austria, ASME Paper No. GT2004-53832.

Sewall, E.A., Tafti, D.K., 2004, "Large Eddy Simulation of the Developing Region of a Rotating Ribbed Internal Turbine Blade Cooling Channel," Proceedings of the ASME Turbo Expo 2004, Vienna, Austria, ASME Paper No. GT2004-53833.

Sewall, E.A., Tafti, D.K., Graham, A.B., Thole, K.A., 2005, "Experimental Validation of Large Eddy Simulations of Flow and Heat Transfer in a Stationary Ribbed Duct," *International Journal of Heat and Fluid Flow*, In Press.

Sewall, E.A., Tafti, D.K., 2005, "Large Eddy Simulation of Flow and Heat Transfer in the Developing Flow Region of a Rotating Gas Turbine Blade Internal Cooling Duct with Coriolis and Buoyancy Forces," Proceedings of ASME Turbo Expo 2005, Reno-Tahoe, Nevada, 2005, ASME Paper No. GT2005-68519.

Sewall, E.A., Tafti, D.K., 2005, "Large Eddy Simulation of Flow and Heat Transfer in the 180º Bend Region of a Stationary Ribbed Gas Turbine Internal Cooling Duct," Proceedings of ASME Turbo Expo 2005, Reno-Tahoe, Nevada, 2005, ASME Paper No. GT2005-68518.

Sewall, E.A., Tafti, D.K., 2005, "Large-Eddy Simulation of Flow and Heat Transfer in the 180-Deg Bend Region of a Stationary Gas Turbine Blade Ribbed Internal Cooling Duct," ASME Journal of Turbomachinery, **128**, pp. 1-9.